ON RECESSED CAVITY FLAME-HOLDERS IN SUPERSONIC CROSS-FLOWS

A Thesis
Presented to
The Academic Faculty

by

Ghislain J. Retaureau

In Partial Fulfillment
of the Requirements for the Degree
Doctor of Philosophy in the
School of Aerospace Engineering

Georgia Institute of Technology
May 2012

ON RECESSED CAVITY FLAME-HOLDERS IN SUPERSONIC CROSS-FLOWS

Approved by:

Suresh Menon, Advisor
School of Aerospace Engineering
Georgia Institute of Technology

Jechiel I. Jagoda
School of Aerospace Engineering
Georgia Institute of Technology

Jerry M. Seitzman
School of Aerospace Engineering
Georgia Institute of Technology

David E. Scarborough
School of Aerospace Engineering
Georgia Institute of Technology

Robert W. Pitz
School of Mechanical Engineering
Vanderbilt University

Date Approved: March, 30th 2012

To my parents.

ACKNOWLEDGEMENTS

In looking back at my academic journey, I must acknowledge several individuals whose love, support, and guidance have made this dissertation possible. For this, I am eternally thankful and graciously indebted. For as Einstein has said: "if we see far, it is because we have stood on the shoulders of giants." This is true for my own personal education as it is in Einsteins original context of the progress of science and understanding of our world.

There are countless friends, fellow students at the Combustion Laboratory, and professors who deserve mention but cannot possibly be enumerated with realistic brevity. I am obliged instead extend my sincerest thanks the following incomplete group of individuals for their noteworthy impact: Prof. Michel Bruneau who enabled my long love with Matlab and calculated science, Prof. Bob Mahan for the gracious extension of a scholarship with Georgia Tech, and Prof. Serge Lewy for his support and our long discussions on aeroacoustics. At Georgia Tech, I must give my sincerest thanks to Prof. Jechiel Jagoda, who has helped me repeatedly in dire straits.

Among my friends, there are several who stand out for their support. Firstly, I must thank Lander Ibarra and Arnaud Thabot, who made the frightening pilgrimage with me from France to a whole new life at Georgia Tech. I must also thank my best friends Robert Combier and Adam Maser for their incredible humor, sarcasm, and cunning sense of "We need to do something now, the clock is ticking". This is as much yours as it is mine.

I also would like to thank an off-the-chart beautiful and smart girl, my partner Lucy Petrova for her love, her kind support, and her understanding.

I must also acknowledge my dear family: especially my mother Catherine, for her

unwavering love and encouragement. In my darkest, most hopeless moments, she reignited my passion and determination to complete this academic adventure. *Ma chre Maman, je tadore, et je te remercie infinitivement.* I must also thank my father, who shares with me a love for engineering and a spirit of *Tu le dis pas a maman, OK?* (Don't tell mum, Ok?). My brother Antoine and my sister Cecile, deserve a sincere *Merci!* as well.

Finally, this thesis would not exist without the continuing support of my thesis committee advisor Prof. Suresh Menon who has bet on me to take care of the experimental research. Over the last 5 years you have been my professor, advisor, mentor, and sometimes tormentor. I can think of no appropriate mechanism of thanks other than to dedicate the scramjet rig and its design to you.

TABLE OF CONTENTS

LIST OF TABLES

LIST OF FIGURES

NOMENCLATURE

A

A	: Pre-exponential factor	
A_{aft}	: Aft step surface area	(m^2)
A_e	: Exit cross-section area	(m^2)
A_i	: Surface area of the i-th inner side of the cavity	(m^2)
A_t	: Throat cross-section area	(m^2)
A^*	: Cross-section area at M=1 (throat)	(m^2)
A_{δ_ν}	: Effective boundary layer cross-section area	(m^2)
a	: Reference contour offset parameter	
alt	: Altitude	(m)

B

b	: Arrhenius temperature exponent	

C

C_I	: Characteristic constant of the C_I-curve	
$C_{I,i}$	: C_I constant of C_I-curve emanating from node i	
C_{II}	: Characteristic constant of the C_{II}-curve	
$C_{II,i}$	: C_{II} constant of C_{II}-curve emanating from node i	
c	: Speed of sound	$(m\ s^{-1})$
c_p	: Specific heat capacity	$(J\ kg^{-1}K^{-1})$
$c_{p,a}$	: Actual specific heat	$(J\ kg^{-1}K^{-1})$
$c_{p,r}$	: Reference specific heat	$(J\ kg^{-1}K^{-1})$

D

D	: Cavity depth	(m)
Da	: Damkohler number	
$d(,)$	: Distance operator	

E

$\mathbf{e}_i$	: Unit vector of the Euclidian basis in the $i-th$ direction	

F

$[F]$	: Fuel concentration	$(mol\ m^{-3})$
f	: Reference contour function	

G

H

H	: Gate function	
$h+$	: Incoming mixture enthalpy	$(J\ g^{-1})$
$h-$	: Outcoming mixture enthalpy	$(J\ g^{-1})$
H_i^+	: Molar enthalpy of incoming species i	$(J\ mol^{-1})$
H_i^-	: Molar enthalpy of outcoming species i	$(J\ mol^{-1})$
	:	
h_o	: Stagnation enthalpy	$(J\ g^{-1})$

I

Ign	: Igniter	

J

K

K_V	: K-factor	
K	: Reference contour amplitude parameter	
k_s	: Reference contour stiffness parameter	
k	: Heat conductive coefficient	$(W\ m^{-1}\ K^{-1})$
k_r	: Rate constant	$(m^3\ mol\ s^{-1})$

L

L	: Cavity length	(m)
l_o	: Reference contour arclength	
l'_o	: Center of the gate for quality factor	

M

M	: Mach number	
M_{CH_4}	: Molar mass of methane	$(g\ mol^{-1})$
$M_{C_2H_4}$	: Molar mass of ethylene	$(g\ mol^{-1})$
M_{cf}	: Cross-flow Mach number	
M_a	: Molar mass of air	$(g\ mol^{-1})$
M_{H_2}	: Molar mass of hydrogen	$(g\ mol^{-1})$
M_i	: Mach number in the i-th direction	
M_{flight}	: Flight Mach number	
M_∞	: Free stream Mach number	
m	: Cavity mass	(kg)
m	: Mass	(kg)
$\dot{m}$	: Mass flow rate	$(kg\ s^{-1})$

$\dot{m}_a$	: Cavity air mass flow rate	$(kg\ s^{-1})$
$\dot{m}_{air}$	: Cross-flow air mass flow rate	$(kg\ s^{-1})$
$\dot{m}_{air,inviscid}$	: Inviscid air mass flow rate (cross-flow)	$(kg\ s^{-1})$
$\dot{m}_{a,stoic}$	: Stoichiometric air mass flow rate (cavity)	$(g\ s^{-1})$
$\dot{m}_{CH_2}$	: Methane mass flow rate	$(g\ s^{-1})$
$\dot{m}_{C_2H_4}$	: Ethylene mass flow rate	$(g\ s^{-1})$
$\dot{m}_f$	: Fuel mass flow rate	$(g\ s^{-1})$
$\dot{m}_{H_2}$	: Hydrogen mass flow rate	$(g\ s^{-1})$
$\dot{m}_{air,max}$	: Maximum mass flow rate (cross flow)	$(kg\ s^{-1})$
$\dot{m}_{O_x}$	: Oxidizer mass flow rate	$(g\ s^{-1})$
m_P	: Pressure exponent	
m_T	: Temperature exponent	
$\dot{m}^+$	: Incoming mass flow rate	$(g\ s^{-1})$
$\dot{m}^-$	: Outcoming mass flow rate	$(g\ s^{-1})$
$\dot{m}_a^*$	: Characteristic air mass flow rate (cavity)	$(kg\ s^{-1})$

N

n	: Number of nodes	
n	: Surface normal vector	
$\dot{n}_i$	: Molar flow rate of species i	$(mol\ s^{-1})$
n_s	: Number of species	

O

$[O_x]$	: Oxidizer concentration	$(mol\ m^{-3})$
o	: Frame origin	

P

P	: Static pressure	(Pa)
P_{cav}	: Cavity floor pressure	(Pa)
P_{fb}	: Fuel back pressure	(Pa)
P_i	: Pressure port i	(Pa)
P_{inj}	: Injector pressure	(Pa)
P_o	: Stagnation pressure	(Pa)
$P_{o,c}$	: Combustor stagnation pressure	(Pa)
$P_{o,max}$	: Maximum stagnation pressure	(Pa)
$P_{o,\infty}$	: Free stream stagnation pressure	(Pa)
P_s	: Storage pressure	(Pa)

P_{strat}	: Stratospheric pressure	(Pa)
P_{trop}	: Tropospheric pressure	(Pa)
P_{cf}	: Cross-flow static pressure	(Pa)

Q

$\dot{Q}_{aft}$	: Aft ramp wall heat loss	(W)
$\dot{Q}_w$	: Wall heat loss	(W)
$\dot{Q}_{w,cav}$	: Cavity wall heat loss	(W)
$\dot{q}_w$	: Wall heat flux	$(W\ m^{-2})$

R

R	: Gas constant	$(J\ kg^{-1}\ K^{-1})$
R_u	: Universal gas constant	$(J\ K^{-1}\ mol^{-1})$
$\mathbf{r}$	: Position vector	
r_o	: Position vector	
r_{st}	: Stoichiometric fuel-air ratio	

S

S_{Lo}	: Stoichiometric laminar burning velocity at 300 K, 1 atm	$(m\ s^{-1})$
$[s]$	: Mixture molar concentration	$(mol\ m^{-3})$
s_i	: Time-smoothed signal i	
$[s^+]$	: Incoming mixture concentration	$(mol\ m^{-3})$

T

T	: Static temperature	(K)
T_a	: Activation temperature	(K)
T_{cf}	: Cross-flow static temperature	(K)
T_{cav}	: Cavity floor temperature	(K)
T_f	: Fuel temperature	(K)
T_o	: Stagnation temperature	(K)
$T_{o,max}$	: Maximum stagnation temperature	(K)
T_{O_x}	: Oxidizer temperature	(K)
T_p	: Product temperature	(K)
T_s	: Storage temperature	(K)
T_{strat}	: Stratospheric temperature	(K)
T_{trop}	: Tropospheric temperature	(K)
t	: Time	(s)

U

$\mathbf{u}$	: Velocity vector	$(m\ s^{-1})$
u_{cav}	: Cavity velocity (shear layer bottom)	$(m\ s^{-1})$
u_i	: Velocity component in the i-th direction	$(m\ s^{-1})$
u_∞	: Free stream velocity	$(m\ s^{-1})$

V

V	: Cavity volume	(m^3)
$\dot{V}_{fuel}$	: Volumetric flow rate of fuel	$(m^3\ s^{-1})$
$\dot{V}_{N_2}$	: Volumetric flow rate of nitrogen	$(m^3\ s^{-1})$
V_s	: Storage volume	(m^3)

W

W	: Cavity width	(m)
w	: Gate quality factor	
w_w	: Quality factor	
w_1	: High quality factor	
w_2	: Low quality factor	

X

X_i	: Abscissa of node i
$X_{ij}^{C_I \cap C_{II}}$	: Abscissa of intersection between C_I and C_{II}-curves
x_i	: Axis in the i-th direction
x^*	: Normalized abscissa (unit throat height)

Y

Y_{CH_4}	: Methane mass fraction
$Y_{C_2H_4}$	: Ethylene mass fraction
Y_{H_2}	: Hydrogen mass fraction
$Y_{ij}^{C_I \cap C_{II}}$	: Ordinate of intersection between C_I and C_{II}-curves
Y_i	: Ordinate of node i
y^*	: Normalized Ordinate (unit throat height)

Z

α

α	: Mach angle	(rad)
α_o	: Thermal diffusivity of fuel-air mixture at 300 K, 1 atm	$(m^2\ s{-}1)$

β

β	: Aft ramp angle	$(^o)$

Γ, γ

γ	: Ratio of specific heats	
Γ_o	: Contour	

Δ, δ

$\Delta\dot{m}_{air}$	: Mass flow rate correction term for boundary layer	$(kg\ s^{-1})$
ΔT	: Temperature difference	(K)
Δn_i	: Stoichiometric molar change of species i	(mol)
δA_t	: Error on throat cross-section area	(m^2)
$\delta\dot{m}_a$	: Error on air mass flow rate	$(kg\ s^{-1})$
δP_o	: Error on stagnation pressure	(Pa)
δT_o	: Error on stagnation temperature	(K)
$\delta\gamma$	: Error on specific heat ratio	
$\bar{\delta}_\nu$	: Viscous boundary layer average thickness	(m)

θ

θ	: Flow or deflection angle	(rad)
θ_{max}	: Maximum flow angle	(rad)

λ

λ_i	: i-th root	

ν

ν	: Prandtl-Meyer angle	(rad)
ν_e	: Prandtl-Meyer angle at nozzle exit	(rad)

ρ

ρ	: Fluid density	$(kg\ m^{-3})$
ρ_a	: Actual fluid density	$(kg\ m^{-3})$
ρ_{cav}	: Cavity average density	$(kg\ m^{-3})$
ρ_{cf}	: Cross-flow density	$(kg\ m^{-3})$
ρ_r	: Reference fluid density	$(kg\ m^{-3})$
ρ_∞	: Free stream density	$(kg\ m^{-3})$

τ

τ_{bd}	: Characteristic blow down time	(s)
τ_c	: Characteristic time scale for chemistry	(s)
$\tau_{chem,1}$	: Characteristic time scale for fast chemistry	(s)
$\tau_{chem,2}$	: Characteristic time scale for slow chemistry	(s)
τ_d	: Time to reach the shear layer from injectors	(s)
τ_f	: Characteristic time scale for flow	(s)
τ_i	: Time length for sliding average i	(s)
τ_i	: Turn over time of recirculation i	(s)
τ_{ign}	: Ignition delay	(s)
τ_p	: Product residence time	(s)
τ_r	: Characteristic response time	(s)
τ_{run}	: Runtime	(s)
τ_{sh}	: Shear layer residence time	(s)

Φ, ϕ

Φ	: Fuel-air equivalence ratio	
ϕ	: Velocity potential	(s^{-1})

η

η	: Progress variable	

ω

$\dot{\omega}$	: Reaction rate	$(mol\ m^{-3}\ s^{-1})$
$\dot{\omega}_i$	: Reaction rate of the i-th reaction	$(mol\ m^{-3}\ s^{-1})$
$\dot{\omega}_{NRG}$	: Energy based reaction rate	$(mol\ m^{-3}\ s^{-1})$
$\dot{\omega}_{TS}$	: Time scale based reaction rate	$(mol\ m^{-3}\ s^{-1})$

Misc.

$()^*$	: Quantity evaluated at the throat
LES	: Large Eddy Simulation
LEMLES	: Linear Eddy Modelling Large Eddy Simulation
SCM	: Standard Cubic Meter
SCMPS	: Standard Cubic Meter Per Second
SLPM	: Standard Liter Per Minute

All pressures are absolutes.

SUMMARY

Flame-holding in a recessed cavity is investigated experimentally in a Mach 2.5 preheated cross-flow for both stable and unstable combustion, with a relatively low preheating. Self-sustained combustion is investigated for stagnation pressures and temperatures reaching 1.4 MPa and 750 ^{o}K. In particular, cavity blowout is characterized with respect to cavity aspect ratio ($L/D = 2.84 - 3.84$), injection strategy (floor - ramp), aft ramp angle ($90 - 22.5^o$) and multi-fuel mixture ($CH_4 - H_2$ or $CH_4 - C_2H_4$ blends). The results show that small hydrogen addition to methane leads to significant increase in flame stability, whereas ethylene addition has a more gradual effect. Since the multi-fuels used here are composed of a slow and a fast chemistry fuel, the resulting blowout region has a slow (methane dominant) and a fast (hydrogen or ethylene dominant) branch. Regardless of the fuel composition, the pressure at blowout is close to the non-reacting pressure imposed by the cross-flow, suggesting that combustion becomes potentially unsustainable in the cavity at the sub-atmospheric pressures encountered in these supersonic studies. The effect of preheating is also investigated and results show that the stability domain broadens with increasing stagnation temperature. However, smaller cavities appear less sensitive to the cross-flow preheating, and stable combustion is achieved over a smaller range of fuel flow rate, which may be the result of limited residence and mixing time. The blowout data point obtained at lower fuel flow rate fairly matches the empirical model developed by Rasmussen et al. [81] for floor injection $\Phi = 0.0028 D_a^{-.8}$, where Φ is the equivalence ratio and D_a the Damkohler number. An alternate model is proposed here that takes into account the ignition to scale the blowout data. Since the mass of

air entrained into the cavity cannot be accurately estimated and the cavity temperature is only approximated from the wall temperature, the proposed scaling has some uncertainty. Nevertheless the new $\Phi - D_a$ scaling is shown to preserve the subtleties of the blowout trends as seen in the current experimental data.

CHAPTER I

INTRODUCTION

Hypersonic flight is commonly achieved with the use of rocket engines, which provide a constant impulse independently from the flight Mach number. Such engines use onboard oxidizer reserves that drastically increase the weight of the overall vehicle and lead to a limited range and payload. The introduction of an air breathing engine for hypersonic flights is considered a desirable alternative for stratospheric flights in terms of weight and component layout optimization, since the air is provided from the atmosphere as in conventional jet engines. However, the development of a hypersonic air breathing engine remains a considerable engineering challenge due to the conditions encountered at high Mach numbers. In particular, the challenge is to have a fully operational Supersonic Combustion Ramjet (Scramjet), in which the flow entering the combustor has to remain supersonic since a complete deceleration to subsonic speeds would cause significant enthalpy losses, and therefore a poorer pressure recovery and a higher drag. The Scramjet is a concept in which the hypersonic inflow is conditioned through a diffuser and brought to a lower but supersonic Mach number using a series of oblique shocks as shown in Fig. 1. The post shock conditions provide higher static pressures and temperatures (Ram effect) that are beneficial to the combustion process.

The residence time remains small, regardless, and thus limits the fuel-air mixing and therefore the combustion completion in the engine. The flow in the combustor reaches 400 m/s at the Ramjet-Scramjet transition flight regimes (lower limit) whereas this study deals with cross-flow velocities of about 900 m/s. These values are tremendously higher than any laminar flame speed, which is the order of a few meters per second. Even when accounting for the turbulent transport, the velocity at which the flame counter-progresses is still far beyond the airstream velocity such that no direct flame anchoring is possible. High speed flows are, in fact, used to extinguish fires [24]; and the key is to have stable combustion, since blowout is inevitable if no flame stabilization method is used. Moreover, in order to produce a steady hypersonic flight, the combustion has to be efficient enough to overcome the losses occurring in the engine and the overall drag of the aircraft. To overcome this problem, design solutions have recourse to efficient flame-holding techniques. There are several ways commonly employed for the stabilization of flames in a supersonic airstream :

- When partially or fully mixed fuel-air interacts with a shockwave.
- By creating a recirculation region in which fuel and air mix and react at lower speeds.
- When unmixed fuel and air are present in coherent structures and a diffusion driven burning process takes place.

As indicated previously, non-premixed combustion with fuel injected into a supersonic cross-flow is challenging; this is due to the short residence times in the combustor which limits the overall mixing. Ignition and flame stabilization in a Scramjet combustor have remained as major issues for a long time and are still of current interest -even when hydrogen is considered as a fuel [68, 72, 73]. When hydrocarbon fuels (e.g., ethylene or kerosene [91, 97, 103]) are used, additional issues arise in terms of liquid fuel vaporization and mixing time delay that have to be accounted for.

Transverse injection comes first as the most intuitive choice, in which fuel is directly injected into the high speed cross-flow [16, 17]. The fuel jet appears as a perturbation to the flow, which undergoes a multiple shock formation leading to boundary layer separation in the vicinity of the injection site. Nonetheless, the increased pressure, temperature and mixing (notably streamwise vorticity) that results from this injection method provide adequate conditions to anchor the flame in the downstream region. However, such a technique induces large pressure losses due to the strong bow shocks formed by the fuel jet. These losses can be reduced by using an angled injection; however, the auto-ignition point shifts further downstream [64]. Therefore, this type of injection needs to be complemented by a flame-holding technique to provide sufficient flame anchoring [58, 44], and remains a matter of interest since primary fuel injection is achieved from the upstream walls of the combustor [63]. In addition, substantial mixing is achieved when operating in dual-mode ($M_\infty \approx 4$), due to the presence of the pre-combustion shock train that produces a local flow separation and forms a large low-momentum region near the side walls [9]. As a result, the flame progresses from the side to the centerline. In contrast, there is a relatively limited mixing in a full supersonic combustor, due to less shock-induced flow distortion and a short residence time. Under this type of regime, the flame anchoring mechanism relies on higher flow enthalpies, above $M_\infty = 5$, as well as a greater interaction with the flame-holders.

The stabilization of the mainstream combustion is usually ensured by the presence of flame-holders, which provide adequate conditions for flame anchoring. Several types of flame-holders have been tested in the past and are discussed further below. The flame-holders are modifications in the duct geometry such as obstacles (protrusion) or cavities (recession). Under supersonic regimes, the presence of these features induces the creation of shocks and shears layers, in which substantial fuel-air mixing is achieved. Spatially evolving reacting shear layers is one canonical configuration to

understand flame stabilization in supersonic mainstreams [71, 78]. It is noted that the combustion affects the shear layer structure in several ways: the turbulent level increases with the combustion intensity, and reduces the presence of coherent structures. As a result, the shear layer growth is governed by volumetric expansion from the heat release, rather than by pairing process. The heat release may shift or change the shear layer alignment.

Bluff bodies in supersonic combustion were first encountered in after burners and rocket exhausts. They remained the one key flame stabilization strategy during the 60-70's, and were also used in ramjet configurations [28, 94, 66]. Bluff bodies (e.g., compression ramps) that protrude into the supersonic flow have been shown to improve mixing and flame stabilization by creating a recirculation region in their wake. This technique is still considered as a potential alternative for flame stabilization in a supersonic flow. Recent improvements on strut design have focused on mixing enhancement such as increasing streamwise vorticity by creating multiple steps on the trailing section of the body, in the spanwise direction [31]. The implementation of protruding bodies in the supersonic airstream can also result in pressure losses. As a consequence, there is a trade-off between flow intrusion and efficiency: the larger the obstacle the smaller the recovery factor. That is why smaller struts are currently studied [45, 34]. In order for the flame to spread across the mainstream, staggered ramps and struts were also studied [10]. Both configurations have about the same total pressure recovery at the combustor exit, however struts exhibit a better mixing efficiency.

In the experimental studies discussed above, pressure, temperature and flow rate measurements are commonly used to monitor the combustor regime. Nevertheless, non-intrusive methods are generally preferred when dealing with supersonic flows since the presence of probes and junctions produce undesired shocks which alter the downstream part of the flow. Flow visualizations, such as laser doppler velocimetry

[78] or hydroxyl tagging velocimetry measurements [52], give spatially resolved velocity fields, while Raman scattering experiments [77] reveal the chemical composition of the mixture.

In general, numerical and experimental studies are complementary approaches, in which experiments provide validation at some specific locations of the domain, while the numerical results allow entire flow fields to be analyzed. Regardless, the numerical studies suffer from the acute sensitivity of the kinetics while solving for complex flow fields. The VULCAN Navier-Stokes simulations conducted by Baurle et al. [12, 9] revealed that the results are relatively sensitive to choice of the turbulent and kinetic model. Complex models account for more intermediate reactions such as radical formation (OH, H and O), which may lead to endothermic steps in the early burn. As a result, no ignition may be observed depending on the kinetic model, since timing between the chemistry and the flow is critical. In addition, the modeled levels of turbulent mass and heat transfer have a drastic impact on the final solution, especially when the combustor is operated in dual-mode, due to the sensitivity of the pre-combustion shock-train [9]. The pronounced sensitivity of the simulations remains a limitation of the predictive capability of CFD models used to compute supersonic combustion problems, such that the numerical results need to be supported by the experimental measurements for the same geometry and conditions.

1.1 The Cavity Flame-Holding Technique

Cavity flame stabilization is an approach that has been explored in recent years [105, 11, 14, 59, 107] as a potential design for an operational scramjet. The fuel and air entering the cavity mix and react in a relatively lower speed recirculation flow. Since the cavity is submerged, pressure losses due to geometry generated shocks are reduced. The residence time being longer, mixing is more efficient and combustion is potentially more stable. This hot zone can then potentially act as an ignition or

flame-holding source for the remaining fuel that is injected into the supersonic cross stream (primary injection). However, cavity flame stabilization in a supersonic flow is still not properly understood since there are many factors, such as cross flow Mach number, temperature and turbulence level, cavity dimensions, fuel injection location and fuel type, that contribute to the combustion and the stabilization processes.

1.1.1 Definition of the case of study

Figure 2 shows the problem description chosen for this study. The global frame used to describe the domain D is defined by a direct basis $B(\mathbf{e}_i)_{i=1}^3$ and an origin O located at the leading edge of the cavity. Each point in D is characterized by its flow properties: density ρ, velocity $\mathbf{u}$, enthalpy h, pressure p, temperature T and mass fractions for each species $\mathbf{s}$. The fluid is compressible, perfect and Newtonian whose mass, momentum, energy and chemical kinetics are governed by the classical conservation laws and state equations:

$$\frac{\partial \rho}{\partial t} + \nabla.(\rho \mathbf{u}) = \dot{\rho}_s \tag{1}$$

$$\rho \frac{D\mathbf{u}}{Dt} = -\nabla p + \nabla.\left(\mu(\nabla u + \nabla u^T)\right) + \nabla(\lambda \nabla.u) \tag{2}$$

$$\rho \frac{Dh}{Dt} = \frac{Dp}{Dt} + \nabla.(k\nabla T) + \Phi_T \tag{3}$$

$$\frac{D\mathbf{s}}{Dt} = \dot{s}_s + (\nabla^T \mathbf{D} \nabla)s \tag{4}$$

$$P = \rho R T \tag{5}$$

where $\mathbf{D}$ is the diffusivity tensor. A fully developed supersonic airstream flows along the 1-direction in a channel infinitely high and wide, such that the geometry is nominally two-dimensional. The cavity is formed by an open volume adjacent to the channel. Its geometry is defined by three parameters, which are the length L, the depth D and the aft angle β. The fuel is injected in the cavity from a fuel injector located in the cavity typically at the floor or on the aft ramp.

1.1.2 Flame-Holder Geometry

Previous studies have examined the design of the cavity shape [14, 15]. The first experiments were carried out on rectangular cavities submerged in a two dimensional flow. In this case, the length and the depth are the only parameters, which characterize the cavity shape. Short cavities are said to be "open" (derived from acoustic terminology) when the shear layer re-attaches at the trailing edge. Consequently, this type of cavity exhibits greater flow field stability due to limited interaction with the cross-flow. The transition from open to close cavity occurs at aspect ratios (L/D) around 7. The cavity length also drives the mass exchange since air from the cross-flow enters the cavity through the shear layer. This aspect is discussed in more detail subsequently in this section.

The induced drag also increases with the cavity length [11], such that longer cavities are more likely to lower the recovery factor in the sense given by Baurle et al. [11]. In fact, the portion of air which enters the cavity experiences a drastic stagnation pressure loss as revealed by the sub-atmospheric pressures measured in the cavity. Therefore, the cavity length must be sized with the vessel height such that only a small portion of the overall air contributes to the flame-holding process. In contrast, the depth affects the residence time and no flame is observed if the depth is too small. Heller et al. [41] observed that the strength of the leading shock may also decrease with higher aspects ratios. The overall size of the cavity conditions the range of fuel flow rate over which combustion can be stabilized. As the cavity volume increases, the amount of mixture stored in the cavity is greater, such that there is more matter to react and support the reaction. That is why cavities with higher aspect ratios are stable over a greater range of fuel flow rates and provide larger heat release.

Some approaches suggest inclining the downstream step in order to modify the

characteristics of the shear layer. Decreasing the angle suppresses the acoustic feedback [8] and eventually changes the separation wave from a recompression wave to an expansion fan at lower angles. As a consequence, aft ramp cavities exhibit more stable, two dimensional flow fields than rectangular cavities [33]. This type of cavity also has a higher drag and a smaller residence time than their rectangular counterparts. Some designs also suggest decreasing the downstream step height, which allows the shear layer to progressively overshoot the trailing edge such that its effect is minimized. The residence time is generally estimated from laminar flow field calculations, however turbulent exchange has been shown to heavily impact the entrainment and ejection of mixture about the cavity [11], and is discussed subsequently in this section. The estimation of the residence time remains complex from both theoretical and experimental viewpoints.

1.1.3 Injection Strategy

Two type of injection schemes have been studied in the past, the first one is passive injection [107, 47] in which no fuel is injected in the cavity. Fuel and air mix upstream, and a portion of the mixture reacts in the shear layer of the cavity where mixing and residence time are more favorable to the combustion process. In contrast, an active injection setup has fuel being injected directly into the cavity [55, 67, 93]. The latter appears to be more desirable as it shows a greater stability compared to passive injection, since a relatively small amount of fuel from the main stream is entrained in the cavity [37, 83].

Various active injection strategies have been studied in the past [37]. Fuel was injected from the upstream edge, the floor or from the aft ramp of the cavity. It appeared that among the three injection locations, the ramp injection offers a stable combustion over a wider range of fuel flow rates, as it provides a more uniform fuel-air

distribution. In the case of floor injection, a greater portion of the fuel has a tendency to be ejected in the shear layer upper region, since floor injectors are oriented perpendicular to the supersonic cross flow. This is why the overall combustion is lean as observed by a large presence of OH radicals [80] when using floor injection. While fuel-air mixing is also a function of the fuel jet momentum, most of the tests have been carried out using injectors with different arrangement patterns and diameters, depending on their location (floor or ramp). Consequently, fuel was injected at different momenta for a given fuel flow rate, and the effect of fuel jet momentum is not clearly isolated from the effect of fuel location. Cavity injection location has also been studied with the presence of primary injection [36, 59, 48], but the knowledge of mechanisms that drive stability of cavity burning remains limited.

1.1.4 Fuel Type

Impact of fuel composition has also been investigated in the past, and cavities are generally fueled with hydrogen, methane or ethylene. Methane-fueled cavities usually exhibit a smaller stability domain than when being fueled with hydrogen or ethylene. This is primarily due to methane's slower kinetics [37, 82], such that the characteristics of the fuel-air chemistry are found in the overall combustor response, at least for these three gaseous fuels. JP-7 is also considered a potential fuel for initial on-board storage [60], and may be used as primary fuel with direct upstream injection. Some designs suggest using the fuel as a heat sink for cooling the flight vehicle. JP-7 is therefore expected to heat up and dissociate into smaller hydrocarbons. Separate studies on cracked JP-7 lead to several fuel blend compositions [79, 61, 70, 29] that attempt to capture the breakdown process. Nevertheless, there are no results in open literature on cracked JP-7 fueled cavities or optimum fuel composition against scramjet flight regime. Only a few types of fuel have been used to carry out cavity burning studies, and this does not provide a broad range of chemical times and heat contents to

provide evidence on the pure effect of kinetics. In addition, only a limited number of data points have been provided to isolate the blowout limit trends, especially in recent studies [80] where video diagnostics were used. Blowout limits are presented as boundaries, but these are rather extended regions in which probability of blowout becomes substantial.

1.1.5 Flame Location

The flame structure has been investigated by Rasmussen et al. [80] using OH- and CH_2O-PLIF visualizations at various locations and fuel flow rates. The study confirms that the reactions takes place mainly in the shear layer, and the flame sits on top of the hot product recirculation zone. The latter knowledge is essential for the understanding of flame stabilization mechanisms. The flow features are also altered by the injection location and strength, creating different concentration maps. That is why for instance, combustion with floor injection sustains at higher fuel flow rates, since the excess of fuel is ejected in the downstream region of the boundary layer.

1.2 Mass Transfer between Cavity and Cross-Flow

The shear layer is an important feature, it is the region where substantial mixing is achieved between fuel, oxidizer and products, and is generally where most of the reactions take place. The knowledge of the shear layer structure is crucial to characterize the mass transfer between the cavity and the cross-flow. The fuel flow rate can be determined, e.g., with mass flow controllers. However, the air enters the cavity through the shear layer with a relatively complex phenomenon, which is yet not fully understood. So far, most studies assume that air entrainment from the main stream into the cavity is driven by turbulent exchange only [25, 26]. The models used to estimate the air entrainment for cavities are derived from bluff body studies [99, 51, 100] in which mass transfer occurs through a free shear layer, therefore ignoring the presence of the trailing edge of the cavity. In addition, recent aeroacoustic studies on

recessed cavity revealed some of the complex structure of the shear layer. At the opposite of a free shear layer, the interactions between the leading and the trailing edge regions produce a closed loop flow system, which eventually exhibits classical receptivity characteristics.

This phenomenon was first modeled by Rossiter [87, 42] for an open cavity submerged in a subsonic and transonic cross-flow, and is relevant in the design of cavity flame-holders for scramjet applications [13]. The mechanism involves aeroacoustic interactions between the cavity and the shear layer. The shear layer interacts with the trailing edge and gives rise to acoustic disturbances. The latter propagate back to the leading edge and stimulate the creation of large vortical structures. The coherent relation between events taking place at both edges leads to a phase locking of the shear layer structure which in turn, can be tuned to the acoustic modes of the cavity for some particular Strouhal numbers (frequency$\times$length/velocity). In the presence of a supersonic cross-flow, the aeroacoustic feedback does not benefit from the upper (supersonic) part of the shear layer, since all acoustic disturbances are convected downstream, but acoustic waves propagate upstream in the subsonic part of the shear layer and the cavity. Thus, a complex mechanism takes place in which acoustic waves, shear layer and shock waves interact.

Figure 3 depicts the scenario according to which the aero-acoustic feedback reorganizes itself at supersonic regimes [109]. A Type 1 wave is attached to the leading edge and is technically a compression or expansion wave depending on if the shear layer "flaps" up or down, respectively. It is sometimes referred as a quasi-steady compression wave. The flapping characteristic of the shear layer is related to the creation of large coherent structures, which grow as they convect downstream. These structures cause the supersonic flow to be deflected, and therefore, induce a Type 2 wave (compression), which convects downstream with the structure itself. Depending on the shear layer mode, there may be several Type 2 waves. The interaction of the

shear layer and the trailing edge causes a bow shock or Type 3 wave. Studies have shown that addition-removal of mass is important in this region and can even become periodic if the shear layer mode couples to an acoustic mode of the cavity [41]. The bow shock - leading edge interaction generates acoustic disturbances which propagate back to the leading edge, through the cavity. Eventually, these internal waves perturb the shear layer forming a Type 4 wave in the cross-flow, which moves upstream at about the speed of sound in the cavity. The process involving Type 1-4 waves is closed loop and is fed energy by the cross-flow. Consequently, this phenomenon exhibits a high receptivity when acoustic and shear layer modes coincide. The cavity pressure oscillations affect the entrainment of the air from the cross-flow to the cavity by changing the vortex size and spacing in the shear layer as well as the downwash at trailing edge region.

One can argue that combustion has a tendency to disturb the shear layer by locally changing temperature and fluid composition. The coherent buildup of these oscillations may be altered under burning conditions, and the scenario discussed above may still occur, however, the effect may be considerably weakened. Numerical studies conducted by Wang et al. [98] showed that combustion inhibits the feedback loop and gives place to broad band turbulence. However, weakened oscillations are observed with non-reacting flow while fuel is injected in the cavity, such that this aeroacoustic phenomenon may be inherent to the ignition phase. This is why pure mixing studies are partially relevant to the combustion cases since combustion has a tendency to suppress the cavity acoustic instabilities [22]. It is however arguable to assume that the mass exchange occurs along the shear layer via turbulent exchange. Heller [41] emphasized the periodic mass addition-removal at the trailing edge, as the lower part of the shear layer is recirculated. This downwash may contribute importantly to the overall mass transfer, especially for rectangular designs where the aero-acoustic coupling discussed above is pronounced.

Studies on free shear layers revealed that its growth is related to the amount of air entrained from the cross-flow. In the description made by Dimotakis [25, 26] on free shear layers, the surrounding flow is assumed to be irrotational. The entrainment mechanism is then divided in three phases through which the irrotational fluid in the vicinity of the shear layer is progressively swept in the turbulent region (Fig. 4).

1. **Induction Phase :** The fluid in the vicinity of the vorticity-bearing region acquires lateral motion through the Biot-Savart induced velocity field. Although the fluid remains irrotational, it has large-scale structure motions and is considered as a part of the turbulent flow.

2. **Dystrophy :** Via successive entanglements, the inducted fluid enters a region of high shear in which it becomes rotational under action of viscosity and cascade down to viscous scales in the Kolmogorov sense.

3. **Infusion :** Additional diffusive processes such as molecular mixing and heat conduction may be considered beyond these scales. This phase may occur simultaneously with the previous one depending on the Schmidt numbers of the mixture present in the inner structure of the shear layer.

Based on this description, Dimokatis and Slessor [92] have derived a model for air entrainment that accounts for compressibility effects. It is therefore used as a common way to estimate of the equivalence ratio for the cavity.

1.3 Mixing Control

From this perspective, efforts have been spent in enhancing mixing, to increase the growth rate of the shear layer. Compressible boundary layers exhibit a remarkable stability, which is problematic when one wants to increase the mixing efficiency while limiting the pressure losses. One cavity enhanced mixing approach [106, 89] uses the acoustic-shear layer coupling described previously (Rossiter) in which the growth

rate is increased by the strengthening of the shear layer oscillations. Upon proper adjustment of the cross-flow velocity, longitudinal or transversal acoustic modes of the cavity can be strongly excited. A greater fraction of kinetic energy is taken from the supersonic cross-flow and transferred to coherent structures. As they convect downstream, these big rollers progressively turn into small-scale structures with intermixed air and fuel.

Recent studies on dual scramjet combustors [54] show that multiple thermo-acoustic instabilities can be produced from shock-flame or upstream injector-flame interactions. However, the feedbacks vanish once the test section becomes fully supersonic. Shock enhanced mixing [65] is another approach that is used to disturb the shear layer structure and increase its growth rate. A weak shock is generated from the opposite wall and is targeted toward the mixing layer. Disturbances are created from shock to shear layer interactions. Leading step design for mixing enhancement has also been considered in order to increase the streamwise vorticity using the presence of steps arranged in the spanwise direction [30] (three-dimensional cavities). As a result, strong spanwise pressure gradients are created at the step discontinuities inducing the formation of streamwise rolls. The back pressure is also known to influence the shear layer thickness [37] as high back pressures induce fast shear layer growth. This aspect is fundamentally interesting but is not practical from a scramjet application viewpoint since the back pressure is commonly low, because of the exit nozzle and the high altitude.

Recent advancements on flame-holding in supersonic flow include the use of plasma techniques to initiate the combustion process and anchor the flame. Applied to the case of cavity flame-holding [46], a plasma is seen both as a means to control the shear layer flow features and generate radicals which participate in the chemical reactions. In these cases, the complexity of the study is increased and fluid mechanics, kinetics and electromagnetism concepts have to be included in the analysis.

1.4 Stability of Cavity Flame-holders

Since the cavity is used to stabilize the primary flame in the supersonic main stream, the study of the cavity flame-holder stability comes first before implementing the primary injection. Some approaches attempt to characterize the stability of cavity burning alone with respect to some parameters of influence [82] such as supersonic cross-flow regime, the fuel type, the injection location and the cavity geometry. The estimation of the time scales has been derived for bluff bodies in supersonic flows with premixed flame in the past [110, 74] and were used to estimate the Damkohler number. This work has been adapted for direct cavity fueling by Driscoll et al. [27], and lead to the establishment of an empirical law for blowout limits [81]. However, there is a limited theoretical understanding of the phenomenon despite a group-scaling approach. Experimental results have shown that there exists some fuel mixtures that are more advantageous than others [82, 86], but the optimal fuel composition remains unknown. Some of these issues are addressed in this study. In particular, combustion and flame stability is investigated for different fuel mixtures as a function of cross-flow conditions (stagnation pressure and temperature), and cavity aspect ratio.

1.5 The Georgia Tech Scramjet Facility

The experimental campaign is carried out at the Georgia Tech Combustion Laboratory using a research combustor built explicitly for the study of supersonic combustion. The combustor is fed by a continuous blowdown system, including a heater to raise the flow enthalpy. In the first phase of the project a supersonic combustor facility is designed and built, and connects to the existing laboratory set up. However, the emulation of flight conditions from a ground facility is challenging especially for scramjet studies for which a considerable amount of fluid must be heated at high temperatures (1400-1600 K) in order to recreate the post ram conditions past the diffuser. As a consequence, the heating process typically requires above 1 MJ per

kg/s of air.

Some facilities overcome this problem by using a vitiation process [39, 53]. However, the airstream is contaminated with the vitiation products and this has consequences on the validity of the combustion measurements [95] since the kinetics involved in the reactions are heavily dependent on the incoming mixture composition. Instead, the Georgia Tech scramjet facility provides a Mach 2.5 preheated supersonic inflow at lower temperatures (T_o = 300 - 750 K) than the ones encountered during a scramjet flight. Thus, no attempt to reproduce a true flight conditions is possible here. Nevertheless, the non-vitiated heating provides cleaner inflow conditions albeit at lower values of preheat. The geometry is similar to the proposed designs and therefore this study provides some additional off-design operating conditions that could also be used for model development and validation.

1.6 Objectives

This study attempts to determine the cavity fueling strategy, for a set of cross-flow conditions, which ensure a stable burn. Flame stability is investigated in order to establish the range of conditions in which the flame is stabilized as well as for getting a better understanding on the mechanisms involved in the sustainment of the flame. The behavior of the flame holder is studied in a supersonic airstream without primary injection. The isolated response of the flame-holder is in fact useful to determine the initial range of fueling rates as well as a better understanding of flame stabilization on recirculating products. In an actual scramjet engine, cavity flame-holders must also perform without primary injection from a safety perspective and are sometime used as an ignition source. The presence of primary injection is expected to produce a shift in the stoichiometry toward the richer bounds as air incoming from the cross-flow is then seeded with fuel, such that it is important to find the range of fueling rate without primary fuel.

The following are the key objectives and rationales for this research:

1. **Design, build and validate a supersonic combustor facility.** This project requires a new facility for the study of supersonic combustion. The experimental setup extends from the Georgia Tech Aerospace Combustion Laboratory facility and proper flow conditioning must be achieved given the initial laboratory infrastructure capability to reach a target Mach number and a range of static pressure and temperature. As a new facility, the validation of the wind tunnel is first before beginning any combustion studies. The geometry and the range of condition must be relevant to actual scramjet engines as it is considered in the field, such that experimental results obtained with this setup are accepted in the current Scramjet study literature.

2. **Investigate Flame-Holding and Cavity Burning in a Supersonic Cross flow.** The second goal is to achieve cavity burning in a supersonic flow and quantify the range of static pressure and temperature for which the flame is stabilized. Cavity burning is demonstrated with new design (geometry and injection strategy) and conditions. In order to quantify the effect of free-stream pressure and temperature on flame stability, the facility is operated for a wide range of conditions. The combustion parameters such as the equivalence ratio and the Damkohler number are also investigated. This part of the study brings an insight on the typical environment and fueling conditions that are necessary to ensure combustion.

3. **Determine Sensitivity of Cavity Stabilized Flames to Preheating, Cavity Geometry and Fuel Type.** Since the cavity is used to stabilize a primary flame in the supersonic cross-flow, the sensitivity of the flame-holding mechanism is investigated as a function of the geometry, the injection location and the fuel type. This study quantifies the change of the stability domain with

respect to the preheating of the cross-flow, cavity geometry, fuel injection strategy and fuel type. This effort leads to the identification of the designs, the flow conditions and the fuels which provide enhanced flame-holding capabilities.

4. **Characterize Conditions for Cavity Blowout.** This goal is to identify the fundamental parameters which compete for the existence of the flame. Blowout events are fairly detectable because of the abrupt and large change of pressure, temperature and species concentration encountered during extinction. As a result, important information on flame stability can be extracted from cavity blowout. The flame structure must also be reported for some pertinent cases to identify the triggers in cavity blowout, and deduce complementary criterions on flame stability. The blowout data must be compared with common scaling laws on cavity blowout in supersonic cross-flow. Moreover, for better consistency, a relatively large number of blowout data points must be obtained on the same facility, since the data used by Rasmussen et al. [81] in their blowout model was collected from various setups, vessel and cavity configurations.

1.7 Task Summary

- **Task 1**: Build a supersonic combustor facility.
  (a) Identify technology and methods commonly used in the field of supersonic combustion.
  (b) Review the existing facility capabilities.
  (c) Deduce the global architecture of the overall test facility.
  (d) Estimate the flight simulation envelope given the current laboratory capability.
  (e) Design and build the wind tunnel, in particular the nozzle which is used to condition the flow at a targeted Mach number with the proper static

pressure and temperature range.

(f) Design and build the combustor while accounting for flexibility, optical access, flow rate, pressure and temperature measurements. The combustor design must minimize the number of junctions and potential misalignments to avoid undesired shocks.

(g) Design and build a control system and data acquisition platform.

(h) Consider safety issues through a risk assessment process.

- **Task 2**: Wind tunnel validation.

  (a) Identify shock features using flow visualization techniques. Compare with common literature on cavity submerged in a supersonic flow.

  (b) Evaluate the vessel Mach number and compare to the predicted one.

  (c) Verify the structural limits predicted by the components ratings.

- **Task 3**: Stable combustion. Evaluate the combustor response with respect to :

  (a) Cross flow static pressure

  (b) Cross flow static temperature

  (c) Fuel composition

  (d) Injection strategy

  (e) Cavity geometry

- **Task 4**: Study on stability. Characterize cavity blowout as a function of :

  (a) Cross flow static pressure

  (b) Cross flow static temperature

  (c) Fuel composition

  (d) Injection strategy

(e) Cavity geometry

- **Task 5**: Evaluate flow and reaction timescales for the test cases and deduce the Damkohler number.

- **Task 6**: Intersect the new data with available blowout studies using scaling laws.

1.8 Thesis Outline

Both stable and unstable combustion are studied for various fuel blends of methane-hydrogen and methane-ethylene. Methane is used as a main fuel and is supplemented its lower heat generation by the higher heat generation of hydrogen or of ethylene. Some of the characteristic properties of the various fuel blends tested in the experiments are obtained in a study on kinetics via numerical simulations.

The above task list suggests this document to be organized as follow : Chapter II is dedicated to the design of the Georgia Tech Scramjet facility. The discussion begins with Sections 2.1 and 2.2 on the reproduction of flight conditions from a ground test facility and emphasizes on its problematic as well as the common technologies used in the generation of supersonic flow pertaining to hypersonic flight. The relations between flight and ground conditions yield a particular wind tunnel design. The wind tunnel and the combustor design are reported in Section 2.3, and in particular, the capability of the Georgia Tech Scramjet Facility is compared to the existing Scramjet ground test facilities. The implementation of sensors, control systems, and safety procedures is discussed in Sections 2.5, 2.6 and 2.7.

The facility is then used to investigate stability of cavity burning. Information on the its basic operation is reported in Chapter III, with the methods used to trigger and identify blowout, in addition to some particular methods used to post process and represent the data. The experimental results are then reported in Chapter IV.

Stable combustion is first investigated with respect to cross-flow conditions, fuel composition, injection strategy, and cavity shape in Section 4.3. The typical conditions required for flame stabilization are therefore identified before unstable combustion is discussed in Section 4.4, where blowout is then studied with respect to some new fuel compositions, flow conditions and cavity geometries. The data is then analyzed with physical concepts in Chapter V. In particular, the blowout data is reported in Subsection 5.1. The results are then compared to the previous studies on cavity burning, using the model defined by Rasmussen et al. [81] in Section 5.3. In addition, an alternate scaling law for cavity blowout is derived from the data collected in this study and other physical concepts. The discussion ends on the role of energy balance and time scale matching in blowout in Section 5.4. Finally, the conclusion and the future plans are presented in Chapter VI and VII.

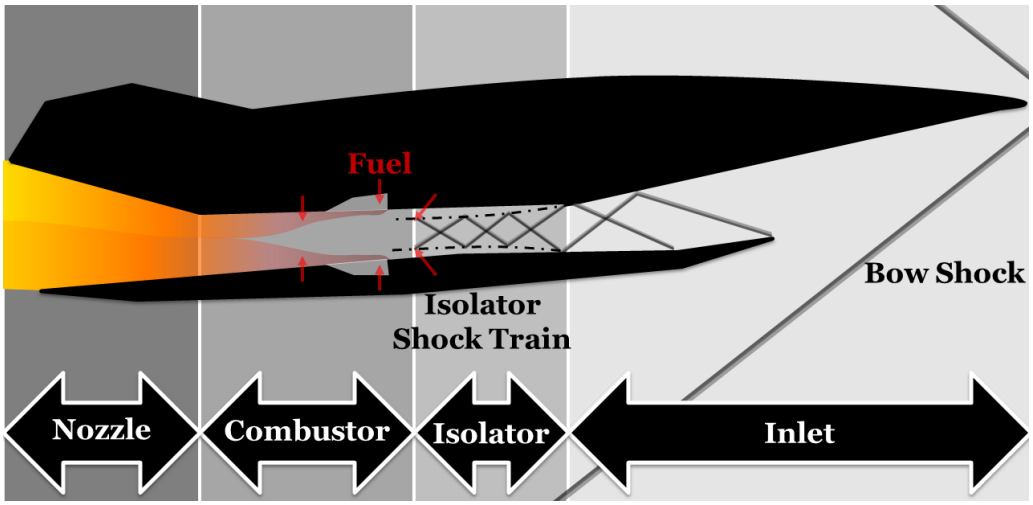

(a) A bow shock is caused by the overall aircraft structure moving into the stratospheric air at speeds above five times the speed of sound. The supersonic inflow is slowed down in the inlet and the isolator through a series of shocks (shock train). The flame main flame is anchored in the supersonic airstream with the help of cavity flame-holders (technology shown).

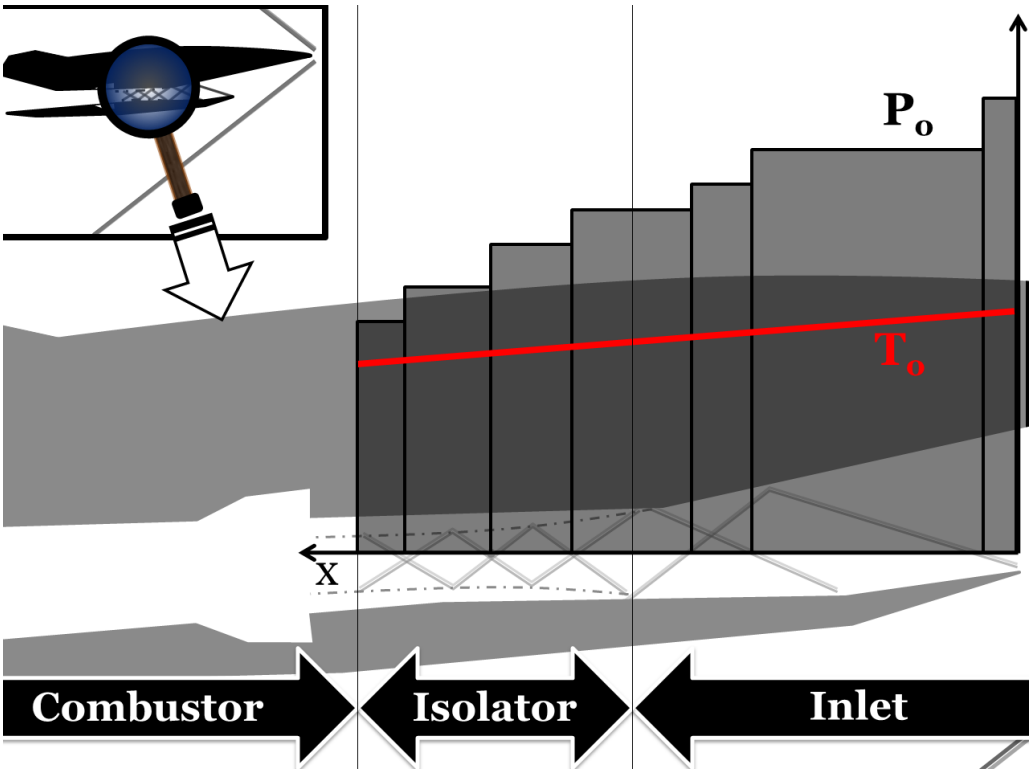

(b) Each shock produces an increase of static pressure and temperature, which favors for ignition and burn. However, this process is irreversible and the losses must be compensated by the combustion process for the engine to be efficient.

Figure 1: Illustration of the Supersonic Ramjet combustor concept and the main issues.

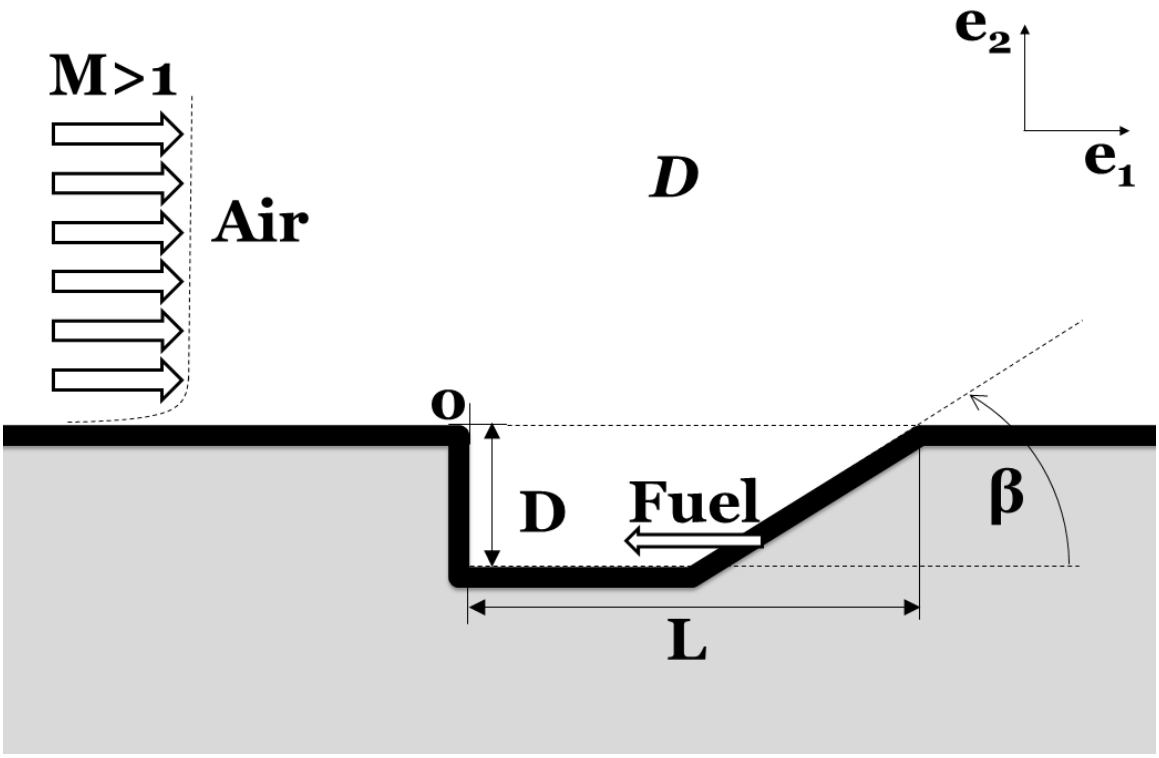

Figure 2: A recessed cavity in a supersonic airstream is fueled. The supersonic inflow and the fuel supply are inputs.

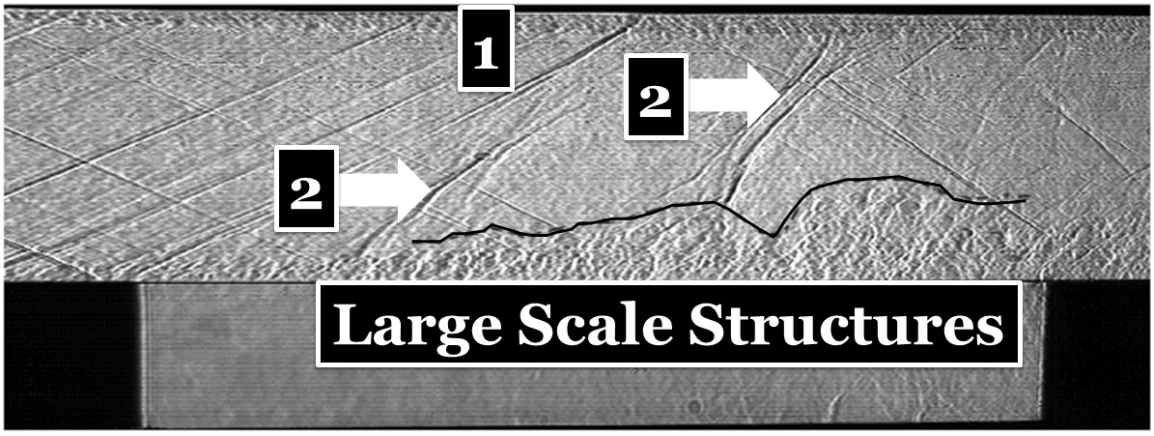

(a) Type 1 wave is a quasi-steady compression wave which emanates from the leading edge. Type 2 waves are compression waves which convect downstream with the large structures present in the shear layer.

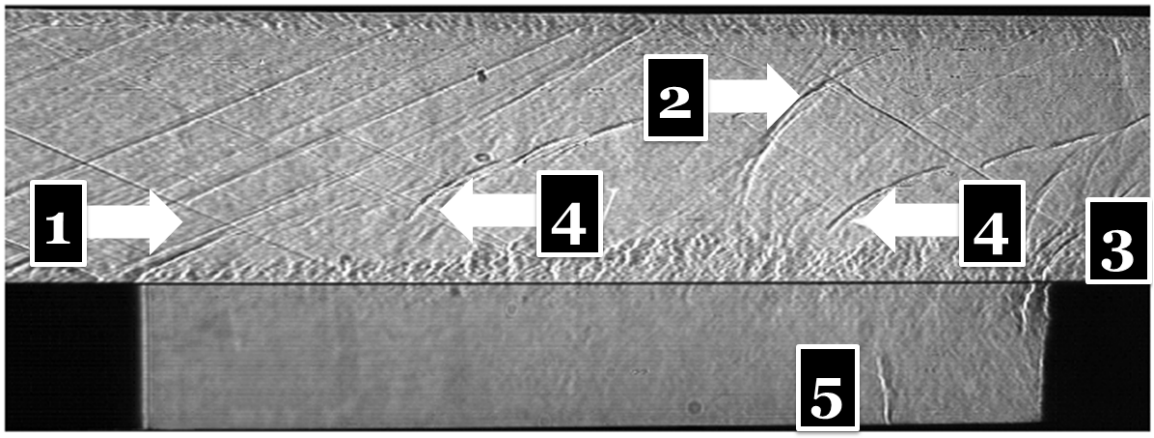

(b) Type 3 wave is the result of shear layer - trailing edge interaction. Type 4 waves are in fact generated by acoustic waves convecting back in the cavity. Type 5 wave observed by Zhuang et al. [109] appears at random locations such that its role in the mechanism is difficult to relate.

Figure 3: Aeroacoustic feedback under supersonic regime [109].

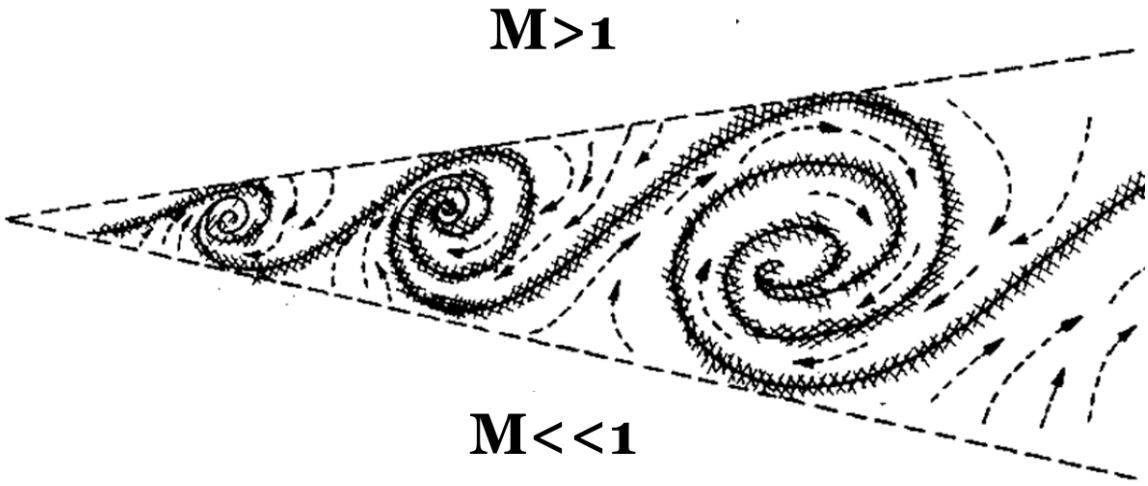

Figure 4: Mass entrainment in a free shear layer. Both upper and lower regions are assumed to be irrotational. The inducted and viscous fluid is indicated by the dashed and crosshatched lines, respectively. Solid line indicates molecularly mixed (high-Schmidt-number) fluid [25, 26].

CHAPTER II

DESIGN OF THE GEORGIA TECH SCRAMJET GROUND TEST FACILITY

The Georgia tech Scramjet facility has been designed and built for the purpose of this study and future prototyping effort on Scramjet studies, as mentioned in **Task 1**. The experimental setup is shown in Fig. 5. The structure is made of stainless steel, quartz and ceramic parts which can withstand high temperatures during an extended period of time. A supersonic wind tunnel can generate a supersonic flow with different stagnation temperatures in order to investigate the sensitivity of the combustor response to the flow enthalpy. The facility capability summary is given in Appendix B.

A wind tunnel brings the flow to the adequate conditions before entering the combustor. Parameters such as stagnation pressure and temperature can be varied during the tests for a nominal Mach number, and is held fixed under chocked conditions. Since reproducing hypersonic flight conditions from a ground facility remains a challenge, these conditions are only partially emulated, given the initial capability of the Georgia Tech Aerospace Combustion Laboratory. The static pressures and velocities generated by the wind tunnel may be equivalent to these encountered in a combustor during hypersonic flight, nevertheless due to heating capability limits, the stagnation enthalpy does not match the actual flight values. As a consequence, combustion is stabilized in a colder supersonic flow.

The wind tunnel is connected to the combustor, which is the focus of the main study. A particular design is studied in which fuel is injected in a recessed cavity. As noted in the Introduction, the cavity design offers less stagnation pressure loss due to

geometry generated shocks. The flow in the cavity is mainly subsonic and may have several recirculations, which provides a longer residence time.

A digital control system interface is designed for users to monitor and control the combustor regimes. The system records user actions, sensor and video data. A safety algorithm allows the control panel to warn or override a user action to prevent the facility from structural damages.

The relations between flight and ground test conditions are presented at the beginning of this section, and emphasizes on the problematic in emulating hypersonic flight from a ground test facility. A review of the technologies used to overcome the design challenges is made and is completed by a list of the main existing Scramjet ground test facilities. The design of the wind tunnel is presented in a step-by-step process, in which the capability of the Georgia Tech Aerospace Laboratory yields a particular vessel size and Mach number. The design of the combustor is then discussed in Section 2.4 and is then followed by the instrumentation of the facility. The last part of this section deals with the controls and the safety precautions put in place to manage system with high power.

2.1 Emulating Flight Condition from a Ground Test Facility

The emulations of hypersonic flight conditions in a ground facility is relatively challenging due to the high speed and high flow enthalpy which need to be reproduced by the test facility. This part of the study introduces the mechanisms and the systems that are used to put a fluid into motion, and bring it to the target flight conditions. The process of bringing the flow from the storage to the testing condition is called flow conditioning, which is performed in the wind tunnel. The analysis carried out in this section suggests a design of the wind tunnel for supersonic-hypersonic applications.

Before tackling the problem of wind tunnel conception, a relationship is drawn between the air flowing inside a ground test facility and the airflow entering an aircraft

Figure 5: Photo of the experimental setup.

engine. In one case, energy is spent in setting the fluid into motion whereas in the other one, the whole structure is rammed into the fluid at rest. As a consequence even if the energies in play differ, both ground facility and aircraft flow solutions should be in fact, identical.

2.1.1 Equivalence between Global and Moving Frame Description

Moving the aircraft or the fluid were both used in the past history of aerodynamic research as seen on the picture taken at the Institut Aerotechnique in 1912 by the presence of rails (Fig. 6(a)). The concept of wind tunnel was later preferred for the majority of ground testing studies due to the steadiness and the controllability of the air stream as well as its compactness.

The relation between the ground and the aircraft frame is illustrated in Fig. 7:

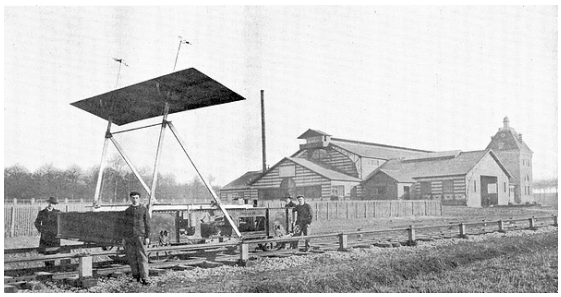

(a) Moving frame in stagnant air. The photo was taken in 1912 [3], a cart was pushed by a car at maximum speed of 30 m/s. The instrumentation was carried on board.

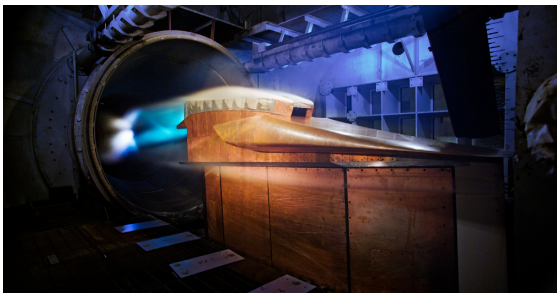

(b) Fixed frame in moving air [5]. This type of setup is compact and more controllable, and has been opted in the majority of aerodynamic studies. There is also less energy spent in setting the fluid in motion than the entire experimental setup.

Figure 6: Fixed Vs. moving frame.

The passengers on a moving aircraft see the fluid as being in motion (Fig. 7(a)). The flow has a kinetic energy even if from a ground viewpoint, it has not (Fig. 7(b)). This common observation illustrates the relativistic aspect of the flow description and is the starting point of the discussion to relate flight conditions and wind tunnel regimes. This notion is also known in classical mechanics as invariance of the solution by change of the reference frame : The problem remains identical whether the frame or the flow is moving. The change from the global (ground) to a moving frame (aircraft) implies an offset velocity (Fig. 7(c)). No kinetic energy is technically added to the stagnant air, and it is rather an artifact of the problem description.

However, in order to achieve flow stagnation in the moving frame, kinetic energy must be given to the flow until its velocity matches the moving frame velocity. The same process is performed by a ground test facility in which the flow is accelerated from rest (i.e. stagnation) to recreate the air stream around the aircraft (Fig. 7(d)).

The process used to accelerate the flow is important to the definition of the stagnation state (Fig. 7(d)). Figure 8 shows that static flow properties are virtually linked to a stagnation state and the relation between both is the acceleration process. The latter is a priori arbitrary however, it is preferable to capture the actual phenomenon

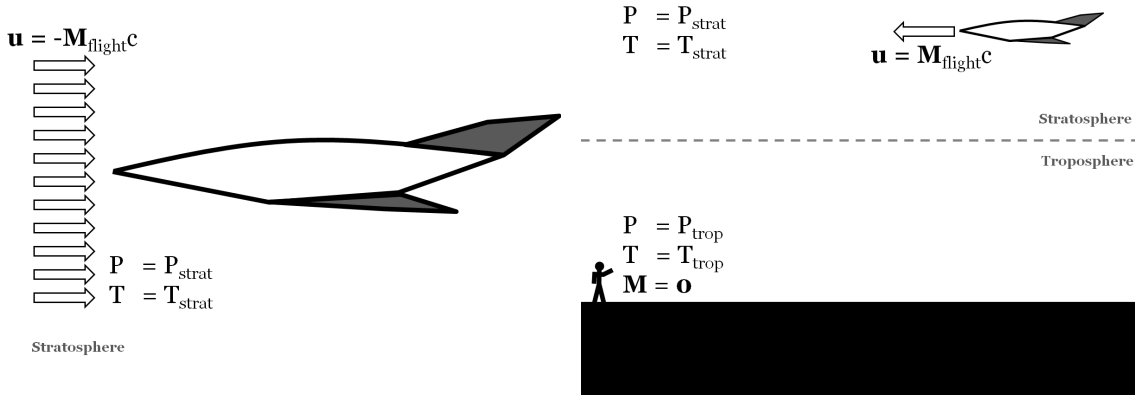

(a) In the aircraft frame, there is a moving flow. The pressure and the temperature are tropospheric in the case of Scramjet flight, as well as the air composition.

(b) From a ground viewpoint, the air is assumed to be stagnating. This contrasts with Fig. 7(a) and shows that kinetic energy of the flow is relative to the reference frame.

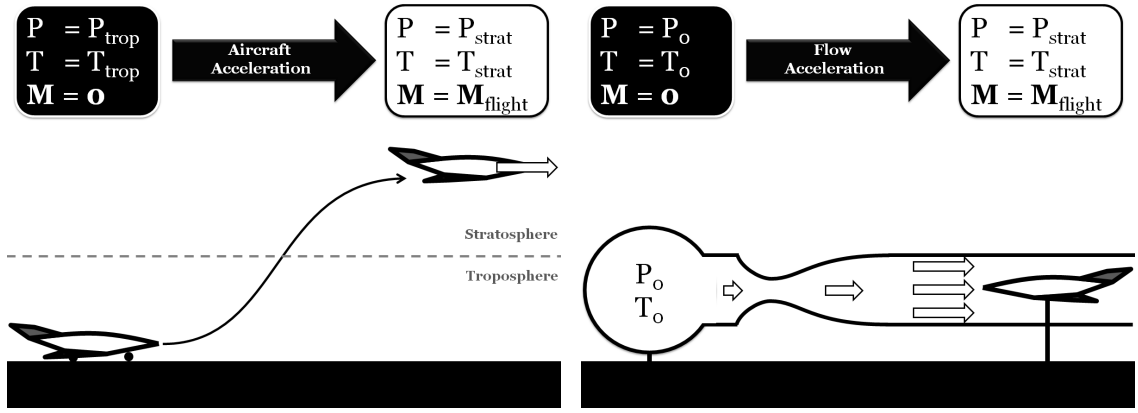

(c) The flow in the frame of the aircraft is at flight speed and atmospheric conditions ...

(d) ... whereas a ground test facility needs different initial conditions to produce the same flow.

Figure 7: Flight (left) and Ground testing (right) problematic.

occurring in the wind tunnel.

In most of the ground test facilities, the flow is brought to supersonic - hypersonic velocities using a nozzle and therefore limiting the dissipation of momentum and heat. If well designed, nozzles provide a fairly isentropic acceleration. In this case, isentropic flow relationships may be used to relate stagnation to static quantities, even if these remain approximate. The nozzle flow is assumed to be inviscid, adiabatic and reversible. The classical adiabatic flow relationships are then given in Eq. (6) and

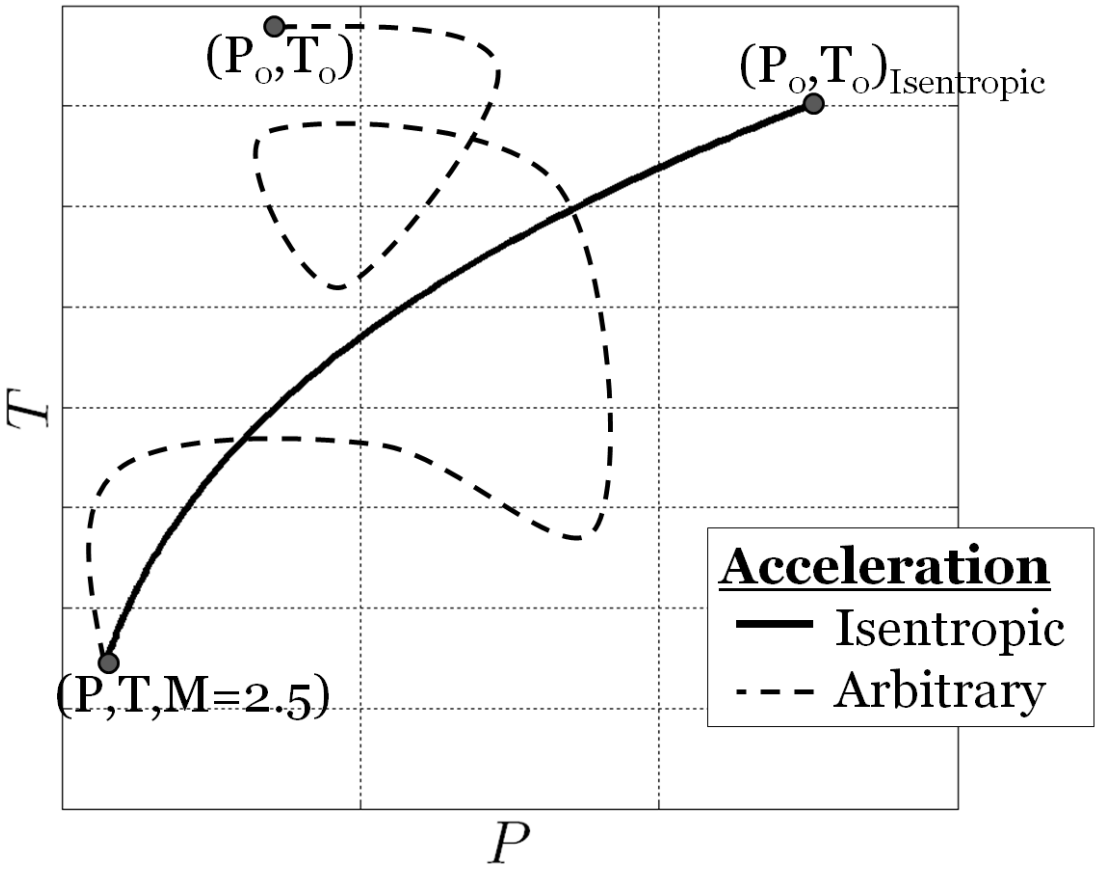

Figure 8: The same static pressure, temperature and Mach number can be reached from many stagnation states depending on the acceleration process.

(7) for the pressure and the temperature, respectively.

$$\frac{p_o}{p} = \left(\frac{T_o}{T}\right)^{\frac{\gamma}{\gamma-1}} \tag{6}$$

$$\frac{T_o}{T} = 1 + \frac{\gamma - 1}{2} M^2 \tag{7}$$

In this study, the stagnation state of the flow is defined with respect to an isentropic process. According to this estimate, the stagnation pressure and temperature are higher than the targeted static conditions. As a consequence for a ground test facility, the air must be compressed and heated before being sent to the nozzle. Especially, one can see that the higher the Mach number, the greater the stagnation pressure and temperature. Some difficulties arise when emulating hypersonic flights (M $>$ 5) where a tremendous amount of work (compression) and heat needs to be given to the

initial fluid. This important observation plays a major role in the limitation of the ground test facility capability.

The relationships between wind tunnel and flight regimes suggest a particular type of design for a supersonic - hypersonic combustor facility (from upstream to downstream):

1. **Storage and Heater**: The flow is pressurized and heated.

2. **Nozzle**: Converts the potential energy (pressure) into kinetic energy. The flow becomes supersonic or hypersonic.

3. **Isolator**: The pressure rise due to combustion results in the translation of the leading shock structure (or shock train) toward the throat. The isolator is the extra length added between the nozzle and the test section, to prevent aerodynamic unstart of the wind tunnel under intensified combustion.

4. **Test Section**: This part of the wind tunnel contains the singularity that is tested, as well as the instrumentation.

5. **Exhaust**: The flow is ejected in the atmosphere and may be filtered to remove hazardous combustion products.

2.1.2 Flight Condition Emulation Domain

The set of conditions (pressure, temperature, velocity and composition) that needs to be achieved in the wind tunnel in order to emulate the targeted flight conditions are determined as follow

$$p_o = p\left(1 + \frac{\gamma - 1}{2}M^2\right)^{\frac{\gamma}{\gamma-1}} \tag{8}$$

$$h_o = c_p T\left(1 + \frac{\gamma - 1}{2}M^2\right) \tag{9}$$

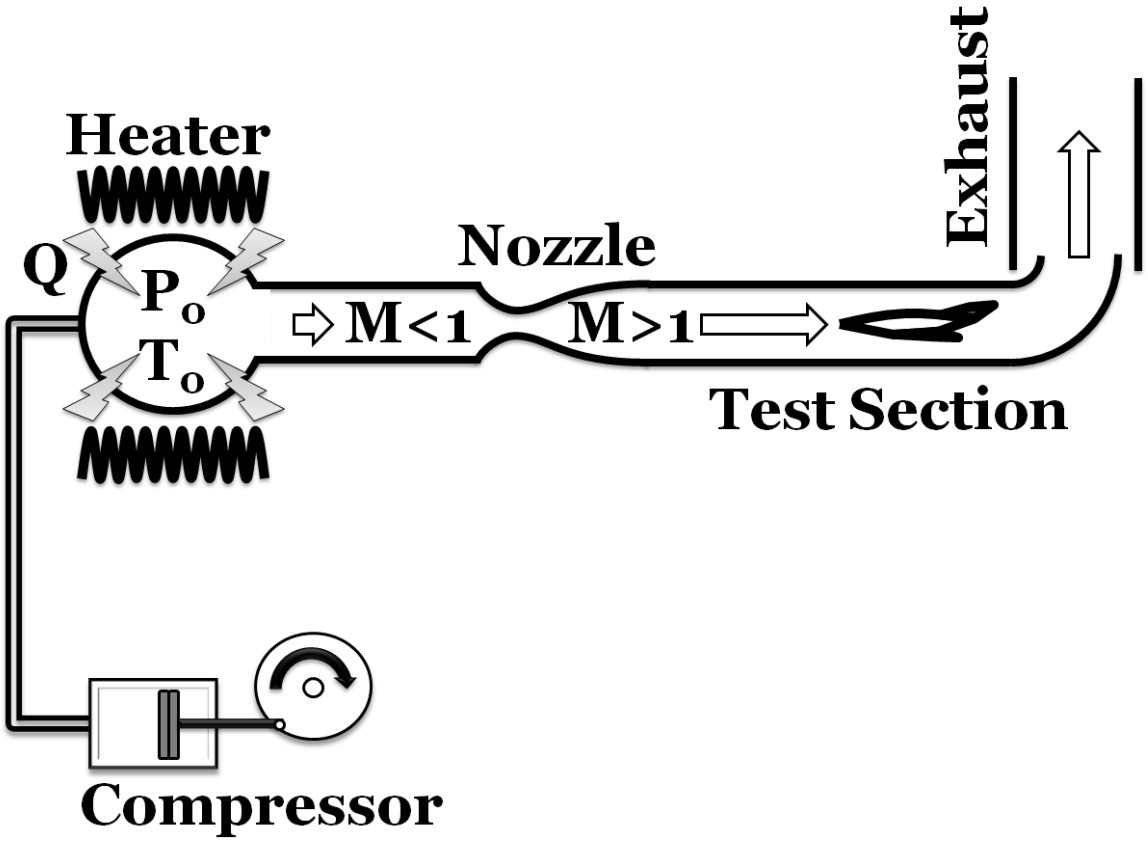

Figure 9: Basic architecture of a wind tunnel which attempts to recreate supersonic-hypersonic flight conditions. (1) The air is compressed in a tank, and heated to reach higher stagnation pressures and temperatures required for supersonic - hypersonic flight conditions. (2) It is then accelerated through a nozzle until reaching the adequate velocity, static pressure and temperature. (3) The test section includes the part that is being tested. (4) The airflow is ejected in the atmosphere through a large exhaust pipe.

c_p, c and γ are obtained from atmospheric data [4, 1, 2]. The stagnation quantities can be related to the corresponding flight scenario, i.e., Mach number and altitude, using Eqs. (9) and (8). The map in Fig. 10 gives the stagnation pressure and the temperature that one would set before isentropically accelerating the flow from rest to a desired Mach number and altitude. These pressures and the temperatures are quite important in the supersonic range and reach relatively high values at Mach numbers above 5. That is why the emulation of hypersonic flight conditions is known to be

relatively costly, since a considerable amount of work (pressurization) and heat need to be given to the flow.

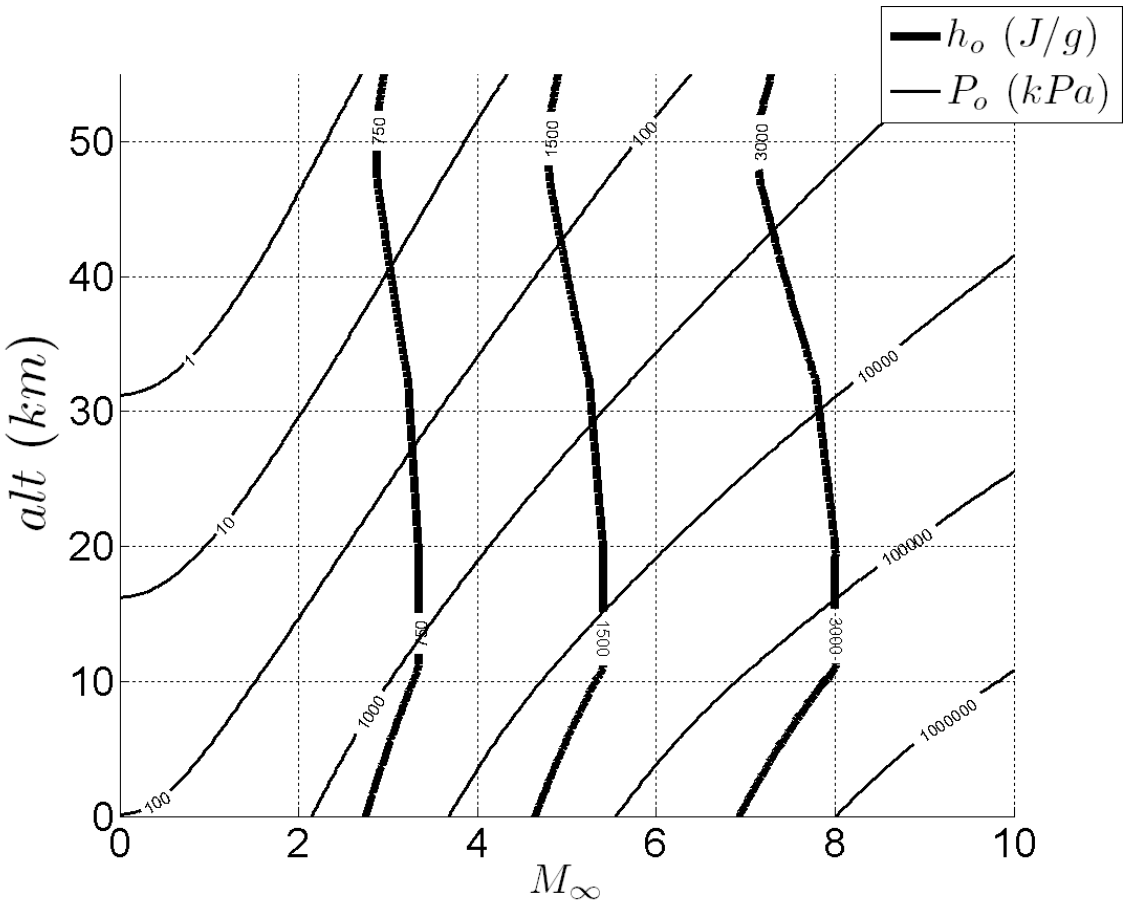

Figure 10: Flight scenario as a function of the stagnation quantities, assuming an isentropic acceleration of the flow.

It appears that the values of stagnation enthalpy for hypersonic flight begin at 1400 J/g, which is already considerable. For instance to emulate a Mach 5 flight, a 10 kg/s airflow requires about 10 MW of power, which is 1% of the net electric power generated by a nuclear reactor. This is only the power transmitted to the fluid, the actual power delivered by the heater may strongly exceed this value depending on the type of technology used.

2.2 Flow Conditioning

The type of wind tunnel architecture is obtained from the flight conditions and the flow acceleration process that are considered. This section emphasizes the various wind tunnel components commonly used to achieve the proper stagnation conditions in accordance with **Task 1(a)**.

2.2.1 Flow Energizing Methods

As suggested by isentropic the model, the fluid is stored at rest, and requires large amount of heat to be transferred during the conditioning phase. Heaters are used to elevate the flow enthalpy and are critical to the determination of the wind tunnel capability. Depending on the type of facility, the heat may be added while the fluid is in motion (1) or while settling (2) (Shock tubes NASA's High Enthalpy Facility [39]).

1. **Pros of heating a fluid in motion :** High power may be involved due to the mass flow rates of the mainstream.

2. **Pros of heating fluid at rest :** The intense heating-cooling as well as pressurization-depressurization cycles induce a substantial wear on the storage tanks (higher ratings are needed for the storage components).

Several flow heating technologies are used to transfer energy to the fluid. One of them is flow arc heating, which consists in establishing an electrical arc in a moving fluid, the flow then acts as a resistor in which energy is dissipated. The strong convection of the flow prevents the heat to build up in the heater. For instance, Huels-type heaters (Fig. 11(a)) have a swirl chamber in which the arc is vortex stabilized between two coaxial electrodes [101]. Increasing the stagnation pressure also increases the resistance of the flow, and therefore the risk to arc with the walls of the heater, which may lead to substantial damages of the structure [19]. Depending on the mass flow

rate, arc heating facilities may require relatively high powers to ensure proper heating, for instance the H3 facility at the AEDC consumes up to 43 MW [40].

Heat exchangers are also used to transfer energy to the flow (Fig. 11(b)). The heat can be generated by resistors [50, 108] or by combustion such as in Gas-fired heat exchangers [35]. The transfer of energy is achieved by heat conduction through the walls of the exchanger, which prevents the flow from being contaminated with the combustion products. Only a limited part of the total heat generated is transferred to the fluid, such that heat exchangers are less efficient than arc heaters.

Air vitiation [38] is used when relatively high enthalpies must be reached while limiting the cost and the design complexity (Fig. 11(c)). Combustion is stabilized in the airstream, and the resulting flow is then air-diluted in order to reduce the contamination. Oxygen replenishment and hydrogen fueling may be used to rebalance the oxygen content and avoid methyl-contamination, respectively. Vitiators have a relatively high efficiency and power since the heat is generated by the flow itself. However, flow contamination may cause problem when studying kinetics or molecular studies are carried out, such as in combustion. Some corrections are accounted for the vitiation effects however, the actual impact of flow contamination on complex phenomena such as flame stability in supersonic flows is not properly known.

The flow heating techniques are illustrated and summarized in Fig. 11 and in Table 1.

Table 1: Comparison between heating technologies.

Technology	**Pros**	**Cons**
Arc Heating	Good efficiency. Highest Temperatures.	Important electric consumption, residual ionization.
Heat Exchanger	Higher power.	Low efficiency.
Vitiation	Good efficiency, high power, low cost	Flow contamination.

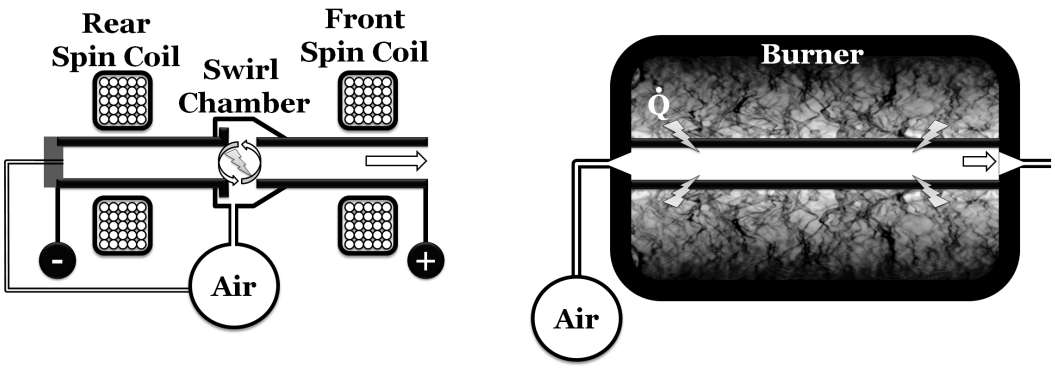

(a) Arc heating technology (Huels-type shown): An arc is created in the flow. Electric energy is dissipated into heat as in a resistor.

(b) Heat exchanger : The flow convects along a heated surface. In this case a burner is shown as the heat source, resistors can also be used.

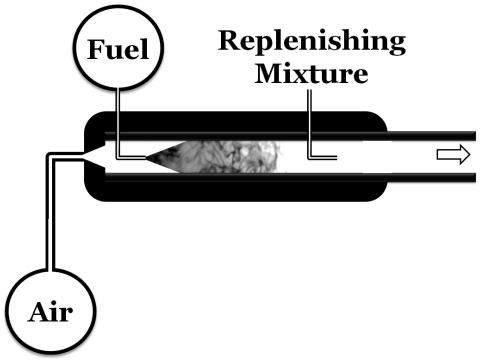

(c) Air vitiation : Combustion is achieved in the airstream. Replenishment of the mixture is eventually needed to minimize the contamination effects.

Figure 11: Common flow heating technologies used in ground test facilities.

In practice, the conservation of enthalpy does not hold since heat is exchanged between the flow and the wall during its journey to the combustor. Depending on the wall heat flux and the velocity, the total enthalpy may depend on the axial location. Consequently, stagnation temperature measurements must be carried out meticulously.

2.2.2 Air Storage and Delivery

Obtaining the adequate stagnation pressure is another challenge in the design of the facility, given the relatively high values found in the supersonic and hypersonic ranges, shown on Fig. 10. High pressurization is a characteristic of supersonic - hypersonic ground test facilities, in addition to heating. This excludes the possibility of having a fan to generate this type of air stream. Instead, the air must be compressed in storage tanks to reach a high potential energy. The air storage facility is put under important stresses and must bear the pressurization-depressurization cycles, such that choice of the materials and the rating of its components are critical.

Two common type of air delivery methods are shown in Fig. 12 and discussed in Table 2 :

- An impulse facility [62] is depicted in Fig. 12(a) in which the air is compressed at a target stagnation pressure and temperature in a storage tank. The total amount of air stored is then delivered in one short burst. The abrupt release of the air is ensured by a fast acting valve or by the rupture of a pressure calibrated membrane (burst disk). The fluid is heated in the storage facility due to high powers involved, and the lack of temperature controllability during the test run. Such a technique generates relatively high rates of heated flow, such that only transient regimes are studied.

- A blowdown facility [50] is shown in Fig. 12(b). The air is also compressed in a storage tank, and delivered progressively through a bleed valve. These type of facilities have longer runtimes than the impulse ones and allow steady regimes to be studied.

Moreover, reproducing flight conditions from a ground facility is only about matching the stagnation pressure and temperature. The air that is rammed into the engine (Fig. 1) has different composition than the air collected at the ground level, since

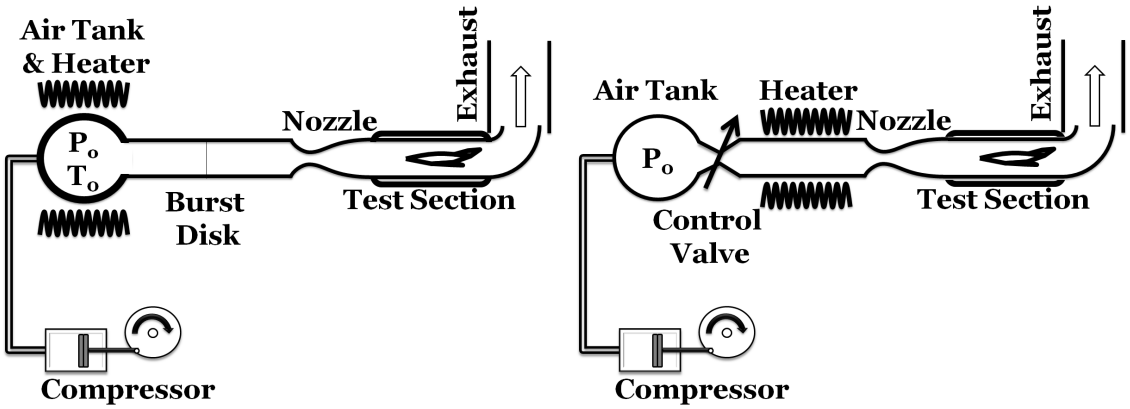

(a) Impulse facility. The storage tank is reinforced for higher temperature ratings.

(b) Blowdown facility. Heating is achieved while the flow is convects to the nozzle.

Figure 12: Common types of supersonic - hypersonic ground test facilities.

Table 2: Summary of storage technologies.

Technology	Pros	Cons
Shock Tube	High static pressure and temperature.	Transient regimes only. High ratings for storage.
Blowdown	Steady regime. Controllability.	Limited simulation envelope.

the stratosphere has a particular air composition which changes with the altitude. However, this is a minor issue compared to heating and pressurization, which cause higher discrepancies when not performed properly.

2.2.3 Review of Existing Supersonic and Hypersonic Test Facilities

The capability of several existing Scramjet test facilities is reported in Table 3, to fulfill **Task 1(b)**. Only blowdown systems are listed and most of the facilities listed in this table use vitiation as a flow energizing method to access to the bottom range of Scramjet flight conditions.

The NASA Langley Scramjet Test Complex [39] includes five facilities. The Direct-Connect Supersonic Combustion Test Facility (DCSCTF) is primarily used for combustor studies which implies that the nozzle exit conditions attempts to match the

combustor intake. In contrast, the Combustion Heated and Arc Heated Scramjet Test Facilities attempts to match the free stream conditions.

Test Cell 18 [59, 54] and 19 [38] from the AFRL are plugged to the same laboratory facility which can provide 7.7 kg/s of heated air at peak stagnation pressure and temperature of 5.17 MPa and 922 K, respectively. An additional cold line can supply the same flow rates of air such that the stagnation temperature is quickly adjusted. The maximum mass flow rate can reach up to 15.4 kg/s. Test Cell 19 is used for developing combustion technology whereas Test Cell 18 is used for upscale experiments.

The University of Michigan Supersonic Combustion Laboratory (UMSCL) [102] has a vertical test section and run at relatively smaller air flow rate (0.4 kg/s typical). However, it covers equivalent free stream Mach numbers up to 5.3 with the use of vitiation. The University of Virginia Supersonic Combustion Facility (UVSCF) [50] is a fully vertical rig and also has an electric heater with which a vitiator that can be used to reach higher stagnation temperatures [32]. Initially, the wind tunnel was design to achieve conditions of a Mach 5 flight.

Table 3: Operating regime of scramjet test facilities.

Facility	M_∞	P_o (kPa)	T_o (K)	M	P (kPa)	T (K)	Energizing Method
NASA DCSCTF [39]	4.0	790	911	2.0	100	533	Vitiation
	7.5	2685	2100	2.7	103	1058	Vitiation
AFRL Test Cell 19 [38]		3203	922	2.0	409	511	Preheat
		3203	922	3.0	87	329	Preheat
		3203	922	4.5	11	182	Preheat
AFRL Test Cell 18 [59, 54]	3.5	690	889	1.8	120	530	Preheat
	6.0	690	1222	2.2	64	620	Vitiation
UMSCL [102]	4.3	590	1040	2.2	55	525	Vitiation
	5.4	590	1400	2.5	34	605	Vitiation
		590	650	2.4	40	300	Preheat
UVSCF [50]	5.0	807	1250	2.0	103	660	Preheat
		1896	1250	3.0	51	425	Preheat

2.3 Design of the Wind Tunnel

The wind tunnel design requirements (**WTDR**) and the constraints (**WTDC**) are listed subsequently in this section, and lead to a specific design solution.

As discussed in the previous section, the emulation of hypersonic flight conditions from a ground facility is relatively demanding in terms of means. The flow is conditioned to match the air stream properties at the combustor inlet as shown in Fig. 13. The following points are important to emphasize when dealing with this approach :

- The stagnation quantities and the Mach number at the combustor inlet differ from the free-stream. The flow in the combustor is generally supersonic, as the Mach number drops through the shock train.
- The relation between free stream conditions and combustor inlet is tied to a diffuser-isolator design.

The relation between free-stream and combustor inlet is not unique: a wide range of free-stream conditions may be yield by a given combustor inflow, depending on the diffuser that is being considered. In particular, the drop of stagnation pressure through the Scramjet inlet is tied to the diffuser-isolator efficiency (recovery factor) which depends on the design. The higher the efficiency, the more stagnation pressure is required for the ground facility to reproduce the proper flight conditions.

By choosing this alternative, the stagnation pressure required for ground testing is lower than the values shown on Fig. 10, and extends the simulation envelope given a pressurization capability. However the stagnation enthalpy remains high even at the combustor entrance, despite the wall heat losses that take place in the diffuser.

In general, pressure, temperature and Mach number can be matched independently in a ground test facility since the pressure, the temperature and the Mach number are controlled by three distinct processes. At the opposite, the flow created

in the aircraft inlet by the ram effect is a natural process, and all of these three parameters are dependent. From a fundamental viewpoint, it is still possible to study combustion in lower heated flows.

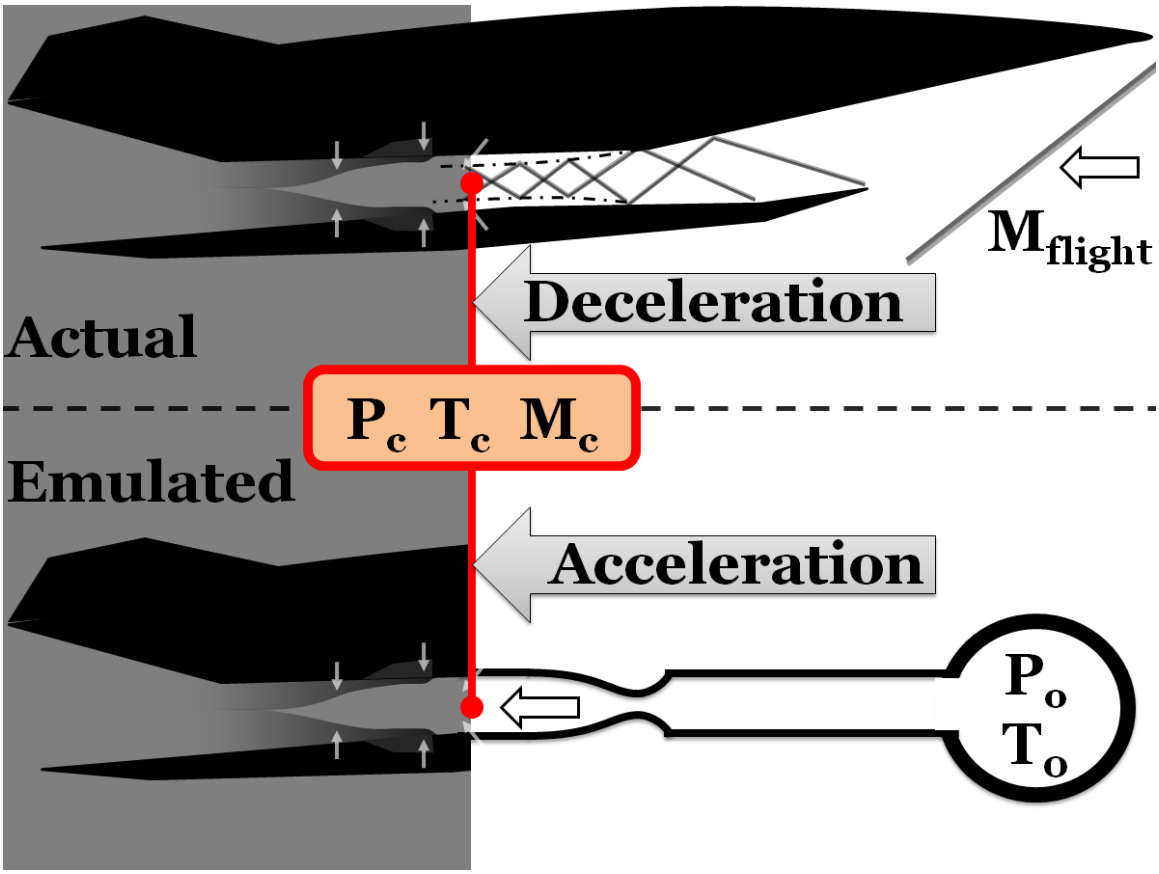

Figure 13: Matching of the flow conditions at the combustor inlet between flight (up) and ground facility (down). The stagnation pressure produced at the ground facility is relatively lower than the actual free stream to match the same condition at the combustor inlet.

The design of the wind tunnel involves the determination of its size and the cross-flow Mach number based on the storage conditions (pressure, volume and temperature). As noted, the approach is based on the relationship between the free-stream and the wind tunnel shown in Fig. 13. The solution must satisfy the design requirements listed below.

- **WTDR1** : The range of static pressure and velocities should pertain to the

values found at the actual combustor inlet (Fig. 13).

- **WTDR2** : Combustion should be studied under a wide range of flow conditions.
- **WTDR3** : The runtime should be long enough to reach thermal steady state and make the study of steady combustion regimes possible.
- **WTDR4** : The facility should be as large as possible, while benefiting from the full heating capability, i.e. by operating under the maximum heater flow rates.

2.3.1 Georgia Tech Aerospace Laboratory Capability

The key design feature of the facility is deduced from the previous discussion as required in **Task 1(c)**, and is depicted in Fig. 14.

The research facility includes compressors as well as storage and control systems for air and methane. A blow down system and a heater (**1-4**) provide a non-vitiated primary airflow. The air is compressed in at 19 MPa in a storage facility (**1**) of 16.7 m^3 (3115 SCM of air). The compressor operates at 0.1833 SCMPS such that the loading process takes about less than 5 hours. The air is delivered to the experiment room via a 5 MPa line (**5**). An electric valve (**3**) allows the airflow to be controlled in real time. A close loop (PID) system drives the valve such that pressure targets are reached within a second, and the stagnation pressure can be stabilized with an error of $\pm$ 0.7 kPa. However, the multiple orifices and junctions present on the air line produce stagnation pressure losses. As a consequence, the stagnation pressure is re-measured shortly before the airflow enters the nozzle.

A gas-fired heater (**4**) (as in Fig. 11(b)) provides a preheated airflow at temperature between ambient and 808 K. A control system adjusts the burner strength (combustion chamber temperature) to the air mass flow rate (differential pressure). The heater burner can be shut off during the test in order to produce a temperature

drop through time.

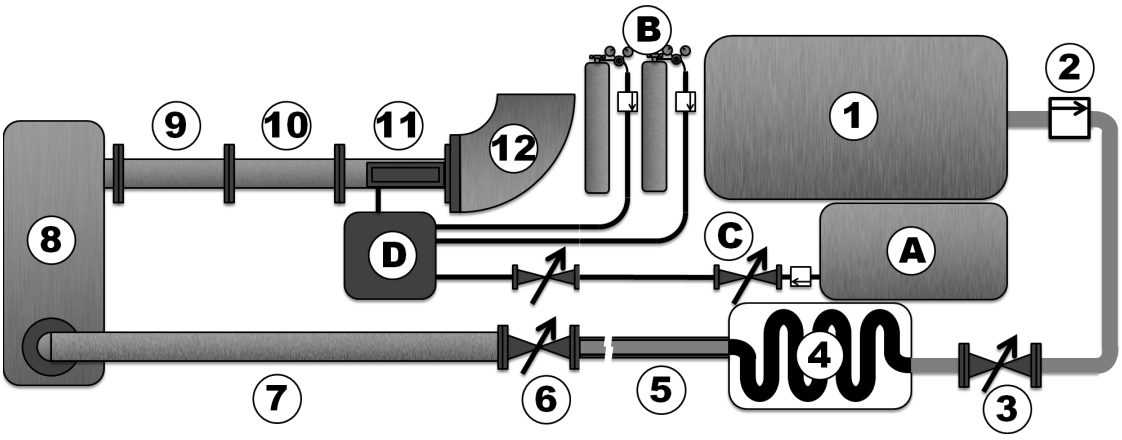

Figure 14: Facility Schematic. (**1**) Air storage tank (9755 SCM at 20 MPa). (**2**) Shut off valve. (**3**) Air flow controller. (**4**) Heater (Burner up to 808 K). (**5**) Heated pipe. (**6**) Manual shut off valves. (**7**) Insulated pipe (65 mm glass wool and thermally reflecting sleeve). (**8**) Settling tank. (**9**) Expansion joint (thermally insulated). (**10**) Flow straightener (thermally insulated). (**11**) Test section. (**12**) Exhaust. (**A**) Methane storage tank (1675 SCM at 34.5 MPa). (**B**) Fuel cylinders with pressure regulators and shut off valves. (**C**) Methane shut off valve and flow controller. (**D**) Fuel control and injection system.

An electric tape heater is wrapped around the pipe to limit the wall heat losses occurring along the pipe network. Henceforth, there is a limited air flow rate for which a temperature target can be reached. As the flow rate is reduced, less heat is taken from the heater, and the fluid spends more time in the pipe network. Consequently, high temperature targets cannot be reached at low flow rates. At the opposite, if exceeding the maximum flow rate specified for the heater, the target temperature may not be reached as insufficient heat is transferred to the flow (power limitation). This explains the trends found in the heater response shown in Fig. 15.

Several safety precautions have been taken in order to adapt the rig to the Georgia Tech Laboratory infrastructure, these steps are detailed in Section 2.7. A 101.6 mm diameter, Schedule-40 pipe connects the stagnation tank to the wall outlet (**7**). It is thermally insulated with a 63.5 mm-thick glass wool jacket, and an infrared reflecting stainless steel sheet. The air is settled in a tank (**8**) ($\oslash$ 0.6 m $\times$ 2.8 m)

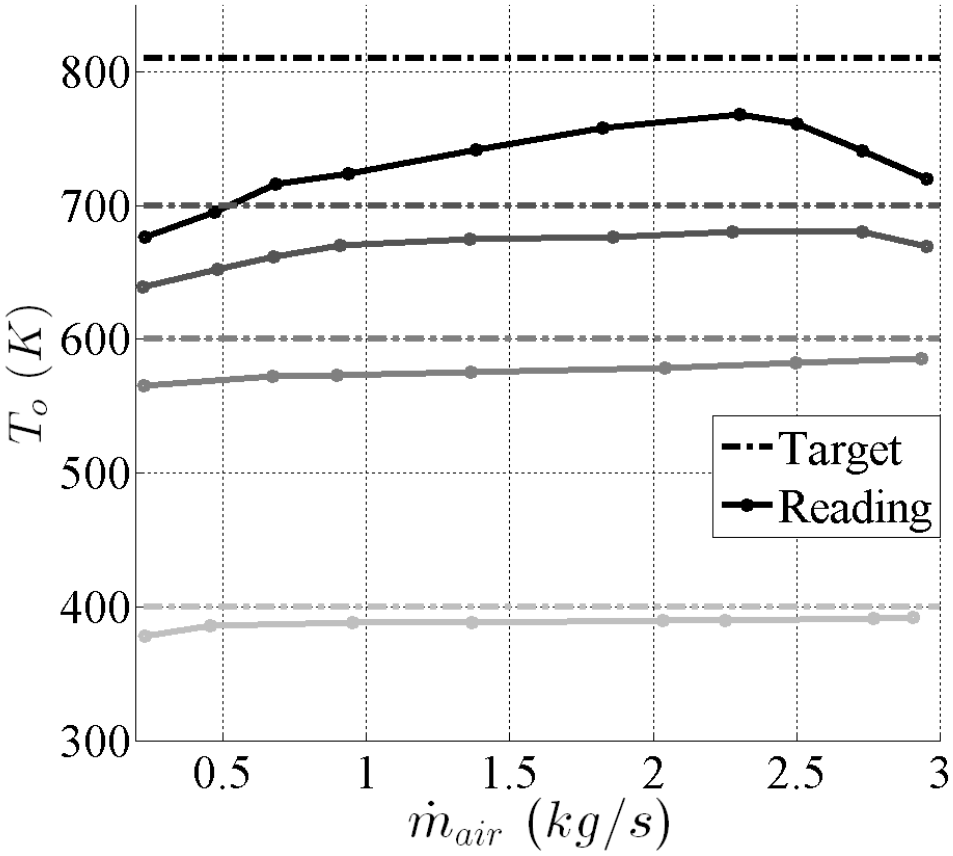

Figure 15: The heater response is the actual flow temperature as a function of the air mass flow rate, given a target temperature. The temperature is measured in the experiment room. The temperature value is a 1 minute time average measured at (**11**) of Fig. 14, at the end of a 5 min run under constant inputs.

where stagnation quantities are measured before entering the nozzle. In addition, the settling tank provides a 180^o flow turn while limiting the centrifugal effects. It is not thermally insulated, and is the pressure-limiting element by having the lowest structural rating (2.2 MPa @808 K). The structural expansion of the tank under heating was thought to put the rest of the structure under stress. To compensate for this effect, a 0.6 m long flexible hose (**9**) has been initially inserted. It is currently substituted by a straight pipe (101.6 mm ⊘, Schedule 40) since no substantial uplift has been observed during testing. In addition, the annular structure of the flexible joint may cause periodic flow features in the mean flow. Another 0.92 m long pipe

(**10**) (101.6 mm ⊘, Schedule 40) connects to the test section (**11**) in which grids can be arranged to produce homogeneous turbulence. The current set up does not use any grid, such that both pipes (**9**) and (**10**) act as a flow straightener. These elements are thermally insulated with glass wool jackets and stainless steel sheets in order to limit the heat losses.

2.3.2 Design Constraints

The size of the test section vessel is mainly determined by the flow rate limitation and the Mach number. Since a nozzle is used to accelerate the flow to supersonic speeds, the air mass flow rate $\dot{m}_{air}$ can be estimated from a chocked nozzle isentropic relationships (Eq. (10)).

$$\dot{m}_{air} = A_t \sqrt{\frac{\gamma}{R}} \left(\frac{\gamma + 1}{2} \right)^{-\frac{\gamma+1}{2(\gamma-1)}} \frac{P_o}{\sqrt{T_o}} \tag{10}$$

The variables involved in the determination of $\dot{m}_{air}$ are labeled in Fig. 16.

Therefore, the sizing of the wind tunnel is ruled by the following constraints :

- **WTDC1** : *Large cross-section area → limited stagnation pressure range under proper heating.* A large wind tunnel cross-section area implies a higher mass flow rate and therefore a risk to run into the limitation of the heater. According to Eq. (10), the air mass flow rate is proportional to the stagnation pressure. Consequently, the throat cross-section area A_t affects the stagnation pressure range for which the flow is properly heated.

- **WTDC2** : *Small cross-section area → Low Reynolds number and small supersonic core.* A small cross-section area may also be undesirable. Under the effect of combustion and high back-pressure the boundary layer can grow and crop the supersonic region. The unstart of the wind tunnel may occur when the upper and lower boundary layers connect to the point that the supersonic

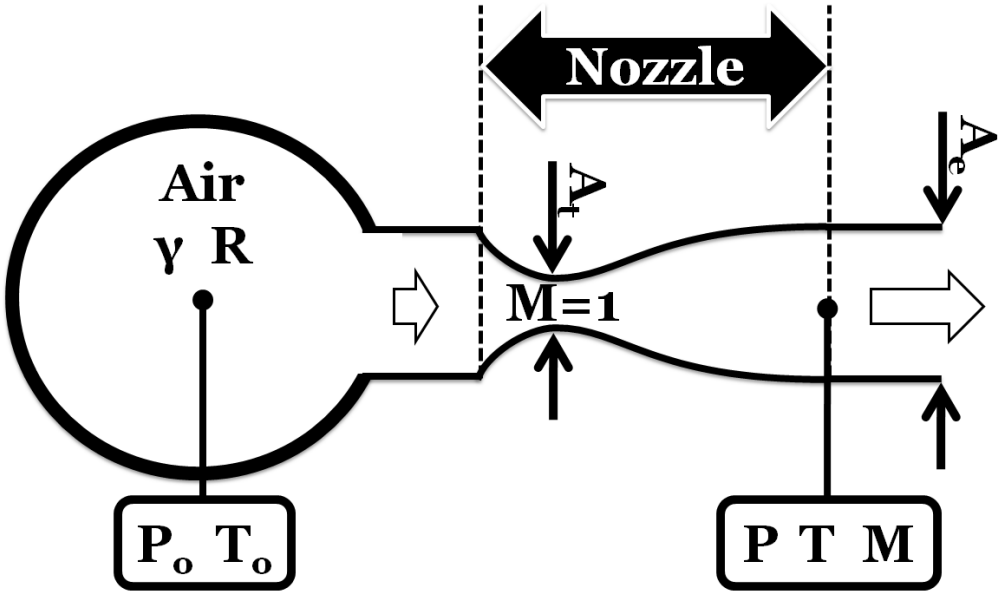

Figure 16: Nozzle under post-choked conditions. The Isentropic flow is assumed with constant specific heat ratio.

mean flow vanishes. The growth of large turbulent scales also becomes limited, which does not reflect a realistic Scramjet engine.

2.3.3 Cross-Flow Mach Number and Emulation Domain

Given the difference between the heating capability and the values found in Fig. 10, the reproduction of hypersonic flights is not possible without heat addition to the cross-flow. This constraint brings a question on the focus of the experimental effort: whether the study will be on the fundamental concepts involved in cavity flame-holding, or on the reproduction of the actual Scramjet flight conditions, such as in performance studies. As discussed in the Introduction Chapter, this study is fundamental and does not attempt to recover the complete flight enthalpy. However, the results may still pertain to the field of Scramjet research. The value of the Mach

number of the combustor is chosen at the low range in the hypersonic flight, to reduce the enthalpy mismatch (M = 5-7).

In addition to the enthalpy issue, the stagnation to static pressure ratio p/p_o is particularly low at higher Mach number (Eq. (6)), as most of the potential energy is been converted into kinetic energy. Consequently, the reproduction of the static pressures encountered in the combustor may also be challenging, even when emulating the flow at combustor inlet, due to the relatively high stagnation pressures (tenth of atmospheres). This must be accounted in the choice of the cross-flow Mach number.

Therefore, the current study opted for a Mach 2.5 cross-flow [67, 104]. This value matches hypersonic flight of Mach numbers ranging from 6 to 7 depending on the inlet design and the flight altitude. Given the facility pressure capability, it is also possible to reach atmospheric pressure in the vessel. As a result, this choice of cross-flow Mach number meets **WTDR1** and **WTDR2**.

The simulation envelope is obtained by propagating the facility capability (Stagnation pressure and enthalpy limits) in the model defined by Eqs. (8) and (9). The result is reported in Fig. 17, as required by **Task 1(d)**. As mentioned at the beginning of this section, the stagnation pressure of the free-stream shown in Fig. 10 differs from the one at the combustor inlet. This is marked by the dashed line (projected flight conditions) and the solid lines (actual facility limit), respectively. Even when assuming a perfect inlet (no losses), the stagnation pressures produced by the facility match flight Mach numbers above 5 at altitudes greater than 20 km as seen on Fig. 17 by the area above the red curve.

The stagnation enthalpy does not conserve through the diffuser of the aircraft owing to presence of wall heat losses. However, this type of loss remains limited, and only a small portion of the total heat is exchanged with the structure, such that the free stream enthalpy remains relatively closed to the values at the combustor inlet. The projected flight enthalpy shown on Fig. 17 lies below the hypersonic range (M

≈ . 3-4).

In summary, the pressure and the flow velocity can be matched with the current facility for hypersonic flight regimes (M > 5) however due to limited heating capability, the stagnation enthalpy remains lower than the actual flight values.

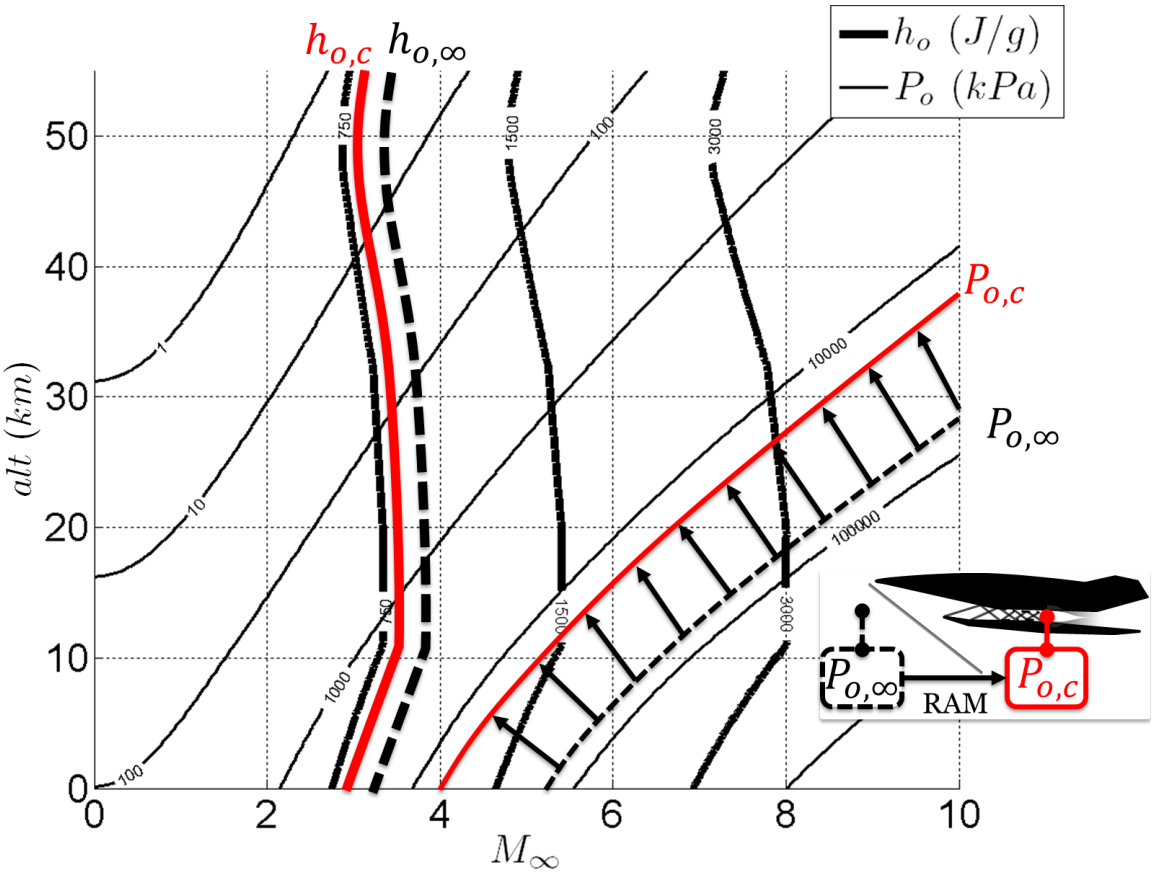

Figure 17: GT Scramjet equivalent flight regime capability. The stagnation quantities at the combustor inlet differ from the free stream (Fig. 13). The maximum stagnation pressure and enthalpy produced by the Georgia Tech facility are plotted in red. Stagnation pressure losses as well as heat losses occur in the diffuser such that the projected flight conditions are systematically higher. The difference depends on the diffuser efficiency.

2.3.4 Sizing of the Throat

The Georgia Tech Aerospace Laboratory heating facility can process up to 2.26 kg/s of air at 808 K. Above this flow rate, the maximum preheat temperature systematically

decreases as seen on Fig. 15. Therefore to benefit from the full heating capability of the facility, the Scramjet facility must operate below this value.

WTDC1 and **WTDC2** summarize into maximizing the throat area while remaining below maximum flow rate $\dot{m}_{air,max}$. The highest flow rates under preheat are reached for the maximum stagnation pressure $P_{o,max}$ and temperature $T_{o,max}$, as suggested by Eq. (10). The maximum throat area is

$$A_t = \dot{m}_{air,max}\sqrt{\frac{R}{\gamma}}\left(\frac{\gamma+1}{2}\right)^{\frac{\gamma+1}{2(\gamma-1)}}\frac{\sqrt{T_{o,max}}}{P_{o,max}} \tag{11}$$

where $P_{o,max}$ is given by the lowest rating of the elements that compose the rig shown on Fig. 14 which is 2.2 MPa ((**8**) in Fig. 14). Given these values ($\gamma = 1.4$), the cross-section area of the throat should be 7.05 10^{-4} m^2, at most. The next step in the design of the wind tunnel is to estimate the minimum runtime under heating conditions, and at maximum flow rate.

2.3.5 Runtime

Equation (10) is expressed in terms of mass of air present in the tank, recalling that $P_o = mRT_o/V$:

$$\dot{m}_{air} = \underbrace{A_t\frac{\sqrt{\gamma R}}{V}\left(\frac{\gamma+1}{2}\right)^{-\frac{\gamma+1}{2(\gamma-1)}}\sqrt{T_o}}_{\tau_{bd}^{-1}}m \tag{12}$$

Equation 12 is a first order, ordinary, differential equation ($\dot{m}_{air} = m/\tau_{bd}$) whose solution yields a decreasing exponential. The characteristic bleed time τ_{bd} is the time it takes to deplete 63.2 % of the initial air supply, which is found to be about 305$\pm$ s depending on the storage temperature. Regardless, in the case of this study, the nozzle of the facility is the flow rate-limiting element.

The mass flow rate must be held below 2.26 kg/s due to the heater limitations, such that it would take at least 27 minutes to deplete the air tank. However due

to the nozzle physical behavior, it is not possible to maintain such a flow rate until complete depletion. In fact, Eq. (10) stipulates that the storage pressure P_s must be greater than 3.5 MPa to ensure air delivery at 2.26 k/s (neglecting pressure losses through the pipe network). Under constant air flow rate, the tank pressure yields a linear form with respect to time, and is obtained from Eq.(13).

$$\frac{\partial P_s}{\partial t} = -\dot{m}_{air}\frac{RT_s}{V_s} \tag{13}$$

The minimum run time is obtained when the storage pressure matches the minimum pressure to ensure a given flow rate. The runtime is shown in Fig. 18 as a function of the flow rate if the latter is held constant during blowdown. The facility can perform at full flow rate during 22 $\pm$ 3 min, depending on the storage conditions ($P_s(0)$ = 17 - 19 MPa and T_s = 273.15 - 310 K). Noticing that an extra margin must be accounted for some additional pressure losses which occur :

- in the pipe network owing to the presence of junctions, turns and orifices.
- during the preheating phase of the facility. Some air is run through the pipe before startup in order to heat the rig structure.

Nevertheless, the compressor operates during the tests which limits the effect of the two points discussed above. With proper preparation, the runtime of this facility allows thermal steady states to be reached, such that it qualifies for the study of steady regimes of supersonic combustors, and satisfy **WTDR3**. For this particular case, the sizing of the wind tunnel gave a relatively long runtime. Generally, there could be a the trade-off between vessel size, runtime and cross-flow temperature, if the runtime is limited.

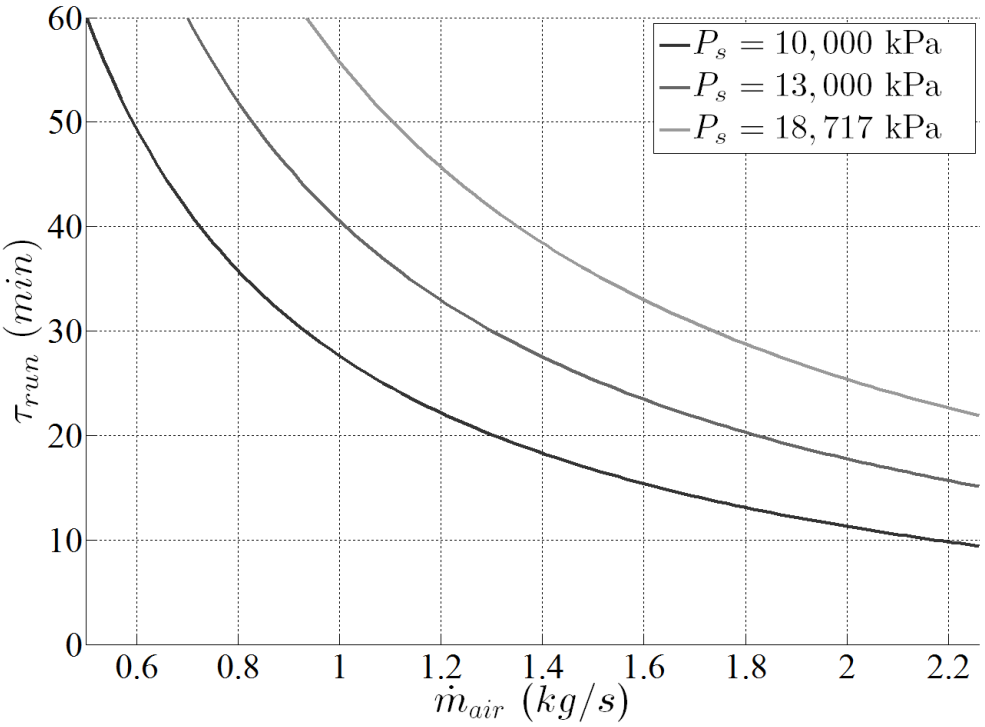

Figure 18: Georgia Tech aerospace laboratory facility runtime capability accounting for the heater flow rate ratings, as well as the presence of a flow rate-limiting orifice ($A_t = 2.75\ 10^{-4}$ m^2). The fluid is stored at 300 K under various storage pressures (initial tank pressure given in the legend). The model assumes a constant flow rate during the blowdown of a calorically perfect and dry air fluid.

2.3.6 Nozzle Design

De Laval nozzles are generally employed to achieve a shock-free acceleration of the flow into a one-dimensional vessel. The exit Mach number is a known function of the exit to throat area ratio, such that the design of the nozzle contour remains the only delicate issue. A De Laval nozzle is divided into three main regions shown in Fig. 19(a).

1. **Compression** : This region ranges from the inlet to the throat. It is a converging section in which the incoming subsonic flow is accelerated ($M < 1$, $dA < 0$). The progressive constriction of the flow results in a raise of the static pressure. In this study, the compression region has a circular contour.

2. **Expansion** : Past the throat, the flow becomes supersonic and enters a diverging section in which, it is accelerated through a series of expansion waves ($M > 1$, $dA > 0$) .

3. **Cancellation** : This section is made to bring the diverging flow to parallel into a one-dimensional channel without shock formation. The transition between expansion and cancellation region is marked by the inflexion point of the profile, which corresponds to a change in flow turning (shown as a black dot in Fig. 19(a)). The design of its contour must be performed carefully as an inward deflection of the flow provided by the wall induces the formation of shocks.

The static to stagnation pressure profile is shown in Fig. 19(b) as a function of the axial location for a typical De Laval nozzle. During start up, the progressive ramp up of the stagnation pressure leads to an increase of the velocity at the throat. While the nozzle is still subsonic, the flow slows down past the nozzle and regains static pressure as progressing downstream in the diverging section. At this stage, the stagnation pressure is relatively low and the nozzle flow is subsonic (**1**).

Under further increase of the stagnation pressure, the throat becomes sonic (choked). There is a critical ratio p^*/p_o at which this phenomenon occurs. Past the chocking conditions, the flow expands to supersonic speeds in the diverging section. The static pressure drops as potential energy is converted into kinetic energy. The relation between change of pressure and cross-sectional area is deduced from Eqs. (14) and (6) with the boundary condition at the throat given in Eq. (15).

$$\frac{dM}{dx_1} = \frac{M\left(1+\frac{\gamma-1}{2}M^2\right)}{A(M^2-1)}\frac{dA}{dx_1} \tag{14}$$

$$\left(\frac{dM}{dx_1}\right)^* = -\frac{1}{2}\sqrt{-\frac{\gamma+1}{A}\left(\frac{d^2A}{dx_1^2}\right)^*} \tag{15}$$

This expression yields a decreasing trend illustrated in Fig. 19(b) for a diverging contour, such that the static pressure at the nozzle exit does not systematically match the back pressure p_e. The latter is generally higher (under-expanded nozzle) during the experiments. The mismatch between both pressures justifies the presence of a normal shock in the diverging section whose strength yields a specific axial location (**2**). Increasing the stagnation pressure, moves the normal shock downstream, and the nozzle may become fully supersonic to produce the desired Mach number at the exit (**3**).

As a consequence, the supersonic solution always exhibits a lower static pressure (generally subsonic in this study) than the subsonic flow. This is an indicator on whether the wind tunnel undergoes an aerodynamic start. This notion is important to retain as the coupling between the nozzle and the combustor produces complex aerodynamic behaviors.

2.3.6.1 Method of Characteristics

The method of characteristics is commonly used in the determination of the expansion and cancellation contours of 2D-nozzles. It involves an iteration process, in which the flow characteristics are carried through the domain from a set of initial conditions.

Derivation The characteristic curves are obtained from two-dimensional compressible flow relationships. This section first assumes a fluid flowing supersonically, irrotationally, and shock-free. Under these assumptions Eq. (2) is multiplied by the velocity to obtain an equation for kinetic energy conservation.

$$u_1^2 \frac{\partial u_1}{\partial x_1} + u_1 u_2 \frac{\partial u_1}{\partial x_2} + \frac{u_1}{\rho} \frac{\partial p}{\partial x_1} = 0 \tag{16}$$

$$u_1 u_2 \frac{\partial u_2}{\partial x_1} + u_2^2 \frac{\partial u_2}{\partial x_2} + \frac{u_2}{\rho} \frac{\partial p}{\partial x_2} = 0 \tag{17}$$

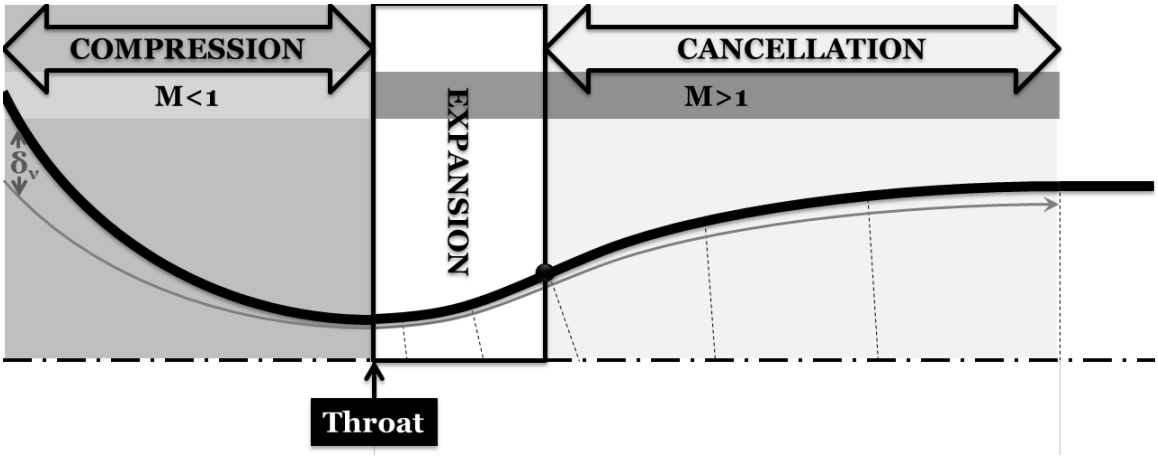

(a) A typical nozzle profile. The compression region has a circular contour and ends at throat where the profile derivative vanishes. The inflexion point of the diverging section marks the limit between the expansion and the cancellation regions. Noticing the presence of a boundary layer which may be accounted in the design of the nozzle, as it changes the effective cross-sectional area.

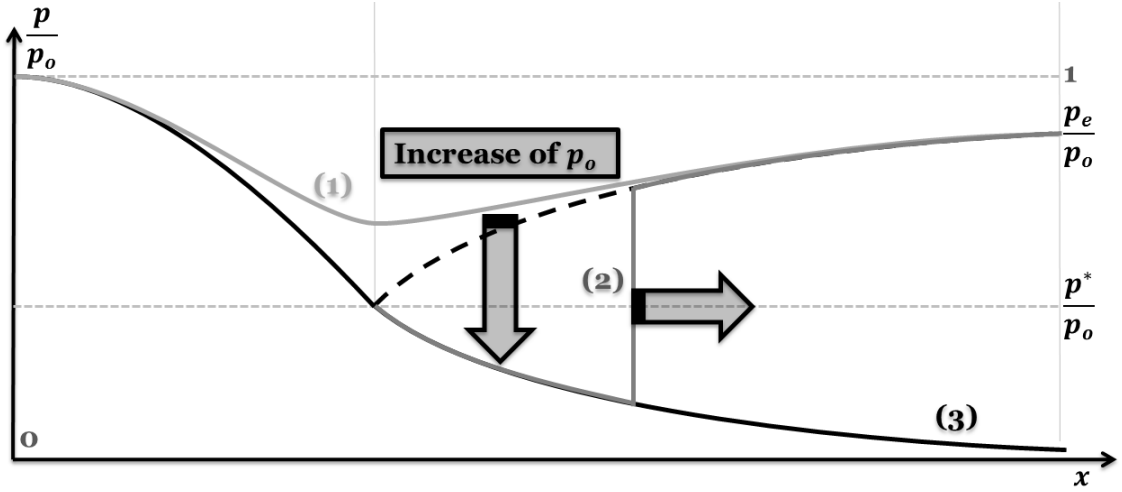

(b) Static to stagnation pressure profile for a typical nozzle shape. The pressure reads as the potential energy such that low ratios correspond to high velocity. Three scenarios are presented : (**1**) a subsonic solution for which the stagnation pressure is low. Under further increase of the latter, the nozzle becomes chocked (dashed line). A supersonic region is created past the throat if sufficient stagnation pressure is given to the flow (**2**). The presence of a normal shock is due to mismatching with the back pressure. An increase of the stagnation pressure from this point moves the normal shock downstream and eventually leaves the nozzle fully supersonic (**3**).

Figure 19: De Laval nozzle used to produce a supersonic flow at a desired Mach number.

Components of Eqs. (16) and (17) are added and the pressure terms are substituted using Eq. (1) with the above assumptions and Eq. (5).

$$u_1^2\frac{\partial u_1}{\partial x_1} + u_1u_2\left(\frac{\partial u_1}{\partial x_2} + \frac{\partial u_2}{\partial x_1}\right) + u_2^2\frac{\partial u_2}{\partial x_2} - \frac{c^2}{\gamma}\left(\frac{\partial u_1}{\partial x_1} + \frac{\partial u_2}{\partial x_2}\right) = 0 \tag{18}$$

Equation (18) is expressed in term of velocity potential functions and yields the form of an elliptical partial differential equation.

$$\left(1 - \frac{u_1^2}{c^2}\right)\frac{\partial^2\phi}{\partial x_1^2} - 2\frac{u_1u_2}{c^2}\frac{\partial^2\phi}{\partial x_1\partial x_2}\left(1 - \frac{u_2^2}{c^2}\right)\frac{\partial^2\phi}{\partial x_2^2} = 0 \tag{19}$$

Equation (19) is equivalent to the null space of the following elliptic operator, which only involves the Mach number along the x_1 and x_2-axis.

$$\begin{pmatrix} \frac{\partial}{\partial x_1} & \frac{\partial}{\partial x_2} \end{pmatrix}\begin{pmatrix} 1 - M_1^2 & M_1M_2 \\ M_1M_2 & 1 - M_2^2 \end{pmatrix}\begin{pmatrix} \frac{\partial}{\partial x_1} \\ \frac{\partial}{\partial x_2} \end{pmatrix} \tag{20}$$

Such operators have proper directions (analog to conic sections) along the characteristic curves C_I and C_{II} which is given by Eq. (21).

$$\frac{dy}{dx}|_{\pm} = \frac{-\frac{u_1u_2}{c^2} \pm \sqrt{\frac{u_1^2+u_2^2}{c^2} - 1}}{1 - \frac{u_1^2}{c^2}} \tag{21}$$

Recalling that $\mathbf{u} = |\mathbf{u}|[\cos\theta \ \ \sin\theta]^T$ and $\tan\alpha = (M^2-1)^{-1/2}$, Eq. (21) can be expressed in terms of local flow angle θ and Mach angle α for what is in fact, the two characteristic curves which emanate from a point with physical properties θ and α (Fig. 20(a)).

$$\frac{dy}{dx}|_{C_I} = \tan(\theta - \alpha) \tag{22}$$

$$\frac{dy}{dx}|_{C_{II}} = \tan(\theta + \alpha) \tag{23}$$

A simple relation between the Prandtl-Meyer angle and the flow angle can be derived for C_I and C_{II} curves [88] such that the physical properties of the flow are carried along the characteristic curves.

$$C_I = \nu + \theta \tag{24}$$

$$C_{II} = \nu - \theta \tag{25}$$

where C_I and C_{II} are the characteristic constants.

In summary, the method of characteristics allows the physical properties of the flow to be carried in the domain from an initial set of nodes. At each point of the domain, there are two flow characteristics which satisfy two independent relations (Eqs. (24) and (25)) carried respectively by two characteristic curves C_I and C_{II}. The system of equation is closed wherever the characteristic curves intersect, such that the flow properties are found at every intersection between C-curves. Henceforth, the following algorithm is used to build a program :

1. The new series of nodes are determined by intersecting all characteristic curves from the parent nodes as shown on Fig. 20(b).

2. The physical properties of the flow are then determined using Eqs. (24) and (25) knowing the C_I and C_{II} constants from the parents nodes.

3. The constant C_I and C_{II} for the children nodes are again determined using Eqs. (24) and (25) but this time, with the known physical properties (θ , α).

4. A new set of characteristic curves are found using Eqs. (22) and (23). Noticing that the Mach angle is found from the Prandtl-Meyer angle by solving Eq. (26) for α knowing ν.

$$\sqrt{\frac{\gamma+1}{\gamma-1}}\tan^{-1}\sqrt{\frac{\gamma-1}{\gamma+1}\tan^{-2}\alpha} - \tan^{-1}(\tan^{-2}\alpha) - \nu = 0 \tag{26}$$

This process is meant to be iterated in space until proper spanning of the domain. The progression is not known in advance such that depending on the shape of the domain, initialization may be an important issue to consider.

Implementation Define an array of n nodes, $n \in \mathbb{N}^{+*}$. Each node $i \in [1 : n]$ is located at (X_i, Y_i). From each node of the array, emanate a C_I and C_{II} curve. Equation (19) can be approximated by its linear form using a Taylor expansion to the first order, within the neighborhood of (X_i, Y_i) as shown in Fig. 20(a).

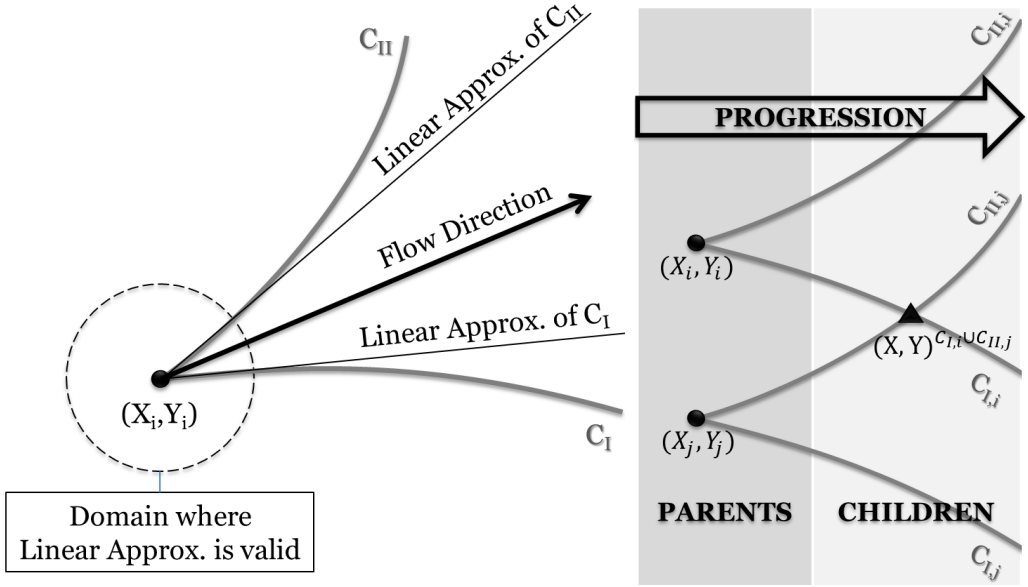

(a) Characteristic curves emanating from the i-th node, there exists a neighborhood in which the curve can be approximated by an affine function whose slope is given by Eqs. (22) and (23). The flow properties are carried along these curves and can be intersected to form a closed system of equation.

(b) Using Eqs. (24) and (25), the flow properties at the intersection between $C_{I,i}$ and $C_{II,j}$ are $\theta = \frac{1}{2}(C_{I,i} - C_{II,j})$ and $\nu = \frac{1}{2}(C_{I,i} + C_{II,j})$. This is then used to compute the characteristic constants at the new point using again Eqs. (24) and (25). From the flow physical properties, it is then possible to compute the slopes of the new characteristic curves which will be used in the next iteration.

Figure 20: Progression mechanism using characteristic curves.

The coordinates of the intersection points between C_I and C_{II} curves emanating

from all nodes of the array are given by the matrices in Eqs. (27) and (28).

$$X_{ij}^{C_I \cup C_{II}} = \frac{X_i \tan(\theta_i + \alpha_i) - X_j \tan(\theta_j - \alpha_j) + Y_j - Y_i}{\tan(\theta_i + \alpha_i) - \tan(\theta_j - \alpha_j)} \tag{27}$$

$$Y_{ij}^{C_I \cup C_{II}} = X_{ij}^{C_I \cup C_{II}} \tan(\theta_i + \alpha_i) + Y_i \tag{28}$$

Both $X^{C_I \cup C_{II}}$ and $Y^{C_I \cup C_{II}}$ matrices are given in Fig. 21(a). The diagonal of the matrix is trivial, as it is the intersection of the node with itself. The j-th diagonal corresponds to the intersection of the i-th node with its neighbor $i \pm j$. Intersecting parent nodes to create children nodes gives the node numbering process. As a result, the progression is specific to the initial conditions and the geometry of the domain. For instance, a progression mechanism is illustrated in Fig. 21(b) in the case of a node array. The forward mechanism, i. e. along increasing x, is given by taking the first upper diagonal of $X^{C_I \cup C_{II}}$ and $Y^{C_I \cup C_{II}}$ as children nodes locations. After which, Nodes $1 \cup 2^+$, $2 \cup 3^+$ and $3 \cup 4^+$ are numbered 4,5 and 6, respectively. The progression mechanism is then performed one more time from this new array, except that there are only 3 nodes to intersect. This shows that a progression may not conserve the number of nodes depending on the initialization and the domain geometry. Regardless in order to maintain the number of nodes constant during the progression, some process use artificial nodes such as boundary nodes where the flow direction is known. For time-optimization purposes, only specific terms in $X^{C_I \cup C_{II}}$ and $Y^{C_I \cup C_{II}}$ are calculated. In the case a n-node array (Fig. 21, n=4), there are $n - 1$ terms to calculate.

The Mesh resulting from the progression mechanism as the collection of all nodes, is handled in the code as a n-structure with the following fields :

- x : position of the node along the x_1-axis.
- y : position of the node along the x_2-axis.
- θ : Flow angle.

- ν : Prandtl-Meyer angle.
- M : Mach number.
- α : Mach angle.
- C_I : Characteristic constant of the C_I-curve.
- C_{II} : Characteristic constant of the C_{II}-curve.

For instance, if the structure is called 'node', then node(i).θ must give access to the value of the flow angle for the i-th node. In general, dynamic memory allocation is required as the size of the structure (number of nodes) may not be known in advance.

The discussion moves on to the design of a 2-D compact supersonic nozzles using this method. Compact nozzles perform flow expansion about an edge (throat) instead of a smooth contour. The expansion waves are shown in Fig. 19(a). If the flow does not separates at the throat, the turning angle θ_{max} is related to the downstream slope at the throat as shown in the figure. There exists a relation between flow turning-angle and the corresponding change of Mach number, and calculations shows [88] that for a nozzle of this type, θ_{max} is half of the Prandtl-Meyer angle at the exit.

$$\theta_{max} = \frac{\nu_e}{2} \tag{29}$$

The progression is shown in Fig. 22(a) ($n = 4$) and is achieved according to the following steps :

1. Equation (26) is used with Eq. (29) assuming a value for Mach number at the exit, since it is a design input. θ_{max} is then used to impose the flow direction at the edge on the downstream side, which is the first initial condition.
2. The second initial condition is found by assuming the presence of an expansion fan anchored at the throat edge through which, the flow is progressively turned,

i.e. θ increase from 0 to θ_{max}. Each wave has characteristic constants C_{II} set equal to zero, such that $\nu = \theta$ (Eqs. (24) and (25)). The Mach angle for each wave is then found by solving Eq. (26) in order to find the Mach angle α. All the fields of the structure are initialized accordingly and the equation of the characteristic line are found using Eqs. (22) and (23).

3. The flow being symmetric about the centerline and as a consequence, its direction is strictly along the x-axis when intersecting with the centerline. This boundary conditions is implemented as follow : the nozzle centerline is treated as a characteristic line whose flow direction is known (Nodes **2**, **7**, **11**, **14** in Fig 22(a)), but its Prandtl-Meyer angle needs to be determined.

4. First expansion wave is intersected with the centerline and give rise to a cancellation wave. The latter subsequently intersects all other expansion waves and generates $n-1$ nodes. Similarly, the i-th expansion wave generate $n-i$ nodes.

5. The first cancellation wave intersects the nozzle contour line which has been found in 1. At this location, the new slope of the contour is the flow angle carried by the out-coming cancellation wave. As a result, the nozzle contour must follow the cancellation process. The contour slope changes each time the cancellation wave intersects with the contour itself. The nozzle shape is refined by increasing the number of expansion waves as seen in Fig. 22(b).

This particular type of initialization at the throat edge allows the characteristic curves to be treated as lines because of the geometrical nature of the expansion waves.

Validation The validation of the program consists into comparing the values of all fields of the structure to the results found in the existing literature. A step-by-step progression is found in Saad's book [88]. The program match the value found in this

book for a specific case, in which the progression is initialized with 5 rays to compute a Mach 2.0 nozzle contour. The comparison between the program used in this study and the literature reference is given in Table 4.

Table 4: Comparison between output values from the program and the results found in the literature for a Mach 2 nozzle. Reference values found in Saad's book [88] are given in brackets.

Region	ν	θ	M
a	0.0000 (0)	0.0000 (0)	1.0000 (1.00)
b	3.3000 (3.30)	3.3000 (3.30)	1.1894 (1.19)
c	6.6000 (6.60)	6.6000 (6.60)	1.3156 (1.32)
d	9.9000 (9.90)	9.9000 (9.90)	1.4316 (1.43)
e	13.1899 (13.19)	13.1899 (13.19)	1.5435 (1.54)
f	6.6000 (6.60)	0.0000 (0)	1.3156 (1.32)
g	9.9000 (9.90)	3.30000 (3.30)	1.4316 (1.43)
h	13.2000 (13.20)	6.6000 (6.60)	1.5429 (1.54)
i	16.4899 (16.49)	9.9000 (9.90)	1.5435 (1.66)
j	13.1899 (13.19)	0.0000 (0)	1.5439 (1.54)
k	16.5000 (16.50)	3.3000 (3.30)	1.6555 (1.66)
l	19.7899 (19.79)	6.6000 (6.60)	1.7677 (1.77)
m	19.8000 (19.80)	0.0000 (0)	1.7681 (1.77)
n	23.0899 (23.09)	3.2899 (3.29)	1.8825 (1.88)
o	26.3798 (26.38)	0.0000 (0)	2.0000 (2.00)

The results do match the literature reference despite the round up used in Saad's book [88]. The other validation method is to recover the tabulated throat to exit area ratios [6] (Eq. (30)) when increasing the number of nodes. The results of the convergence study are found in Table 5.

$$\frac{A}{A^*} = \frac{1}{M}\left(\frac{2}{\gamma+1}\left(1+\frac{\gamma-1}{2}M^2\right)\right)^{\frac{\gamma+1}{2(\gamma-1)}} \tag{30}$$

The refinement of the nozzle contour leads to the tabulated values found in the literature within less than a 100 initial nodes. Therefore the method presented above is retained for the design of the supersonic nozzle. Nevertheless, it utilizes inviscid flow assumption to yield supersonic nozzle design.

Table 5: Throat to exit cross-section area ratio A/A^* as a function of the number of waves emanating from the throat edge.

n	**M = 1.5**	**M = 2.0**	**M = 2.5**
4	1.2200	2.0839	5.3644
14	1.1865	1.7593	2.9338
24	1.1818	1.7219	2.7615
34	1.1799	1.7077	2.7002
44	1.1789	1.6956	2.6687
54	1.1762	1.6356	2.6496
64	1.1762	1.6330	2.6367
Reference [6]	**1.1762**	**1.6330**	**2.6367**

2.3.6.2 Boundary Layer Corrections

As seen in classic boundary layer theory, the core flow can be treated as inviscid, owing the small portion of the kinetic energy swapped into the energy cascade. The action of viscous forces is no longer neglected in the vicinity of the wall, which defines the boundary layer. The method of characteristic discussed above does not capture boundary layer effect. However, supersonic boundary layers are generally small compared to the core flow, such that the correction can be simply added to the characteristics geometry to yield a complete design [76].

Computational methods found in software packages, such as in Fluent (Compressible-RANS) are used to obtain an estimate of the boundary layer thickness. The method of characteristics is then used with the numerical simulations of compressible, viscous nozzle flow in an iterative design process. At each iteration, the presence of the boundary layer modifies the Mach number at the exit (Fluent results), i.e. by modifying the effective inviscid cross-section area, such that a new characteristic design is issued by changing the target Mach number. The design is then re-run into Fluent and eventually produces an exit Mach number closer to the target values. After a few iteration, the nozzle contour is finally obtained with less than 0.01% error from the target value. The final solution is shown in Fig. 23, and is specific to the scale

of the nozzle. In this case, it is required that the nozzle output a M = 2.5 supersonic flow in a 31.75 mm high rectangular vessel. Accounting for boundary layer correction usually leads to a larger cross-section and a greater A/A^* ratio due to growth of the boundary layer from the throat to the exit.

The mass flow rates calculations are based on inviscid assumption such that the actual flow rate is lower than the inviscid values owing to the presence of the boundary layer. The correction is deduced from the displacement thickness of a viscous, compressible boundary layer.

$$\Delta \dot{m}_{air} = A_{\delta_\nu} \int_0^\infty (\rho_\infty u_\infty - \rho u) dx_2 \tag{31}$$

where A_{δ_ν} is the effective boundary layer cross-section area. The boundary layer profile has been solved using implicit turbulent compressible boundary layer method assuming Sutherland's law for the air viscosity [90]. The boundary layer profiles have been computed with the following parameters :

Table 6: Parameters used in the computation of the boundary layer profile using the implicit turbulent compressible boundary layer method. The calculations use the boundary layer thickness at the throat ($\approx$ 0.3 mm) and assume adiabatic walls.

γ	1.4
R	286.9 (J.kg^{-1}.K^{-1})
P_r	0.71
u_∞	575-910 (m/s)
$T_{o,\infty}$	300-750 K
M_∞	2.5
$p_{o,\infty}$	512-2.2 MPa
δ_ν	0.29 mm

The mass flow rate correction is a relatively small fraction of the total flow rate (0.2-0.5 %), such that it has not been taken in account for real time calculations (monitoring). It is still accounted for in the post-processing of the data. Regardless, boundary layer effect remains negligible compared to other types of uncertainty

involved in the calculation of the total air flow rate.

2.3.6.3 Final Design

The static temperature rapidly changes as the flow passes about the throat and expands at higher velocities in the downstream section. That is why the flow properties such as the air mixture composition may depend on the location. In which case, the specific heat ratio is not constant. However the calorically perfect assumption still holds if the flow chemistry is frozen during its journey in the diverging section. This implies that the residence time is much smaller than the dissociation-recombination timescales.

In the most extreme case, the stagnation temperature reaches values as high as 810K, the flow temperature varies from 675K at the throat to 360K at the nozzle exit (Eq. (7)). Accordingly, the specific heat ratio increases from 1.368 to 1.399, at most. This represents a relatively small change (2.27 %) and may not affect the nozzle design to an extended range. After running design cases for both extrema, the impact of the change in the specific heat ratio on A/A^* is less than 3%. Furthermore, the nozzle is built to be used at an extended range of stagnation temperatures. Ultimately, the design is optimized for a particular temperature such that the error on the Mach number is minimized in both heated and non-heated case. The flow is therefore assumed to be calorically perfect and viscous and is designed for an optimum temperature of 400K which is the middle value between the lowest (133K) and the highest (675K) static temperature predicted by simple isentropic relationship (Eqs. (6) and (7)). There is still an inevitable discrepancy on the Mach number when using a single nozzle with a broad range of stagnation temperatures. Given the error on the ratio between throat and the exit cross-section area, the Mach number is calculated within a 0.05 range.

The final design is shown in Fig. 24 and yield a Mach 2.5 nozzle in a 31.75 $\times$ 65.4

mm rectangular channel, which is imposed by the metal suppliers. The corresponding throat area is in fact 6 % higher than the target value found in Subsection 2.3.4. Even when accounting for the boundary layers effects, the highest flow rates (2.26-2.40 kg/s) do not benefit from the full heating capability, as seen on Fig. 15. The choice of the vessel size was done as a compromise between manufacturing standards and **WTDR4**.

The compression region is bounded by a circular contour with a 84.15 mm radius. In order to prevent flow separation due to sharp turn, the throat edge is smoothed using a second order polynomial whose inflection point (end of the expansion region) is located 7.68 mm downstream the throat. The corresponding cancellation contour is computed using the same method described above. The coordinates of the nozzle contour are given in Appendix A with a resolution that must be equal or greater than the accuracy of the machining process (0.05 mm).

2.3.7 Assembly of the Facility

The assembly of the wind tunnel requires additional precautions when dealing with supersonic flows. The presence of accidents in the duct geometry may create undesired shocks which alter the flow characteristics. Therefore, the parts are positioned to avoid misalignments between parts (such as gaskets and joints) as well as windows sockets grooves. This issue is sometime inevitable in supersonic combustors where junctions change under the effect of heat and strain, such that adjustments made at ambient temperature may not sustain the tests. In particular, the thermal dilatation of blocks made of different materials can lead to substantial damages (windows breaking). To avoid this type of problem, the nozzle is embedded in the test section (**11** in Fig. 14) to achieve a smooth shock-free supersonic inflow by reducing the number of junctions and potential misalignments. The design of the test section limits the geometry discontinuities to desired ones, such as the leading and the trailing edges of

the cavity.

The test section is contained in a 635 mm × 114.5 mm × 133.5 mm 316 stainless steel block as shown on Fig. 25. It is an assembly of ground stainless steel blocks of 12.7 mm, 2.54 mm and 38.1 mm thickness since those have less induced machining stress (ground). All parts are positioned using dowel pins within a 0.1 mm accuracy and hold together with quarter-inch steel cap screws. The presence of steel instead of stainless steel in this case is to prevent the screw to grip on the socket at high temperatures. A nickel coating rated at 1600 K is applied on all screwing parts which prevents threads from corroding and provide lubrication. Parts are dismantled on a regular basis for wear-out inspection and design modifications, such that the test section design has to remain simple. As mentioned in Section 2.3.6, the nozzle is designed with boundary layer compensation and provides a Mach 2.5 flow into a 31.75 mm × 63.5 mm rectangular vessel. The profile is wire cut with an accuracy of 0.05 mm with limited machining stress. Both upper and lower parts of the nozzle are positioned with dowel pins and satisfy a 0.1 mm accuracy at the throat under ambient temperature.

As seen for the junctions, the throat area is also subject to change with the expansion of the structure under heating, such that the cross-flow Mach number may be altered. The thermal expansion of the structure in this region remains relatively small since it is mostly caused by the preheated airflow rather than the heat from the combustion. The Mach number being a linear function of the throat area, it follows that the impact of the structure dilatation at the nozzle throat does not substantially alter the Mach number at the exit of the nozzle. A two inches long isolator precedes the leading edge of the cavity and delivers a clean supersonic inflow in the combustor section. This completes **Task 1(e)** in which a supersonic wind tunnel is built accounting for the existing laboratory capability and providing ranges of pressure and velocity which pertains to hypersonic flight.

2.4 Design of the Combustor

The combustor region starts after the isolator, at the cavity leading edge (Fig. 25). The design is oriented to the study of cavity flame-holding in supersonic cross-flow as illustrated in Fig. 2. **Task 1(f)** requires the system to be versatile and properly instrumented for monitoring purpose. The design requirements for the combustor are listed below.

- **CDR1** : Systematic aerodynamic start. The combustor represents an aerodynamic load for the wind tunnel. It is expected to start when increasing the flow rate above chocking conditions. The organization of the flow pictured in Fig. 2 (supersonic flow on top and subsonic flow at the bottom) is rather not trivial.

- **CDR2** : Versatility. The design should allow for the study of different combustor geometries, injection strategy and fuel types.

- **CDR3** : The range of flow conditions produced by the wind tunnel must ensure that the test section can be rendered fully supersonic, i.e. normal shock sitting in (**12**) of Fig. 14 .

2.4.1 Geometry

The cavity is shown in Fig. 26. Its depth is 31.75 mm which is about 80% of the supersonic vessel height. Experimental observations indicate that large cavities may prevent the setup to perform an aerodynamic start. It has been found that startup becomes difficult at aspect ratios (L/D) greater than 2.5 since the cavity represents a substantial aerodynamic load on the wind tunnel. Consequently, the design solution should allow the cavity to reach different sizes and shapes. That is why the cavity is created by sliding a rectangular block away from the leading face. The aspect ratio (L/D) is adjustable continuously from 0 to 5. In order to meet **CDR1**, a startup system is built to perform a systematic aerodynamic start at any of these aspect

ratios. The startup issue is discussed in more details in Section 3.1. The ability to change the combustor geometry while testing contributes to the versatility of the setup and meet **CDR2**.

A diverging ceiling starts 127 mm from the leading edge of the cavity with an angle of 2.5 degree to allow for the conversion of some of the energy released by the combustion to kinetic energy through the expansion of the flow, as in Scramjet engines concepts shown in Fig. 1(a). Two side windows allow flow visualization techniques to be carried over a 292 mm long region starting 19.05 mm before the cavity leading edge. The windows are mounted on graphite and RTV gasket in order to compensate for the structure expansion under heating effect.

A series of tap holes are located on the ceiling every 50.8 mm in order to capture the pressure raise due to the combustion activity as well as to track the shock pattern in the absence of windows. The cavity also has a pressure and a temperature port located on the bottom wall 63.5 mm from the leading step.

2.4.2 Fuel system

A versatile system is built to investigate the effect of fuel mixture composition on combustor stability, and in part to meet **CDR2**. Liquid and gaseous fuels can be injected in the combustor but only gaseous fuel has been studied up to this day. Gaseous fuels are stored in high pressure cylinders at 17.5 MPa. Natural gas is provided by an outdoor facility which purifies the city gas and stores it in three 95 m^3 cylinders at 20.5 MPa. Liquid fuel can be stored and pressurized in a 45.5 m^3 high pressure cylinder (rated for 14 MPa). The fuel is driven out by addition of nitrogen or inert gas. At steady state, the mass of nitrogen added per time unit is equal to the mass of fuel injected in the test section. Six spray injectors (HAGO^{TM}) ensure the rapid breakdown of the fuel into droplets.

Various fuel injection strategies in the cavity are in place, the fuel injectors are

located on the floor, the leading step and on the aft ramp as seen in Fig. 26. Three valves allow the fuel injection to be continuously swept from one location to the other. The fuel injection system ensures the delivery of a fuel blend through an array of six injectors equally spaced along the spanwise direction and located on the floor of the cavity, 6.4 mm downstream the leading step. Each injector is 2.3 mm in diameter. The fuel mixture composition is adjustable using three mass flow controllers (1000 SLPM/1000 SLPM/100 SLPM). Figure 27 depicts the fuel system employed to reach the mixture composition targets. Both fuels are brought from their storage pressure to an identical fuel back pressure. Each mass flow rate controller operates accurately within a 140 kPa pressure drop; therefore it is inserted between two pressure reducers. By changing the fuel density, the back pressure regulates the range of mass flow rate covered by the system. When dealing with a mixture of fuels as in this study, the fuel additive runs in the 100 SLPM channel since smaller flow rates are measured with more accuracy, whereas the main fuel runs in one of the 1000 SLPM channel. A 6000 V spark is also present at the bottom of the cavity. The cathode is a tube (1.8 mm inside diameter) in which additional hydrogen is injected at 838 kPa of stagnation pressure during the ignition phase. This hydrogen stream is turned off once ignition is achieved.

2.5 Instrumentation

It is generally difficult to obtain an accurate estimate of the cross-flow pressure and temperature without altering the downstream supersonic part, due to the intrusion of a flow-facing probe, such as a Pitot tube. Therefore no singularity protrudes into the supersonic flow during the wind tunnel operation (flushed configuration). The mass flow rates are measured via pressure and temperature transducers installed on the setup (air) or using separate devices (fuel).

All transducers are connected to the control panel through shielded coaxial cables

using Amphenol-BNC standard connectors. A National Instrument DAQ board is used for the data acquisition ,and its specifications are given in Appendix A.

2.5.1 Pressure

As mentioned previously, the pressure is measured at various wall locations to track the shock patterns and to monitor the combustor startup and operation (P_{1-7} in Fig. 25). The measurements give the static pressure of the supersonic air stream since the pressure is measured at recessed holes located on the wall of the test section.

However, the actual stagnation pressure supersonic free-stream is determined using an empirical relationship involving P_1 in Fig. 25 and pressure transducer mounted on the settling tank P_o.

The pressure is also measured across the fuel line and shortly before the injectors, for the mass flow controllers to operate in their optimum range. The injector pressure is used to determine if the injectors are choked.

Each pressure transducer is connected to the test section via stainless steel tubing whose internal diameter and length are 4.9 mm and 609 mm, respectively. The transducers output a signal from 0 to 5 VDC which scales linearly with their respective full pressure span. The transducers cut off frequency is 1 kHz which is the fastest transducer response used on this facility, therefore the data is sampled at 2.205 kHz to meet the Shannon-Nyquist criterion with a typical 10.25 % extra span for anti-aliasing filtering. The static pressure is deduced from the time average value of the pressure signal. The length of the moving average is 0.2 second and involve 440 points which is sufficient enough to reduce the noise fluctuations by over 98 %. Since the static pressure is measured, there is no damping in the pressure signal, however the average process introduces a phase shift, which is accounted for while post-processing the data. The transducers ranges and ratings are chosen based on initial estimates for pressure rise due to combustion (Table 7). All pressure transducers have an accuracy

of ± 0.25% of their respective full span.

Table 7: Pressure instrumentation: the pressure tap hole locations are defined in Fig. 25.

Pressure Port	P_o	P_{fb}	P_{inj}	P_1
Range (kPa)	101-2170	101-2170	0.26-790	0.53-206
Accuracy (kPa)	5.2	5.2	2	0.5
Pressure Port	P_2 or P_{cav}	P_3	P_4	P_5
Range (kPa)	0.53-206	0.38-413	0.38-413	0.38-413
Accuracy (kPa)	0.5	1	1	1
Pressure Port	P_6	P_7	P_8	
Range (kPa)	0.38-413	0.31-620	0.31-620	
Accuracy (kPa)	0.38-413	0.31-620	0.31-620	

2.5.2 Temperature

Several thermocouple probes are present on the experimental setup, notably in the settling tank, the fuel line, the cavity and at the ceiling of the test section.

Thermocouples behave as thermal capacitors and have a characteristic heating/cooling time which pertains to the wire diameter : small wires heat up fast but do not range to high temperatures, hence the compromise in determining the thermocouple wire size. All thermocouple are K-type and are directly mounted on a cold junction compensator. The accuracy of all K-type thermocouples is ± 0.75% of the measured temperature in Celsius. The thermocouple signal is amplified 25 times to increase the signal to noise ratio. The response is then linearized with standard polynomials for K-type thermocouples. The stagnation and fuel temperature thermocouple have a 14 AWG wire with an ungrounded junction. Since fast response is needed to measure effects of ignitions and blowouts, 24 AWG wires and exposed junctions are used for the thermocouples installed inside the test section. The characteristic response times are estimated for each thermocouple using the step cooling method. It is assumed that the thermocouple response is capacitive with a given response time τ_r.

$$T(t) = \Delta T \left(1 - e^{-\frac{t}{\tau_r}}\right) \tag{32}$$

The pre-amplifiers and the cold junction compensators have a linear response over the 0-100 Hz range, such that no significant phase and magnitude error is induced. Both best fitting model and experiments are shown in Fig. 28 for the cavity thermocouple. The response time of all thermocouples are summarized on Table 8. Noise addition is mainly due to electronic component noise (thermal noise) and ground fluctuations. It may become problematic as the range of voltages output by the thermocouple probes is relatively small (typically a dozen of mV). This is why the signal conditioners are powered by chemical batteries and located in the vicinity of the probes. In addition, the presence of thermocouple on a facility requires a meticulous electrical grounding.

Table 8: Temperature instrumentation: the port locations are shown in Fig. 25.

Temperature Port	T_o	T_f	T_{cav}	T_{cf}
Range (K)	6-1363	6-1363	6-1143	6-1143
Accuracy (K)	0-8	0-8	0-6.5	0-6.5
τ_r **(s)**	1.21	1.19	0.31	0.30

A thermocouple probe is inserted into the settling tank to estimate the stagnation temperature. However, the fluid exchanges heat with its surrounding while convecting in the flow straightener (**9** and **10**). The stagnation temperature at the throat may differ from the one in the settling tank, especially when dealing with a heated flow. The determination of the cross-flow stagnation temperature involves more than one probe as discussed subsequently.

T_1 is located next to P_1 in the spanwise direction such that P_1-T_1 and P_{cav}-T_{cav} are facing each other. The downstream distance of T_1 is chosen such that the shock which emanates from the cavity leading edge falls downstream, leaving T_1 in the unperturbed region. This probe does not directly measures the cross-flow

temperature owing to the presence of a boundary layer near the wall. Compressible boundary layer theory suggests that the stagnation temperature is restored if the wall is adiabatic. In reality the wall temperature is lower due to heat losses such that the stagnation pressure of the cross-flow lies between T_o and T_1. An empirical relationship involving T_1 and T_o has been established by measuring the stagnation temperature downstream the nozzle during the wind tunnel calibration phase. The cross-flow static temperature is deduced upon proper knowledge of the Mach number and compressible flow relationships for the free stream (Eqs. (6) and (7)). T_{cav} is used in ignition and blowout detection and gives a rough estimate of the stagnation temperature, since enthalpy from the cross-flow is mostly conserved.

2.5.3 Flow Rates

2.5.3.1 Air

The overall airstream flow rate is based on Eq.(10) onto which a correction for the boundary layer is added.

$$\dot{m}_a = \dot{m}_{a,inviscid} - \Delta\dot{m}_a \tag{33}$$

The air stream flow rate measurements require the stagnation quantities to be accurately measured. The stagnation pressure sensor is connected to the settling tank and measures the absolute pressure with an accuracy of 5.2 Pa. The probe protrudes in the tank (by 0.3 m) to avoid thermal boundary layer effect.

The boundary layer correction translates into a change in the effective cross-section area at the throat. As mentioned previously, it does not significantly impact the overall value. The error on the air mass flow rate is calculated from Tables 7 and 8.

$$\frac{\delta\dot{m}}{\dot{m}} = \frac{\delta P_o}{P_o} - \frac{\delta T_o}{2T_o} + \frac{\delta A_t}{A_t} - \frac{2^{-\frac{\gamma-3}{2(\gamma-1)}}(\gamma+1)^{-\frac{\gamma+1}{2(\gamma-1)}}(-2\gamma\ln(\gamma+1)+\gamma\ln(4)+\gamma-1)}{(\gamma-1)^2}\frac{\delta\gamma}{\gamma} \tag{34}$$

The fractional uncertainty on the air mass flow rate does not exceed 0.03.

2.5.3.2 Fuel

The Fuel mass flow rate is measured by volumetric flow controllers installed on each fuel channel. These devices require a set point (incoming to the device) and a reading signal (out coming from the device) to measure and regulate the fuel flow rate. There are two type of technology used on the experimental setup. For both cases, a part of the incoming flow is bypassed in a small channel and turned laminar. In thermal volumetric flow controllers, the flow convects from a heating coil to a passive coil (sensor). The mass flow rate is pertinently related to the amount of heat carried by the flow. The rate of matter flowing through the coil is proportional to the temperature gradient measured at its winding. Henceforth, the temperature dependent resistance differential modulates an electric signal, which is conditioned to generate an 0-5 VDC output signal. The output is usually expressed in term of a relative gas such as nitrogen in SPLM. The characteristics of the fluid are then accounted subsequently in the voltage to data conversion, as follow :

The volumetric flow rate of the fuel flowing through the sensor is proportional to the rate of nitrogen.

$$\dot{V}_{fuel} = K_V \dot{V}_{N_2} \tag{35}$$

where K_V is $\frac{\rho_a c_{p,a}}{\rho_r c_{p,r}}$ taken at the standard conditions (a stands for actual (fuel) and r for reference (N_2)). Some numerical values reported in Table 9 for the fuel types used in this study. The volumetric flow rate is expressed at standard condition and is then converted to mass flow rate unit.

Table 9: K-factors for the fuel types used in this study.

Fuel	K_V**-factor**
H_2 ($\leq$10 SLPM)	1.0106
H_2 ($\geq$10-100 SLPM)	1.35
H_2 ($\geq$100 SLPM)	1.9
CH_4 ($\leq$10 SLPM)	0.7175
CH_4 ($\geq$10 SLPM)	0.75
C_2H_4	0.6
C_2H_6	0.5

The second type of flow controller uses the relation between the flow rate and the pressure drop through a channel (Poiseuille equation). Therefore a differential pressure transducer measures the pressure at both ends of a laminar flow element. Given the fluid viscosity, the volumetric flow rate is deduced and corrected to a set of standard conditions. There is no need to account for the K factor for this type of sensor.

The experimental setup has one pressure drop (1000 SPLM) and two thermal devices (100 and 1000 SPLM). Their specifications are listed in Table 10.

Table 10: Mass flow controllers specifications.

	Thermal	**Pressure Drop**
Accuracy	$\pm$ 1.5 % FS, including linearity over 15 to 25 ^{o}C and 69 to 413 kPa, $\pm$ 3 % FS for units $\geq$ 100 SLPM from 0 to 20 % of range.	$\pm$(0.8 % of reading + 0.2 %FS)
Repeatability	$\pm$ 0.5 % FS	$\pm$ 0.2 % FS
Pressure Rating	3,450 kPa	1,000 kPa
Max Pressure Drop	345 kPa	700 kPa
Response Time	5 s to within 2% of set point over 25-100 % FS	0.7 s to within 2% of set point over 100 % FS

2.6 Acquisition, Monitoring and Controls

The panel is shown in Fig. 29 has been designed and built for data acquisition, monitoring and control of the facility, as mentioned in **Task 1(g)**.

2.6.1 Hardware

A considerable effort is made to obtain an intelligible interface in order to avoid confusion, as a substantial amount of data needs to be carefully monitored by the user during the test.

A control panel has been built for control and monitoring purposes during the tests. The main panel is a welded steel structure covered with a foam liner and vinyl and has two 20" LCD screens wired to a main desktop unit. The user interacts with touch sensors located behind Plexiglas plates. Touch sensors have replaced the physical switches commonly used on regular control panels (**1** in Fig. 29). There are no mechanical or moving parts in this type of switches. Moreover, touch sensors have a much greater life span than regular switches, as they are not subject to mechanical wear. A chip (QT 1110) detects the variation of capacity caused by the user's hand on the Plexiglas plate facing a sensing pin, and outputs a logic signal (TTL) that reflects its state: (0) if touched and (1) if not. Blue and red LED's indicate the sensor state. As a result, the implementation of touch sensors provides a full digital switching interface. There are 24 touch sensors which are connected to the main computer via an USB interface. As a result, there are no physical wiring between touch sensors and controllers.

A program checks the sensor states 10 times per second. Each touch sensor is configurable to execute a custom action. The program manages all the user actions and outputs through the LPT port a signal that drives a relay box with 24 relays seen on Fig. 30. Each of those relay have two-states and allows the small power signals collected from the computer to control signals of higher power needed for actuators,

valves and igniters. Each relay has a mechanical switch for manual override for safety purposes.

There are 4 feeding voltages available provided by a power supply: 5 VDC, 12 VDC, 24 VDC and 110 Vac. Each supply support a 100 watts load except for the 110 VAC supply which supports up to 2000 watts.

The data acquisition board is a National Instrument PCI 6629 which has a 250 kS/s sampling rate that can be multiplexed on 32 analog channels. Each analog input channel has a ± 10 v or ± 5 v range which is coded on 16 bits. 48 digital inputs are used to capture the user switching actions, and 24 digital outputs are used as motive voltage to drive solenoids relays.

The pressure and the temperature transducers have a limited bandwidth of 0-1 kHz and 0-40 Hz respectively, which suggest an optimum sampling rate. Regardless, only static quantities measured in this study, such that there is limited concern on high frequency issues, i.e. phase and amplitude discrepancies induced by tubes resonances or transducer responses. Optimizing the sampling rate has the advantage of keeping low transfers rates for real time applications, and a reduced load on the RAM memory. Nevertheless, the sampling rate should be high enough to allow for noise reduction by sliding time average while capturing the proper time scales. Typically, the sampling rate used during the test is about 125 S/s per channel.

The main desktop unit has a 2.4 GHz quad core with a 1024 MHz FSB. 3Gb of RAM memory is cadenced at 800 MHz. The board also has four analog outputs that are used for flow controllers target points. The digital to analog sampling frequency is 833kS/s and can be multiplexed on four 16 bits DA-converters.

Some hardware limitations issues may appear when dealing high sampling rates. Initially after launching a data acquisition session, the data is directly stored in the RAM memory where the transfer occurs at higher rates (800 MHz pipeline). The RAM memory may get full after a certain time, and the excess of data is redirected

to the hard drive at much lower rates. If the product between the sampling rate and the number of channel is too high, the system may experience data flooding after a limited time from launch, which usually results in a computer crash. As a consequence, there must be enough RAM memory ensure that a full test can be run without experiencing hard drive access. Preliminary tests and memory allocation calculations have shown that 1 Gb of RAM corresponds to 157 minutes of testing at 2,205 S/s for 24 channels. This type of problem was solved by pre-allocating the memory for the test.

Three desktop units are connected to the overhead displays. Each of these computers can run a separate program using the data that is collected. Typically, mixture space trajectories, the heat fluxes, large displays and video data can be visualized on the overhead screens. An additional large screen is used to display live HD video data from the main camera installed in the experiment room. The control room is also equipped with a projector for demonstrations.

2.6.2 Software

The acquisition software is developed on a Matlab platform using a complex GUI user interface and involving several computers. Matlab has embedded DSP targets and a wide range of signal processing tools. The following toolboxes are required to run the data acquisition software:

- DAQ toolbox
- Real time toolbox
- Signal processing toolbox
- Gauge toolbox
- Java Toolbox

- Datafeed Toolbox

The computation load is distributed among the four cores of the main CPU : The acquisition and the displays programs are run on separates cores. The acquisition program stores and streams the data from the DAQ card to a private network of computers. Therefore, the main computer is a server on which clients, i.e. displays programs are logged. Running separates Matlab sessions and programs reduces the computation load, and therefore the risk of crashing during the test. The client programs can be restarted independently and logged onto the server during the test while preventing the recording process to be interrupted.

Figure 31 shows the graphical user interface loaded on the main screens. The channels properties, the sampling frequency and title of the experiment are displayed on the right screen of the main control panel (Fig. 31(a)). All channels have names which are entered by the user, and their value may be sent to numerical displays and/or graphs. The program is able to recognize word radicals such as "stag", "press" and "temp". For instance, if a user enters "Stagnation Temperature", a string finder algorithm detects that it corresponds to T_o used in air mass flow rate formula. If the channel names are judiciously chosen, there is no need to specify which channel is used for the calculation of other quantities, such as the equivalence ratio. The channel names are also stored and used to label the data during the post-processing phase. In addition, a safety algorithm ensures that the flow conditions do not exceed the ratings of the facility. The safety thresholds are either manually or automatically (name detection) assigned to each channel.

A channel type can be selected via a drop down menu, in which all the available sensors are listed. The sensitivity curves of available sensors and actuators are entered in the program during a preliminary inventory. By selecting a channel type the user attributes an input range, a sensitivity curve and a voltage-to-unit conversion algorithm. The channel has a status button for activation before launching the

acquisition session.

A drop down menu also allows the data to be sent in one of the three real time graphs anytime during the test. Otherwise, the display button generates a numeric indicator on the left screen for real time monitoring (Fig. 31(b)). Each of these indicator are labeled by the name of the channel, and peak LED indicates if a safety threshold is about to be exceeded. Presets can be saved and loaded in order to avoid setting up the entire interface at each tests, such that during the experimental campaigns, it takes less than a minute to start the program and launch the acquisition system.

Shortly before launching the acquisition process, the main program automatically writes a voltage-to-unit sub-routine and saves it under a time stamp. This program is unique to each configuration and is used to convert in real time the data from the card to the physical quantities which need to be monitored. It is also used during the post-processing phase. Once the acquisition is launched, the controls are locked during 10 seconds while the offset of each channel is measured and saved in a separate file. The same procedure is repeated at the end of the test once the wind tunnel is shut off. The offsets are used to center the data if needed, compare the test run at different days, monitor any sensor drift or malfunction. The program also logs on the Atlanta weather forecast station to get the weather conditions such as atmospheric pressure, temperature and humidity. This data is saved with the experiment description entered by the user in an information file. In general, the test run data comes with a matrix of the raw voltages, an information file, a voltage-to-unit program and the channel offset file.

When starting the GUI, the following instructions are executed :

1. A streamer pipeline is opened. Computers may log on the server with login names and passwords.

2. The programs load the full GUI interface on both screens of the main control panel and the appropriate skin appearance. All buttons on the screen have specific callback functions that are executed each time those one are activated.

3. A virtual DAQ object is created to emulate a Matlab environment from the actual DAQ card.

4. Safety thresholds are loaded from a text file; they are used to warn the user when entering a non-safe regime.

5. All object handles created are stored in one handle structure which is passed as an argument in all sub-routines of the program.

6. The user enters the experiment title, set up the channels and the sampling rate via on-screen interface. The information entered via switches and text boxes is used to initiate the DAQ board properly. A preset button allows the user to load a saved preset. A sub-routine generates numeric displays on the left screen for each channel that the user wants to monitor. At this stage, the touch sensors are still not configured.

7. A voltage-to-unit conversion program is automatically written, saved and ready to be executed based on the channel configurations. The name of the program has a time stamp. It is unique to the type of configuration that is run.

8. The memory is allocated to ensure a given runtime.

9. The configuration of the touch sensors interface is made by opening an additional window in which all 24 touch sensors can be assigned to a digital output via a callback function. Some callback functions are listed in Table 11.

10. When launching the data acquisition, a timer function is executed every 0.1 seconds described on Figure 11. The timer function captures the user actions

and sends the command signals through the LPT, USB and DA ports, to the solenoids and the controllers. The software peeks on the acquired data, apply the appropriate conversions from measured voltages and refresh all the displays. The user action can be also recorded on a common time frame.

Table 11: Callbacks functions used in this study to control the combustor. When maintained touched, a "Shift" function can be used to access to a second callback layer therefore emulating a 47 switch interface. A preset function also loads a saved touch sensors configuration.

Callback Function	**Callback Action**	**Example**
Toggle Switch	The assigned output is set active only when being touched.	Ramp actuators
Latch Switch	Inverses the state of the output.	Fuel valves, igniter.
Fuel Rate Up (slow)	Increases the fuel flow rate set point by 1% of the FS.	Flow controllers
Fuel Rate Down (slow)	Decreases the fuel flow rate set point by 1% of the FS.	Flow controllers
Fuel Rate Up (fast)	Increases the fuel flow rate set point by 5% of the FS.	Flow controllers
Fuel Rate Down (fast)	Decreases the fuel flow rate set point by 5% of the FS.	Flow controllers
Fuel Zero	Sets fuel flow rate set point to zero.	Flow controllers
Abort	Shuts off all fuel lines and turns off igniter.	Emergency procedure
Shift	Accesses to a second callback function layer when touched simultaneously with another sensor.	"Shift" + "Fuel Rate Up (slow)" = "Fuel Rate Up (fast)"
Record	Stores user actions in a matrix 10 times per seconds	
Play	Callback functions are executed on a following pre-recorded user actions timeline.	
Stop	Stops playing/recording session.	
Pause	Holds the recording/playing session.	

The timer function cycle is the process through which the user interacts with the experimental set up. The state of the touch sensor interface is recorded ten times

per seconds and stored in a Boolean matrix, which indicates if the sensor is touched or not. The respective callback functions are executed whenever **true** resulting in a change of the voltages at the pins of the LPT ports and the analog outputs (Port Array in Fig. 32). The TTL and continuous signals drive the actuators relays and the mass flow controller set points, respectively.

The combustor state is monitored via transducers signals which comes in a channel matrix of raw voltages. The channel matrix are converted to a data matrix using the voltage-to-unit program. The physical data is then compared to the safety thresholds entered based on the components rating of the facility. A safety algorithm may inform and correct the user action based on if the thresholds are exceeded. Recalling that manual override is always possible using the relay box switches. The data is then streamed out for display.

The sensors and video signal as well as user actions can be recorded on the same time frame. This gives the opportunity to reproduce the test as identical as possible since most of the user events can be recorded and "played" again. Moreover, the post-processing of the data is performed on the same platform, which avoids to transfer/convert the files between softwares.

2.7 Functional Hazard Assessment

An assessment on safety is carried out in this section in fulfillment of **Task 1(h)**. The safety assessment complies with the NASA Procedural Requirements and more specifically to the NPR 8705.5, as this approach is largely applied in the domain of aerospace. Figure 34 is the fault tree diagram. Due to the absence of redundancies in the design of the system, any failure may lead to abort the test.

The various failures reported in Table 12 with their respective failure classification from the NPR 8000.4 risk matrix.

The lack of redundancy in the design is compensated by an increase in the robustness of the structure. The infrastructure of the air supply is designed to handle pressures and temperature ranging up to 5 MPa and 810 K, respectively. The overall limitation of the air line is imposed by the settling tank which is the weakest element, with a maximum pressure of 2.2 MPa at 800 ^{o}K. Given the initial capability of the laboratory facility, the user may prescribe set points above the design limitations. To avoid structural damage, a pressure-calibrated burst disk is installed on the settling tank. The rupture of the disk occurs when the pressure reaches 90% of the tank pressure rating. As a result, the air escapes by a 63.5 mm diameter hole, and causes a pressure drop. This precaution also prevents the pressure to overshoot in case of wind tunnel obstruction. In addition, a mass flow limiter is installed upstream the settling tank. The mass flow limiter is a simple orifice plate that produces a pressure drop and protect the facility from being exposed to the high pressures handled by the laboratory infrastructure. The fuel line built with seamless stainless steel tubing connected with Swagelok^{TM} connections rated at 35 MPa. This value is about twice the highest pressure used on the entire setup. The typical pressure in the fuel line is no higher than 1.1 MPa due to the presence of flow controllers. As a result, an abnormally high pressures will lead to flow controller damage.

From a control perspective, running a test on a digital control panel may compromise safety, especially when giving partial or full authority to the computer. Due to the presence of flammable products and the relatively high powers involved, the situation may become hazardous if the computer response is not adequate, i.e. when reaching out from the control envelope. Therefore, the relay box has 24 manual switches for each relays as shown on Fig. 30, which allow the operator to override the computer actions. In case of power outage or fuse box overload, the controls are ineffective while fuel may keep flowing in the combustor. The facility must then go back to a safe configuration. Consequently, all fuel valves are normally closed, such

that in case of power outage, all fuel lines are shut. However, the airflow is maintained at low flow rates to flush the setup from any residual combustion compounds. In addition, the experiment room is equipped with a high pressure exhaust system in which the air continuously flows through the room to the main exhaust.

The mass flow controllers are not used as shut off valves as mentioned in the controller user's manual. Instead, several electric valves are used to enable or disable the fuel delivery. There is one main solenoid valve per channel which is located near each storage tank/bottle, such that in case of line rupture downstream the valve, the fuel line can still be closed. Another solenoid valve is located in the vicinity of the test section (fast shutter). All channels also have manual valves.

The electric load distribution is also a problematic in the setup of the facility. The solenoids and the igniter generate induced currents when being switched. The preliminary tests revealed that these currents are high enough to trip the fuses. In this case, the control panel shuts off while the rest of the facility may keep running. Following this incident, the electrical components have been wired to the fuse box based on their electric load and their importance. The main computer and the touch sensors are wired to a common resettable fuse, since they are critical components and represent a steady electric load. The igniter is also wired on a separate circuit with a higher breaking capacity.

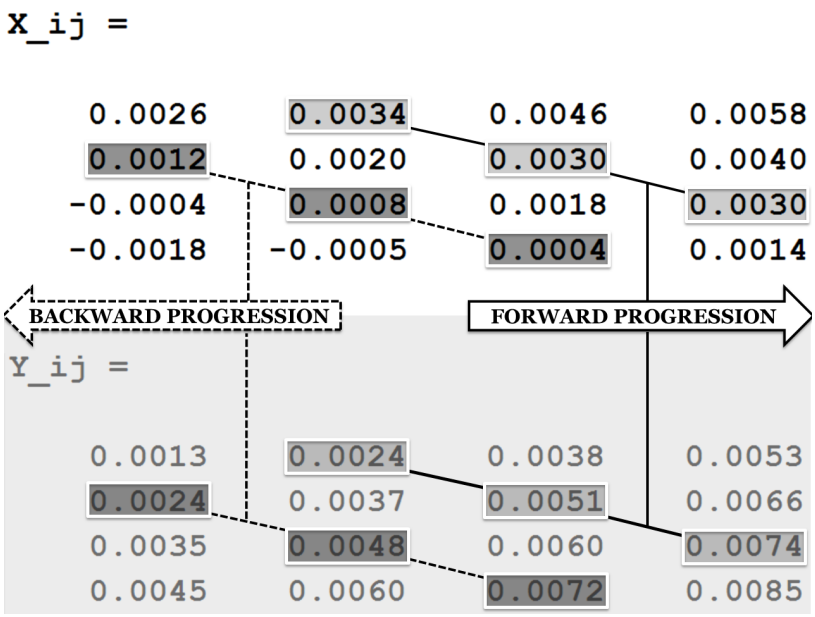

(a) Coordinates of intersection nodes between C_I and C_{II} referring to Eqs. (27) and (28) in the case of the parent node array shown in Fig. 21(b). The upper and lower second diagonal of the matrices corresponds to a forward and backward progression, respectively.

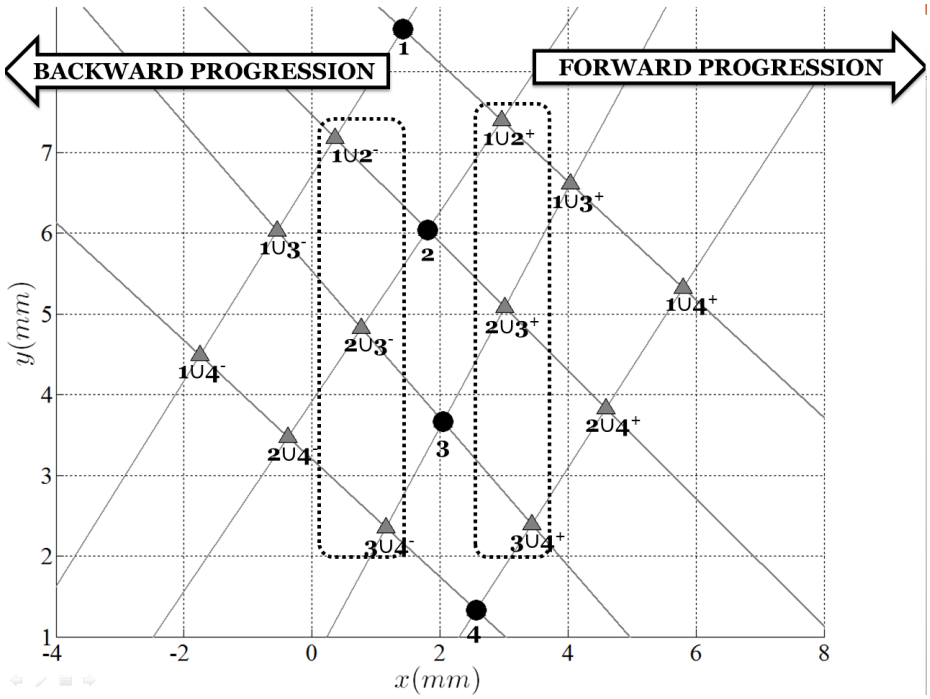

(b) Nodes 1,2,3 and 4 constitute the initial array. All C_I and C_{II}-curves have been traced and leave two possible directions for the progression. The children array is selected based on the proximity to its parent, in order to limit the error made by the linear approximation (Fig. 20(a)).

Figure 21: Intersection between C_I and C_{II} in the case of a node array.

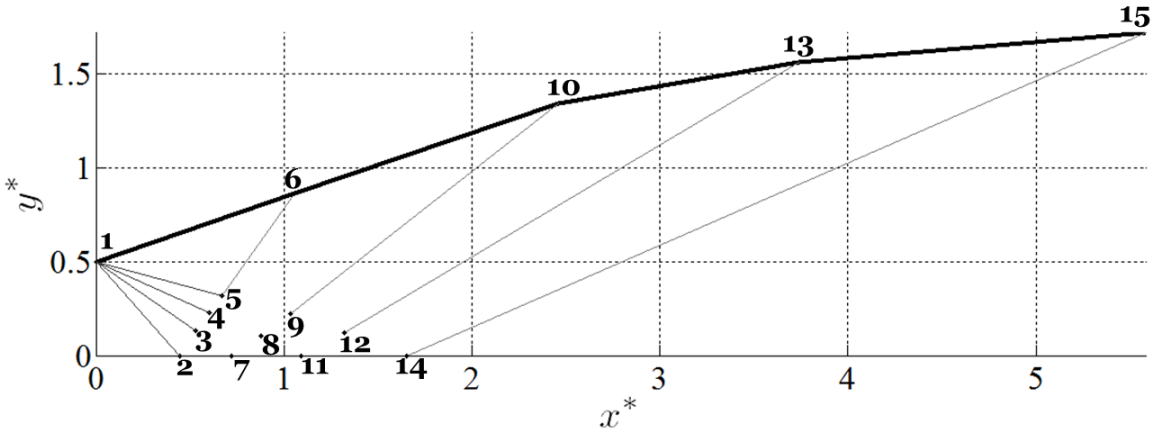

(a) Progression from 4 rays. The nodes are numbered with respect to their occurrence in the progression.

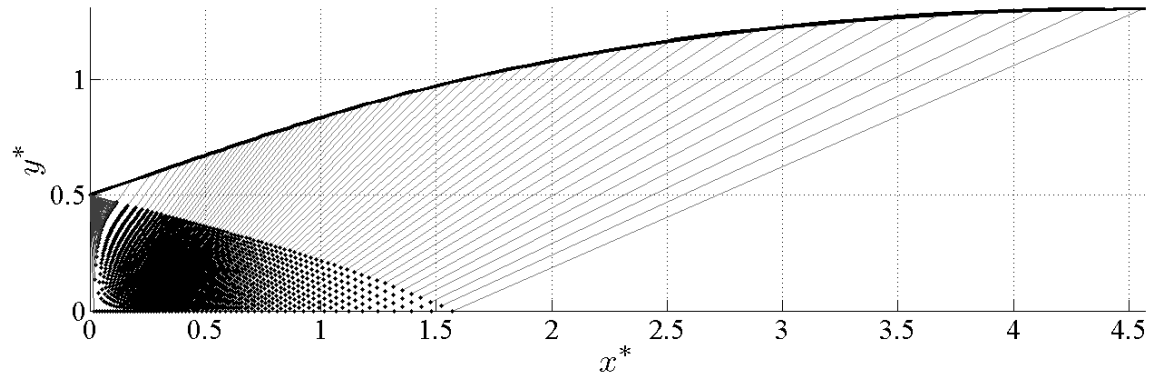

(b) Same algorithm run with 64 initial expansion waves (contour smoothing). The expansion fan is captured with a varying angular step : $(10^{-4}; \theta_{max}^{1/s})^s$, with $s = 2.5$, in order to refine the high curvature region of the contour.

Figure 22: Mach 2.5 compact nozzle contour with unitary throat height, designed using the method of characteristics ($\gamma = 1.4$).

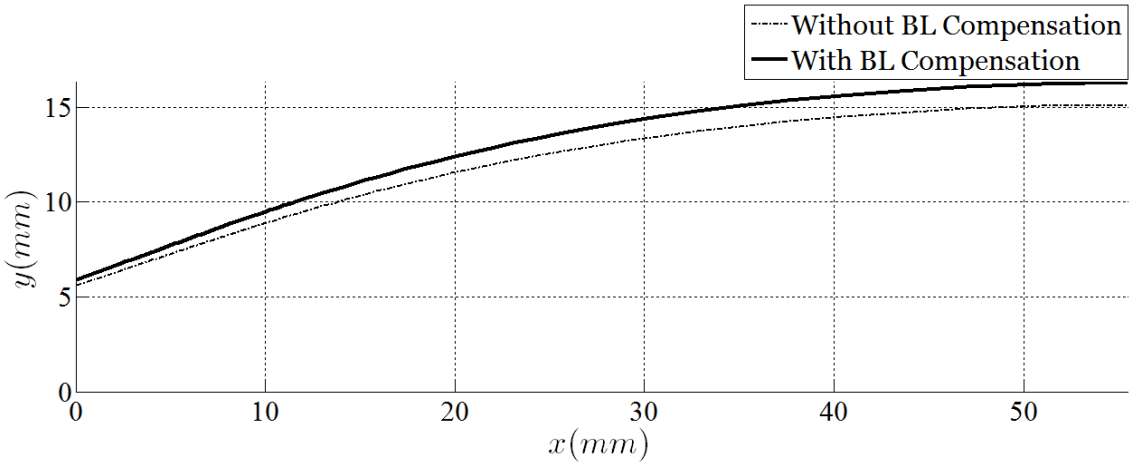

Figure 23: Comparison between initial characteristic design and boundary layer compensated nozzle profile : M = 2.5 in a 31.75 mm high vessel. The air static temperature at the exit was assumed to be 270K ($\gamma = 1.401$), which corresponds to 608K of stagnation temperature. The simulations were run with frozen chemistry.

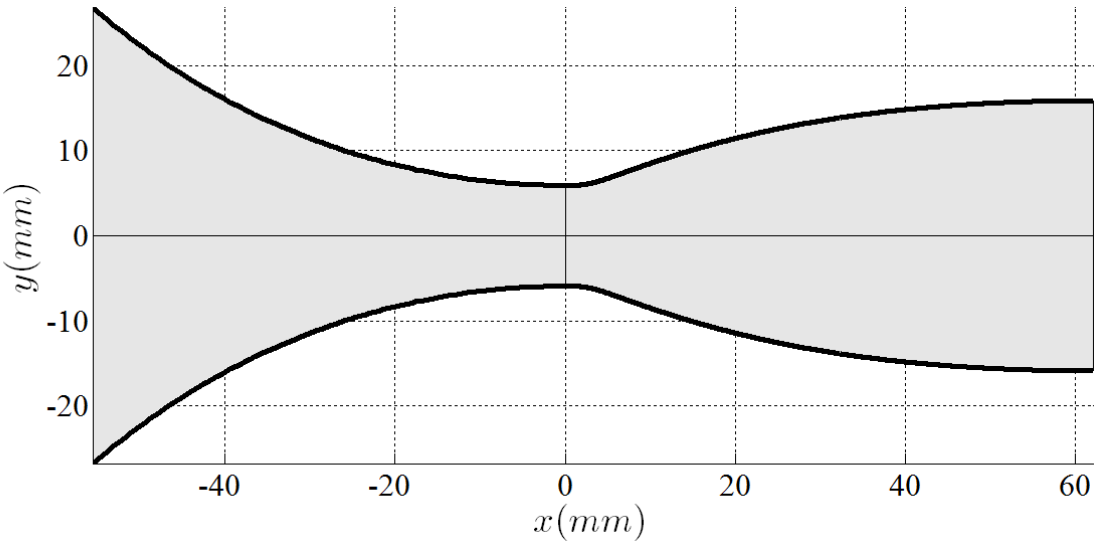

Figure 24: Final nozzle design : Mach 2.5, boundary compensated for air at 400K. The converging section has a circular contour.

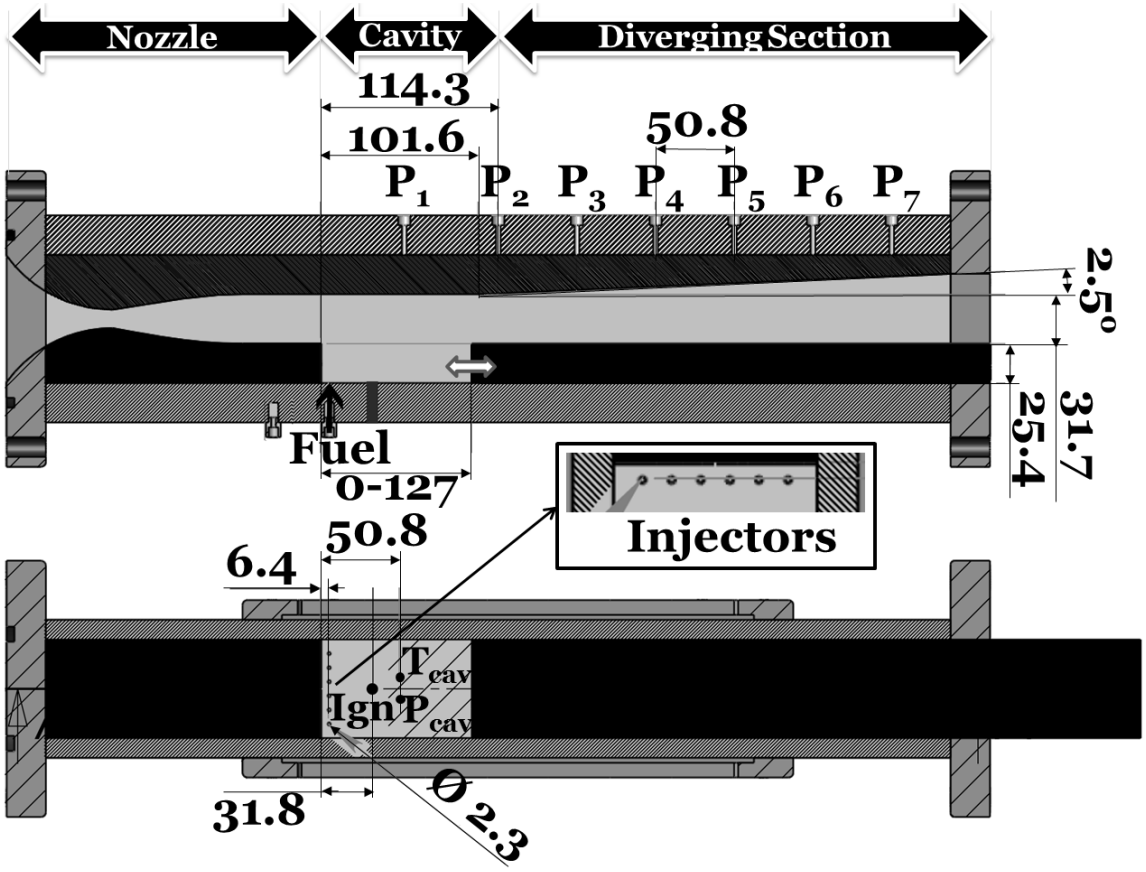

Figure 25: Test section cut view, L/D = 3.84 shown (dimensions are in mm).

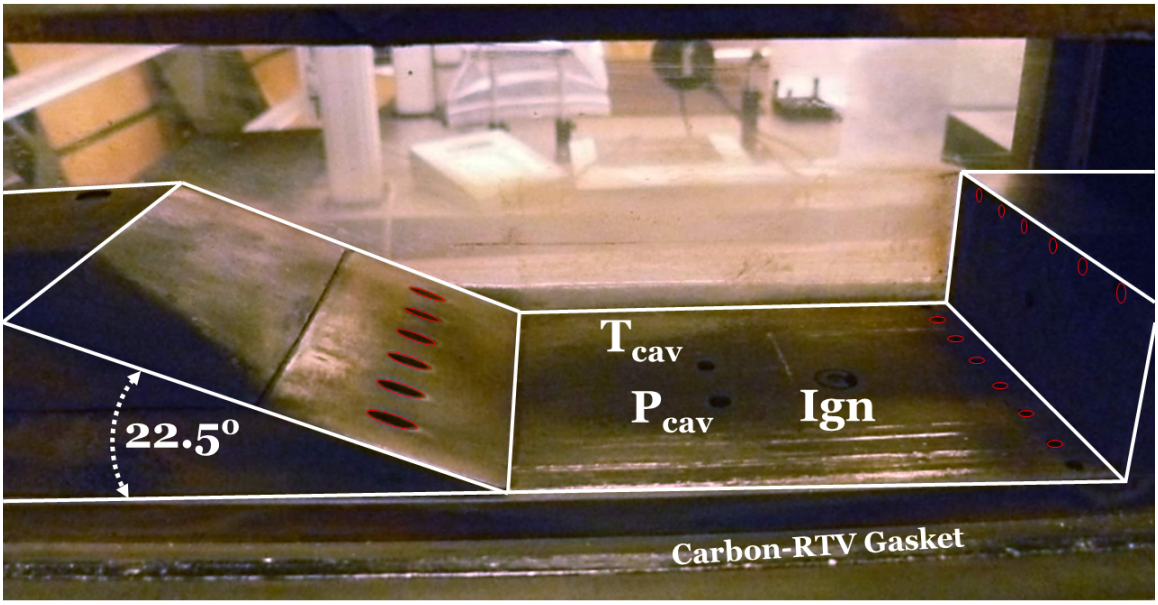

Figure 26: Photo of the cavity with a 22.5^o aft ramp. Leading step, floor and ramp Injectors arrays are visible (in red).

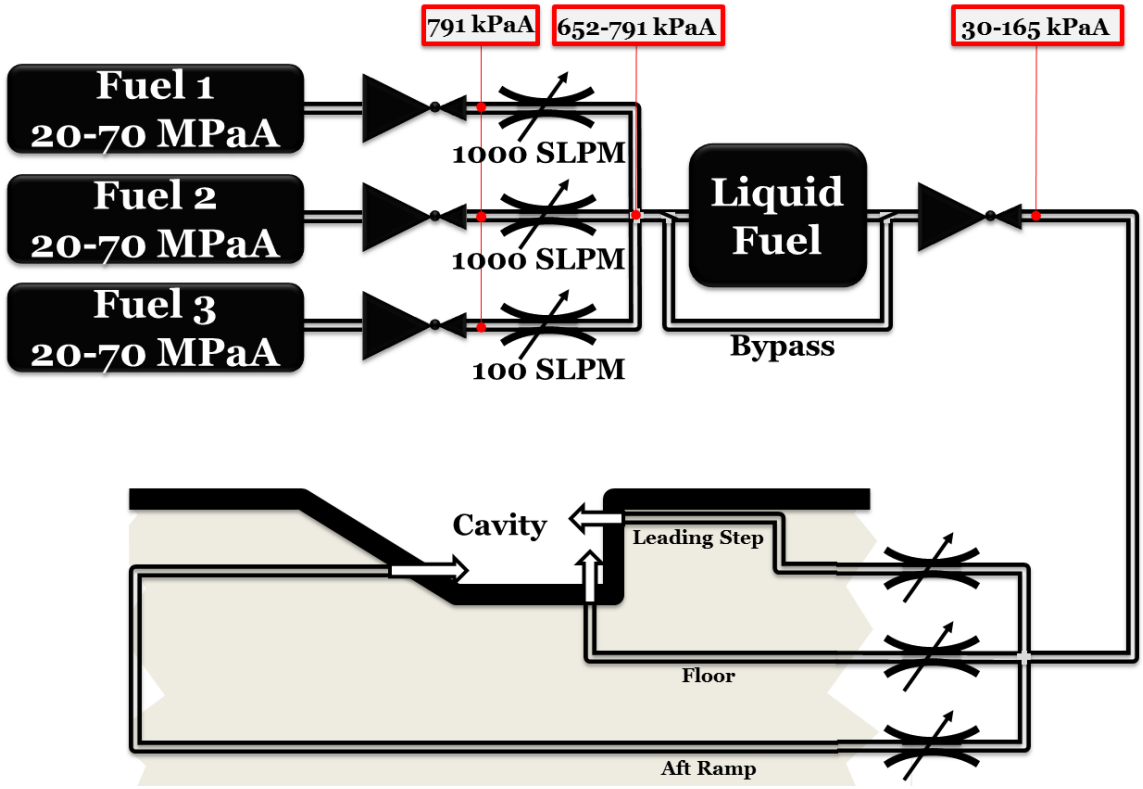

Figure 27: Fuel system network under typical operating conditions.

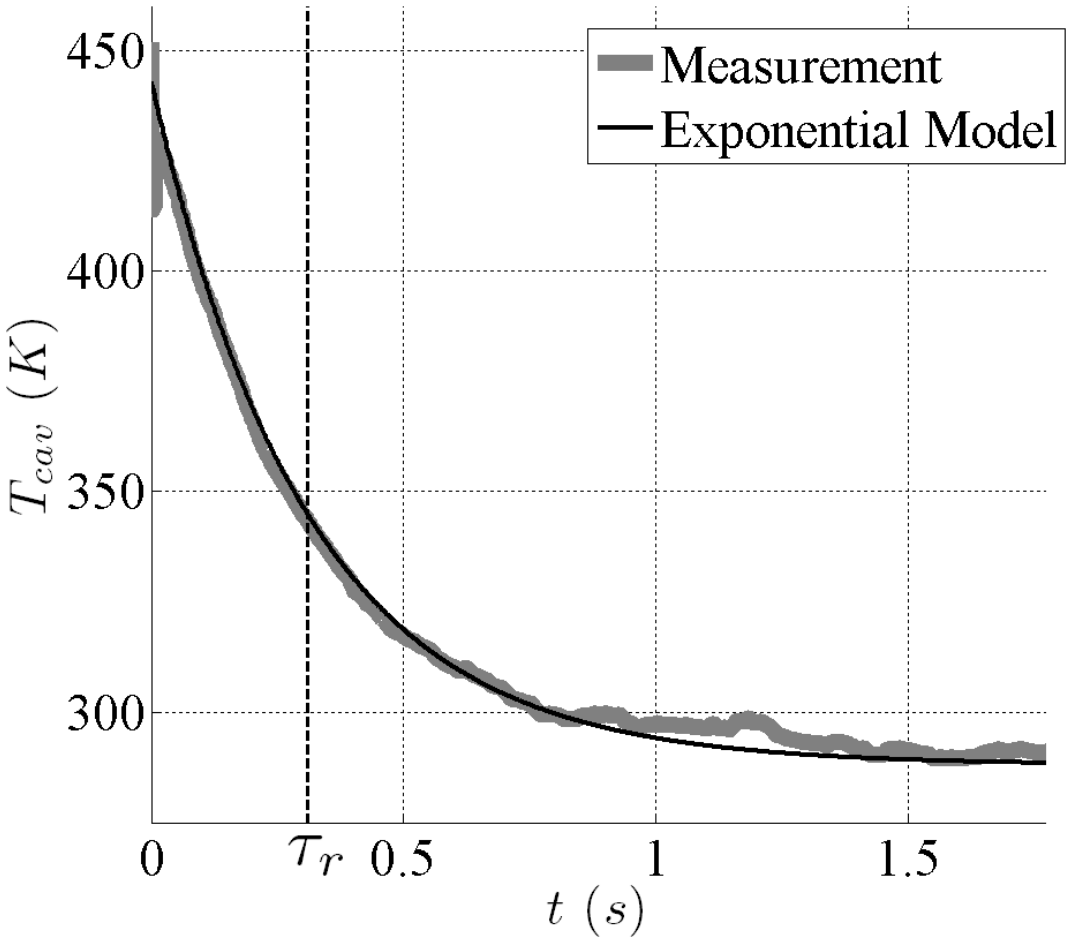

Figure 28: Cavity thermocouple time response.

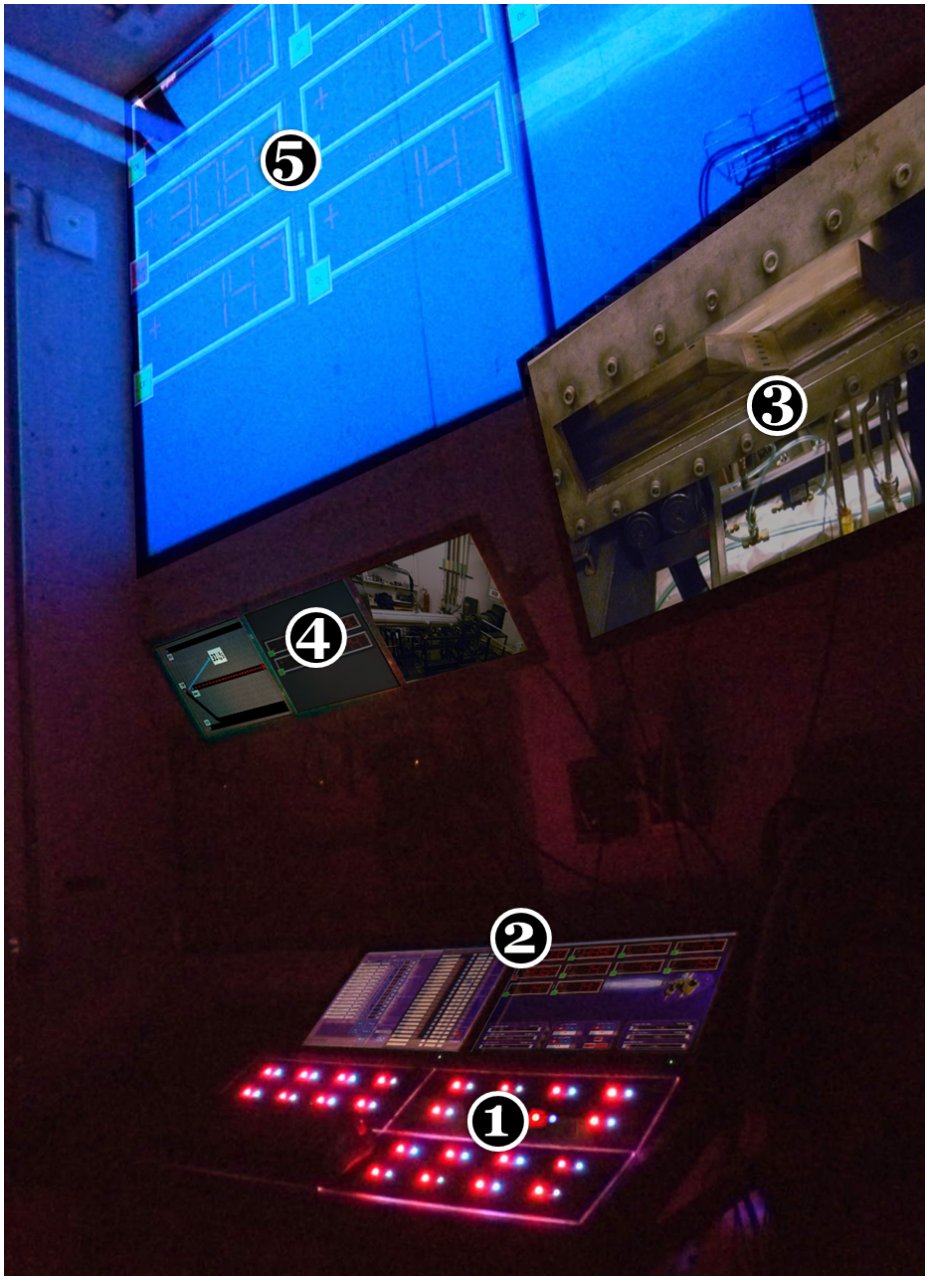

Figure 29: Control room. (**1**) : touch sensor interface with LEDs indicating the state of the switches. (**2**) : Main screens used for the test configuration and numerical displays. (**3**) : Live video from the HD camera in the control room. (**4**) : Overhead screens connected to three different computers for more complex, real-time representation of the data, or additional monitoring. (**5**) : Projector screen for visitors.

Figure 30: Relay box (top) with 24 mechanical switches, and power supply (bottom).

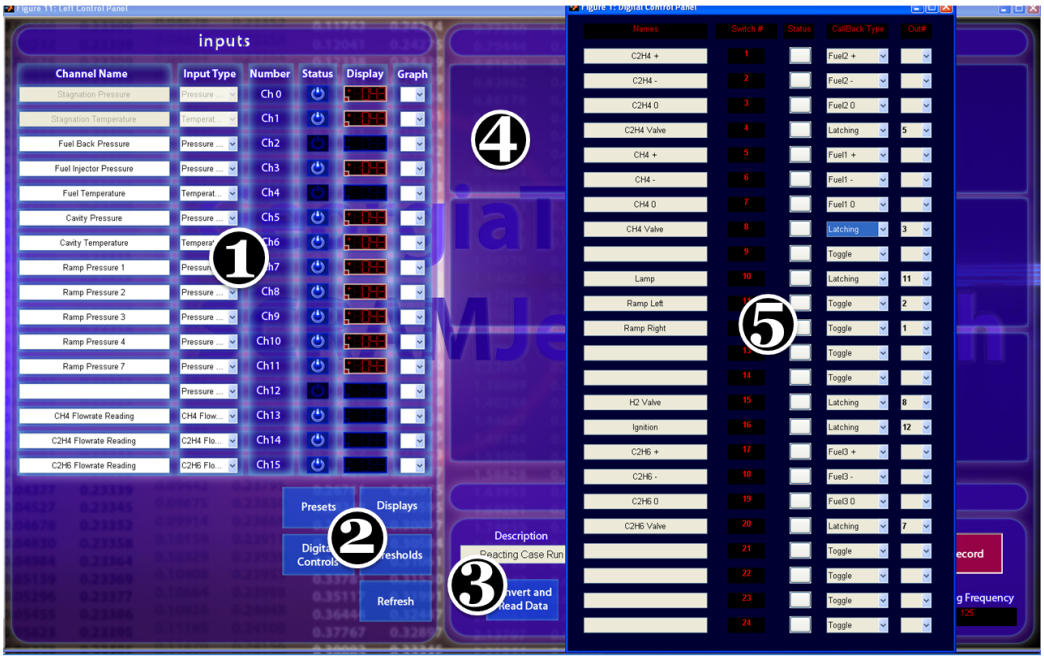

(a) Snapshot of the left display. (**1**) : Channel name, type, number, status, display and graph options. (**2**) : Load preset, load displays, edit safety thresholds, edit controls and refresh GUI. (**3**) : Data acquisition system setup, record-stop, experiment description and plot data. (**4**) : Real-time graphs. (**5**) : Touch sensors name, number, status, callback and output relay.

(b) The right screen. (**1**) : Numerical displays and peak LEDs. (**2**) : Fuel flow rates readings. (**3**) : Fuel flow rates targets. (**4**) : Ignition detection LED, nozzle choked LED, read-data from streamer. (**5**) : Air and fuel mass flow rate, equivalence ratio.

Figure 31: Control panel main displays.

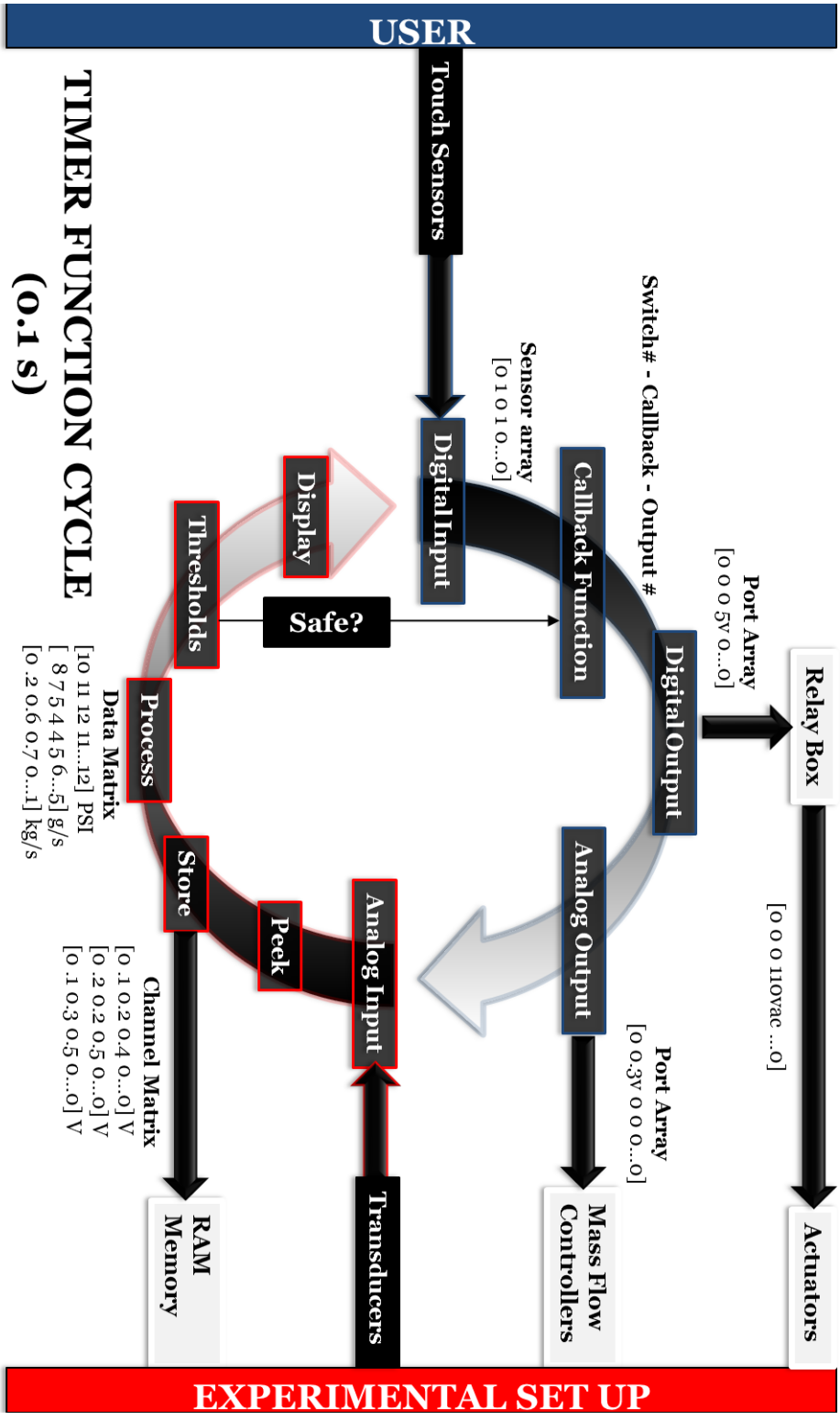

Figure 32: Timer Function Cycle.

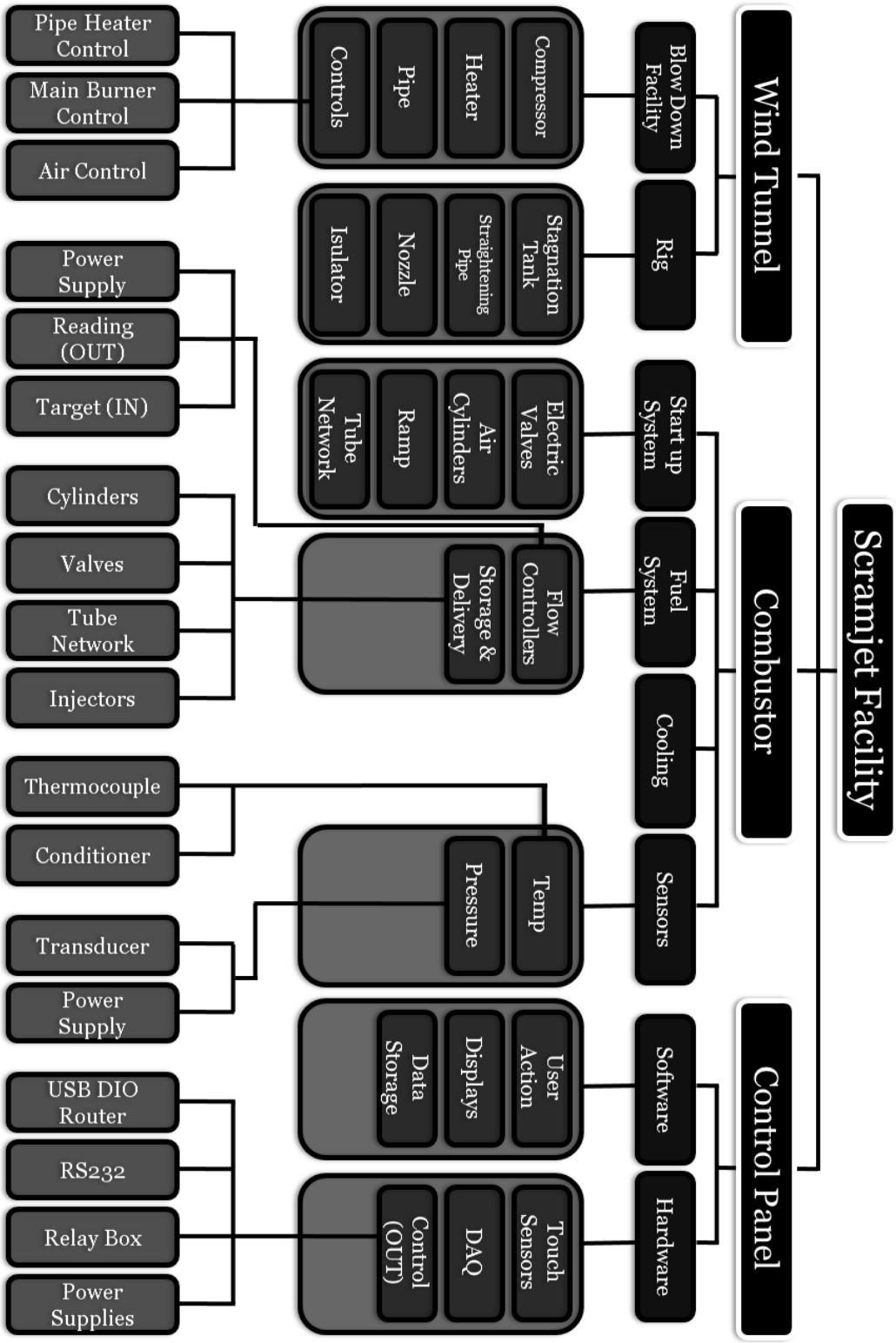

Figure 33: Functional tree diagram.

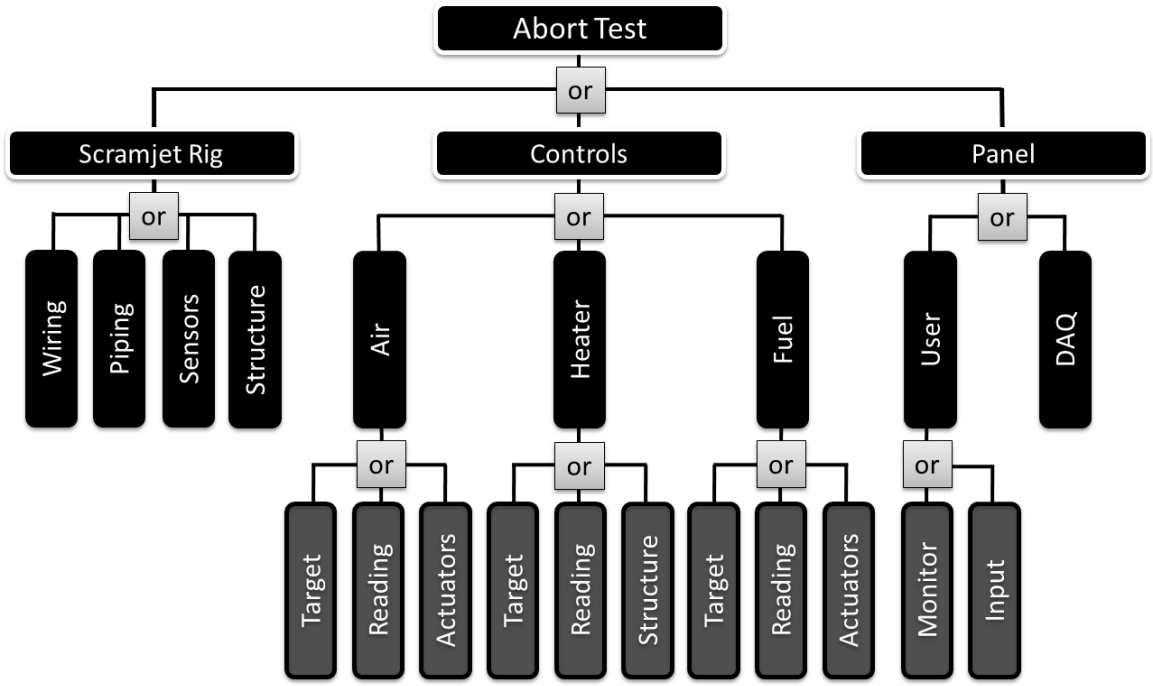

Figure 34: Fault tree diagram.

Table 12: Failure description and classification following the NPR 8000.4 risk matrix.

Function	Failure	Consequences	Type
Structure	Welds, screws, windows, pressure and temperature overshoots.	Cracks and junctions: leaks and misalignments causing shocks. Windows: cracks, leakage. Possible wind tunnel obstruction. Test section: severe structural Damages.	E-I
Tubing	Fittings, tubes.	Fittings: leaks. measured flow rates entering the test section are not correct. Tubes: leakage or rupture. Fuel is dumped in the experiment room.	E-I
Sensors	Electronic or mechanic part.	Failure to monitor. State of the system visualized by the operator is not the actual state. Decisions taken by the operator are no longer adequate.	D-III
Target	Wiring, controller.	Failure to control. Control system is unable to reach the targets.	D-II
Reading	Wiring, controller.	Failure to monitor and control. Control system does not display the actual state. Decisions taken by the operator are no longer adequate.	D-II
Actuators	Wiring, coil.	Failure to control.	C-IV
Monitor	User, timer function cycle.	Failure to monitor. Some events are not seen by the operator.	C-IV
Input	User	Wrong target. Overshoot. Can lead to structural failure.	C-II
DAQ	Data acquisition or storage.	Crash. Data overflow. Loss of Data.	C-IV

CHAPTER III

METHODS AND PROCEDURES

3.1 Startup Procedure

The ratio between the cavity depth and the wind tunnel vessel height is 0.8, such that the cavity represents a considerable load for the wind tunnel and transition to supersonic regimes can be difficult. The wind tunnel may or may not start depending on the cavity length. It has been found experimentally that systematic startup occurs below L/D = 2.25 for this facility. Above this ratio, startup may not occur systematically. The probability of starting up decreases as L/D increases and it becomes relatively difficult to start the wind tunnel at L/D $>$ 3. The system is therefore aerodynamically bi-stable, since two regimes can be run with the same stagnation conditions. This issue could have led to limitations in the study since only short cavities are investigated. A solution had to be found to overcome this problem.

Therefore to allow systematic startup with high reliability, a variable geometry is used. In this approach, two air cylinders drive a movable aft block shown on Fig. 35. It also offers the possibility to study combustion for various aspect ratios. The startup of the wind tunnel is visualized using a Schlieren system and reported in Fig. 36. Before startup, the aft step is brought against the leading step such that the smallest cavity is formed (Fig. 36(a)). In this configuration, the apparent load on the wind tunnel is reduced. Thus, the air flow rate is progressively increased until the nozzle is choked. The test section is then rendered supersonic upon further increase of the air supply (Fig. 36(b)). At this point, the aft block is moved downstream and the cavity is formed with the desired length (Fig. 36(c)). The flow is then allowed to reach steady state. This startup procedure is relatively simple and gave successful

and reliable startups for all cavity aspect ratios investigated. Any operating condition targets is reached within 30 seconds from start when running a non-preheated cross-flow. However when preheat is used, hot air is run in the facility at a low flow rate (0.2 kg/s) before start up in order to heat up the facility. Once the wind tunnel is started, 2 to 5 minutes are spent in supersonic regime to reach the target temperature since the stagnation temperature is also a function of the air flow rate. This initial startup time does not cause any major issue given the runtime capability (over 20 minutes) of this facility.

The interface between the aft ramp and the bottom part of the test section is lubricated with anti-seize compound. The aft block is spring-loaded on the bottom part of the test section such that the clamping force (which can reach up to 10 kN) is maintained constant. Regardless, the static pressure in the test section after startup is sub-atmospheric, which gives a tendency for the ramp to be "sucked in". If the clamping force is not adjusted properly, the ramp may move upward once supersonic regime are reached. The spring compression is therefore adjusted by rotating bolts to prevent this effect. As a result, the ramp cannot be moved if the wind tunnel is subsonic, since the clamping force is usually too strong for the actuators.

3.2 Ignition-Blowout Procedure

The majority of the experimental effort is dedicated to the characterization of the flame stability. Therefore a rigorous procedure is needed to ignite the cavity and then systematically bring the combustor toward its blowout limits, and is described below.

3.2.1 Ignition

The first step takes place in a non-reacting flow at a steady flow regime : The igniter is switched on and fuel starts flowing into the cavity. Ignition depends on the size and the arc power of the igniter, as well as the overall mixture present in the cavity and

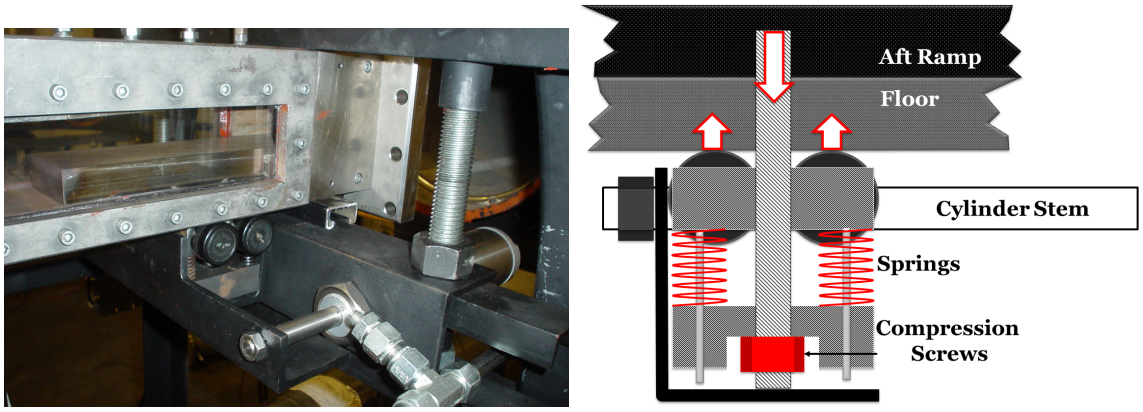

(a) Photo of the test section with the startup system. The ramp is assembled on a cart which allows the clamping force to be adjusted with a system of 4 springs. Two air cylinders can develop up to 1 ton of moving force.

(b) Schematic view of the ramp-chart-cylinder assembly. The arrow indicate the clamping force coming from the reaction between the springs and the wheels of the chart.

Figure 35: System used to move the aft block.

it is usually performed at a favorable fuel flow rates (0.6 g/s) and hydrogen dominant fuel mixtures (90% hydrogen and 10% of methane in mass proportion), typically far off from the blowout regions investigated in this study. As noted earlier, additional hydrogen is run in the igniter tube to support the ignition process. If the conditions are adequate ignition is followed by a sudden temperature rise. The latter is captured by the thermocouple located on the cavity floor.

Figure 37 shows an ignition scenario as the fuel flow rate is being increased. Two flame regions appear around the injectors and along the leading edge, respectively, as seen in Fig. 37(a). The latter location indicates that this reaction zone is supported by hot walls. This type of flame-wall interaction is important for stabilization of the flame and will be discussed further below. Sudden combustion activity surges are visible (few tenth of milliseconds) in Fig. 37(b) during which the two regions attempt to merge. If the fuel flow rate is further increased, the bottom reaction zone grows and merges with the other flame region located in the shear layer (Figs. 37(c) and 37(d)).

(a) The aft block is brought against the leading step before the ramp up of the air flow rate. In this configuration, the aerodynamic load is minimized by having the smallest cavity (no cavity is formed in the rectangular case shown).

(b) The increase of air flow rate eventually brings the test section to a supersonic regime. An oblique shock wave appears at the junction between the aft block and the leading step of the cavity. Its angle can be related to the Mach number of the flow.

(c) The aft block is then moved downstream when activating the air cylinders. As a result, a recessed cavity is formed in a supersonic cross-flow with the desired flow conditions. Generally, the static pressures measured in the test section are sub-atmospheric, and indicate that potential energy of pressure has been converted into kinetic energy.

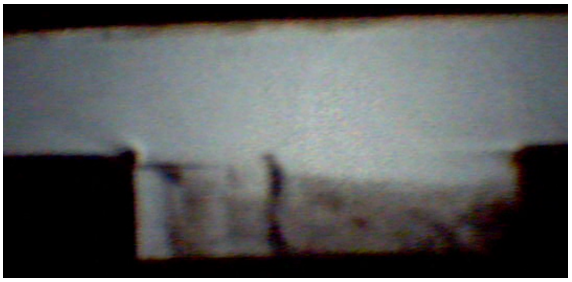

(d) On this image, the startup did not occur : the stagnation pressure and temperature are the same as in Fig. 36(c). The static pressures measured in the cavity are relatively higher than in the latter case. A strong compression point is visible at the trailing edge. The shear layer is also much less visible and its angle is lower.

Figure 36: Time average Schlieren images during wind tunnel startup.

3.2.2 Fuel Mixture Adjustments during Combustion

Once ignited, the igniter and the additional hydrogen supply are switched off. The combustion process may hold without external aid. This defines self-sustained combustion. In this study, the characterization of the combustor stability is carried out for self-sustained combustion only.

The combustor is maintained at this regime until wall steady state temperature is reached, which takes about 10 seconds. The fuel mixture is then adjusted to a gross mixture composition target. This step does not take more than 2 seconds to

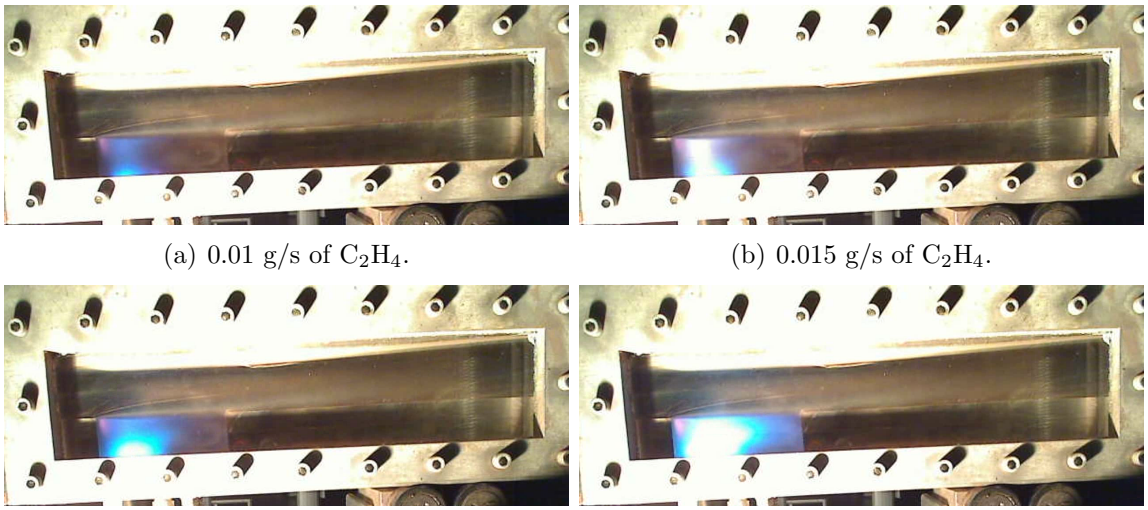

(a) 0.01 g/s of C_2H_4. (b) 0.015 g/s of C_2H_4.

(c) 0.02 g/s of C_2H_4. (d) 0.04 g/s of C_2H_4.

Figure 37: Progressive fuel ramp up with spark and additional hydrogen supply. The flame sits near leading edge and shifts toward the trailing edge as the overall fuel flow rate increases.

be executed. However, if the mixture changes rapidly, the controller readings do not correspond to the actual mixture being injected due to the time it takes for the fluid to travel from the mass flow controller to the injectors. An estimate of this lag is obtained as function of the mass flow rate, the length of the pipe network and the time average fuel composition, and is accounted for in the post processing of the data. In the next step, a slow tuning phase is necessary to ensure that the mixture composition injected in the cavity fairly coincides with the controller readings. The fuel mixture composition is slowly changed such that each change has time to take effect. A real-time algorithm regulates the fuel delivery. The total error on the fuel mixture at blowout is within 1% of the mass flow controller full span.

3.2.3 Blowout Procedure

Some fuel mixture compositions or flow rates will cause the flame to disappear (extinct) and a sudden temperature drop is recorded by the thermocouple in the cavity. The combustion may cease due to lack of fuel (low fuel flow rate studies) or oxidizer

(high fuel flow rate studies). These blowouts are sometime referred as lean or rich blowout, respectively. Figure 38 shows two frames in a sequence of a blowout when maximum fuel flow rate is reached. The flame seen in Fig. 38(a) may be supported by the recirculating products in the cavity. A small change in the fuel mixture composition causes this flame to blowout and disappear 33 ms latter, leaving a red glowing region where the hot products were(Fig. 38(b)). This glow does not necessarily come from the back steel wall as it has been observed even with the quartz windows.

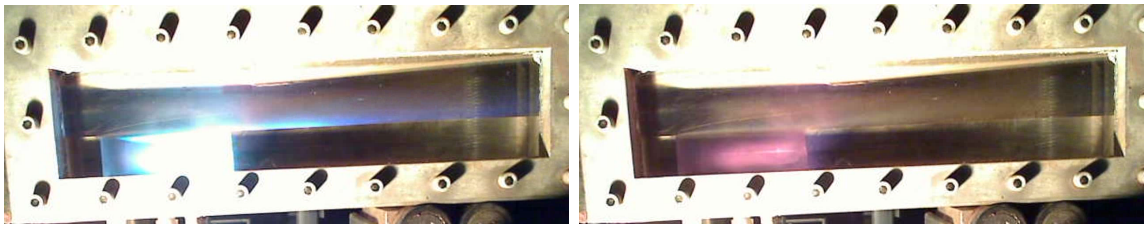

(a) t = 0 ms : blowout is imminent, the flame liftoff is visible as well as the reaction in the downstream boundary layer.

(b) t = 33 ms : remnant products are still visible by a red-orange glow. Similar observations have been made with both quartz windows on.

Figure 38: Flame blowout in excess of fuel.

3.3 Blowout Detection

An accurate real-time technique was developed to detect ignition and blowout events from the data collected without using the video data since some of the test were carried without windows. Figure 39 shows the temperature data in which the structure behaves as a thermal capacitor such that after ignition, it takes about 10 seconds for the combustor walls to stabilize at their steady temperature. An efficient algorithm is used to post process the data in which the temperature measured in the cavity is used to detect the ignition and blowout phases. Two sliding averages $s_1(t)$ and $s_2(t)$ are computed as

$$s_i(t) = \frac{1}{\tau_i} \int_{t-\frac{\tau_i}{2}}^{t+\frac{\tau_i}{2}} T_{cav}(t')dt', \ \tau_i = 1, 10 \tag{36}$$

where τ_i = 1,10 s for i = 1,2 are two different time intervals. The first average s_1 is carried over 1 second, which is approximately the characteristic response time of the thermocouple, whereas, the second average s_2 is carried over 10 seconds, which corresponds to the characteristic response time of the cavity structure. A trigger signal is then defined as

$$Trigger = \frac{s_1 - s_2}{s_2} \frac{ds_1}{dt} \tag{37}$$

If the temperature is quite steady in time, the two averages tend to the same values and the difference $s_1 - s_2$ is small. Note that s_1 has a faster time response than s_2 owing to a higher cut off frequency (1Hz) such that at ignition or blowout, the two signals phase out and the difference increases above or below 0. This variation is substantial if the temperature exhibits a coherent increase or decrease, which lasts about the time average span of s_2 ($\approx$ 10 seconds). An empirical threshold is defined using the video data to indicate an event. If the trigger becomes less than the threshold value, a partition is created in the data, as shown in Fig. 39. The algorithm separates the reacting from the non-reacting data based on the average temperature in each partition. It is important to keep the algorithm simple to allow for real time applications. Typically, 254 blowout events have been processed using this method within a couple of minutes. The error induced by the time uncertainty on the fuel mixture composition does not exceed 0.1% of the full span of each fuel channel since the fuel mass flow rates slowly evolve when reaching blowout.

3.4 Mixture Space

The data is represented in the mixture space (Fig. 40) since various fuel compositions are investigated. Figure 40(a) shows a typical ignition-blowout procedure as a function of the fuel mixture composition for a methane-hydrogen fuel blend. Starting from a stable combustion operating point, the fuel mixture composition is changed

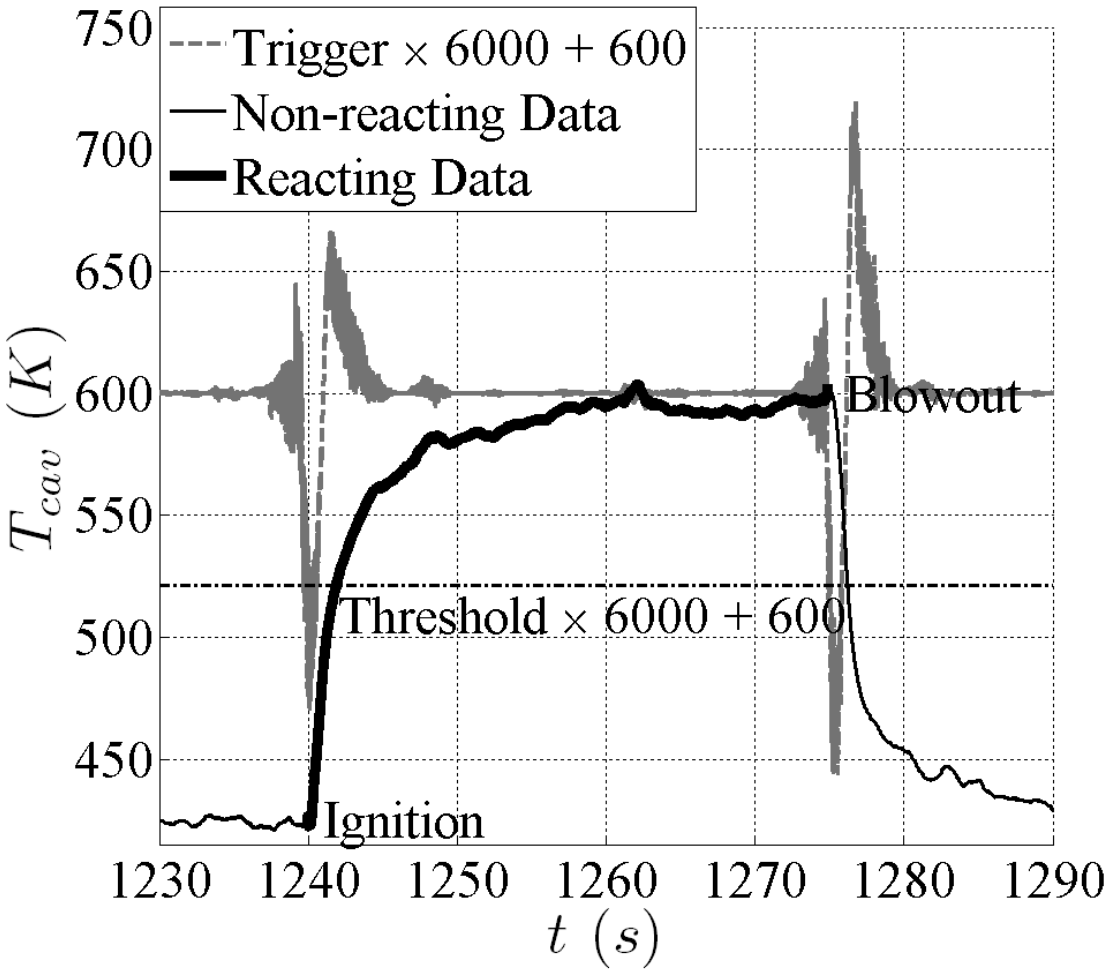

Figure 39: Ignition and blowout event tagging.

slowly to determine the blowout limit for various mixture compositions. There appears to be no uniqueness in the blowout mixture since many combinations of air, ethylene, methane and hydrogen can result in blowout, even when the wind tunnel operating conditions are held fixed.

For visualization purposes, the overall mixture is represented in a three dimensional space where a given regime is a point whose coordinates are the mass flow rates of air, methane and hydrogen. The blowout limit then draws a region that separates stable combustion from the mixtures for which no combustion is sustainable. The stable combustion domain forms a volume in which lies all the mixture compositions

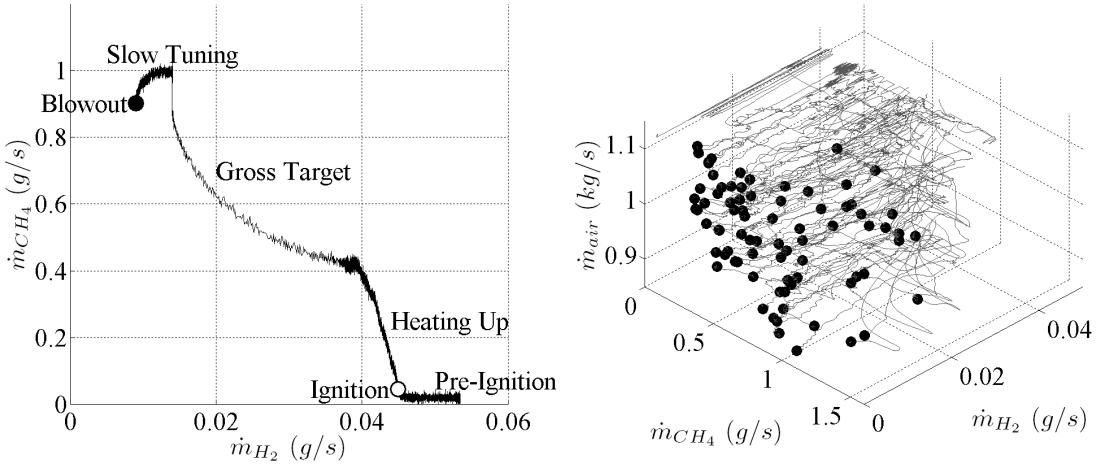

(a) Ignition - Blowout procedure in the mixture space.

(b) Stable domain and blowout region in the mixture space: Mixture trajectories (grey lines) and blowout events (black symbols).

Figure 40: Construction of the experimental blowout region : (a) depicts a single orbit in the mixture space whereas (b) is the collection of all orbits (burn data). The end points form the blowout region.

that resulted in stable, self-sustained combustion. This volume is expected to be a function of the preheat temperature, the fuel injection location and the cavity aspect ratio. Figure 40(b) shows the experimental data in terms of trajectories in the mixture space. These are the paths that satisfy ignition and burning such that it is possible to estimate the size of the stable combustion domain. All the trajectories terminate in blowout points, which then draws a surface beyond which no flame is observed.

There are no accurate measurements of the actual amount of air that is entrained into the cavity. Many parameters control the air entrainment, including the size and the stability of the shear layer established at different air flow rates and combustion regimes. Consequently, the stagnation pressure is shown on the third axis as an indicator of the overall air mass flow rate and the static pressure of the cross-flow.

3.5 Equivalence Ratio

The instantaneous effective equivalence ratio is deduced from the mass flow rate measurements (Eq. (33) and (35)), and is computed for the cross-flow (overall equivalence ratio) or the flame-holder based upon knowledge of the rate of air entrained into the cavity. Because of the discrepancies between the actual fuel flow rate and the readings discussed in Section 3.2.2, the equivalence ratio is only meaningful at steady fueling rates.

$$\Phi = \frac{\frac{\dot{m}_f}{\dot{m}_a}}{\frac{\dot{m}_f}{\dot{m}_{a,stoic}}} = \frac{\dot{m}_{a,stoic}}{\dot{m}_a} \tag{38}$$

where the stoichiometric mass of air $\dot{m}_{a,stoic}$ is readjusted based on the fuel composition, since the latter changes with time.

$$\dot{m}_{a,stoic} = M_a \left(\frac{1}{2}\frac{\dot{m}_{H_2}}{M_{H_2}} + 2\frac{\dot{m}_{CH_4}}{M_{CH_4}} + 3\frac{\dot{m}_{C_2H_4}}{M_{C_2H_4}} \right) \tag{39}$$

where M_a is the molecular weight of air. Several type of equivalence ratios are used in cavity flame-holding studies depending on the air flow rate reference that is being considered. The overall equivalence ratio is used in studies with primary injection and is based on the total air flow rate (Eq. (33)) and the total fuel flow rate injected in the cross flow. Another definition used by Rasmussen et al. [81] for data scaling purposes is carried out on the cavity only, and involves a characteristic air flow rate $\dot{m}_a^*$ which accounts for the shear layer entrainment. The actual equivalence ratio for the cavity requires a precise knowledge of the entrainment mechanism under fueling, and is usually a rough estimate.

3.6 Heat Transfer Measurements

The rectangular aft block of the cavity was instrumented with several thermocouples to estimate the wall heat loss. The thermocouple response do not range up to flame

temperature, therefore, the probes are shielded inside the ramp structure to avoid response saturation. Thermocouple measurements from the inner structure of the test section has been done in the past [23, 49, 57, 7], and the reconstitution of temperature profiles is a common procedure.

In this setup, the thermocouple tubing is run through channels, as shown in Fig. 41. However, due to machining limitations, there is a small gap between the probe and the structure which depends on the bore out tolerance. From a heat transfer perspective, the presence of this gap is seen as an abrupt change in the thermal conductivity, and may deflect the heat flux in the vicinity of the probe. Therefore, the gaps were filled with high temperature solder, which acts as a thermal seam and reduces the intrusive effect of the measurement devices.

Furthermore, to capture the spatial dependencies of the temperature distribution in 3 dimensions, the thermocouple tips have been arranged to form a parallelepiped (interpolation domain). The location of the probes allows the system to capture streamwise the gradients and curvatures along all three dimensions (independent basis), as well as the intensity and the symmetry of the temperature distribution. The spacing between the probes is chosen assuming a relatively low wavenumber of the heat distribution, in which the gradients along the x_1-direction are considered to be larger, hence the aspect ratio of the interpolation domain. The temperature distribution is then extrapolated to the leading step based on the heat equation, and assuming a polynomial form of the solution. The extrapolation method is described in Appendix B and also involve the steady-state assumption. Therefore, the heat transfer calculations are only meaningful when carried out on the steady-state data.

The wall heat loss is given below in Eq. (40).

$$\dot{Q}_w = \int_A \underbrace{-k\nabla(T).\mathbf{n}}_{\dot{q}_w} \, dA \tag{40}$$

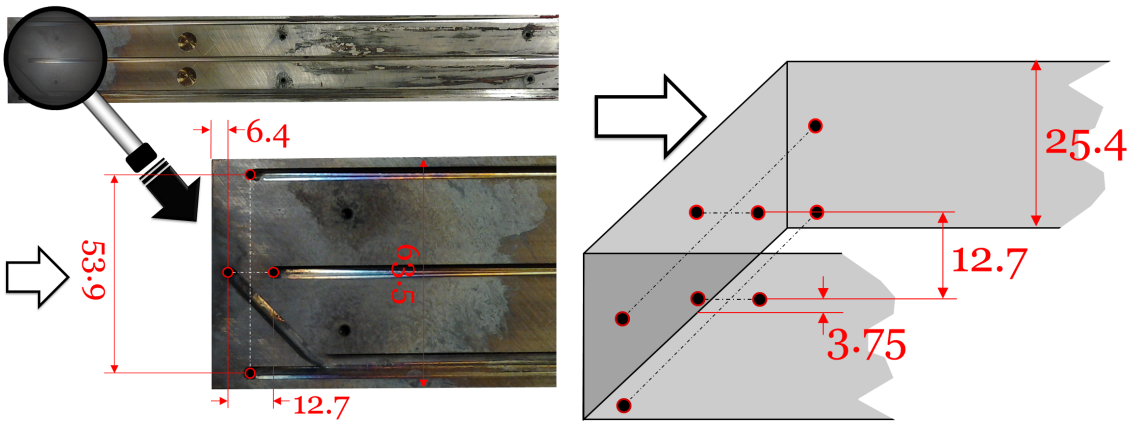

(a) The thermocouple are inserted through the ramp block. In order to capture the variations of the temperature in each direction, the tip of the probes (red circles) are arranged in a cross pattern. The grey stain visible on the picture, is a residue of the high temperature solder which is used to fill the gap between the structure and the thermocouple tubing.

(b) Isometric view of the ramp and the 8 thermocouple tips. The same cross pattern as in Fig. 41(a) is duplicated at two heights to delimit the interpolation domain.

Figure 41: Thermocouple instrumentation set up employed to measure the heat transferred from the cavity to the aft step (dimensions are in mm). The arrow indicates the direction of the flow.

where the interpolated temperature is derived in Appendix D.

$$T = \lambda_0 \prod_{i=1}^{i=5}(x_1 - \lambda_i) \prod_{j=1}^{j=5}(x_2 - \lambda_j) \prod_{k=1}^{k=5}(x_3 - \lambda_k) \tag{41}$$

Therefore the extrapolation process simplifies into finding the temperature distribution given in Eq. (41) which fits best to the temperature measurements. This type of process is a residue minimization between the experimental data and the temperature model. The problem is non-linear and the convergence of the solution may not always be guaranteed, such that the initialization is performed carefully.

The initial temperature distribution is obtained from polynomial best fit on the experimental data normalized by its mean value, in each direction. This provides a first guess for the roots λ_i, $i \in [1:15]$. λ_0 is a scaling factor which is determined by minimizing the residue with the guessed solution. From this initial distribution,

the residue may converge and oscillate around a new minimum, since perfect matching between experimental data and polynomial model in Eq. (41) is unlikely. The minimization process provides refined values of λ_i. From a practical perspective, the temperature at a given time is deduced from the solution found at the previous time step, such that the initialization process described above is usually performed once per burning segment. Given the degrees of freedom of the temperature model, the experimental data is matched with an average error of 11 K.

The heat flux is then determined from the temperature gradient at the wall which is calculable since the temperature distribution in Eq. (41) is volumetric, however the heat conductive coefficient k also depends on the temperature. A model for k as a function of T is deduced from best fit on the data found in heat transfer literature [43, 18, 75], for stainless steel (Eq. (42) gives values of k in W m^{-1} K^{-1}).

$$k = 0.018T + 14 \tag{42}$$

The temperature distribution estimated from the discrete probe measurements is shown on Fig. 42, and shows that residue minimization yields a solution which captures the presence of the flame resting the leading edge.

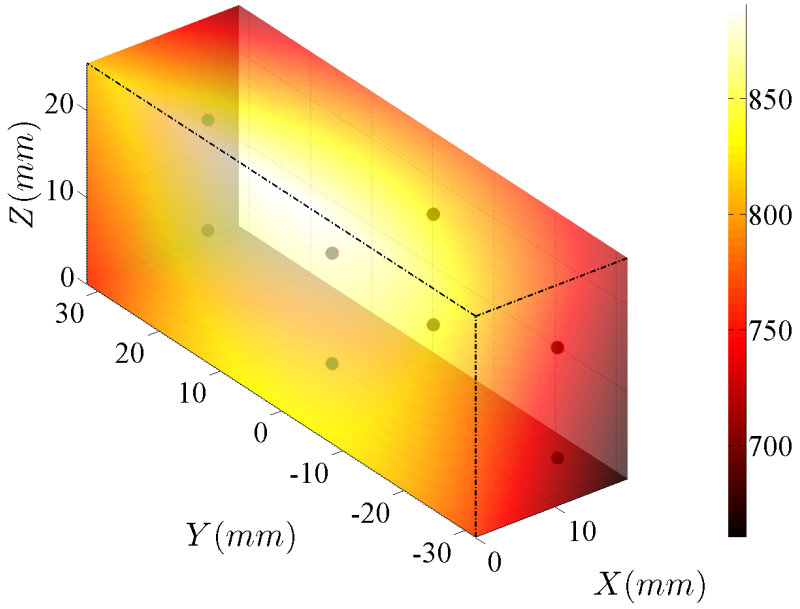

(a) Isometric view of the temperature distribution (in K) extrapolated from the 8 temperature probes (black dots). The thermal signature of the flame is captured by the extrapolation technique, and the heat flux is deduced from the temperature gradient across the aft step.

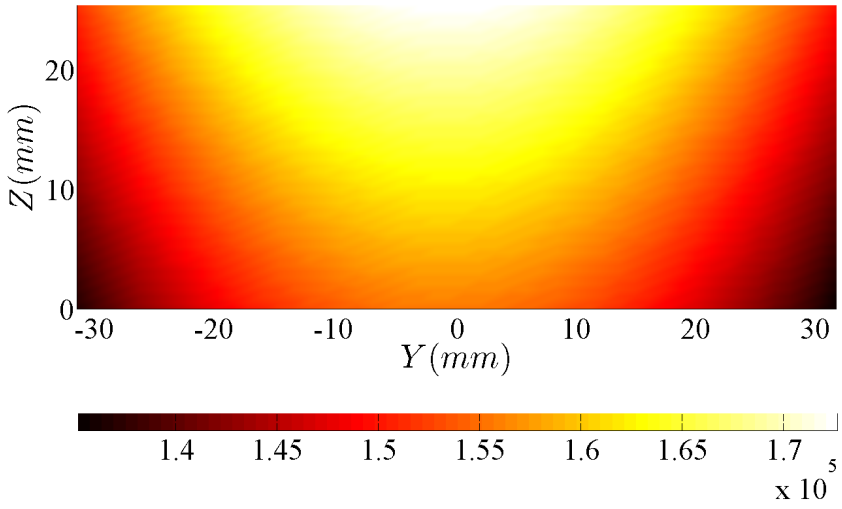

(b) Normal heat flux on the aft step in W/m^2.

Figure 42: Example of temperature and heat flux distributions obtained from data extrapolation (Appendix B) at a given steady state.

CHAPTER IV

RESULTS

Combustion studies began after completion of the wind tunnel validation campaign. The tests have been carried for stagnation pressures ranging from 500 to 1400 kPa and with low and high preheat. The experimental data is discussed for both stable and unstable combustion, and is complemented by a kinetic study in which the intrinsic properties of the fuels used in this study are compared.

Table 13: Test matrix

	Fuel	Fuel Flowrate	L/D	β	Inj.	P_{cf}	T_{cf}
Case 1	CH_4-H_2	0-1.3 (g/s)	3.84	90^o	Floor	34-58 kPa	135±2.5 K
Case 2	CH_4-H_2	0-1.3 (g/s)	3.84	90^o	Floor	34-58 kPa	248±10 K
Case 3	CH_4-C_2H_4	0-1.3 (g/s)	3.84	90^o	Floor	33-53 kPa	248±10 K
Case 4	CH_4-C_2H_4	0.5-2.2 (g/s)	3.84	90^o	Floor	56 kPa	135±2.5 K
Case 5	CH_4-C_2H_4	0.5-2.2 (g/s)	3.84	90^o	Floor	56 kPa	293±10 K
Case 6	CH_4-C_2H_4	0.5-2.2 (g/s)	2.84	90^o	Floor	56 kPa	135±2.5 K
Case 7	CH_4-C_2H_4	0.5-2.2 (g/s)	2.84	90^o	Floor	56 kPa	293±10 K
Case 8	CH_4-C_2H_4	0.5-2.2 (g/s)	3.84	22.5^o	Aft	56 kPa	293±10 K

4.1 Wind Tunnel Validation

The estimation of the cross-flow Mach number is made by two different techniques, which require an estimate of the specific heat ratio. The heating capability of the facility allows static temperature to reach about the standard temperature (298.15 K) such that γ is 1.4 with maximum preheat.

4.1.1 Pressure

As in Pitot probe measurements, the Mach number can be retrieved from the static and the stagnation pressure, assuming the value of γ. The stagnation pressure is

measured at the entrance of the nozzle, instead of in the supersonic mainstream where normal shock calculations are required.

The static pressure is measured at Port P_1 and this method assumes no stagnation pressure loss between both pressure measurement point. The Mach number is determined from Eq. (6) and reported in Fig. 43 for a typical validation test run. As discussed in Section 2.3.6, the nozzle is designed for a certain temperature (or viscosity), consequently the cross-flow Mach number is expected to change with the cross-flow conditions. Therefore the heater is switched on or off during the test to capture the Mach number dependency on the incoming flow temperature. Figure 43 shows the estimated Mach number as a function of the stagnation pressure during a typical test run. The decreasing trend is probably due to the temperature-air flow rate relationship from the heater (Fig. 15). Overall, the values of the Mach number are relatively closed to the design target value, and this method shows that $M_{cf} = 2.48 \pm 0.04$, including the deviation on all the validation data.

4.1.2 Flow Visualization

A time average Schlieren visualization was used to measure the shock angle around a wedge block, as shown in Fig. 44. A 38.1mm wide - 10^o wedge is placed at nozzle exit, and rests on two rods inserted through P_1-P_{cav} and T_1-T_{cav} ports (Fig. 44(a)). Since the wedge is an obstructing obstacle, a higher wedge angle may prevent aerodynamic start of the wind tunnel. The 10^o deflection angle is chosen to cause a readable shock feature, given the design Mach number. Figure 44(b) shows a time average video data from a Schlieren movie, while running a preheated flow ($T_{cf} = 293 \pm 10$ K). Both heated and non-heated flow have shown a relatively subtle difference in the shock angle. The cross-flow Mach number is found by solving Eq. (43) assuming the ratio of specific heats.

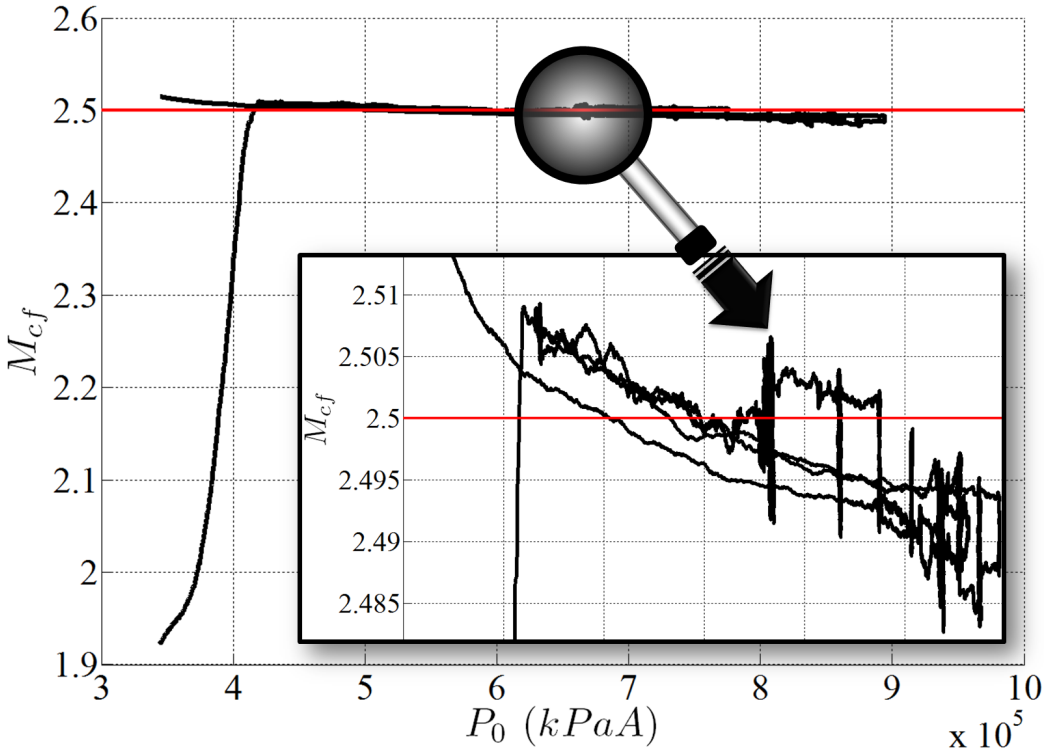

Figure 43: Mach number as a function of the stagnation pressure measured at the nozzle entrance. The decreasing trend corresponds to the progressive heating of the flow during the run (T_o = 300 to 761 K).

$$\cot(\theta) - \tan(\alpha)\left(\frac{(\gamma+1)M^2}{2(M^2\sin^2\alpha - 1)} - 1\right) = 0 \tag{43}$$

where θ and α are the deflection and the shock angle, respectively. The error on α is $\pm$ 1^o due to the image resolution and the noise. From the Schlieren video data collected during the calibration campaign, the cross-flow Mach number was found to be 2.49 $\pm$ 0.09.

4.2 Kinetics Study

Well-stirred model calculations are primarily done in order to obtain the intrinsic properties of the air-fuel mixtures being used in this study, such as heat release and ignition delay times : There is no attempt to capture or imitate the cavity internal

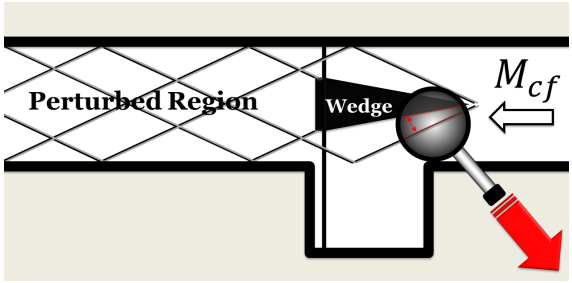

(a) Setup of the wedge block in the supersonic vessel. The block is supported by two steel rods inserted through the pressure and temperature ports, and lies in the unperturbed region past the isolator.

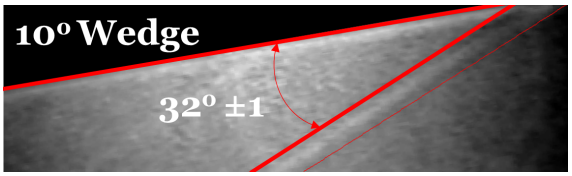

(b) Time average Schlieren image of the shock generated at the bottom of the wedge (T_{cf} = 293±10 K). The shock angle σ is determined using a Matlab program which identifies the shock contour from the grayscale data.

Figure 44: Wedge flow measurements for cross flow Mach number validation.

features, such as the mixing layer and the recirculations. A well-stirred reactor model is used with adiabatic walls and at constant pressures of 0.5 and 1 atm, corresponding to the range of static pressure encountered in the combustor. The chemical reaction is simulated using Cantera with the GRI mechanism (using 345 reactions and involving 53 species), and the range of the fuel mixture compositions is chosen to cover the fuel-air stoichiometry encountered in this study. All the observations made in this section pertain to the range of conditions and fuel compositions investigated only.

The ignition delay is obtained from the progress variable :

$$\eta(t) = \frac{\int_0^t \dot{\omega} dt}{\int_0^\infty \dot{\omega} dt} \tag{44}$$

Equation 44 indicates the advancement of the reaction from 0 to 1. The ignition delay is the time t which yields a prescribed value of η. The latter is chosen such that the overall reaction is exothermic and irreversible (passed the activation stage). Figure 45 shows an example of ignition delay estimation based on kinetic data. The ratio between the shaded area and the area under the reaction rate curve is equal to 0.7.

Similarly, the heat release is based on the well-stirred calculations and is deduced

from the difference between the initial and the final enthalpy, i.e. as the combustor reaches equilibrium.

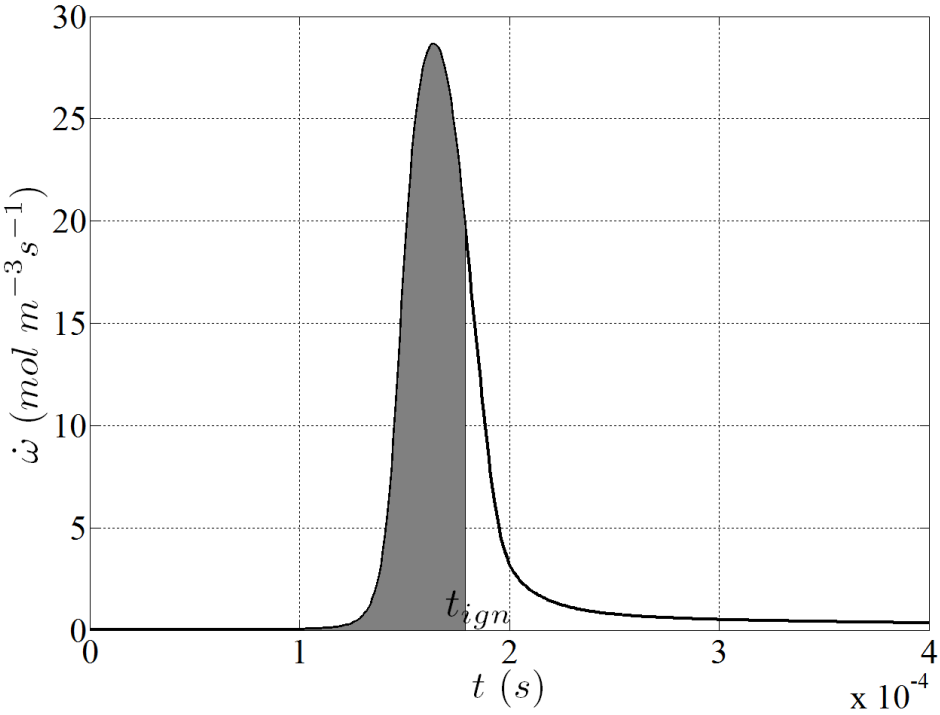

Figure 45: Ignition delay calculation (Eq. (44) with η=0.7). The kinetic data is obtained from Cantera simulations (using the GRI-Mech 3.0) of a constant pressure batch reactor (P = 50.7 kPa) with the following initial conditions : Y_{CH_4} = 0.03, $Y_{C_2H_4}$ = 0.12, T(0) = 1400 K. The overall reaction rate is the norm of the reaction rate vector : $\dot{\omega} = \sqrt{\sum_i \dot{\omega_i}^2}$.

The results are reported in fuel maps in Fig. 46, 47 and in Appendix C. The heat release is shown in Fig. 46 with an initial temperature of 1400 ^{o}K. The maps are presented for fuel blends made from methane-hydrogen (Figs. 46(a) and 46(b)) and methane-ethylene (Figs. 46(c) and 46(d)). The heat release is relatively independent from the pressure, since the trends are similar for both simulated pressures (within 15 J/g). The stoichiometric region is indicated by the thick line in Fig. 46, and separates the map into a fuel-lean (below) and fuel-rich (above) regions.

In the fuel-lean region, methane is more sensitive to hydrogen addition than with

ethylene, as less hydrogen is needed to reach equal value of heat release. The high sensitivity of methane chemistry to hydrogen is a key characteristic, which is also discussed in the following section on the experimental results. Regardless, both fuel blends behave differently in the fuel-rich region. The heat released from the combustion of methane-hydrogen becomes relatively independent of fuel composition as opposed to methane-ethylene fuels, as indicated by the decreasing lines of constant heat release on Figs. 46(c) and 46(d).

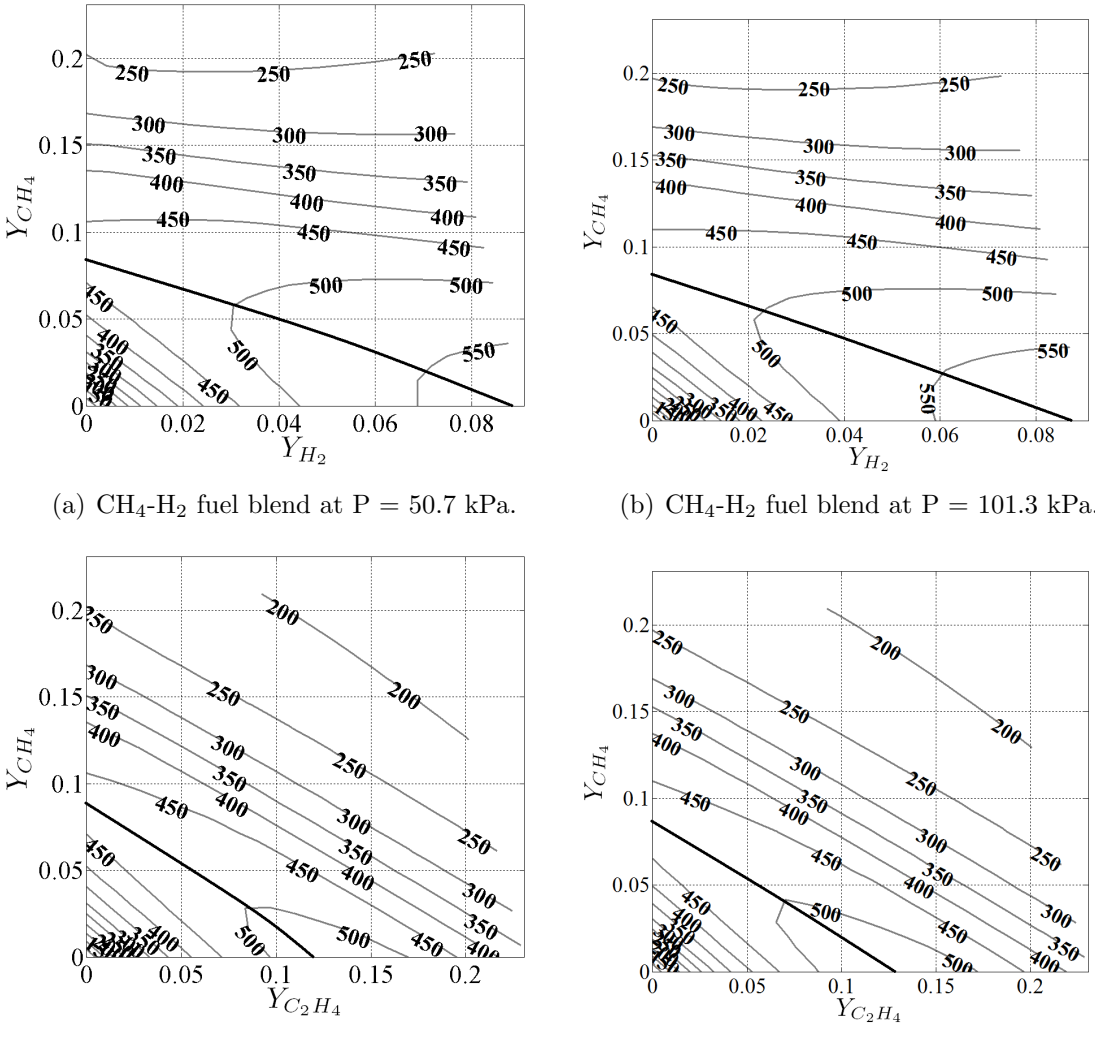

(a) CH_4-H_2 fuel blend at P = 50.7 kPa.

(b) CH_4-H_2 fuel blend at P = 101.3 kPa.

(c) CH_4-C_2H_4 fuel blend at P = 50.7 kPa.

(d) CH_4-C_2H_4 fuel blend at P = 101.3 kPa.

Figure 46: Heat release maps in J/g, with an initial mixture temperature of 1400 ^oK.

In this study, ignition delay is the time at which 70% of the reaction is completed (Eq. (44) with $\eta(t_{ign}) = 0.7$). Figure 47 shows the ignition delay for both fuel blends investigated in this study with an initial temperature of 1400 ^{o}K. The tested fuel mixtures lead to a broad chemical time range (from 3.10^{-5} to 10^{-2} s), and a small addition of ethylene or hydrogen to methane results in drastic reduction of the mixture ignition delay. However, the largest change is seen for hydrogen addition, and mostly occurs in the 0 - 0.02 range of mass fraction, as seen in Figs. 47(a) and 47(b). Within the simulated range, the sensitivity of the fuel maps on the pressure shown a reduction of about 60 % in the ignition delay when increasing the pressure from 0.5 to 1 atm; however, the trends of the maps remains the same. In contrast, methane-ethylene fuel has a more gradual trend, as seen on Figs. 47(c) and 47(d) by the progressive decrease of the ignition delay under ethylene addition. Similarly to the heat release maps, the ignition delay data shows that methane has an acute sensitivity to hydrogen addition, as both fuels have relatively different heat contents. The difference in the kinetic behaviors obtained with hydrogen and ethylene addition to methane makes it interesting for experimental combustion studies.

The values of the ignition delay are relatively sensitive to the temperature of the initial mixture, as seen in both simulations and experiments using multifuel mixtures [20, 96]. In the present study, there is no precise knowledge of the temperature distribution inside the cavity for each experimental case. Regardless, the results from numerical simulations by Choi et al. [21] indicate that the average cavity temperature is about 1000 ^{o}K and the temperature in the product region is of the order of 1400 ^{o}K, as seen in Fig. 48.

Because the temperature profile is spatially dependent, there is no single estimate for the temperature used in ignition delay calculations. Instead, the ignition delay maps are obtained for a broad range of initial mixture temperature. The latter is set to 1000 K, 1400 K or 2000 K (where 1400 K is retained as a nominal value) to reach

auto-ignition with no radicals present in the initial mixture. Then, the simulations are run until chemical equilibrium is reached (or dT/dt is 0.5 %).

Additional results are given in Appendix C for initial temperatures of 1000 K and 2000 K, and the trends discussed in the above paragraph are similar for all temperatures investigated, however, the magnitudes are different. Ignition delay at 1000 K and 2000 K is 3 to 4 orders of magnitude apart, with the values presented in Fig. 47 being in the middle range. Consequently, the data obtained in this kinetic study gives only a qualitative description of the fuel-air properties employed in this study.

4.3 Stable Combustion

During self-sustained combustion, the values of the quantities measured in the combustor remain relatively constant over time, under constant inputs. This notion is used to define a stable regime. Some of the data collected during the slow adjustment of the fuel supply (Fig. 40(a)) is used to investigate stable cavity burning. The results reported in this section also contribute to **Tasks 3 (a)**, **(b)** and **(c)**. Initially, pure air-methane combustion was not stable within the tested conditions and without a spark. The presence of a fuel additive, such as hydrogen or ethylene, was shown to improve the kinetic properties of the fuel, and allows stable combustion to be established with methane as a primary fuel. The following discussion focuses on key input parameters involved in the combustor stability, such as the cross-flow conditions, fueling rate and composition.

4.3.1 Effect of the Cross-Flow

Figure 49 shows the typical values of ceiling pressure measured during an ignition-blowout sequence. The first pressure port remains relatively unaffected by the combustion, however a pressure surge is measured at $P_{2\text{-}4}$ during ignition due to the additional hydrogen supply used for this purpose. Port 8 measures a drop of the

static pressure which may be the result of a shock moving downstream. The igniter and the additional hydrogen supply are then immediately shut off as labeled on the figure. The combustion is then maintained for another 3.3 minutes and the fuel mixture is slowly adjusted. The cavity pressure decreases as the fuel supply is progressively turned down until reaching the minimum burning pressure (pressure at blowout).

Figures 50, 51 and 52 show the pressure and the temperature data measured during stable combustion for both methane-hydrogen and methane-ethylene fuel mixtures. However, the sudden change of mixture composition near ignition does not allow the data collected from this phase to be compared with sufficient accuracy. Therefore, the stable combustion data analysis is carried out near blowout.

The cavity pressure is shown as a function of the stagnation pressure for Cases 1 and 2 in Fig. 50(a). The linear trend in the data follows the cross-flow pressure (typical P/P_o linear trends from Eq. (6)), despite the dispersion, which is due to the change in combustion regime. A similar behavior is observed for the combustion of methane-ethylene fuel mixtures in Case 3. The pressure difference between the cross-flow and the cavity is not only due to the combustion activity. Initially, the pressure in the non-reacting cavity is higher than the cross-flow static pressure due to the presence of an oblique shock (which emanates from the leading edge as seen in Fig. 50(b)). In addition, there is also a jump of pressure across the shear layer, such that the pressure difference between P_1 and P_{cav} is usually between 5 and 9 kPa without combustion.

Figure 51(a) shows the cavity temperature as a function of the stagnation pressure, for the same test cases. The cavity temperature tends to increase with the stagnation pressure, which may give evidence of a more efficient burn. The floor temperature may also be a function of the overall temperature due to the heat release, such that the hotter wall may imply more complete combustion. On the other hand, the change in

the internal flow features (caused by a change in the fueling or the cross-flow regime) may change the heat transferred to the thermocouple as well. To address this point, the reacting data was further analyzed and revealed that the cavity floor temperature decreases when approaching blowout for both high and low fueling rates, as shown in Fig. 51(a), such that this type of behavior may be more likely a heat release effect. The contribution from both the structure (reduced heat transfer) and the reaction (increased heat release) supports the observed trend.

Figure 51(b) shows the cavity temperature difference between the reacting and the non-reacting flow. While the cavity temperature for the reacting case may be related to the flame temperature, the temperature measured in the cavity for the non-reacting case is close to the cross-flow stagnation temperature (300-600 K). Furthermore, the cases without preheat exhibit the highest temperature difference, since combustion is established from cooler air.

4.3.2 Effect of the Fuel Mixture

The combustion of methane-hydrogen and methane-ethylene fuel behaves similarly near blowout; however, the actual values of pressure and temperature measured in the cavity differ. For illustrative purposes, the data collected for both fuels is compared under similar conditions. Figure 52 shows key differences between the combustion of both fuel mixtures for a stagnation pressure ranging from 848 to 937 kPa. The segmentation of the data is due to the selection algorithm, which ensures that the conditions between the compared cases match correctly.

The cavity pressure is presented as a function of the total fuel mass flow rate in Fig. 52(a) for Cases 2 and 3. The fuel composition may vary and this explains the dispersion of the data. The stable combustion data shows that the combustion of methane-hydrogen mixtures sustains at pressure 10 to 20 kPa lower than for methane-ethylene. In addition, not only does the methane-ethylene data involve the highest

cavity temperatures (ranging up to 1100 K), but it also has the greatest temperature difference between reacting and non-reacting flow as seen in Fig. 52(b). Generally, the combustion of methane-ethylene gives a wider range of response in terms of pressure and temperature. Nonetheless, methane-hydrogen combustion was studied with small amounts of hydrogen. Instead, higher amount of hydrogen may produce a more drastic impact on the combustor response, as observed during the ignition phase, with additional hydrogen supply from the igniter (Fig. 49).

4.4 Blowout Results

Blowout is triggered by changing the fuel supply (composition and fueling rate) while other controllable parameters are held constant, as seen on Fig. 40(a). It is reached when approaching the non-reacting region from self-sustained combustion, as described in Section 3.2. When approaching blowout, the system becomes sensitive to fluctuations. In this study, unstable combustion is defined as the onset of combustion which systematically results in blowout under constant inputs, after the igniter is turned shut off. The mixture composition and cross-flow conditions that give unstable combustion define the blowout region, as it does not provide self-sustained combustion.

According to the concept of mixture space introduced in Section 3.4, the blowout data points are located on a map with respect to the fuel mixture in Fig. 53 for Case 1. To obtain such maps, each ignition-blowout sequence is repeated between 2 and 3 times with the same target in order to capture the data dispersion, and any potential hysteresis. As expected in multi-fuel studies [20, 96], the blowout mixture composition is not unique, and the data points forms a contour in the mixture space that separates the stable combustion region from the non-reacting region (close to the $\dot{m}_{CH_4}$ axis in Fig. 53(b)). The main approach focuses on the tracking of this contour with respect to various parameters of influence. The results reported in this section

also contribute to the completion of **Tasks 4 (a)**, **(b)** and **(c)**.

4.4.1 Data Dispersion

The blowout limit is not a line but rather a region where the probability of blowout becomes substantial, as seen by the scatter of data points in Fig. 53. Analyzing the entire data collected during the experimental campaign shows that no distinct pockets of points have been observed, which would bring evidence of multi-stability (as in bi-stable, for instance). Instead, the data points appear in one region near the $\dot{m}_{CH_4}$-axis, as seen in Fig. 53(b). The ignition-blowout sequence described in Section 3.2 implies that ignition is performed in the same manner, i.e., with a high amount of hydrogen or ethylene, whereas blowout is obtained by a slow decrease of the fuel additive (hydrogen or ethylene). As a result, blowout has not been studied thoroughly with respect to different type of mixture trajectories, to test if the combustor has 'memory'.

The dispersion of the blowout data is a key parameter in the tracking of hysteresis and repeatability of the blowout events, and may be the result of several causes :

- Some of the underlying parameters involved in the flame-holding mechanism are not quantified in this study. The data displayed in Figs. 53 does not provide a full representation of the system state and several parameters may change with the fuel supply.

  One important reason for the dispersion of blowout data may come from the unsteadiness of the observed phenomenon. Even if the combustion process is stable, velocity fields and species concentrations fluctuate in time due to tough levels of turbulence. Near blowout, the combustion process is weakened and the flame-holding mechanism may become sensitive to these fluctuations which may prevent blowout from being repeatable.

- Moreover, the fuel system has limited ability to reach identical targets when

repeating the blowout measurement. During the slow tuning phase described in Fig. 40(a), blowout is reached by decreasing the composition of the fuel additive (hydrogen or ethylene). If this was the case, then the trajectory shown would be strictly parallel to the $\dot{m}_{H_2}$-axis. However, both fuel flow rates are changed as seen in Fig. 40(a), since all fuel channels are coupled as they merge into the same outlet. Consequently, lowering the fuel flow rate in one channel changes the downstream pressure, and affects the response of the other flow controllers. For the same reason, the cavity pressure also affects the flow controller response, since the fuel composition is tied to the combustion intensity. The coupling between flow controllers and the combustor induces some relatively small discrepancies between targets and readings (0.1% of $\dot{m}_f$). It may also be responsible of the coherent drift seen in Fig. 40(a), and prevents blowout points to be reached the same way, despite the effort made in having a consistent ignition-blowout sequence.

However, the deviation of the data from the mean trend in Fig. 53(b) is small compared to the overall fuel flow rate, such that the data dispersion is in fact relatively subtle. This was captured with a 100 SLPM mass flow controller installed on the hydrogen channel to give enough accuracy.

4.4.2 Effect of the Cross-Flow

The cross-flow conditions are determined by the stagnation pressure and preheat temperature, such that it is possible to change its kinetic and internal energy during the experiments. Both affect the cavity response in various ways, as discussed below. However, combustion parameters such as the turbulent scale and intensity are not measured, and therefore the observations are drawn from limited insight provided by the pressure and temperature data. In this section, the data collected for methane-hydrogen fuel mixtures (Cases 1 and 2) is used to illustrate the dependence of cavity

burning on the cross-flow parameters. These observations are equally valid for the methane-ethylene studies.

4.4.2.1 Pressure

The blowout data when represented as a function of the cavity pressure in Fig. 53, suggests that blowouts occurs at low pressure have the highest dispersion. When approaching blowout, the combustion process weakens and the pressure measured in the burning cavity tends to the non-reacting pressure, as discussed in Section 4.3.

Figure 54 shows the cavity pressure as a function of the stagnation pressure, for a typical run. The curve in black is the pressure in the cavity without combustion (non-reacting pressure); it is imposed by the pressure of the cross-flow and follows the stagnation pressure, although both values do not coincide, as mentioned in Section 4.3.1 due to the presence of the shear layer shown in Fig. 50(b). The data points in grey are the cavity pressure measured under reacting conditions. The cavity pressure increases substantially as the combustion process intensifies. Toward blowout, limited reaction may occur when operating at high excess of air or fuel and the cavity pressure becomes fairly proportional to the stagnation pressure, as seen previously in Fig. 51. The black dots are the pressure at blowout which lies close to the non-reacting pressure. Typically, the blowout pressure is only between 2 and 4 kPa above the pressure without combustion. This suggests that as the combustor shifts toward the blowout limit, the pressure in the cavity tends to the pressure imposed by the cross-flow. Hence, the supersonic main stream determines the pressure in the cavity near blowout, such that the cavity pressure becomes mostly a dependent variable, in this particular regime.

At Mach 2.5, the static to stagnation pressure ratio (P/P_o) falls around 0.05 such that the pressure in the cavity is relatively low (20-90 kPa in the tested range), and makes the combustion process potentially unstable. Given, the trend seen in Fig. 54,

the pressure at blowout can be roughly estimated from the post shock conditions by neglecting the jump of pressure through the shear layer.

Figure 56(a) is a representation of the blowout data points as a function of the cavity static pressure and the hydrogen fuel mass fraction ($Y_{H_2} = \dot{m}_{H_2}/(\dot{m}_{H_2} + \dot{m}_{CH_4})$) with a cross-flow static temperature for Case 1, and reveals that at lower static pressure, some blowout events occur at higher hydrogen mass flow rates. Since the hydrogen chemistry is more reactive than methane, more hydrogen may be needed to stabilize the flame when cavity pressure reaches the lower values. This is an example of unfavorable inputs being counteracted by a favorable change in the fueling composition, which is made possible on this facility. The increase of hydrogen concentrations seen below 50 kPa may show that the lack of pressure can be compensated by a higher flame speed and mixture diffusivity in the sense of non-premixed time scale of Driscoll et al. [27].

Consequently the blowout region grows when reaching lower cross-flow pressures: as the cross-flow static pressure is lowered, the combustion is barely maintained without blowout. In this case, the dispersion of the data increases as the blowout events become less repeatable and this is observed for both methane-hydrogen and methane-ethylene fuels (shown subsequently). In addition, no combustion is observed for methane-hydrogen mixtures below 40 kPa in the cavity within the tested conditions. Thus, there is a lower bound on the combustor pressure beyond which no combustion is sustainable.

The pressure may affect the combustion process via many pathways, some of which are relatively difficult to measure in an experiment:

- The pressure may affect the fuel-air stoichiometry of the mixture in the cavity since the density of the entrained air is a function of the cross-flow pressure [92, 26]. However, the cavity equivalence ratio is not determined with accuracy.

- As shown in Fig. 54, the mass of the mixture in the cavity may also increase with the cross-flow pressure. As a result, the range of flow rate at which combustion is stabilized may scale up with the cross-flow pressure, since more mass is involved.

- From a kinetic perspective, the pressure also affects the overall collision rate such that higher cross-flow pressures are expected to provide a more efficient burn.

None of the effects listed above disagree with the observed trends.

4.4.2.2 Temperature

The effect of the supersonic cross-flow temperature on methane-hydrogen combustion is examined in Fig. 53 (Case 1) and Fig. 55 (Case 2). The effect of increasing the cross-flow temperature by 113 K increases the size of the stable domain. The blowout maps exhibit the same trends and the blowout limit is shifted to lower hydrogen flow rate (as low as 0.5 % of hydrogen). Higher cross-flow temperature also results in less data dispersion indicating that blowout events become more repeatable.

The increase in the stable domain may be due to better flame anchoring provided by the higher unburnt gas temperature in the lift-off region, as described by Rasmussen et al. [84]. Stable combustion shows that the temperature difference between non-reacting and reacting flow is reduced (Fig. 51(b)) such that there may be less energy spent in bringing the fuel-air mixture to its flammability limit. Although not fully addressed, the wall heat losses may be reduced as the cavity wall temperature increases with preheating, and provide a more stable combustion. In this case, it may be a structural influence.

So far, the dispersion of the blowout data was mainly associated with low cross-flow pressures (below 50 kPa). However, preheating also affects data dispersion when comparing Fig. 53 to Fig. 55. To see this more clearly, the blowout wall temperature is shown as a function of the hydrogen fuel mass fraction for Cases 1 and 2 in Fig.

56(b). Larger scatter and more mass fraction of hydrogen is seen for cavity wall temperatures below 600^oK, which also turn out to be the lowest cavity pressure in Fig. 54 for Case 1. In addition, blowouts at lower pressure are also colder. Therefore, there is a weak relationship between cavity pressure and temperature at blowout.

4.4.3 Effect of the Fuel Mixture

The progressive change in cavity fueling implies that the fuel mixture composition and fuel flow rate are not held constant when approaching blowout. Several parameters may change when evolving along a mixture trajectory, such as the one shown in Fig. 40(a):

- Changing the fuel composition has some effects on the combustion process, as discussed in Section 4.2, by the high sensitivity of ignition delay and heat release. Although the results found from the kinetics study are not directly applicable to the present case, it suggests that the addition of hydrogen or ethylene to methane fuel strongly affects the flame-holding mechanism at a kinetic level. Thus, the reduction of fuel additive fraction as seen in Fig. 47(a) may decrease the local reaction rate and change the fuel mixture diffusivity (or the local flame speed).

- The fuel jet penetration is another parameter which may change in Figs. 53(b) and 55(b), since the fuel can penetrate into the shear layer under strong fueling, causing different fuel-air mixture distributions. In the case of floor injection, the fuel jet is oriented perpendicular to the mixing layer such that impingement on the latter strengthens with the fueling rate. As a consequence, the air entrainment may change with the fueling rate (and so does the cavity fuel-air stoichiometry). This phenomenon is not accounted in the common air entrainment calculations in cavity flame-holding studies. Therefore the overall fuel flow rate is an important parameter to consider in this analysis. The lines of

constant fuel jet momentum are concentric ellipses centered at the origin of the maps in Figs. 53(b) and 55(b), and suggest that the points located at the top of the blowout region have been obtained with a higher shear layer impingement than the ones at the bottom. Aft injection may not have the same effect, however, from a mass conservation perspective, the fuel matter injected in the cavity must be ejected in the main stream, such that the cavity-cross flow mass exchange is altered by the fuel injection, regardless of the injector location. As a result, the complexity of the mass entrainment mechanism under fueling conditions prevents the actual cavity equivalence ratio at blowout to be known precisely for each point in Figs. 53(b) and 55(b).

- The fuel jet may also alter the internal flow features of the cavity as the fuel flow rate increase. For instance, Rasmussen et al.[80] mentioned about some recirculations created on the side of the fuel jet, and this effect can change the cavity (product) residence time.

4.4.3.1 Methane-Hydrogen Mixtures

It appears that a minimum fuel mass fraction of hydrogen is needed to stabilize air-methane combustion. The blowout maps in Figs. 53 and 55 show that the methane-air flame is stabilized with typically 2 % of hydrogen in the fuel mixture. Therefore, even in small quantities, addition of hydrogen in the fuel blend leads to a significant increase in the stable combustion domain. This characteristic is also seen in the kinetic analysis (Fig. 47(a)), in which a small addition of hydrogen to methane causes a significant reduction of the ignition delay.

At low fuel flow rates (0.2 - 0.4 g/s of methane), the hydrogen is about 6 % and 2 % of the fuel mass flow rate for the non-preheated (Fig. 53) and preheated case (Fig. 55), respectively. The combustor response is also sensitive to the cross-flow static pressure, especially when the latter reaches values below 50 kPa. As discussed

previously in Section 4.3.1. and 4.4.2.1, combustion can be challenging when the fuel concentrations are low, however, the sensitivity of blowout on pressure is milder for the preheated case. Flow visualization carried in this range of fuel flow rates, reveals that the flame is located in the upstream area of the combustor, similarly to the flame shown in Fig. 37(d).

Combustion in the 0.6 - 0.8 g/s range of methane has the best stability among the tested conditions and methane combustion holds with less than 1.15 % of hydrogen. The selectivity of this phenomenon on the fuel mixture composition suggests that in this range, the fuel-air stoichiometry may become favorable for the combustion process to persist at the lowest hydrogen flow rates (0.005 g/s). Nevertheless, it has not been possible to relate this phenomenon to any substantial raise of the floor cavity temperature.

Above 1 g/s of methane, combustion becomes unstable, and the dispersion of the blowout data points is substantially increased. The data dispersion regains sensitivity to the cross-flow pressure similarly to the low fuel flow rate range (0.2 - 0.4 g/s of methane) and hydrogen increases to 3 % of the fuel mass flow rate. Both preheated and non-preheated cases exhibit these trends, so it is clearly not a limited observation. Flow visualization also reveals that the reaction region shifts downstream as the fuel flow rate increases, and a progressive transition occurs around $\dot{m}_f = 0.8$ g/s above which the flame sits near the leading edge, similarly to Fig. 38(a).

4.4.3.2 Methane-Ethylene Mixtures

Blowout with methane-hydrogen mixtures is relatively sensitive to the amount of hydrogen in the fuel. Another study focused on fuels with a more gradual heat content such as methane-ethylene, as seen in Section 4.2. The blowout data obtained from Case 3 is shown in Fig. 57(a) in which, 85 blowout events are reported. The cross-flow is preheated to the same temperature as for Case 2 described previously.

However, Case 3 covers a wider range of stagnation pressures.

The blowout region in Fig. 57(b) exhibits a horseshoe region, which has a slow branch (methane dominant, $\dot{m}_f < 0.6$ g/s) and a fast branch (ethylene dominant, $\dot{m}_f > 0.8$ g/s). The stable domain lies below this contour. Within the tested conditions, it takes more ethylene to stabilize methane combustion than it does when hydrogen is the additive. This may be due to the difference in the chemical times of these different mixtures, as seen on Figs .47(a) and 47(c), as hydrogen becomes immediately effective in small amounts. The mass flow rate of ethylene is between ten and seventeen times greater than the mass of hydrogen injected for the same cross-flow conditions and design. The dispersion of the data is about the same as in Case 2, although it appears reduced on the graph since the range of ethylene flow rate is larger.

Blowout is more gradual with respect to the fuel composition than for the methane-hydrogen counterpart, and this is a key difference between both fuel mixtures used in this study which is already expressed at the kinetic level as discussed in Section 4.2. The slow branch has a linear trend for which 1 part of ethylene is needed to stabilize 4 parts of methane, by mass. Similar to the hydrogen case, blowout at low fuel flow rates with small ethylene addition (less than 0.2 g/s) is found to be fairly independent of the pressure within the tested range. About 0.2 g/s of ethylene is needed to guarantee the flammability of the mixture on the slow branch.

In contrast, blowouts with higher amounts of ethylene, e.g., when ethylene mass flow rate exceeds 0.5 g/s, is more dependent on the cross-flow static pressure. This is seen in Fig. 57(b) by the shift to the right of the fast branch as the cross-flow static pressure increases from 33 to 53 kPa. Figure 57(a) also shows that the blowout trend scales linearly with the cavity pressure.

Therefore, the cross-flow pressure affects the slow and fast branch differently. This behavior is possibly caused by a change of the fuel-air stoichiometry in the combustor as discussed in Section 4.4.2., since the air entrained in the supersonic shear layer is

denser as predicted by the work of Dimotakis [92, 26], and the mass of the mixture stored in the cavity may also increase. In addition, the heat released by the reaction may also increase with the pressure, providing more stability when flame-holding is made critical.

4.4.4 Effect of Cavity Aspect Ratio

Blowout at high fueling rates is also conducted at high static pressures in order to evaluate the effect to preheating and cavity length on the flame-holder stability (Case 4-7). For these cases, the cross-flow static pressure is maintained at 56 kPa and the cross-flow temperature at 135 K and 293 K, and two cavities: $L = 97.5$ mm and 72 mm (L/D = 2.84 and 3.84) are investigated (Fig. 58).

The cavity length is an important parameter in the design of this type of flame-holder. As the cavity length decreases, the blowout region shifts to lower fuel flow rates, as seen in Fig. 58. Since the length of the shear layer is controlled by the cavity length, the mass exchange may be reduced between the cross-flow and shorter cavities, as predicted by Eq. 47. Less air is available for combustion such that shorter cavities may become prematurely saturated with fuel and fuel products [81]. The residence time may also decrease as the flow features (recirculations and shear layer) are smaller in size. In addition from a thermodynamic perspective, the amount of hot matter to ignite and support the flame may be limited by the size of the cavity itself. The current results also suggest that a reduction of 26 % in the cavity length leads to a 60 - 75 % decrease in the maximum fuel flow rates at blowout.

Figure 58 also reveals that shorter cavities are less sensitive to the change in the cross-flow temperature, at least within the tested conditions. There is no obvious explanation for this type of behavior, however, reducing the length of the cavity may limit the influence from the cross-flow, as there may be less exchange of mass and energy between the cavity and the main stream. Some other internal phenomenon

may take over such as wall heat losses.

4.5 Heat Transfer

Heat transfer measurements have been carried out to estimate the wall heat losses in the cavity for energy closure analysis, which is later discussed in Section 5.4.

The wall heat loss data is obtained for Case 5, in which, a blend of methane-ethylene is injected in a rectangular cavity with an instrumented aft block. The wall heat losses are determined using Eq. (40) and the method described in Section 3.6. Figure 59 shows the heat loss data as a function of time with other pertinent parameters such as the cavity floor temperature and the fueling rate.

Ignition is indicated by the sharp increase of the cavity temperature measured at Port T_{cav} (Fig. 25), and is followed by an increase of the cavity heat loss. The heat flux is calculated at each time step by an algorithm which minimizes a data-model residue by roots placement in Eq. (41) (Appendix D). However, only the end-plateau has meaningful values, due to the steady state assumption used in the derivation of Eq. (41).

The fuel flow rate and composition is also reported, and highest aft ramp temperatures are obtained for cavities with higher fueling rate where the flame shifts toward the trailing step, as in Fig. 38(a). The trailing edge is usually in the wake of the flame, and may have the highest wall temperatures as revealed by the glow of the aft structure on Fig. 38. The calculations shows that the magnitude of the normal heat flux $\dot{q}_w$ increases with the temperature. Consequently, the highest wall heat loss may generally occur at the aft step. This assumption is used to estimate a high bound value of the overall heat losses achieved in the cavity:

$$\dot{Q}_{w,aft} = \int_{A,aft} \dot{q}_w \; dA_{aft} \tag{45}$$

$$0 > \dot{Q}_{w,cav} > \min\left\{\dot{q}_{w,aft}\right\} \sum_{i=1}^{4} A_i + \dot{Q}_{w,aft} \tag{46}$$

where A_i is the area of the i-th inner side of the cavity, excluding the aft step. In Eq. (46), the heat flux of the non-instrumented wall of the cavity is assumed to yield the minimum value found on the aft step (Eq. (45)). The heat transfer data has been collected on a limited range of fuel composition and cross-flow regime and is not sufficient to conclude on any specific trends, such as fuel maps. The overall cavity heat loss varies from 1.5 to 2 kW and depends to the amount of ethylene present in the fuel. Pure ethylene combustion gives the highest heat loss and temperatures.

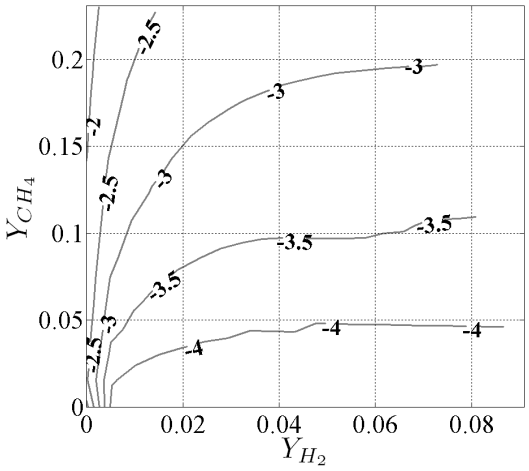

(a) CH_4-H_2 fuel blend at P = 50.7 kPa.

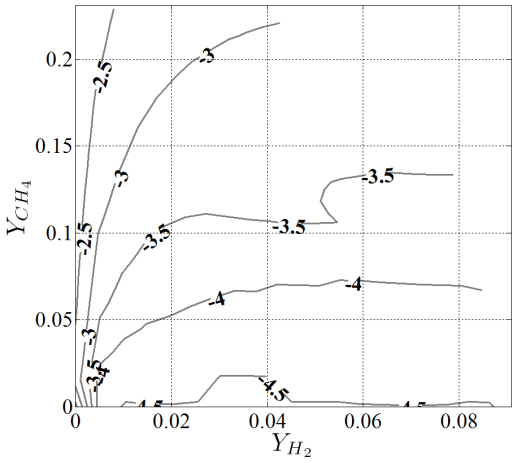

(b) CH_4-H_2 fuel blend at P = 101.3 kPa.

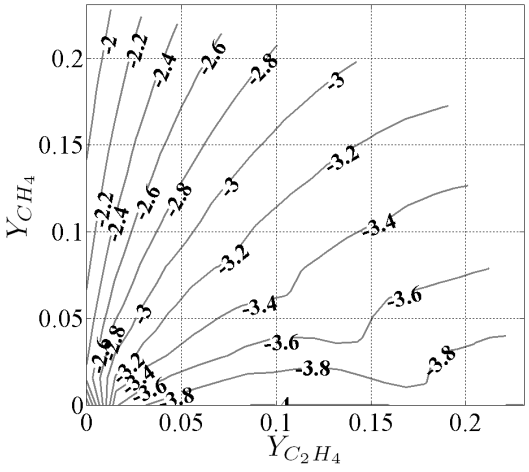

(c) CH_4-C_2H_4 fuel blend at P = 50.7 kPa.

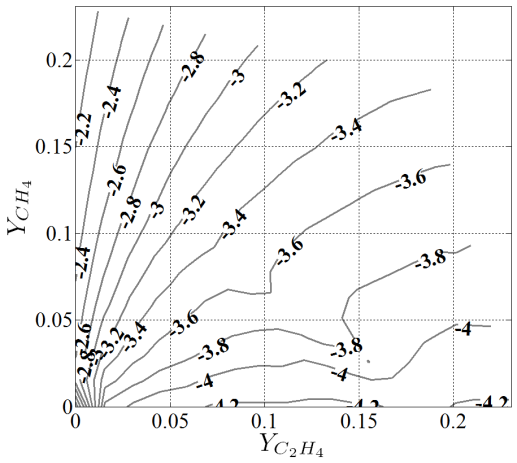

(d) CH_4-C_2H_4 fuel blend at P = 101.3 kPa.

Figure 47: Ignition delays maps ($\log(\tau_{ign})$) in s, for an initial mixture temperature of 1400 ^{o}K.

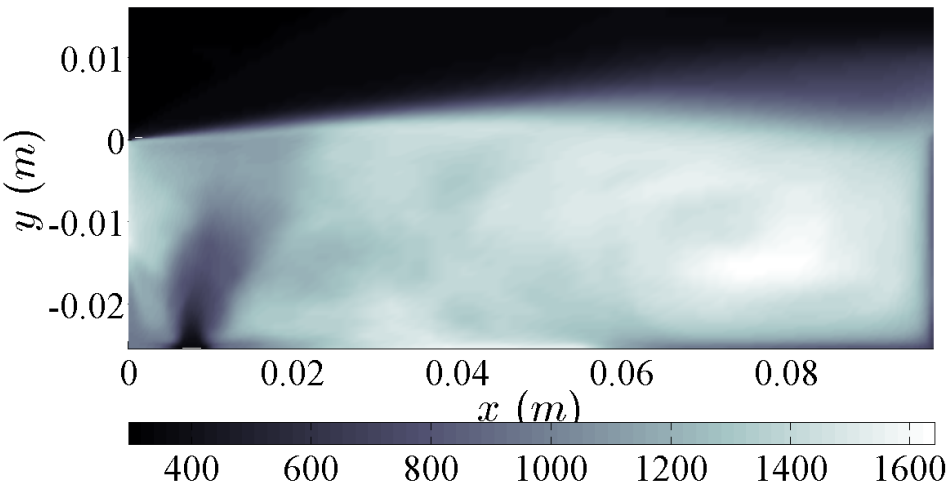

(a) Moderate fuel flow rate: $\dot{m}_{CH_4} = 0.6$ g/s, $\dot{m}_{H_2} = 0.06$ g/s

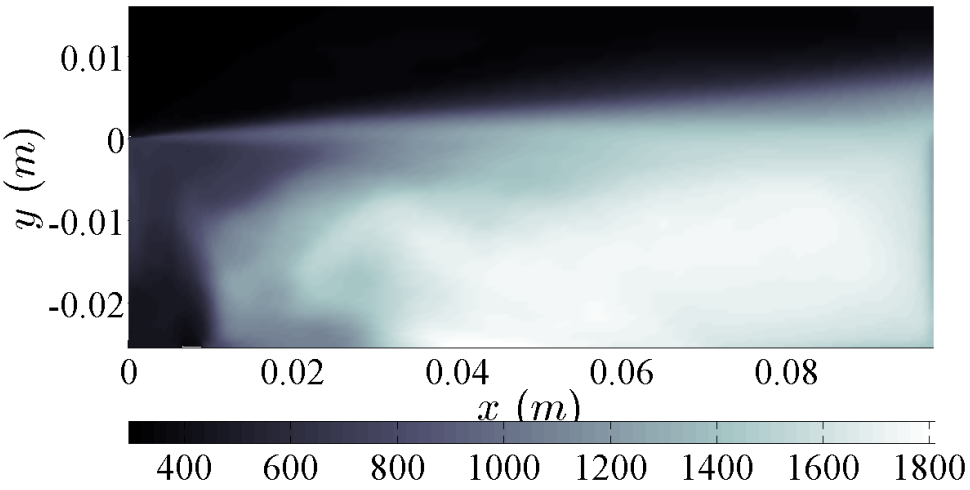

(b) Low fuel flow rate : $\dot{m}_{CH_4} = 0.3$ g/s, $\dot{m}_{H_2} = 0.06$ g/s

Figure 48: Temperature distribution in K ($P_o = 859.7$ kPa) from Choi et al. [21].

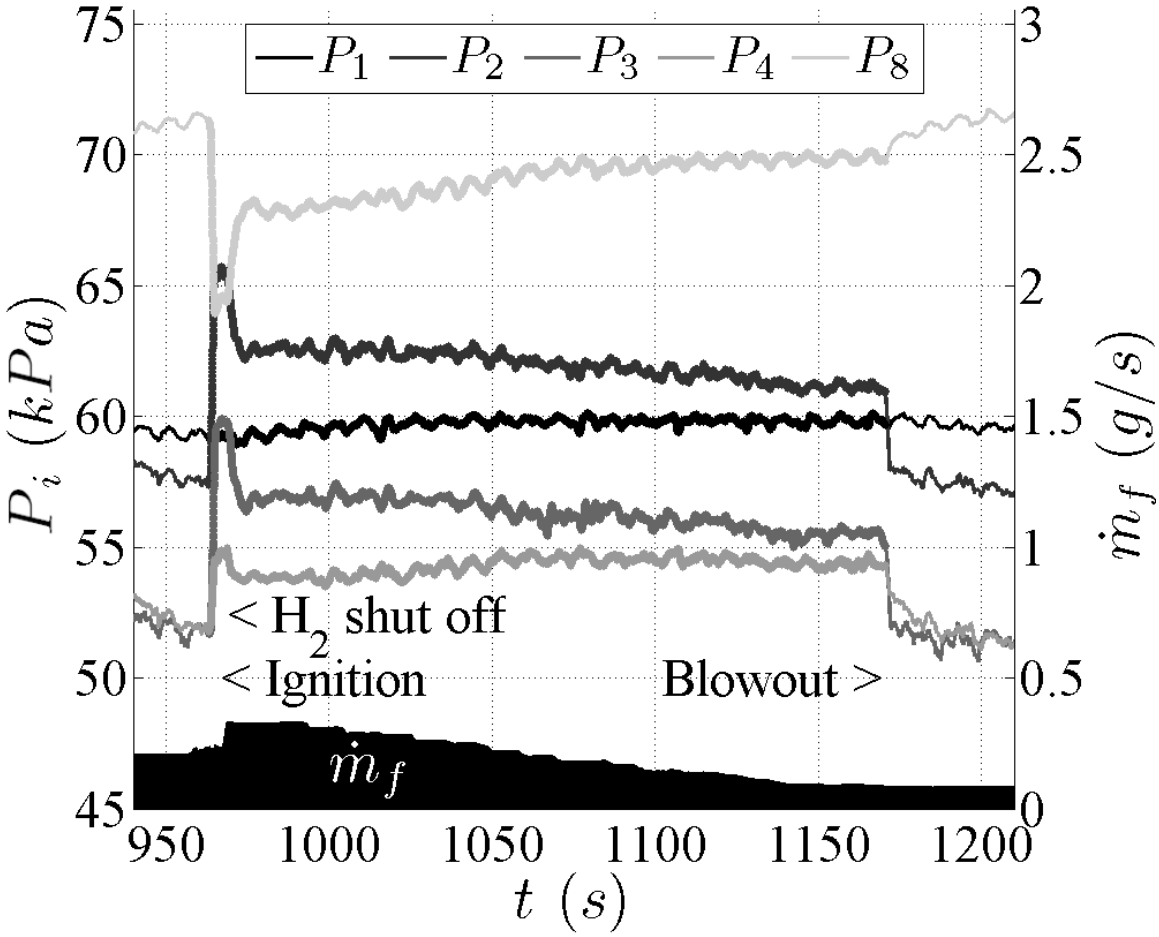

Figure 49: Time history of the ceiling wall pressure during a methane-hydrogen ignition-blowout sequence. The stagnation pressure is 1 MPa, the cross-flow static temperature is 248 K, and L/D = 3.84. The burn data is represented as a thick line.

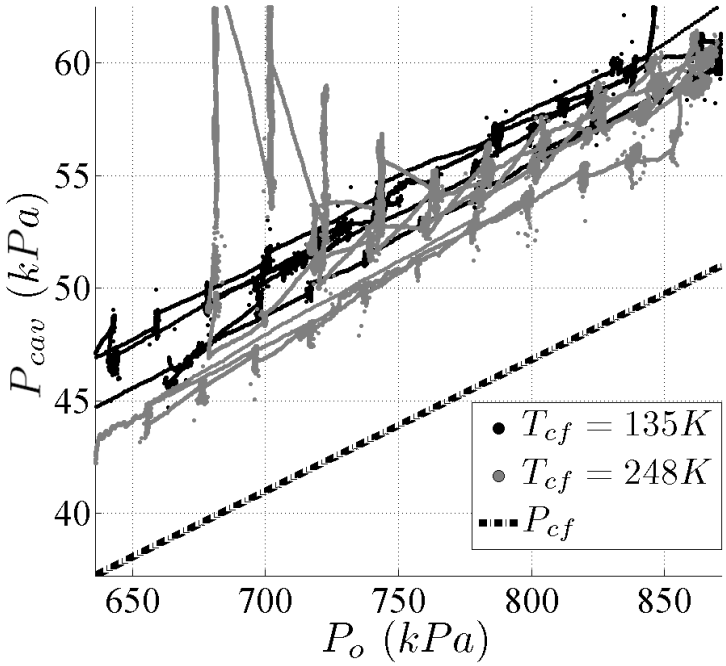

(a) Bottom wall cavity pressure as a function of the stagnation pressure.

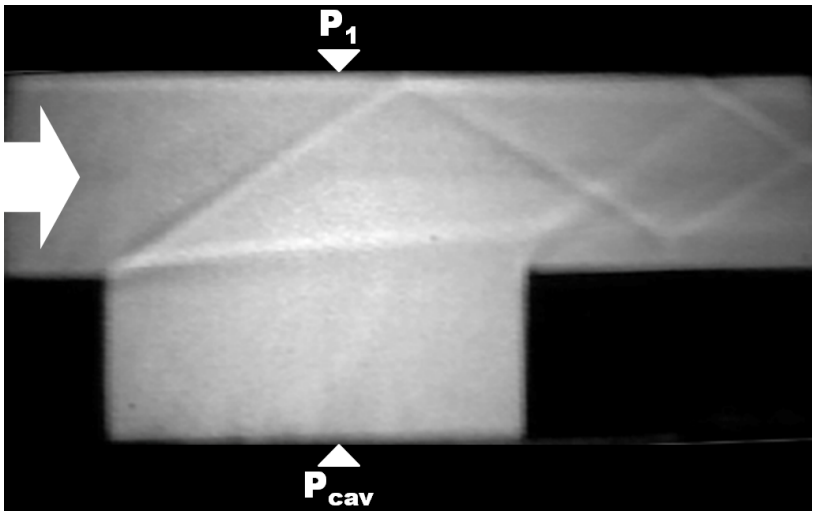

(b) Time average Schlieren visualization of the flow showing in the stream wise direction : the leading edge oblique shock, the mixing layer and the aft edge oblique shock.

Figure 50: Pressure measured during stable combustion of methane-hydrogen mixtures (Case 1 and 2).

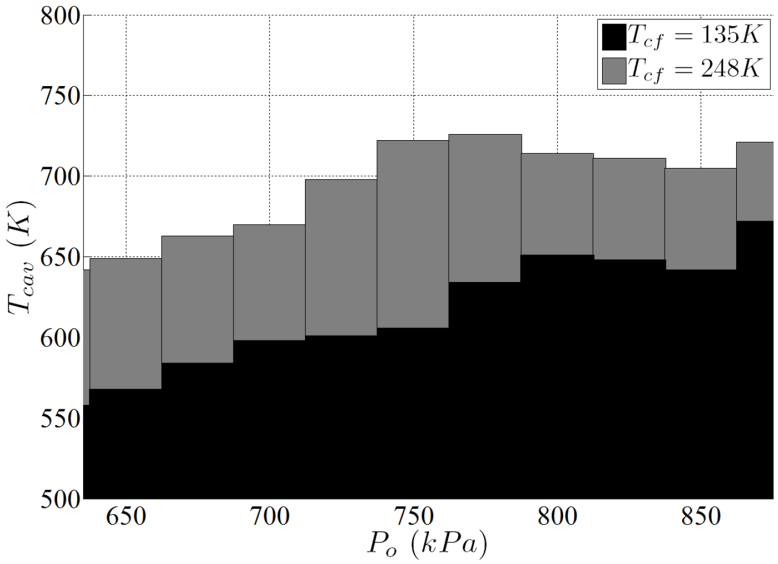

(a) Bottom wall cavity temperature as a function of the stagnation pressure. The reacting temperature is obtained by averaging the temperature data collected during the tuning phase (≈ 10 s).

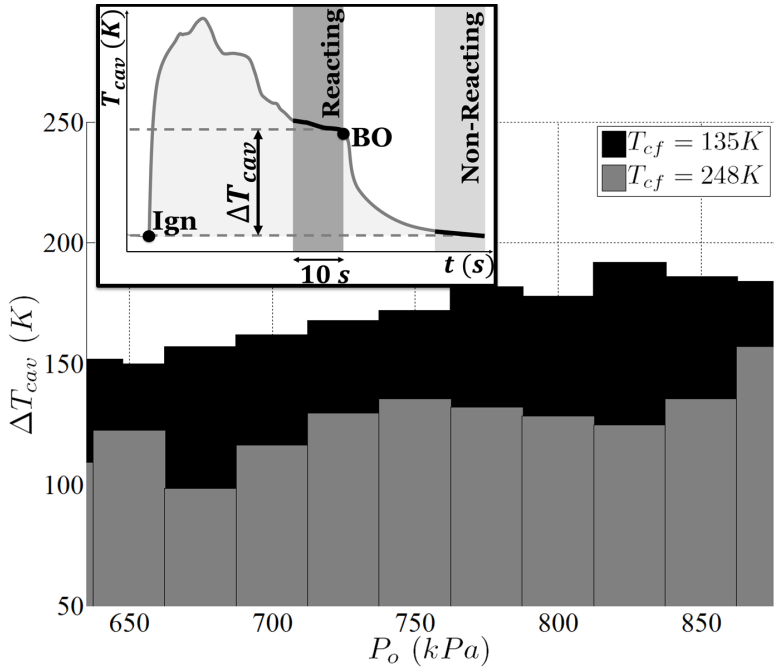

(b) Bottom wall temperature difference between reacting and non-reacting flow. The non-reacting temperature is obtained by averaging the temperature data collected before ignition (≈ 10 s).

Figure 51: Temperature data collected from stable combustion of methane-hydrogen mixtures for Case 1 and 2.

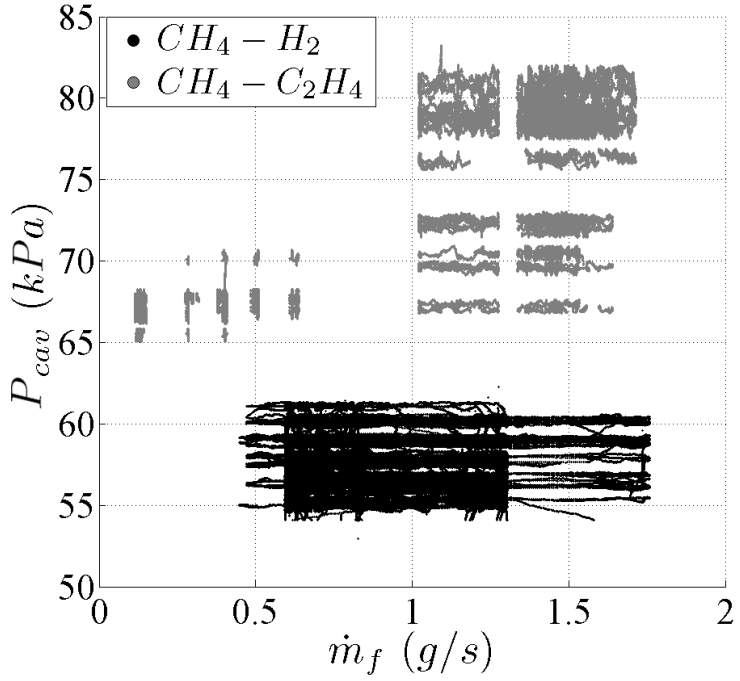

(a) Cavity bottom wall pressure as a function of the fuel mass flowrate.

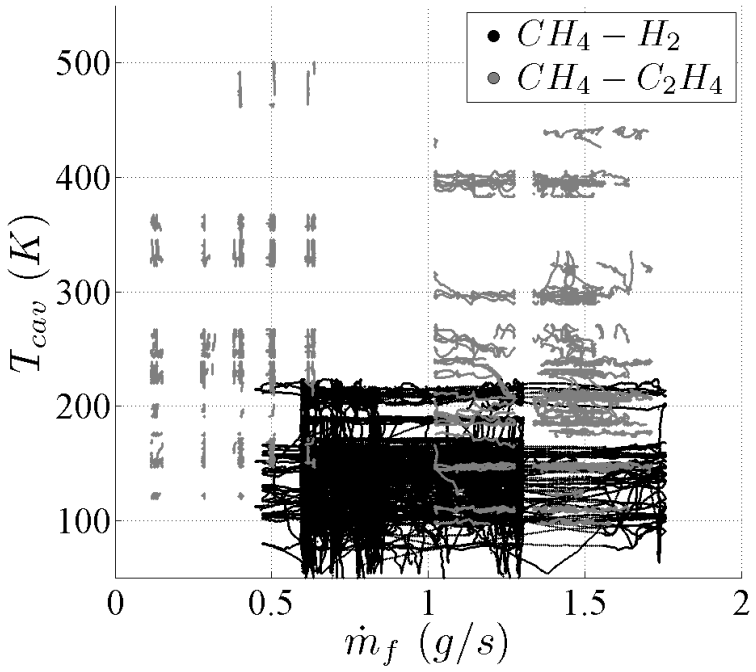

(b) Cavity bottom wall temperature difference between reacting and non-reacting flow as a function of the fuel mass flowrate.

Figure 52: Comparison of stable combustion between methane-hydrogen (Case 2) and methane-ethylene (Case 3) fuels. The data is picked for a stagnation pressure of 893 kPa ± 5%.

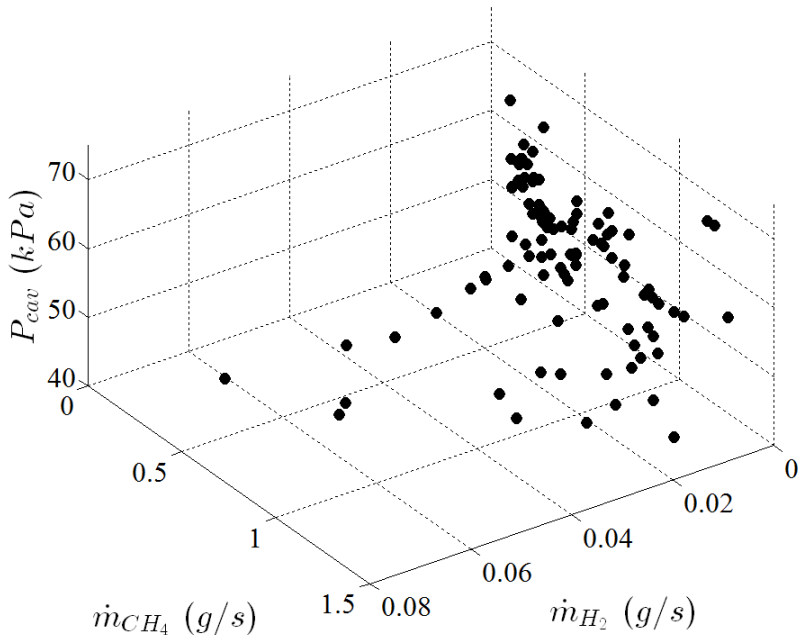

(a) Fuel mixture composition at blowout as a function of the stagnation pressure.

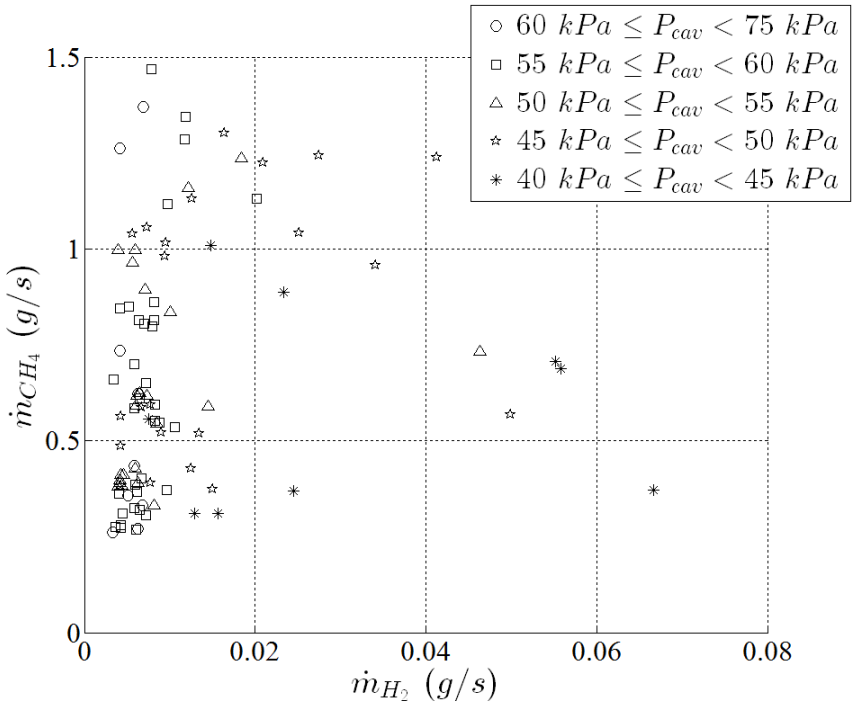

(b) Fuel mixture composition at blowout: the stable domain is located on the right side of the cloud of points.

Figure 53: Blowout of a CH_4-H_2 fuel mixture with a cross-flow static temperature of 135 K (Case 1).

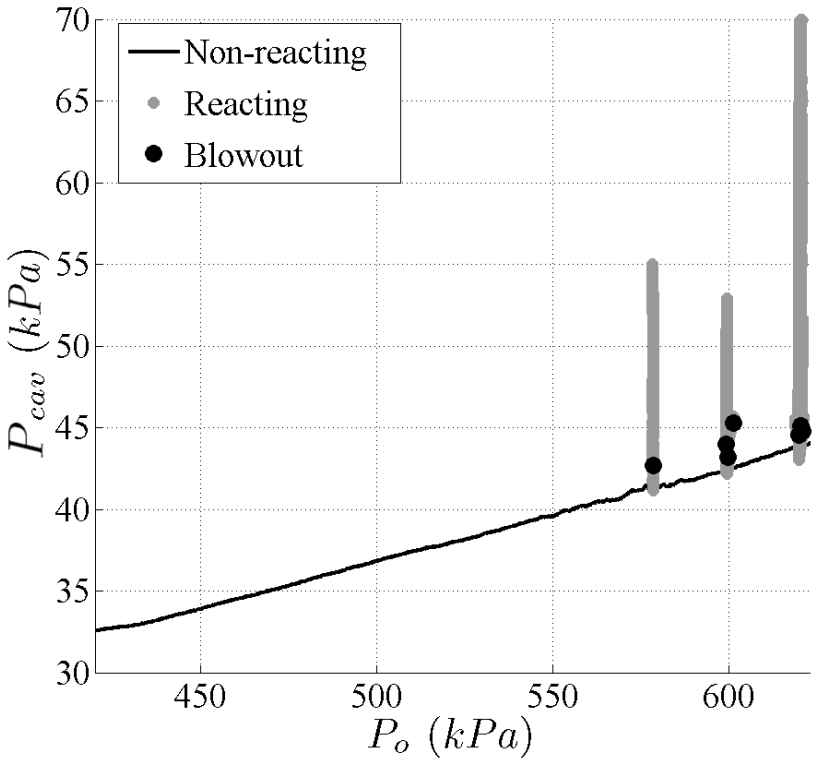

Figure 54: Blowout points as a function of cavity bottom wall pressure and settling tank stagnation pressure for Case 1.

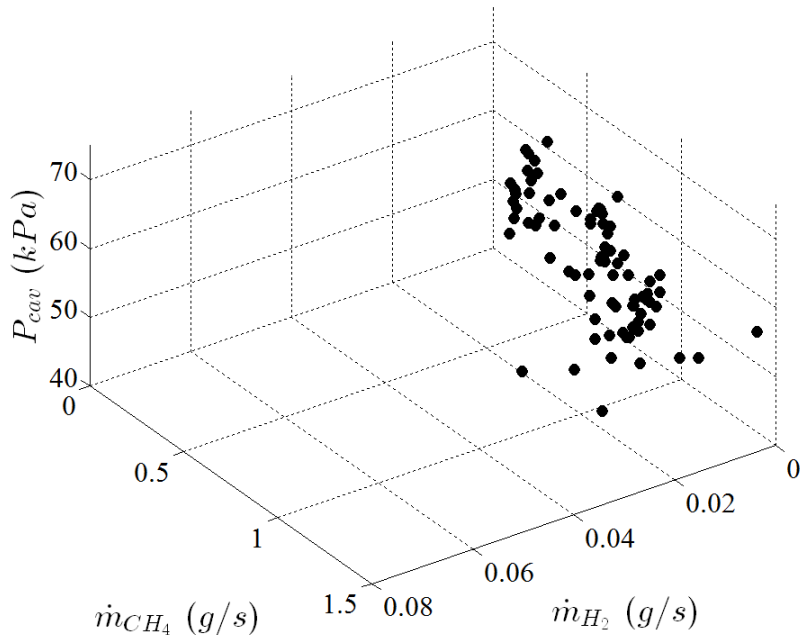

(a) Fuel mixture composition at blowout as a function of the stagnation pressure.

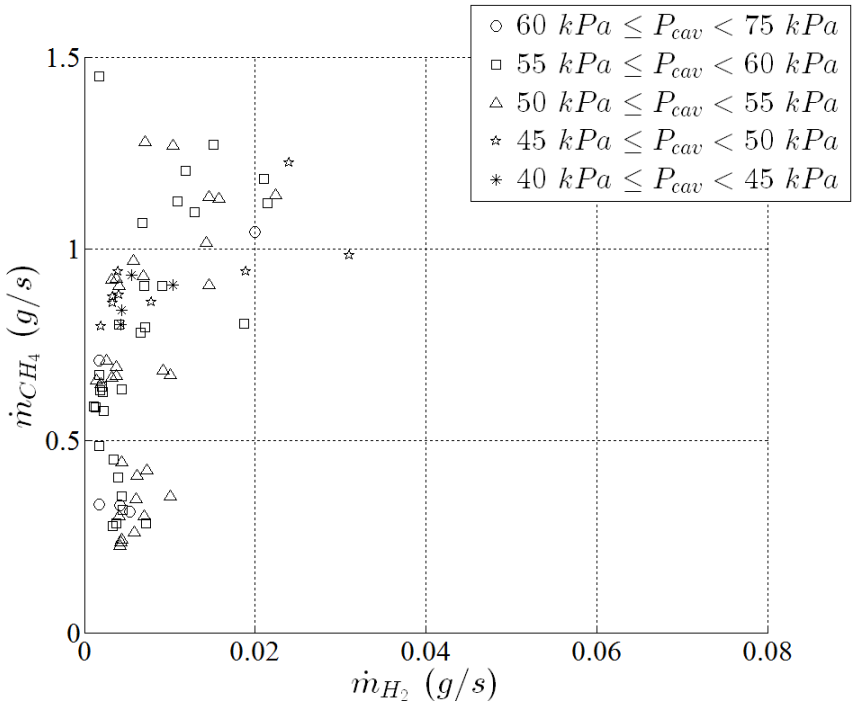

(b) Fuel mixture composition at blowout: the stable domain is located on the right side of the cloud of points.

Figure 55: Blowout of a CH_4-H_2 fuel mixture with a cross-flow static temperature of 248 K (Case 2).

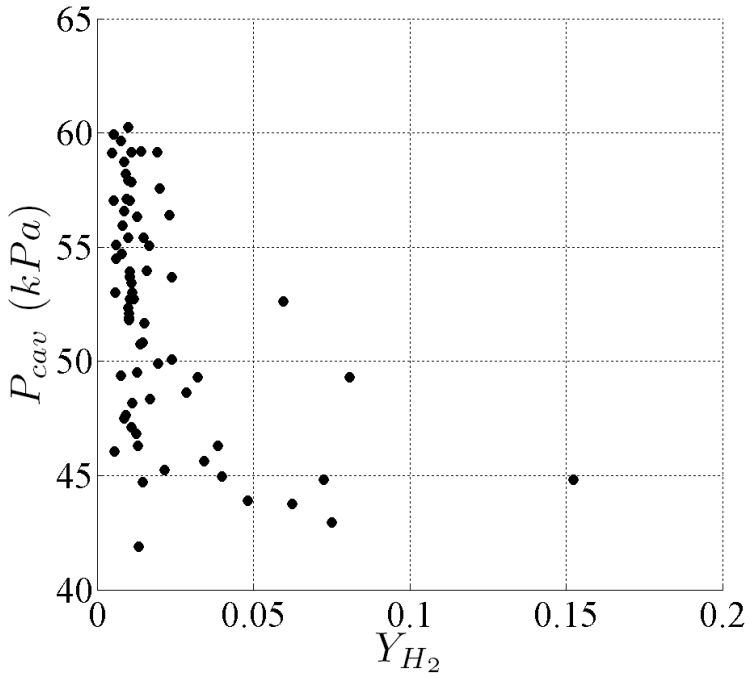

(a) Bottom wall cavity pressure as a function of hydrogen fuel mass fraction at blowout for Case 1.

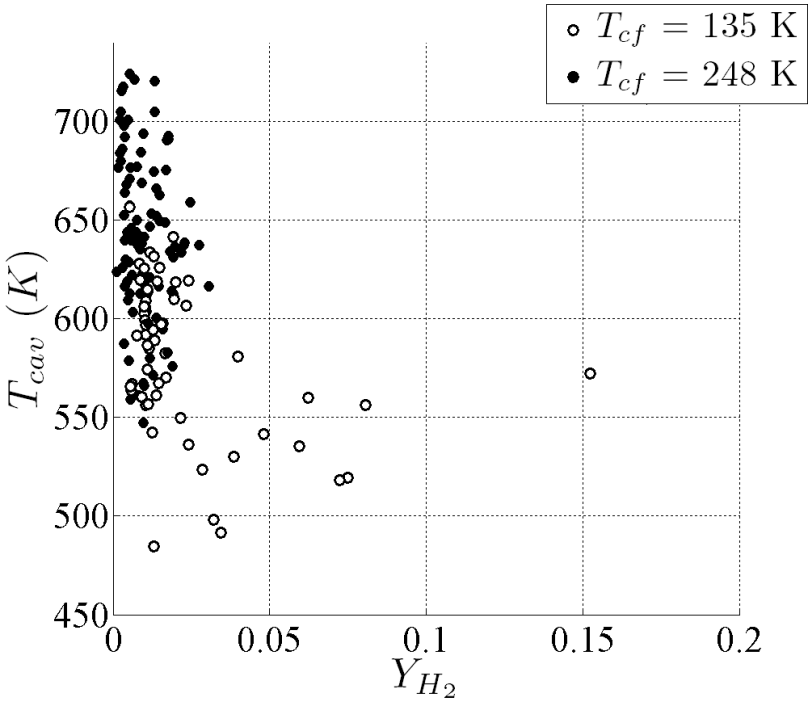

(b) Bottom wall cavity temperature as a function of hydrogen fuel mass fraction for Cases 1 and 2.

Figure 56: Pressure and temperature at blowout

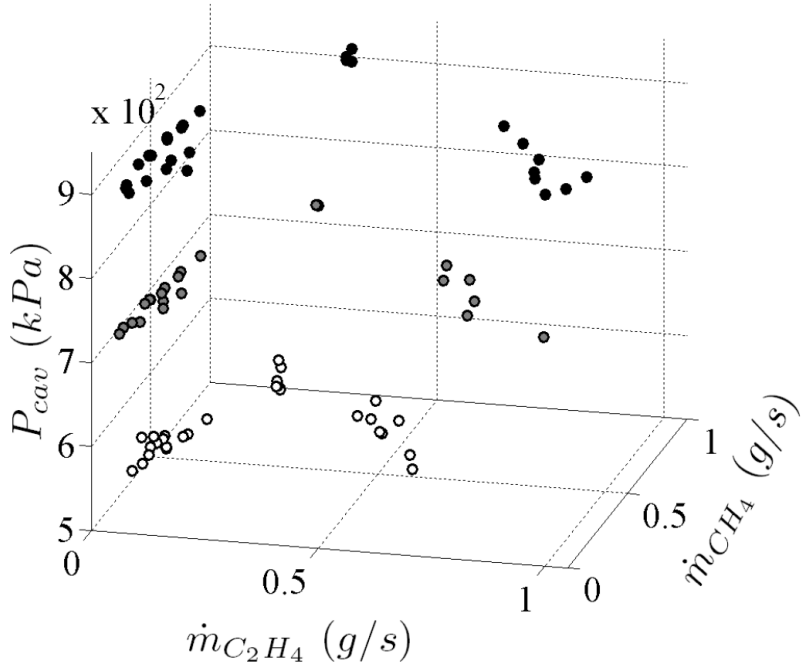

(a) Cavity pressure at blowout as a function of CH_4-C_2H_4 fuel mixture composition.

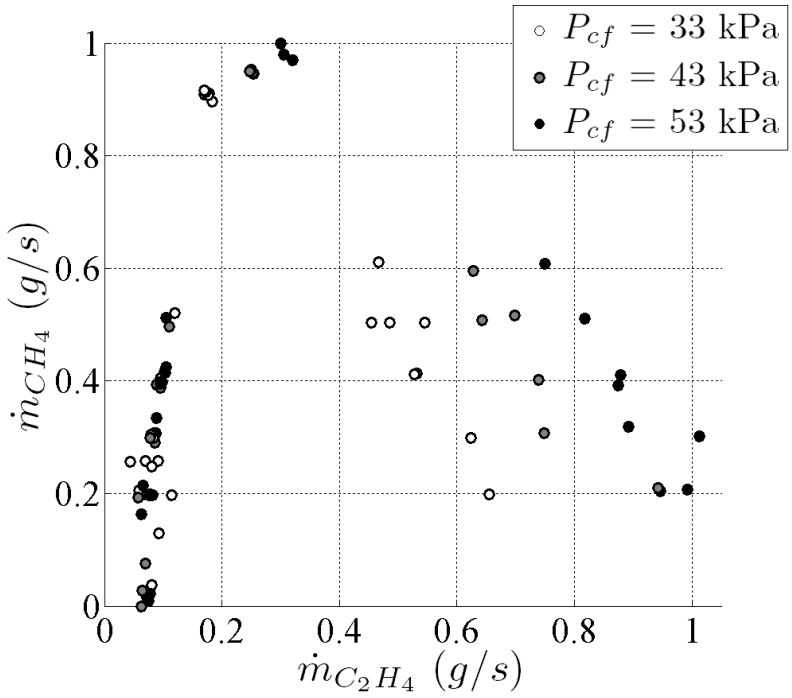

(b) The blowout data points form a horseshoe pattern under which lies the stable domain.

Figure 57: Blowout data points of CH_4-C_2H_4 mixture with a cross-flow static pressure ranging from 33 to 53 kPa, a static temperature maintained at 248 K, and with L/D = 3.84.

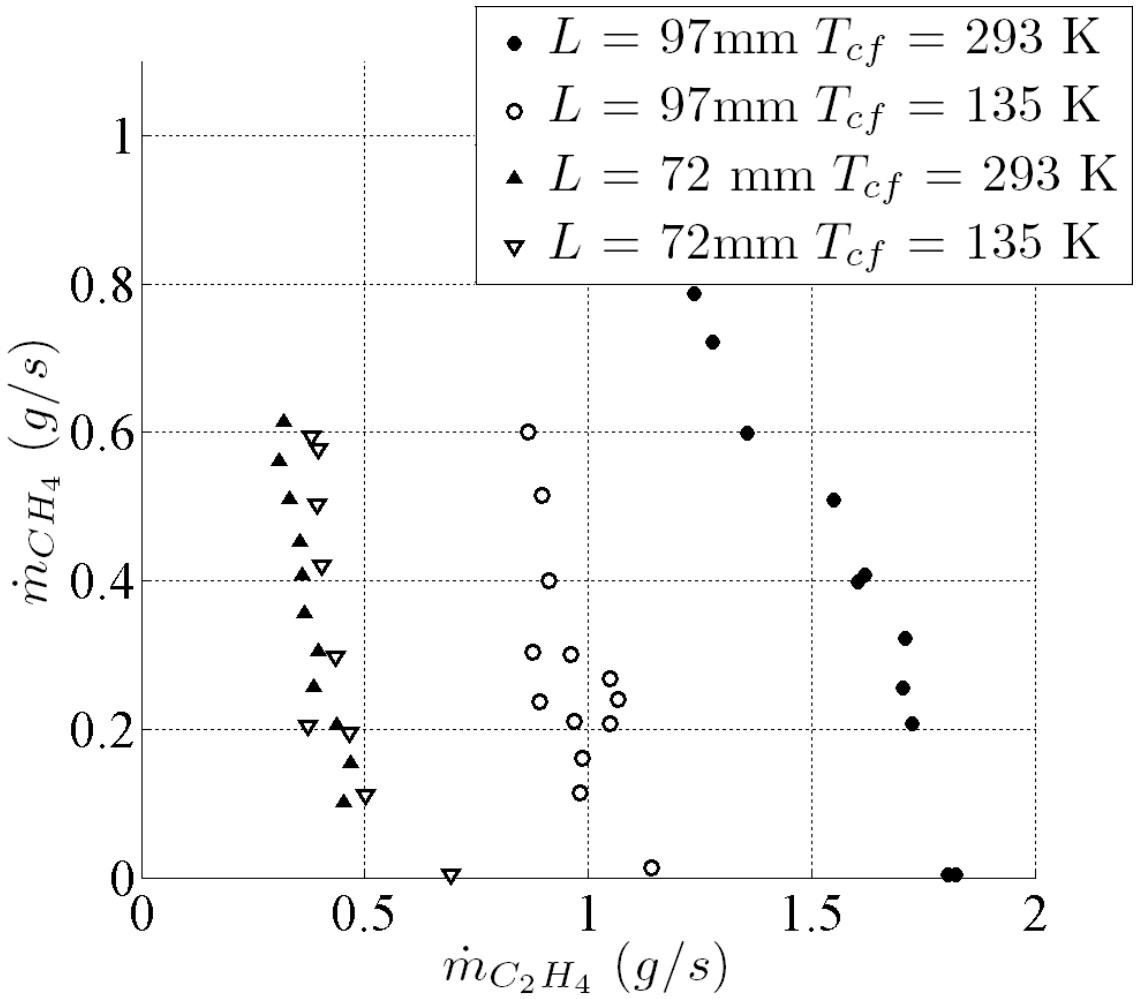

Figure 58: Blowout mixture data points for CH_4-C_2H_4 fuel mixture with a cross-flow static pressure of 56 kPa and static temperature of 135 and 293 K.

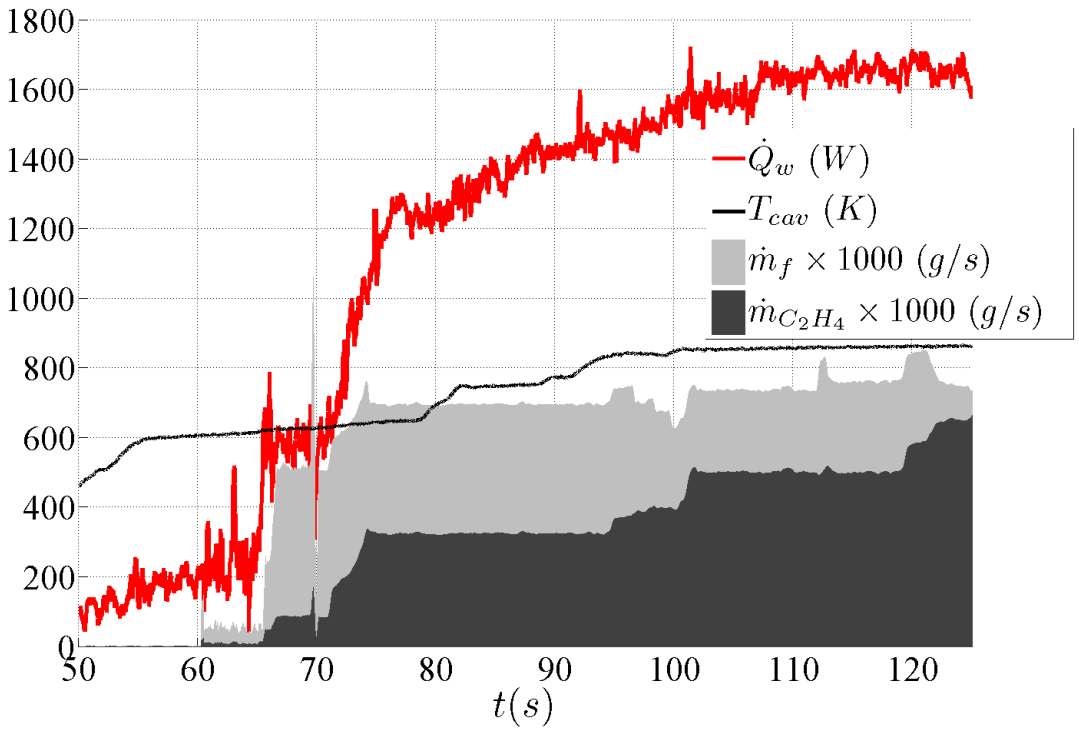

Figure 59: Cavity heat loss, floor temperature and fueling rates as a function of time. The cavity heat loss is calculated using Eq. (46) carried on heat flux distribution similar to the one shown in Fig. 42(b). The floor temperature is measured with an exposed junction thermocouple and indicates the wall temperature, and helps to identify ignition. Fueling rate shows that increasing the fraction of ethylene at constant fuel flow rate elevates the overall cavity wall temperature, and intensifies the heat losses.

CHAPTER V

ANALYSIS

The following discussion provides further insight on the blowout data, and relates the experimental observations to combustion physics. This completes the **Tasks 3** and **4** of this study. Fundamental combustion physics is used to explain the experimental observations. An analysis of the data from these experiments is carried out and compared to the lean blowout model from Rasmussen et al. [81]. In addition, this study proposes a variation of this model which seems to give a better correlation of the data obtained from the experimental campaign.

5.1 Mass Exchange between Cavity and Cross-Flow

As mentioned in the Introduction chapter, the mass exchange between the cross-flow and the cavity is one important aspect in the study of recessed cavities, as it regulates the air supply of the flame-holder and the ejection of its contents.

The mass of air entrained through a free shear layer can be estimated using the model from Dimotakis [26]. An adaptation of this model for hot cavities in a supersonic flow is made by Driscoll et al. [27] and suggests the mass flow rate of the incoming air $\dot{m}_a$ can be obtained by taking one percent of the characteristic air mass flow rate $\dot{m}^*$.

$$\dot{m}_a = 0.01 \underbrace{\rho_{cf} u_{cf} LW}_{\dot{m}_a^*} \tag{47}$$

where L and W are the length and the width of the cavity. In this study, $\dot{m}_a$ ranges from 15 to 47 g/s, given the tested designs and conditions. In comparison, the typical mass flow rate of the cross-flow is about 1 kg/s. Thus, almost 5% of the total air

mass is entrained into the cavity. In term of momentum thickness, only the lower part of the boundary layer may be involved in shear layer entrainment, and most of the mainstream air bypasses the combustor.

However this estimate was originally derived for a free shear layer and does not account for the effect of combustion and the fuel injection strategy. The fuel jet may alter the mass exchange between the cavity and the cross-flow since the jet impinges on the mixing layer with different momenta. Moreover, the topology of the shear layer and the internal flow feature also depend on cavity shape [37] and may change the scavenging of its content.

LES simulations of some data points from Case 2 have been performed by Choi et al. [21], and are in reasonable agreement with the experimental data presented in this study, in particular with the fuel blends compositions at blowout. The numerical data shows that the flow features at stable combustion differ from blowout. In particular, the combustion in the cavity seems to improve the air entrainment due to pronounced unsteadiness of the shear layer, and an increase of its effective volume.

Strong axial convection is typical in supersonic studies and tends to isolate the cavity from the mainstream. The relatively poor mass exchange becomes even more problematic in passive injection designs [47]. However, this aspect turns out to be also vital for the stabilization of the flame as (a) a relatively small portion of the air enters the cavity, and gives a relatively long purging time (residence time) (b) the convection of heat is limited which allows the temperature to build up in the combustor, especially when running with lower cross-flow temperatures.

5.2 Time Scales

The time scales are essential to the scaling and the analysis of the combustion data, especially in the presence of supersonic flows where residence time is limited. Stabilization of flames in flow is sometime explained by proper matching between the rate

at which mass is convected and reacted. As a result, the Damkohler number can be written as the ratio between the flow and the chemical timescales.

$$D_a = \frac{\tau_f}{\tau_c} \tag{48}$$

The Damkohler number is also used to scale the blowout data from flame-holder in supersonic flows [27, 81]. This section provides several definitions of the characteristic time scales pertaining to the cavity flow and chemistry.

5.2.1 Flow Time Scales

The flow time generally refers to the residence time or travel time, and pertains to the pathway, i.e. the flow feature, that is considered.

The shear layer residence time is the time spent by the particle in the shear layer. However the shear layer has a broad range of velocities, and consequently the residence time does not have a unique definition. Studies on shear layers generally use an average value based on the convective velocity. The latter is the average between the cross-flow and the bottom shear layer velocity u_{cav} [26].

$$\tau_{sh} = \frac{2L}{u_{cf} + u_{cav}} \tag{49}$$

According to this definition, the shear layer residence time ranges from 180 to 230 μs in this study.

The product residence time is the time spent by a particle in the cavity. A plug flow combustor approach may be used in which the residence time is the ratio between the cavity mass and the fuel-air mass flow rate.

$$\tau_p = \frac{\int_V \rho_{cav} dV}{\dot{m}_a + \dot{m}_f} \tag{50}$$

This definition requires a precise knowledge of the air entrainment process under cavity fueling, and assumes a maximum scavenging efficiency. The scavenging of the cavity content is a more complex phenomenon due to the mechanism of mass exchange through the shear layer. In fact, early numerical simulations carried on non-reacting cavities in supersonic cross-flows [11] have shown that the escape probability of a particle trapped in the cavity increases with time (air decay rate). This leads to Eq. (51) in which an initial mass is progressively ejected in the mean flow, i.e. purging of the cavity content:

$$\frac{dm}{dt} = -\frac{m}{\tau_p} \tag{51}$$

where τ_p is a residence time for the products in the cavity.

Another definition of the product residence time is the recirculation turnover time, and requires a finer description of the internal cavity flow. Precise quantification of the residence time generally leads to multiple, non-trivial solutions, and may require case per case numerical simulations.

Therefore, the raw LES data obtained by Choi et al. [21] is processed to determine the flow features and their respective timescales. The time average velocity is used to calculate the average streamlines in the cavity, which are shown in Fig. 60. The flow is seeded at some chosen locations (white dots) to emphasize the several flow features that exist in the cavity. Henceforth, the seeding particles have been initiated on the injector and the upstream boundary layer as well as in three noticeable vortical structures r_1, r_2 and r_3. Even if LES accounts for turbulent convection, the time average data does not directly reveal the turbulent mixing which drives the air entrainment and other internal mass transfer processes.

The particle trajectories are calculated by time integration, from the velocity field. The fields are linearly interpolated using a Delaunay triangulation interpolation method. Black dots are connected every 0.1 ms on each streamline. Counting the

intervals between the black dots along a trajectory gives the travel time. Some key time scales are extracted from the LES average data and reported in Table 14. The time scales of interest are the time to reach the shear layer τ_d from the injection site, the time to convect through the shear layer τ_{sh} and the recirculation turnover time τ_r. Each of these flow features behaves differently depending on the fueling rate and therefore the turnover time depends on the type of regime that is considered. These results also suggest that a fluid particle that leaves the injector and is directly ejected in the cross-flow, spends about 1 ms in the cavity. Otherwise, the recirculated pathway yields a longer residence time, and is more favorable for combustion to complete.

Table 14: Characteristic flow times in *ms*. The first and the second numbers are taken for the highest and lowest part of the initial seed, respectively (Fig. 60).

Case	τ_d	τ_{sh}	τ_{r_1}	τ_{r_2}	τ_{r_3}
Lean	0.5-0.9	0.3-0.1	1.5-1.4	2.0-3.4	0.5-0.6
Rich	0.6-0.6	0.2-0.1	0.4-0.6	12.0-32.0	0.6-1.1

5.2.2 Chemical Time Scales

The chemical time scale is the time taken to turn a given amount of reactant into products, or to produce a noticeable change in the species concentration. It can be obtained by taking the ratio between the mixture concentration and the reaction rate $\dot{\omega}$ (in mol m^-3 s^-1).

$$\tau_c = \frac{[s]}{\dot{\omega}} \tag{52}$$

The ignition delay may also be used as a characteristic chemical time as in Eq. (44). From an open system perspective such as the cavity, it is the time elapsed between the instance of mixing fuel and oxidizer together, and the onset of an exothermic self-sustaining reaction. Since the ignitable matter convects in the shear layer, the

ignition delay and the mixing time are revealed by the lift-off distance between the reaction zone and the injectors (low fuel flow rate) or the leading edge (high fuel flow rate). If the mixture does not ignite, then the ignition delay is infinite. Another definition of the ignition delay with multi-fuels [20, 96] is derived from the Arrhenius equation for the generalized reaction:

$$\tau_{ign} = \frac{AT^b e^{-\frac{Ta}{T}}}{[O_x]^{\nu_O}[F]^{\nu_F}} \tag{53}$$

where the numerator is the rate constant and ν_O and ν_F are coefficients adjusted based on a correlation analysis between model and experimental or numerical data.

In general, ignition delay calculations require an initial (or unburnt) temperature as an input, as well as some empirical coefficients. In this study, the choice of the incoming mixture temperature is not obvious as the air, the fuel and the recirculating products likely have different temperatures, so some parametric study is carried out.

5.3 Models for Cavity Blowout

In this section, the blowout data is compared with the existing data on cavity blowout in accordance to **Task 6** of this study. The last part focuses on the formulation of an alternate scaling law which gives a better correlation between the all the data gathered during the experimental campaign.

5.3.1 Damkohler Number at Blowout

Rasmussen et al. [81] observed that lean blowout limits with floor injection follows a $\Phi = 0.0028 D_a^{-0.8}$ correlation. The Damkohler number is given by the ratio of the characteristic time scale between the flow and the chemical reaction [81].

$$D_a = \frac{\frac{D}{u_{cf}}}{\left(\frac{\alpha_o}{S_{Lo}^2}\right)\left(\frac{0.1\ MPa}{P_{cf}}\right)\left(\frac{300\ K}{T_{cf}}\right)} \tag{54}$$

where D is the depth of the cavity, α_o and S_{Lo}^2 are the stoichiometric mixture diffusivity and the stoichiometric flame speed, respectively, both evaluated at 300 K and 1 atm. u_{cf}, p_{cf} and T_{cf} are the cross-flow velocity, presssure and temperature, respectively. The original form of Eq. 54 was suggested by Ozawa et al. [74] for bluff body flames as the body height divided by the axial velocity of the free stream (to obtain a flow time scale) and the premixed flame timescale. An empirical form for the non-premixed flame timescale was derived by Driscoll et al. [27] and adjusted to experimental data obtained from various studies including bluff bodies and struts. Further adjustments of the empirical coefficients for supersonic cavity flame-holding [81] led to the final expression in Eq. 54. The equivalence ratio Φ is calculated from the characteristic air mass flow rate defined in Eq. 47.

Figure 61 depicts the blowout data with respect to the equivalence ratio and the Damkohler number for the lean cases. When approaching lean blowout, the flame region is located upstream, near the injectors [80]. Whereas, for the rich blowout case, the flame sits near the trailing edge. This criterion is used to separate lean and rich blowout events. The overall data agrees well with the model proposed by Rasmussen et al. [81], as seen in Fig. 61(a) in terms of order of magnitude, but a higher deviation is observed for Case 1-3. The effect of cross-flow temperature on the blowout margin can be seen from Eq. 54. The cross-flow velocity is approximated as:

$$u_{cf} = M_{cf}(\gamma R T_{cf})^{1/2} \tag{55}$$

Assuming a perfect gas, the flow time scales with the inverse of the square root of the cross-flow temperature and $D_a \propto \frac{T_{cf}}{u_{cf}} \propto T_{cf}^{1/2}$. Consequently, preheat produces a shift of the data toward the right side of the graph, which is in agreement with what is observed. In addition, the characteristic air mass flow rate decreases with temperature as $\dot{m}_a^* \propto T_{cf}^{-1/2}$. This may explain why richer blowout mixtures are found at higher cross-flow temperatures (248-293 K).

The overall mixture properties such as stoichiometric flame speed and thermal diffusivity are calculated using Cantera, and the non-dimensional ratio S_{Lo}^2/α_o is shown in Fig. 61(b) as a function of the Damkohler number. The change of fuel mixture composition is expressed through this term only. There is only a mild increase of this ratio for methane-ethylene fuel mixture, whereas a much stronger dependency is found for the methane-hydrogen mixtures, in the tested range. This increase produces a shift of the blowout data toward higher Damkohler number, as seen in Fig. 61(a).

5.3.2 Alternate Scaling Law for Cavity Blowout

The model from Rasmussen et al. [81] discussed previously, gives a general description for cavity lean blowout. Thus, this scaling is revisited and extended to the new cases investigated in this study to give a better correlation, especially with reference to the fuel mixtures.

5.3.2.1 Flow Time

Flow visualizations of the flame region [80] suggest that the main reaction may take place in the shear layer where the air, the fuel and the hot product inter-mix. From a Lagrangian viewpoint, a control mass element coming from the main stream spends a limited time in the mixing layer to reach the flammable limit, as shown in Fig. 62. During its journey, the element may receive favorable inputs from its surrounding, i.e. convected species and heat, to achieve ignition before reaching the trailing edge. If successful, the hot products are recirculated to support the overall reaction. Ignition is reached at various axial locations as indicated by the lift-off distance.

The latter may depend on the fuel composition, the stoichiometry and the fuel jet momenta, as observed in the present experiments (Figs. 37(d) and 38(a)) and in the literature [27, 85]. Henceforth, the length of the shear layer may be more relevant in the determination of the flow time scale. In the earlier scaling law [81], the residence time is derived from studies on bluff bodies where the length of the shear layer is a

function of the depth of the cavity [27], whereas in open cavity flame-holder, the shear layer prematurely re-attaches at the trailing edge. Consequently, the length of shear layer is no longer a function of the depth, but is given by the cavity length instead. However, the depth of the cavity may be involved in the determination of the overall storable matter (pertaining to cavity volume) and the product residence time (turn over time of the main vortical structures).

In this study, the characteristic flow time τ_f is the average time spent by a flow element convecting in the shear layer from the leading edge to the trailing edge. Thus, it is based on the convective velocity as in Eq. 49. However, the velocity in the cavity is relatively small compared to the cross-flow velocity such that the convective velocity reduces to $u_{cf}/2$:

$$\tau_f = \frac{2L}{u_{cf}} \tag{56}$$

5.3.2.2 Chemical Time

In this study, cavity blowout is shown to depend on the fueling rate and the composition. The model from Rasmussen et al. [81] does not account for the fuel-air stoichiometry in the calculation of the Damkohler number as the fuel-air mixture properties are evaluated at stoichiometric conditions. Instead, the overall chemical time may be a function of the fuel-air stoichiometry such that the ignition delay times discussed in Section 4.2 can be used to scale the blowout data. Ignition delay calculations are also relatively sensitive to the temperature and therefore, the sensitivity to different initial temperature has been investigated. However, numerical simulations in Fig. 48 show that 1400 K is a reasonable guess for a cavity product baseline temperature. One may use a different value resulting in a shift of the data along the D_a-axis, however, the trends should be similar since the ignition delay maps are similar in the [1000-2000] K range (see Appendix C).

The fuel maps shown in Fig. 47 require a relatively large amount of data and computing time, since each point is the result of a simulation involving 325 reactions and 53 species over thousands of time steps. An analytical model is used to approximate the ignition delay of an fuel-air mixture, with a slow and fast chemistry. The trends observed on the computed fuel maps (Fig. 47) reveals key characteristics that are used in the derivation of this model:

1. **Switching**: The timescales are bounded by a slow (CH_4) and fast chemistry (fuel additive).

2. **Self-Similarity**: Each contour may be approximated from a specific pattern by stretching and shifting.

This section uses a generic notation in which a given fuel-air mixture composition is pointed on the map by $\mathbf{r} = [x\ y] \in \mathbb{R}^{2,+}$, where x denotes the mass fraction of the fuel additive (hydrogen or ethylene) and y is the mass fraction of methane in the overall mixture.

$$x = \frac{\dot{m}_{H_2}}{\dot{m}_f + \dot{m}_a} \ or \ \frac{\dot{m}_{C_2H_4}}{\dot{m}_f + \dot{m}_a} \tag{57}$$

$$y = \frac{\dot{m}_{CH_4}}{\dot{m}_f + \dot{m}_a} \tag{58}$$

The first observation suggests that the ignition delay may be obtained by switching from a fast to a slow chemistry with characteristic times $\tau_{chem,1}$ and $\tau_{chem,2}$, respectively. A gate function H is used to transit smoothly from one type of chemistry to the other.

$$\tau_{chem} = (1 - H)\tau_{chem,1} + H\tau_{chem,2} \tag{59}$$

where H is a normalized $\tan^{-1}$-gate, with a center r_o and a quality factor w.

$$H_{(r,r_o,w)} = \frac{1}{\pi}\left(\tan^{-1}(w\, d_{(\mathbf{r},\mathbf{r_o})}) + \frac{\pi}{2}\right) \tag{60}$$

where $d_{(\mathbf{r},\mathbf{r_o})}$ is the distance between two points located by the vectors $\mathbf{r}$ and $\mathbf{r_o}$, $\mathbf{r_o}$ describes a specific contour and $\mathbf{r}$ points at some location in the domain.

The fuel maps investigated in this study appear have self-similar contours, as mentioned in 2. A reference contour $\Gamma_o = \left\{(x_o, y_o) \in \mathbb{R}^{2,+} \overset{f\in C^\infty}{\to} (x_o, f_{(x_o)})\right\}$ is used to parameterize the center of the gate ($r_o = H^{-1}(1/2)$). Therefore, f is the reference pattern scaled to match the mid-value contour of the map. It has been found that this contour yields an exponential form (Eq. 61) for both methane-hydrogen and methane-ethylene, as observed by Vasil'ev et al. [96].

$$\mathbf{r_o} = \begin{pmatrix} x_o \\ Ke^{\frac{x_o - a}{k_s}} \end{pmatrix} \tag{61}$$

where K, k_s and a are constants which gives the best fit to the data, and are reported in Table 15. This ensures that the analytical and the numerical data is properly matched for the mid-range values. The next step is to match the model along the axes, i.e. for the slow and fast chemistry bounds.

The quality factor w is not constant along Γ_o, and the transition discussed in 1. is typically narrower near the origin, as seen by the convergence of the contours in Fig. 47. Therefore, w must be a function of r_o to capture this trend. The method used to change from narrow to broader gates is the same as in Eq. (59), for which the quality factor changes from a high w_1 to a low value w_2, as progressing away from the origin. As a result, the gating process for w requires a center l'_o and a quality factor w_w to be determined. Figure 63 illustrates the graph of H.

$$w_{(\mathbf{r_o})} = (1 - H_{(l_o, l'_o, w_w)})w_1 + H_{(l_o, l'_o, w_w)}w_2 \tag{62}$$

$$l_{o(\mathbf{r_o})} = \int_o^{x_o} \sqrt{1 + \left(\frac{dy_o}{dx_o}\right)^2} dx' \tag{63}$$

Because the distance between a point and a contour is not trivial, such that the operator d used in Eq. (60) needs to be determined. The Hausdorff distance is typically used in problems where distance between subsets of a metric space are calculated. The signed Hausdorff distance between a point of the domain ($\mathbf{r}$) and the reference contour ($\mathbf{r_o}$) is given as

$$d_{(\mathbf{r},\mathbf{r_o})} = \text{sign}(y - f_{(x_o)}) \min_{\mathbf{r_o} \in \mathbf{\Gamma_o}} \left\{ \sqrt{(x - x_o)^2 + (y - f_{(x_o)})^2} \right\} \tag{64}$$

This definition gives satisfying results, however if the mesh resolution is $N_x \times N_y$, the computation of the Hausdorff distance requires at least $N_x^2 N_y$ logical operations which in turn, may be relatively costly given the purpose of this approach. Therefore, a simpler form is retained for this model in which the signed distance is ordinate-based, as seen in Eq. (65).

$$d_{(\mathbf{r},\mathbf{r_o})} = y - y_o \tag{65}$$

Figure 64 shows the impact of both distance operators on the final form of H. In addition its simplicity, the ordinate-based distance has trends which pertains to the actual contours seen in Fig. 47.

Finally, a relatively accurate approximation of the ignition delays is obtained for both fuel blends used in this study, and reported in Fig. 65. The empirical constants are found based on residue minimization between the model and the discreet maps in Fig. 47, and reported in Table 15. These empirical values do not guarantee a good

fit beyond the range of mass fractions considered in this study. The trends seen in Fig. 47 are fairly captured by the model proposed in this section. The latter is then used in the scaling of the blowout data.

Table 15: Coefficients used in Eqs. (59)-(62).

	$CH_4 - H_2$	$CH_4 - C_2H_4$
$\tau_{chem,1}$	$10^{-4.4}$	$10^{-1.9}$
$\tau_{chem,2}$	$10^{-4.3}$	$10^{-1.9}$
K	0.18	0.40
k_s	0.015	0.07
a	0.0025	0.009
w_1	40	60
w_2	5	5
w_w	10	30
l'_o	$l_{o,max}/2$	$l_{o,max}/4$

5.3.2.3 Representation and Reduction of the Data

The blowout data is reported in Fig. 66 similarly to Fig. 61, however the Damkohler number is computed using Eqs. 56 and 59.

$$Da = \frac{2L}{u_{cf}\tau_{chem}} \left(\frac{T_{cf}}{300^o K}\right)^{m_T} \left(\frac{P_{cf}}{0.1MPa}\right)^{m_p} \tag{66}$$

Equation (66) is also compensated with temperature and pressure terms from Eq. 54 to account for the effect of preheat and vessel pressurization. Moreover, the m_p and m_p-exponents were present in the initial expression by Driscoll et al. [27].

The stoichiometry of the fuel-air mixture is accounted in the calculation of the chemical time (Eq. (58)) such that the estimation of air flow rate is no longer based on $\dot{m}^*$. Instead, the air flow rate is computed as in Eq. 47 [27]. This definition is also used in the calculation of the cavity equivalence ratio.

Even on linear axes, the scaling method presented in this section produces readable trends and captures the subtleties between the various tested conditions and

configurations.

The blowout data is split at $\dot{m}_f = 0.8$ g/s since 0.6-0.8 g/s is a range for which the flame region shifts downstream significantly (Fig. 38(a)). Above this threshold, the data moves to the fast branch as seen in Figs. 66(b) and 66(d). The effect of preheat discussed in Section 5.1.2 is also visible as the preheat produces an upward shift of the blowout data along the equivalence ratio axis and increases the stable domain as seen in Figs. 66(a) and 66(b).

One purpose of data scaling is to collapse the data from different configurations on a common trend. However depending on the topology of the blowout region, this may not be possible given the degrees of freedom of the model (mainly m_p and m_T). For instance, the data obtained with L/D = 2.84 cavity yields a linear trend (Fig. 66(c)). However, increasing the cavity length allows more fuel compositions to burn. A slow and fast branch are formed, for which a given value of equivalence ratio may yield two mixture compositions at blowout (Fig. 66(b)). That is why the blowout data obtained in Cases 3, 4 and 5 cannot be collapsed with Case 6 and 7, since the topology of the solution is different. Instead, the preheat is chosen for data reduction as suggested by Fig. 66(a). The values of m_p and m_T are chosen such that the heated data collapse on the unheated one, and reported in Table 16.

Table 16: Coefficients used in Eq. (66) such that heated and unheated data collapse.

	$CH_4 - H_2$	$CH_4 - C_2H_4$
m_p	0.43	-0.43
m_T	1.0	1.0

The same blowout data is plotted in Fig. 67 with exponents in Table 16. The best fit curves are found for the various cases investigated in this study. Because of the nature of the derivation of the chemical time, the equivalence ratio at blowout can be estimated by a full analytical form, and is given as a function of the cross-flow

regime in Fig. 67.

The range of Damkholer number in Fig. 66(a) for Cases 1 and 2 is relatively small ($1 < D_a < 7$) compared to the broad range of ignition delays reported in Fig. 65(a). This limitation may be primarily due to small hydrogen addition. For instance, the Damkohler numbers are expected to be much higher in hydrogen dominant mixtures, although this has not been investigated here.

This narrow range of D_a may also be due to the lack of accuracy in the estimation of the entrained air flow. The model proposed by Rasmussen et al. [81, 74] used in this scaling (Eq. 47), gives a relatively high air flow rate (up to 57 g/s) compared to the fuel flow rates (up to 1.5 g/s), such that the equivalence ratio does not exceed 1 over the entire data investigated. This model may provide a "leaner" equivalence ratio than the actual values. As a result, the range of ignition delay calculated from the experimental flow rate data is limited to a much smaller range, as seen in Fig. 69, for Case 1. In addition, the actual air flow rate may decrease under strong fueling conditions, as discussed in Section 4.4.3. . Therefore, the actual equivalence ratio and the ignition delay may cover a broader range than the one in Fig. 69. The robustness of this model is tested with respect to the air flow rate, since the latter is an important parameter that could be inaccurately estimated.

Ultimately, it is assumed that there exists a maximum fueling rate $\dot{m}_{f,max}$ above which, no air enters the cavity. This hypothesis relies on the concept of mass conservation and shear layer impingement, in which all the fuel matter is eventually ejected through the mixing layer into the cross-flow. Consequently, under very high fueling rate, the ejection of the fuel matter may prevent the air from entering the cavity (as in a bypass). A simple way to account for this effect is to assume a linear relationship between entrained air and fuel mass flow rate, such that Eq. 47 is modified as follows:

$$\dot{m}_a = 0.01\, \dot{m}_a^* \, \frac{\dot{m}_{f,max} - \kappa \dot{m}_f}{\dot{m}_{f,max}} \ , \ \dot{m} \leq \dot{m}_{f,max} \tag{67}$$

where $\kappa \in [0;1]$ is a coefficient, that accounts for the sensitivity of $\dot{m}_a$ to the effect of fueling. The blowout data is plotted for Case 1 in Fig. 68, with half of the nominal air flow rate (0.005 leading coefficient), $\dot{m}_{f,max} = 1.6$ g/s, and $\kappa = 0.5$. The resulting air mass flow rate is 2.5 to 3.5 times lower than the previous estimation in Fig. 66(a). Even with this crude change, the trend does not differ drastically from the one in Fig. 66(a), which demonstrates a good robustness with respect to the error on $\dot{m}_a$. The cloud of data points extends to higher equivalence ratios as expected, since the air flow rate is lowered.

The dispersion of the data is also reduced in Fig. 68 compared to Fig. 53(b) as some points have collapsed on the mean trend. This effect may be attributed to the curvature of the mapping (in a Riemannian sense) (Fig. 47) used to compute the Damkohler number from the blowout maps. Figure 69 shows that a few point falls beyond the $\log(\tau_{ign})$ = -2.6 contour. If the curvature of the ignition delay map is high, as for a methane-hydrogen multifuel, then the blowout data is more likely to collapse in separate regions (as in segregating mapping). This pertains to the high sensitivity of the ignition delay for small addition of hydrogen.

This scaling method gives the same topology of the ignition delay with respect to the choice of initial temperature (at least in the range investigated [1000-2000] K, Appendix C). This implies that the trends presented in Fig. 67 should not be altered if one changes the air flow rate or the unburnt temperature. However, the actual values of the Damkohler number and the equivalence ratio may change drastically, and both fuel-air stoichiometry and unburnt gas temperature have not been determined accurately. Consequently, this discussion is not quantitative. A possible relation between the Damkohler number and the equivalence ratio at blowout is shown in Fig. 67, but more data is needed to verify this relation.

5.4 Further Discussion on Cavity Blowout

5.4.1 Energy Balance

Cavity blowout is approached in terms of time scale matching between flow and chemistry [27], since timing in supersonic flows is relatively important. However the combustion process also prevails owing to a proper energy balance between incoming and outgoing matter. Even if the reaction may have time to take place in the cavity, combustion may not take place as limited heat release prevents exothermic reactions to remain activated.

Conservation of energy is carried out on the cavity, as for a plug flow combustor. At steady state, the difference between the incoming and outgoing enthalpy yields the wall heat losses.

$$\dot{m}^- h^- - \dot{m}^+ h^+ = \dot{Q}_w \tag{68}$$

where superscripts $^+$ and $^-$ denote the incoming and out coming matter, respectively.

The incoming mixture is the fuel and the air entrained in the shear layer, while products are ejected downstream in the boundary layer as shown in Fig. 70. Equation (68) is then expressed in term of moles for each species i.

$$\sum_{i=1}^{i=n_s} \dot{n}_i^- H_i^- - \dot{n}_i^+ H_i^+ = \dot{Q}_w \tag{69}$$

where $\dot{n}_i^- - \dot{n}_i^+ = \dot{\omega}\Delta n_i$, since air and fuel are consumed stoichiometrically by the reaction at a rate $\dot{\omega}$. Therefore, given the heat content involved in the combustion process, the average reaction rate required to maintain the cavity at a constant energy is

$$\dot{\omega}_{NRG} = \frac{\dot{Q}_w - \sum_{i=1}^{i=n_s} \dot{n}_i^+ (H_i^- - H_i^+)}{\sum_{i=1}^{i=n_s} \Delta n_i H_i^-} \tag{70}$$

For the reaction region to be maintained at some given flammable conditions, the power released from the combustion must match the losses and sensible terms. Failure to overcome the heat losses leads to successive temperature drops which may deactivate the exothermic reactions (blowout). Equation (70) is an energy constraint on the reaction rate. Experimental results on heat transfer revealed that $\dot{Q}_{w,cav}$ is at most 2 kW.

In addition, the reaction must be fast enough to complete within the reaction zone. A chemical reaction timescale is given as the ratio between the incoming mixture concentration $[s] = \frac{P_{cf}}{R_u T_o}$ and the reaction rate as in Eq. (52), whereas the residence time is given by Eq. (49), neglecting u_{cav}.

$$\dot{\omega}_{TS} = \frac{P_{cf}}{R_u T} \frac{u_{cf}}{2L} \tag{71}$$

The solution of the problem yields the energy and the time scale matching constraints given by Eqs. (70) and (71), respectively. Therefore, blowout is assumed to occur whenever the reaction is not prompt enough or has limited heat content.

$$\dot{\omega} = \max \{\dot{\omega}_{NRG}, \dot{\omega}_{TS}\} \tag{72}$$

The present study has proposed an instrumentation and post processing technique to evaluate the cavity wall heat losses. However, heat transfer data has been obtained only for a few runs in Case 5, such that there is a limited insight on the relation between wall heat losses and blowout. Nevertheless, the energy balance may be an important issue to properly characterize of cavity blowout, in addition to the impact of time scales presented here.

5.4.2 On the Experimental Blowout Trends

The presence of a horseshoe pattern in the methane-ethylene blowout data (Figs. 57 and 66(b)) does not correspond to the common trend expected in the literature [27],

in which one Damkohler number yields two possible equivalence ratios (lean and rich values). However, the blowout in complex combustors with broad heat contents may not behave as the basic reactors found in the classic literature. Figure 71 gives a possible explanation for the blowout trends found in this study.

The line of constant Φ are derived from Eq. (38)

$$\Phi = 2\frac{M_a}{M_{CH_4}}\frac{\dot{m}_{CH_4}}{\dot{m}_a} + n_{f+}\frac{M_a}{M_{f+}}\frac{\dot{m}_{f+}}{\dot{m}_a} \tag{73}$$

where the fuel additive is denoted by $f+$ and

$$F_+ \; + \; n_{f+}\, Ox \; \rightarrow \; P \tag{74}$$

which justifies the line pattern illustrated in Fig. 71. There are two blowout limits for each fuel, and a combination of a fast and a slow chemistry yields intermediate values, just as shown in Section 4.2, and also in the studies on multifuel ignition delays [20, 96]. The stable domain is the region in between the lean and rich blowout curves. However pure methane combustion has not been achieved in this study, which implies that the stable combustion domain is cropped. The latter is due to the design and conditions which do not allow pure methane combustion to take place. As a result, the lean and rich limit curves merge before reaching the $\dot{m}_{CH_4}$-axis. Depending on the topology of the fields considered (lines of constant Φ and actual blowout curve) in Fig. 71, the solution transformed to a $\Phi - Da$ representation may yield the pattern seen in Fig. 66(b).

The rich-lean terminology becomes loosely defined when moving along the blowout region since the entrained air flow rate is not known properly (Eq. 47), as there is no accurate estimate for the equivalence ratio. Instead, both branches are differentiated based on the Damkholer number, which inherently depends on the type of chemistry. That is why the slow-fast terminology is retained to designate the branch.

Furthermore, the influence of the cross-flow temperature on cavity blowout may lead to a method that determines the branch where the data lies, if only a small number of points is available. As reported, preheating the cross-flow systematically increases the size of the stable domain. As a result, under higher cross-flow temperatures the slow branch shifts to the left (less of the fast chemistry is needed, as in Fig. 66(a) or lower Damkholer numbers) and the fast branch to the right (more of the fast chemistry is needed, as in Fig. 66(b) or higher Damkholer numbers). For instance in Fig. 66(a), the preheated data lies on the left side of the non-preheated values. Therefore, the blowout data in this figure may belong to the slow branch, which support the existence of a fast branch with a hydrogen dominant fuel. Regardless, the fast limit could not be reached given the range of hydrogen flow rate investigated in this study. Both slow and fast branches exhibit differences in their combustion characteristics:

At lower fuel flow rates ($\dot{m}_f < 0.8g/s$),

- the fuel jet has less momentum and limited penetration into the shear layer is expected. Combustion video data (Fig. 72) reveals that the flame does not span upward into the shear layer, and the reaction region is mostly contained inside the cavity, near the injector region. In addition, the blowout data also yields the slowest chemistries investigated in this study, as revealed by the mixture composition at blowout and the ignition delay maps in Figs. 57, 47(c) and 47(d).

At higher fuel flow rates,

- The flame translates toward the aft step, as seen in Fig. 38(a). The lift off distance increases (L_{pm} in Fig. 62), and shows a late ignition due to rich product saturation [80]. Timing between flow and chemistry may become critical, as there is a finite length to perform fuel-air mixing and ignition within the mixing

layer. In addition, the flame benefits from limited product support, as less surface is shared between the reaction region and the product recirculation. The translation of the flame region can also be the result of the fuel jet penetration into the shear layer. As discussed in Section 4.4.3., fuel pockets with a stronger momentum may reach deeper into the mixing layer where the velocities are higher, increasing the lift-off distance from the leading edge.

Figure 73 illustrates fuel-lean and fuel-rich cavity burning based on the experimental observations from this study, and from Rasmussen et al. [80]. In the methane-hydrogen case (Cases 1 and 2), the shift of the flame region toward the trailing edge of the cavity occurs within what is possibly the slow branch, i.e. blowout with methane dominant fuel mixtures, whereas for methane-ethylene fuel mixtures, the same phenomenon takes place at the transition between slow and fast chemistry (tip of the horseshoe).

Therefore, the characterization of branch type (slow or fast) may not be relevant to the flame position. This supports the theory that the flame position may be governed by the fuel jet momentum (mixing layer penetration) and the stoichiometry of the cavity (product composition) as observed by Rasmussen et al. [80].

The differences observed in the video data suggest that because the flame position changes, blowout may be governed by different mechanisms, e.g., at low or high fuel flow rate. The alternate scaling does not account for the flame position or the effect of fueling strength. As a consequence, there may be a more adequate scaling for each branch since for instance, the model made by Driscoll et al. [27, 81] only applies to blowout at low fuel flow rate. However, the transition between slow and fast chemistry seems to be smooth given the combination of fuel mixtures which have been tested, such that there may not be separate models for blowout between low and high fueling rates, unless an asymptotic approach is considered.

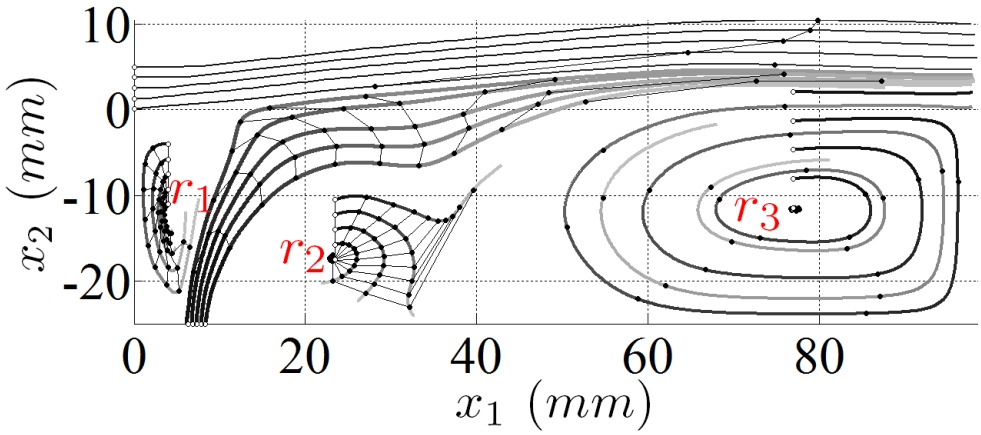

(a) Lean case: $\dot{m}_{CH_4} = 0.3$ g/s and $\dot{m}_{H_2} = 0.06$ g/s.

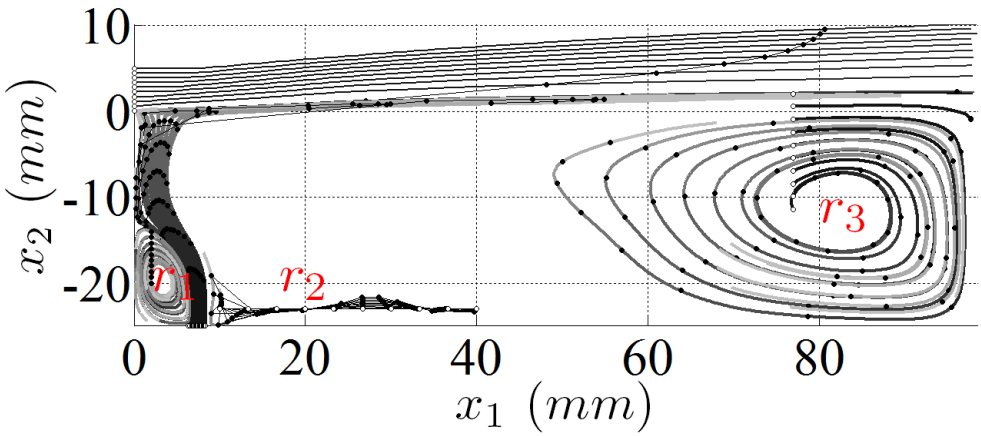

(b) Rich case: $\dot{m}_{CH_4} = 0.6$ g/s and $\dot{m}_{H_2} = 0.06$ g/s.

Figure 60: Particle mean trajectory as a function of time from LEMLES [21] (P_o = 859.7 kPa and T_o = 550 K). The distance between two black dots on a trajectory corresponds to 0.1 ms.

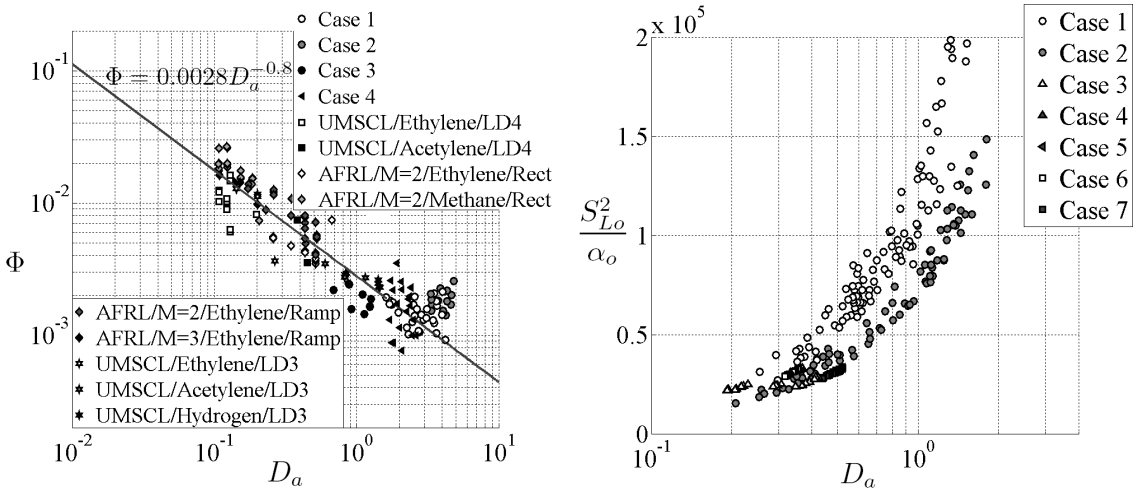

(a) Equivalence ratio as a function of Damkohler number at lean blowout. The blowout data obtained in this study is compared with data from other facilities [81]. The legend reads as *Facility/Fuel/Ramp Type*.

(b) Non-dimensional mixture characteristic as a function of the Damkohler number.

Figure 61: Correlation of the lean blowout data.

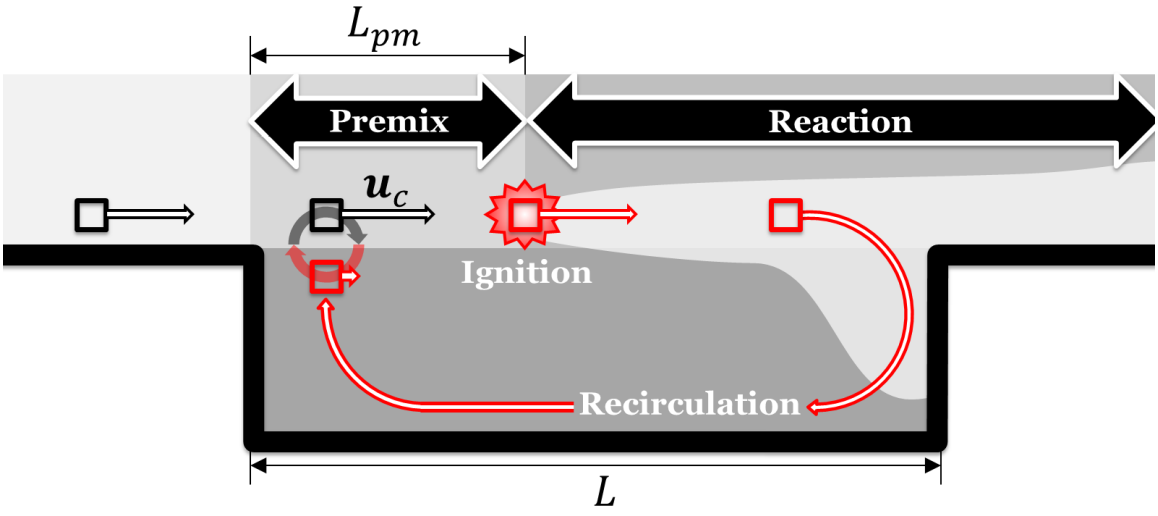

Figure 62: One possible scenario explaining the cavity flame-holding mechanism from a Lagrangian perspective: 1. A particle of fuel or air is entrained in the shear layer. 2. Ignition may occur before reaching the trailing edge, upon proper stimulation from the surrounding (convected and diffused matter into the control mass). 3. The latter case ensures the recirculation of hot product for further flame support.

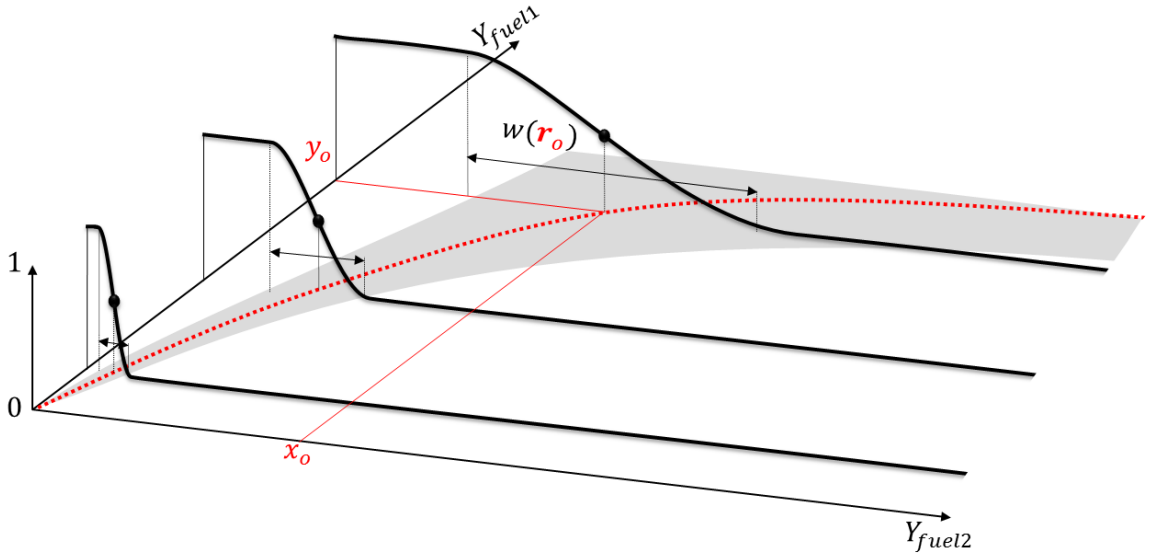

Figure 63: Illustration of the gate used to switch between two different fuel-air chemistry: $H_{(r,r_o,w)} = \frac{1}{\pi}\left(\tan^{-1}(w_{(\mathbf{r_o})}d_{(\mathbf{r},\mathbf{r_o})}) + \frac{\pi}{2}\right)$. The center of the gate is parameterized by the mid-value contour described by $\mathbf{r_o}$. The quality factor is a function of the arc length location l_o as described in Eqs. (62) and (63).

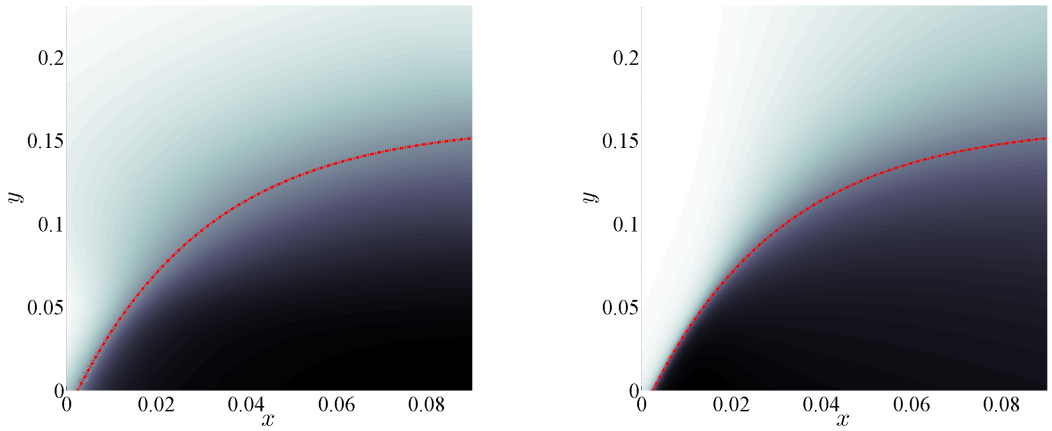

(a) Using the signed Hausdorff distance in Eq. 64.

(b) Using the ordinate-based distance in Eq. 65.

Figure 64: Color plot of the function H (white = 1, black = 0) used for the computation of the $CH_4 - H_2$ ignition delay map (first column in Table 15). The reference contour $\mathbf{r_o}$ is the dashed red line.

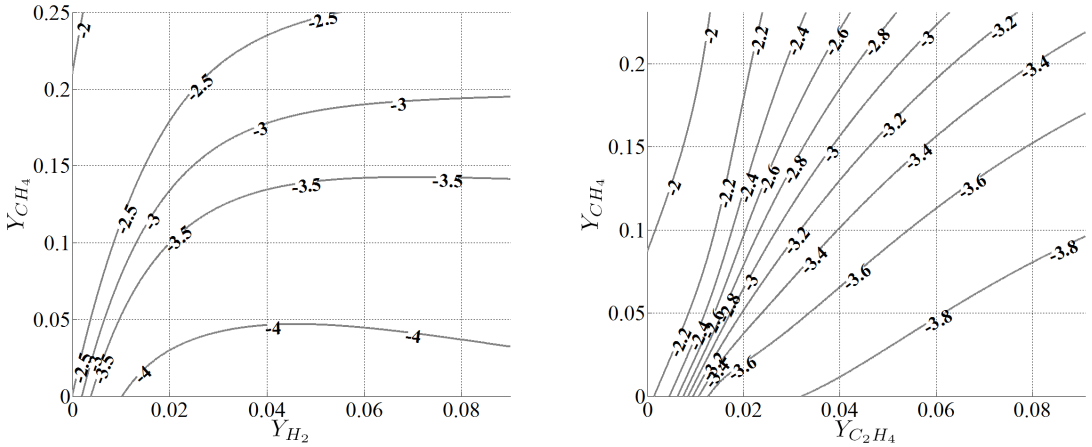

(a) Results for $CH_4 - H_2$, pertaining to Fig. 47(a).

(b) Results for $CH_4 - C_2H_4$, pertaining to Fig. 47(c).

Figure 65: Contour plots ($\log \tau_{ign}$) obtained from the analytic model defined by Eqs. (59)-(63) and (65), using the constant values in Table 15. These maps approximate the ignition delay times reported in Fig. 47.

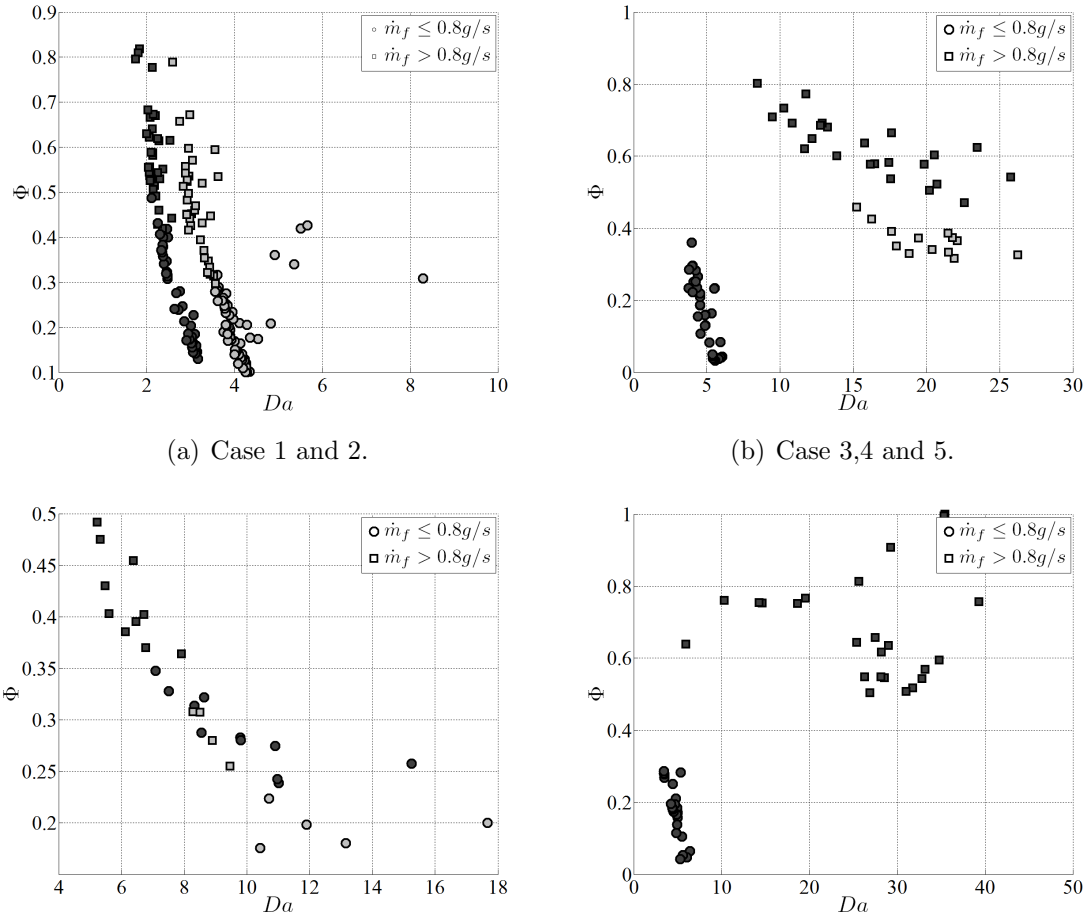

(a) Case 1 and 2.

(b) Case 3,4 and 5.

(c) Case 6 and 7.

(d) Case 8.

Figure 66: Blowout as a function of the equivalence ratio (Φ in Eq. (38)) and the Damkohler number (Da in Eq. (66), where $m_p = 1$ and $m_T = 1$, as used by Rasmussen et al. [81]. The data is obtained with preheat (black) and no preheat (grey).

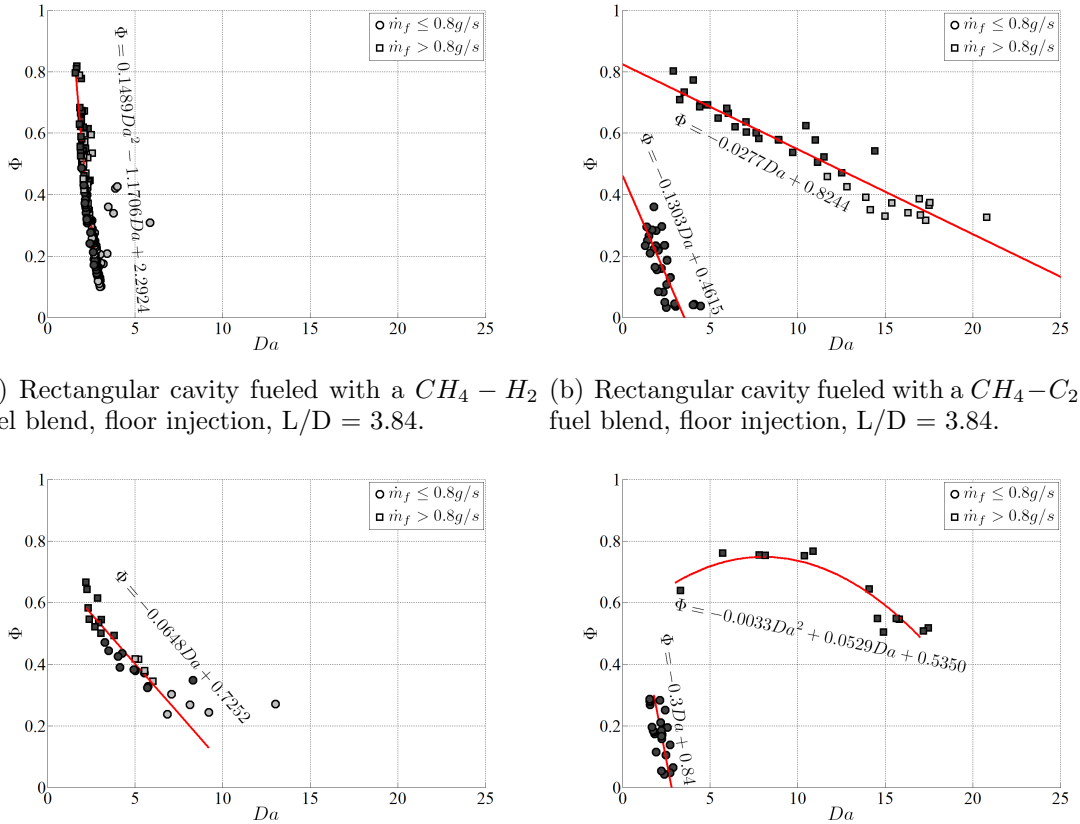

(a) Rectangular cavity fueled with a $CH_4 - H_2$ fuel blend, floor injection, L/D = 3.84.

(b) Rectangular cavity fueled with a $CH_4 - C_2H_4$ fuel blend, floor injection, L/D = 3.84.

(c) Rectangular cavity fueled with a $CH_4 - C_2H_4$ fuel blend, floor injection, L/D = 2.84.

(d) 22.5^o aft cavity fueled with a $CH_4 - C_2H_4$ fuel blend, aft injection, L/D = 3.84.

Figure 67: Blowout as a function of the equivalence ratio (Φ in Eq. (38)) and the Damkohler number (Da in Eq. (66), where m_p and m_T are given in Table 16). The data obtained with preheat (black) and no preheat (grey).

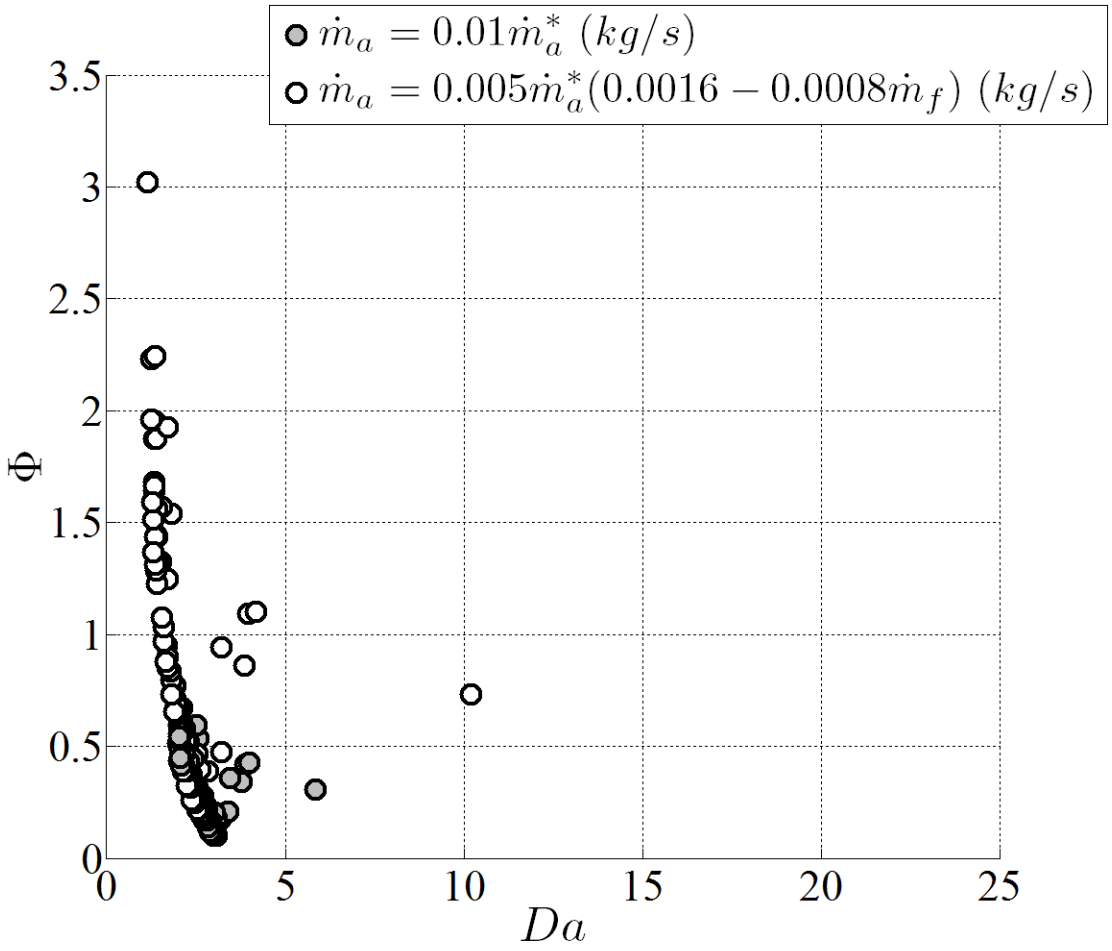

Figure 68: The Blowout data from Case 1 is plotted as a function of the Damkohler number and the equivalence ratio as in Fig. 67(a) except that the computation of the Damkohler number and the equivalence ratio is based on Eq. 67 (white dots) which provides values 2.5 to 3.5 times lower than with Eq. 47 (black dots), and also accounts for some potential fueling effect ($\dot{m}_{f,max} = 1.6$ g/s, $\kappa = 0.5$). The trend is similar between both type computations, however, lowering the air flow rate produces a stretch of the data along the Φ-axis as higher equivalence ratios are reached. The dispersion of the data is also increased, since the data shown in Fig. 69 extends its range under air removal (scaling up).

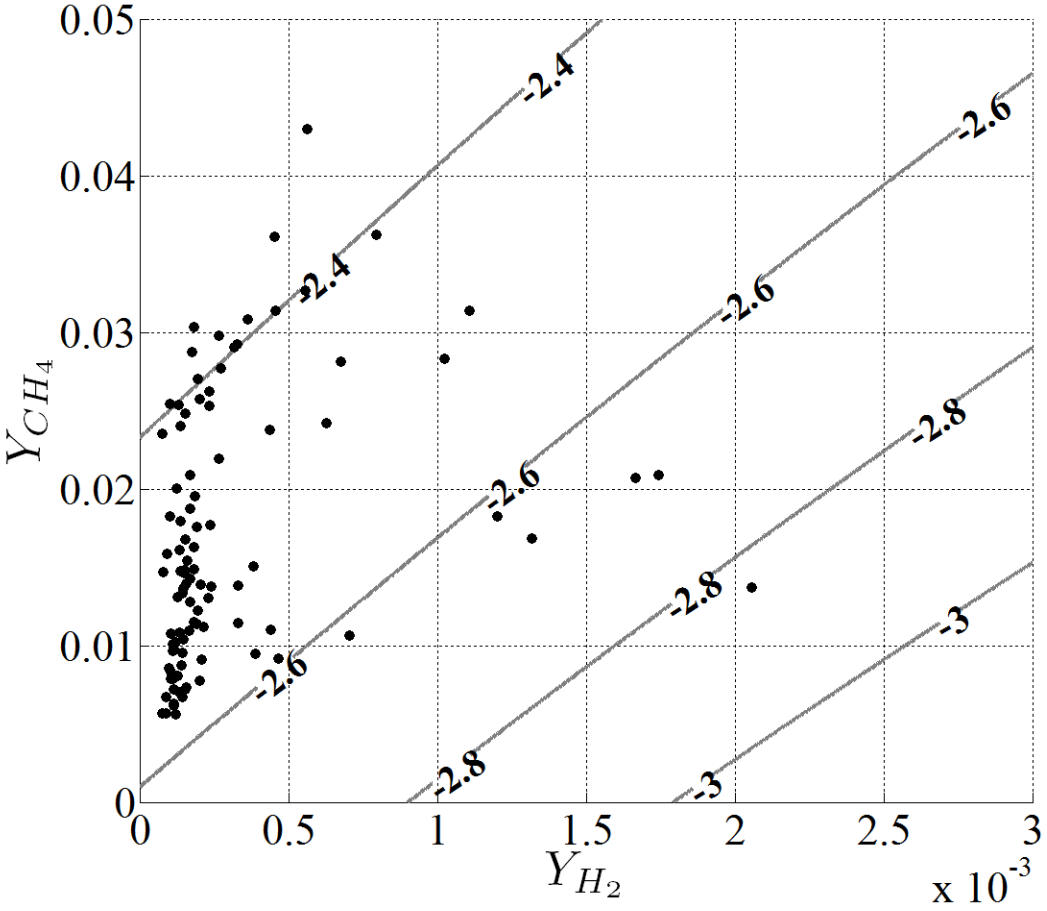

Figure 69: Blowout data from Case 1 plotted on the CH_4-H_2 ignition delay map ($\log(\tau_{ign}$ in s)) in Fig. 65(a). The cavity air flow rate is estimated using Eq. 67 which in turn, provide a relatively lean fuel-air stoichiometry. Therefore, the blowout data points fall into a small region near the origin, such that the resulting range of Damkohler number is limited.

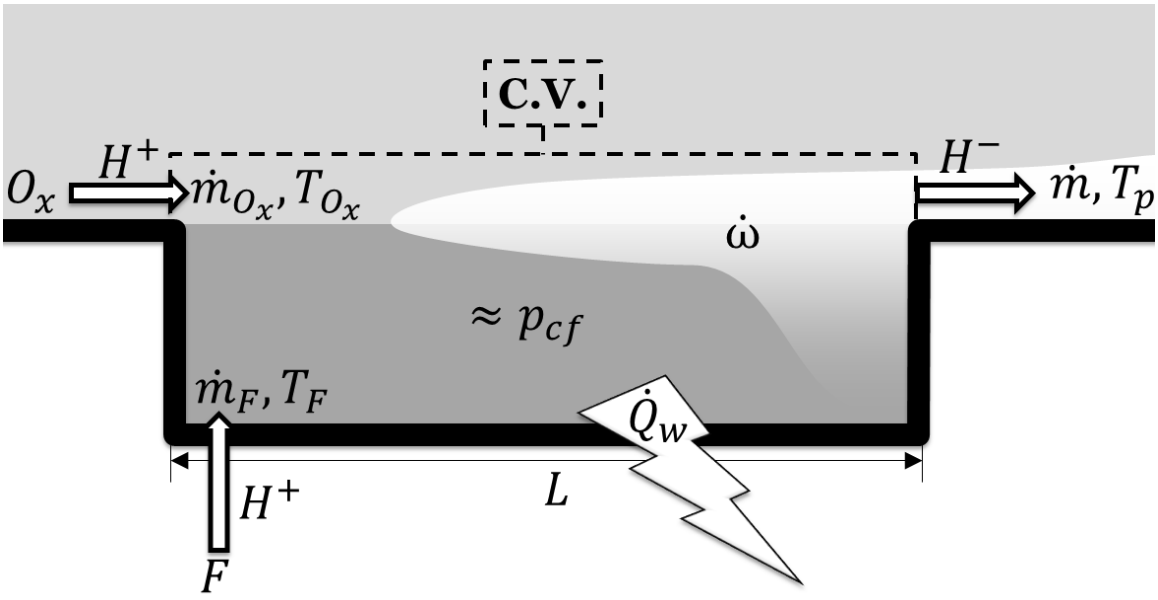

Figure 70: Energy balance on a non-adiabatic cavity at steady state. The air and fuel enter the control volume at temperature $T_{O_x} = T_o$ and T_f, respectively. The reactants undergo a reaction at average rate ω and products are ejected in the downstream boundary layer at temperature T_p. Most the reaction is assumed to take place in a relatively slow region (bottom part of the shear layer). As suggested by the experimental results, the pressure in the combustor at blowout nearly matches the unburn static pressure imposed by the cross-flow.

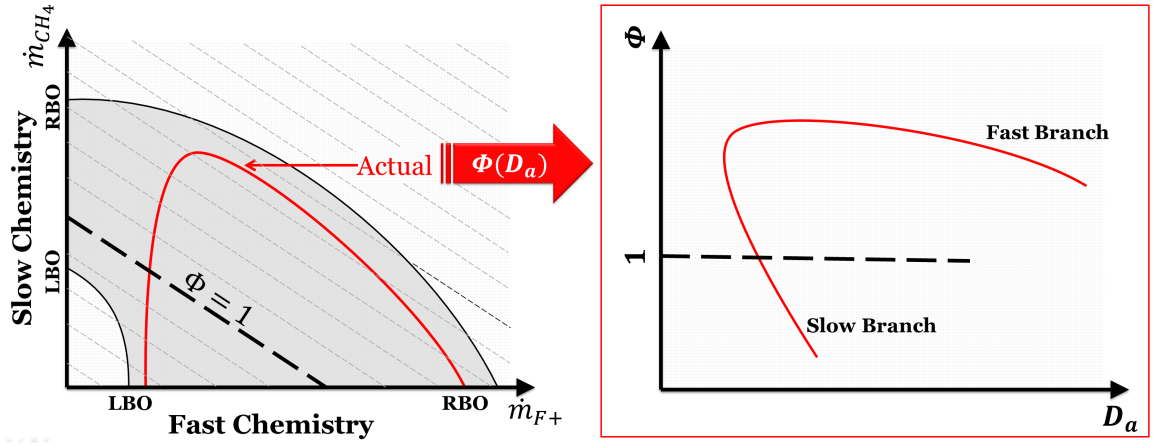

Figure 71: Φ-Da blowout limit trend: The grey shaded area represents the stable combustion domain if this was a plug flow reactor with enough residence time (ideal case). The experiment revealed that blowout still evolves along a lean and a rich contour, as found for the methane-ethylene case. The transformation of the fuel map to a Φ-Da plot may result into the pattern found in Figs. 57 and 66(b).

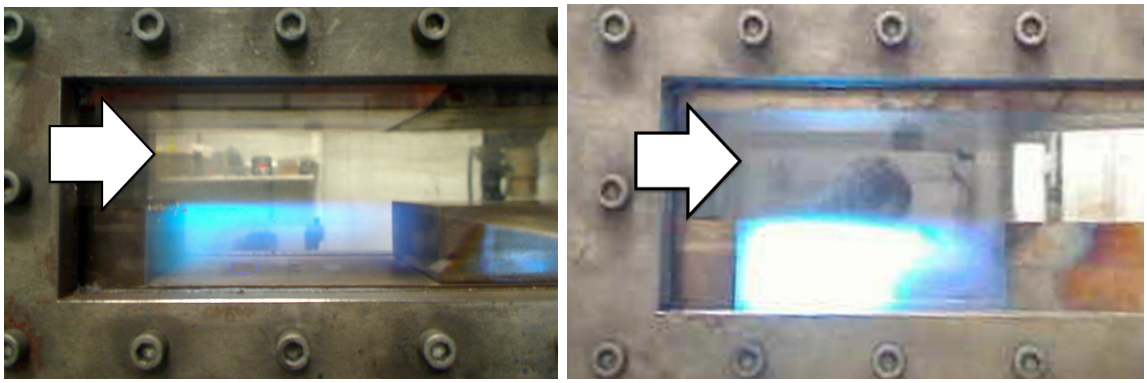

(a) Methane-hydrogen, $\dot{m}_f = 0.42$ g/s (b) Methane-ethylene, $\dot{m}_f = 0.37$ g/s

Figure 72: Rectangular cavity, lean combustion.

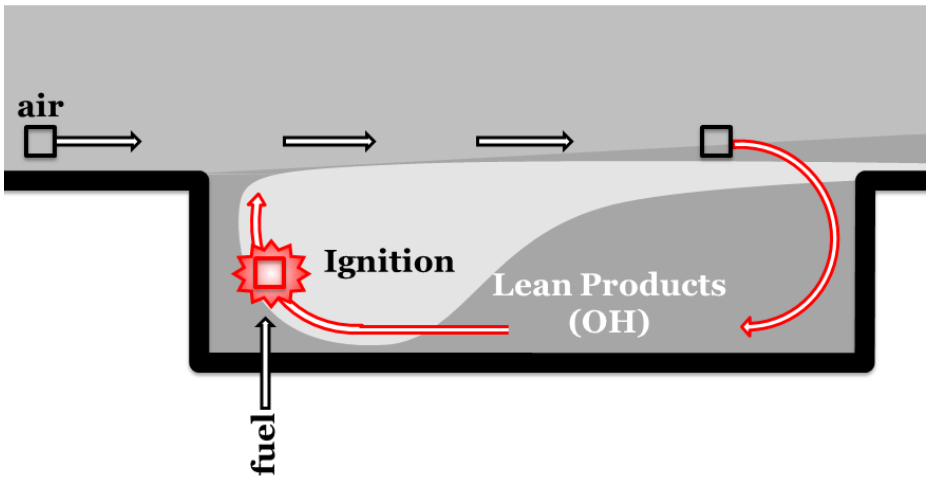

(a) The case with low fuel flow rate benefits from early ignition in the vicinity of the injector array, as hot lean products, such as OH-radicals, are recirculated on the fuel jet with the entrained air. In addition, limited penetration is achieved by the fuel jet and the reaction zone remains contained in the cavity where relatively low speed involved.

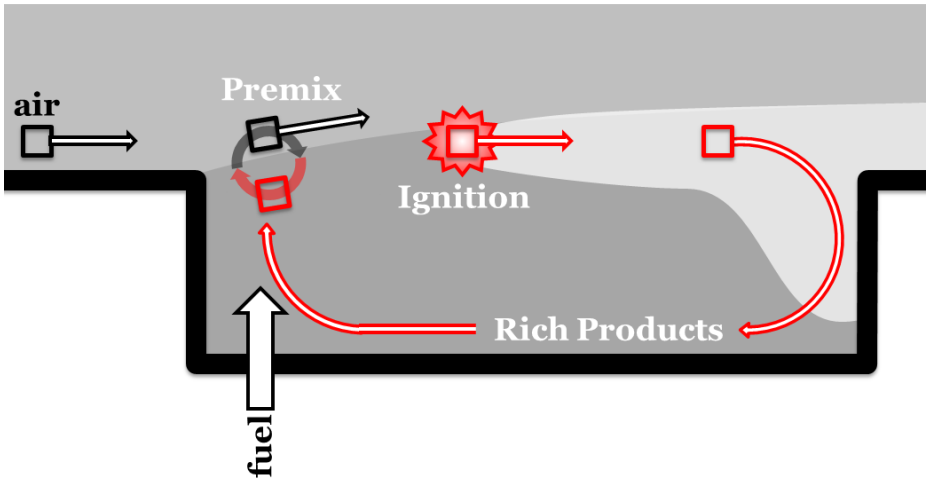

(b) Ignition is reached in the shear layer after the fuel jet and the rich products are mixed with the incoming air, once reaching the leading edge. Consequently, there is a premix region (or lift off) which is visible in Fig. 38(a). The fuel particles may also penetrate deeper into the mixing layer where the velocities are higher (potentially increasing the lift-off region).

Figure 73: Flame location as function of fueling rate in a cavity, with floor injection (from video data and literature [80]).

CHAPTER VI

CONCLUSION AND RECOMMENDATIONS

6.1 Conclusion

Stable and unstable combustion was investigated on a hydrocarbon fueled cavity in a Mach 2.5 cross-flow with a fuel mixture of methane diluted with hydrogen or ethylene. Fuel was injected at the floor or from the aft ramp of the cavity and self-sustained combustion was studied at various cross-flow conditions and for several cavity geometries.

The goal of this study was to provide a better understanding on cavity burning mechanisms, and in particular on the fueling strategy and cross-flow regime which yield a stable burn. A part of the answer is in the study of cavity blowout. The latter is relatively fair to detect due to the drastic changes in the combustor response, and reveals key mechanisms involved in the sustaining of the flame. Therefore the stability of the cavity flame-holder is one important aspect which has been addressed in this study.

The experimental effort started first with the design of a facility for supersonic combustion studies. The set up involves three main systems: the wind tunnel, the combustor and the controls. The wind tunnel delivers a preheated supersonic flow at Mach 2.5 in a 31.8 mm $\times$ 63.5 mm rectangular vessel, with flow rates ranging up to 2.26 kg/s, and for stagnation pressures reaching 2.2 MPa. A gas-fired heat exchanger allows the stagnation temperature to reach 750 K in the vessel. The combustor is seamlessly connected to the nozzle, and has a 25.4 mm-deep recessed cavity inserted between the isolator and the diverging section. The latter is equipped with pressure and temperature sensors, as well as floor and aft ramp injector arrays. The

length has been made variable due to start up issues, and this option has become advantageous in the study of flame-holders with different geometries. The control system includes a digital control panel which runs on Matlab. Real time algorithms have been programmed to record the user actions, identify unsafe regimes and detect ignitions and blowouts. The facility is then used to perform combustion tests with stagnation pressures and temperatures ranging up to 1.4 MPa and 750 K.

The experimental data is reported in fuel maps with respect to cross-flow regime parameters such as the stagnation pressure and temperature. Blowout events are tagged using a post-process routine which also returns the combustor state. Therefore it is possible to characterize pressure, temperature, fueling rate, and composition at each blowout.

Experimental results revealed that fuel composition can play a role in maintaining stable combustion and extending the stable domain. Blowout has been observed over a relatively broad range of fuel flow rate and compositions. The trends found with cavity burning seems to coincide with more fundamental studies on multi-fuels [20]. The blowout region seems to extend continuously from low to high fuel flow rates, however, the fuel-air stoichiometry in the cavity is not accurately known due to the difficulty in modeling the mass entrainment through the mixing layer. The blowout out region forms a horseshoe pattern, below which, lies the stable combustion domain. This study deals with slow chemistry fuel, such as methane, diluted with a fast chemistry fuel (hydrogen or ethylene), and in this particular case, the blowout region can be into a slow branch (blowout with methane dominant fuel mixtures) and a fast branch (blowout with hydrogen or ethylene dominant mixtures). Both branches have been captured with the methane-ethylene data, whereas only the slow branch have been observed with the methane-hydrogen case, due to limitation in the fueling capability, as well as a structural limit on the duration of air-hydrogen combustion for an extended period of time. However, the trends found with the methane-ethylene

case and studies on multi-fuels [96] support the presence of a fast branch for the methane-hydrogen case. The flame position is a strong function of the fueling rate as observed in the video data collected during these experiments and from other studies on cavity flame-holding [84]. The flame has a tendency to shift toward the trailing edge of the cavity with increasing fuel flow rates, this behavior may be caused by a change of the cavity product composition [80], as well as a possible stronger penetration of the fuel into the shear layer (at least for the floor injection case). This phenomenon implies that blowout at low and high fuel flow rate may be driven by different mechanisms. This study on cavities fueled with multi-fuels revealed that the transition of blowout from low to high fuel flow rate is rather continuous. Therefore, blowout may occur at any flame location if it is properly triggered by the chemistry (ignition delay or heat release) and/or the cross-flow conditions (temperature and pressure).

A kinetic study has been carried out to obtain the ignition delay and the heat release maps of the fuel-air mixtures which may exist in the cavity. The results showed that addition of even a small amount of hydrogen greatly influences the ignition delay as it may alter the air-methane combustion mechanism in a more favorable manner. In contrast, ethylene addition to methane has a more gradual effect on the kinetics. Both of these trends are found in the combustor response, and the latter is found to be depending also on the fuel-air stoichiometry. Therefore the scaling of the blowout data may involve kinetic parameters such as the ignition delay from the kinetic study, as well as the fuel-air stoichiometry.

The cross-flow conditions were varied during the test nevertheless, steady state for the measured pressure, temperature and fueling was reached under constant inputs near the blowout region. The pressure and temperature data showed that blowout is also partially governed by the supersonic cross-flow regime. Near blowout, the

pressure drops until the combustor pressure almost coincides with the unburn cross-flow static pressure. The combustion process is barely stable when the static pressure is low, especially when the cross-flow temperature is low. The pressure has been shown to have an important impact, in particular for scramjet studies, where the cross-flow static pressure may reach sub-atmospheric values. In the latter case, the scattering of the blowout data points (lack of repeatability) increases when reducing the cross-flow pressure and eventually forms a low pressure bound, beyond which, no flame can be stabilized in the cavity. That is why in this study, the blowout limit is rather treated as an extended region in which probability of blowout becomes noticeable. The causes of the data dispersion have not been identified precisely, however, it may be related to the unsteadiness introduced by the flow and the combustion reaction instabilities (turbulent combustion), which occur during stable combustion. At low pressure and/or low temperature, self-sustained combustion may become sensitive to unfavorable perturbations of pressure, temperature and mixture. Consequently blowout becomes less controllable, affecting the repeatability of the study.

In contrast, a raise in the temperature of the free stream increases the stability domain, as it provides adequate conditions for the existence of the flame, such as an increased unburn gas temperature and a decrease of the apparent heat losses. In addition, the blowout events become more repeatable (thinning of the blowout region). However there is a weak relation between cross-flow pressure and temperature at blowout, since the highest dispersion is found at the lowest pressures, which also happen to be the coldest blowouts.

Two different cavity aspect ratios (2.84 and 3.84) have been investigated under rich methane-ethylene fueling conditions. The shorter cavity has a smaller stable domain since that "rich" blowout occurs at lower fuel flow rates compared to the longer cavities, as shorter cavity may become prematurely fuel-rich. In addition, the smaller residence time due to a short recirculation length may also contribute to the

limited stability. Cross-flow preheating had a very limited effect on blowout within the tested range, which may be due to the reduced interaction (mass entrainment) between cross-flow and short cavities.

The blowout data collected during this experimental campaign is also compared to the data from other facilities. The lean blowout data agrees with the model defined by Rasmussen et al. [81].

Nevertheless, the latter model does not account for the fuel-air stoichiometry in the calculation of the Damkohler number, whereas the combustor response depends on the fueling rate (and potentially the air flow rate). Therefore, the proposed model accounts for the sensitivity of the fuel-air mixture in the ignition delay time. The latter is deduced from discreet ignition delay maps obtained from the kinetic simulations. It appears that the progressive dilution of methane with a fast heat content fuel additive leads to a decrease of the ignition delay. This is captured by an analytical model defined in this study. The latter is used in the estimation of the Damkohler number. The resulting scaling method preserves the subtleties of the blowout data trend, and a blowout limit model may be extracted from the collapsing of the data on the fast and the slow branches described previously.

However, the actual fuel-air stoichiometry in the cavity is unknown since the mass entrainment is approximated by a model which relies on crude assumptions (free shear layer, no injection). In addition, the sensitivity of the ignition delay calculations on the initial (unburn) temperature is also important, which is primarily due to the Arrhenius form present in the ignition delay formula. To address these issues, a robustness study has been carried out, and the results shows that the scaling preserves the trends, however, the values of the equivalence ratio and Damkholer number remain sensitive to the chosen model parameters for air entrainment and ignition delay. Thus today studies need a better insight on the mass entrainment mechanism while fueling and combustion occur in the cavity.

The last part of this study extends to fundamental mechanisms of cavity flame stabilization. In particular, blowout has been generally approached from a timescale perspective, however the energy is also an important aspect to any combustion problem. Therefore, heat transfer measurements have been carried out in order to estimate the overall cavity wall heat loss. This led to the formulation of a criterion for energy conservation near blowout, which adds to the timescale constraints.

6.2 Recommendations for Future Research

6.2.1 Mass Exchange Measurements

As mentioned in the Introduction chapter, the knowledge of the mass of air entering the cavity remains approximate due to the complexity of the entrainment mechanism, and is needed repeatedly in this study. The models do not account for the presence of the fuel jet nor the effect of combustion, and aeroacoustic feedback. Therefore the series of measurements proposed in this section will help to get quantitative data on the air entrainment from the experimental data.

The time taken by the cavity to purge its content is an essential parameter for the characterization of mass transfer between cavity and cross-flow. This method gives quantitative data based on the knowledge of the mass of tagged flow. The proposed tag is CO_2 which can be traced by absorption measurements. In fact, CO_2 absorption spectrometry has been used in flow and combustion studies [56, 69] for concentration measurements.

6.2.1.1 Principle

Cavities with various shapes may have different response and the formula given by Baurle et al. [11] can be written in a more general manner as

$$\dot{m}_{CO_2} = f(m_{CO_2}) \tag{75}$$

where m_{CO_2} is the mass of tagged CO_2 present in the cavity and f is a real-negative function. This data is essential for the characterization of the scavenging efficiency and the purging time.

Moreover, CO_2 has a noticeable bending mode wavelength (4270nm) which does not overlap with any other species present in ambient air (even wet air), and may be used to seed the cavity flow. Therefore, absorption measurements are carried out in a non-reacting CO_2-fueled cavity, and at stagnation temperatures low enough to avoid CO_2 dissociation. Since the concentration field $[CO_2]$ is not homogeneous in the cavity, a spatial average is needed to get an effective value for m_{CO_2}.

$$m_{CO_2} = \int_V [CO_2] M_{CO_2} dV \approx \int_V [\hat{CO_2}] M_{CO_2} dV \tag{76}$$

where $[\hat{CO_2}]$ is an interpolated map from the measurements points and M_{CO_2} is the CO_2 molar mass.

The function in Eq. (75) can be found from the cavity Heaviside response as follow

1. CO_2 is injected in the cavity at constant mass flow rate until steady state is reached. The mass of CO_2 is estimated using Equation (76).

2. At t_0, the CO_2 supply is shut and the absorption time history is recorded.

3. The CO_2 ejected from the cavity is replaced by the incoming air. The state equation is then used to approximate the mass of air present at $t \to \infty$.

The slope at the origin of $m_{CO_2}(t)$ may be used to estimate the change of CO_2-mass while the injectors are still on. In addition, the mass of entrained air can also be deduced from the steady state CO_2 concentration using the equation of state and the partial pressures. For instance, the maximum CO_2 concentration (approximated by the state equation) is reached if no air penetrates into the cavity (high fueling rate).

However, the concentration of CO_2 decreases as more air is entrained, such that the steady state CO_2 concentration pertains to the entrained air flow rate.

However, this has several drawbacks:

1. the transport of CO_2 does not match the transport of the actual flame products
2. The mixing layer structure is not the same for reacting flows
3. The tests must be carried at lower temperatures

6.2.1.2 Measurement Setup

A series of mid-infrared LED's send beams through the cavity, in the spanwise direction (Figure 74. The beams are intercepted by photoresistors located on the other side. The signal s is then processed to recover the concentration of CO_2 measured at this point.

The calibration of the system is made on the test section with a stagnating flow:

1. **Low Intensity Signal:** The test section is filled up with CO_2 (air is purged through a pressure tap hole), and the lowest intensity signal is measured (s_{min}). The concentration of carbon dioxide $[CO_2]_{max}$ is found using the state equation.
2. **High Intensity Signal (100% transmission):** CO_2 is purged with air, and the highest intensity signal is measured (s_{max}).

The absorption coefficient A for a signal s is then given by

$$\mathbf{A} = 1 - \frac{s - s_{min}}{s_{max} - s_{min}} \tag{77}$$

Since the concentration $[CO_2]$ is proportional of the absorption measured in the cavity

$$[CO_2] = \mathbf{A}\ [CO_2]_{max} \tag{78}$$

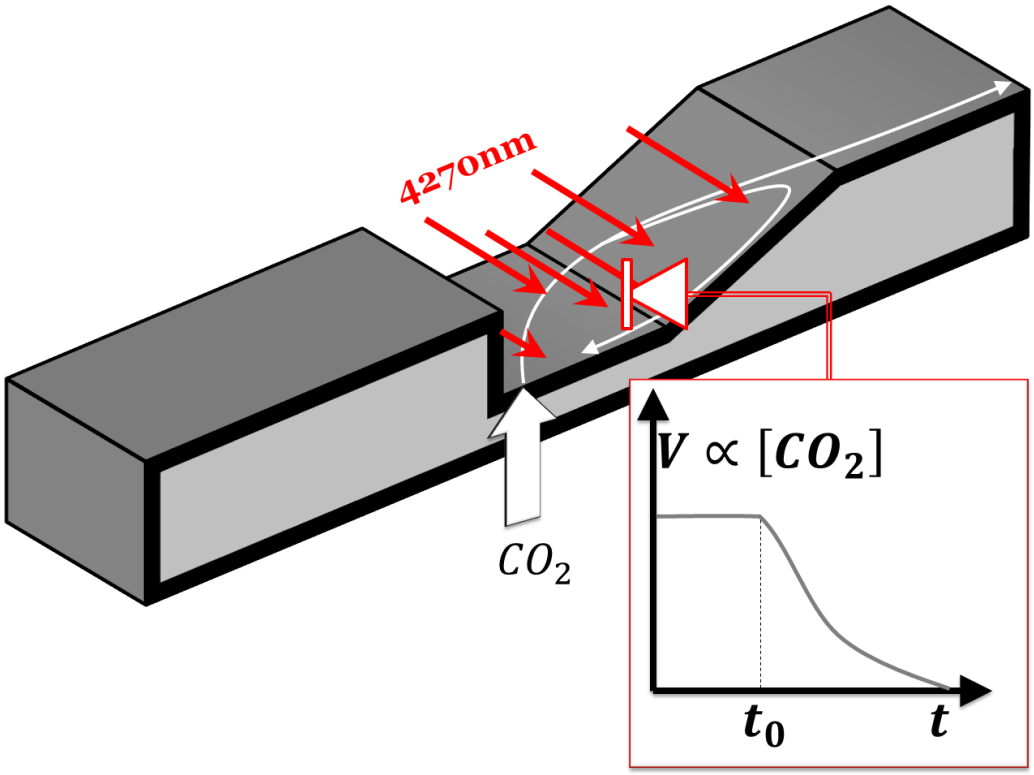

Figure 74: CO_2 absorption measurement setup. A series of LED send beams in the spanwise direction (illustrated by the red arrows) with significant energy in the 4270nm band. The beam is then collected by several photoresistors. The output voltage is proportional to the concentration, as seen in Eq. (78). The mass of tagged flow is then monitored with respect to time.

6.2.2 Raman Scattering Measurements

Raman measurements may be carried out on the current experimental setup to obtain quantitative data on species concentration as a function of the position. The latter reveals the complex species distributions in the cavity, which have been observed by Rasmussen et al. [80], for CH_2O and OH species. Complementary data is required to get a detailed insight on the role of kinetics in the overall flame stabilization mechanism.

The Raman spectroscopy setup is illustrated in Fig. 75. The current test section already has the windows ports modifications for Raman measurements.

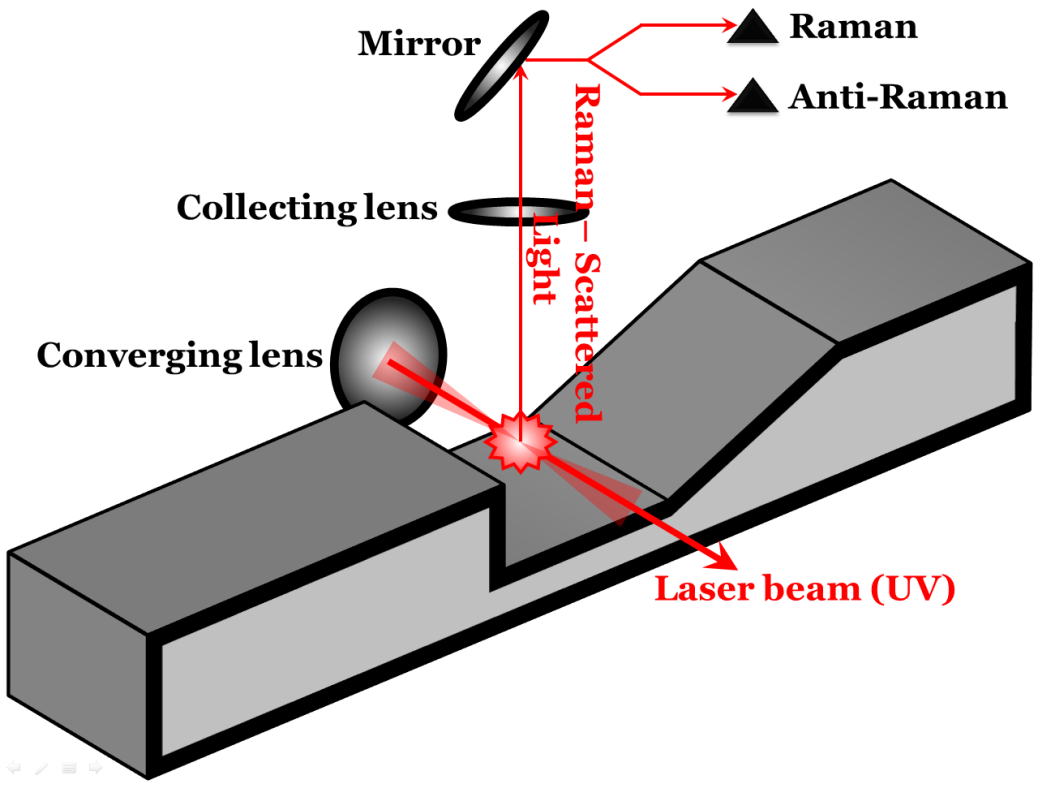

Figure 75: Raman scattering setup. A laser beam (UV) is focused in the cavity where maximum Raman scattering is generated. The scattered light is collected and split-sent to two spectrum analyzers (Stokes and anti-Stokes scattering).

6.2.3 Cavity Enhanced Transverse Injection

The common transverse injection technique uses the post-shock conditions to create a favorable region for flame anchoring. Even with angled injection [64], the stagnation pressure losses are relatively high such that the combustion must be efficient enough to recover from having an intrusive injection technique.

However, the fuel injected in the cross-flow starts a relatively slow pyrolysis given the injection temperature and pressure. A long ignition delay does not lead to efficient combustion, as limited reaction progress is achieved in the engine. Therefore, the proposed design may help to reduce the ignition delay of the primary injection.

Figure 76 shows preliminary CAD design of the injection system. In order to accelerate the reaction process, the reaction is aided by the presence of radicals from

the cavity as in cavity common flame-holder design cases. Except that the primary injection is achieved from the cavity floor, and the products are entrained with the fuel jet, therefore benefiting from a higher penetration factor. To achieve such high fuel flow rates in the cavity, air is bypassed from the aircraft inlet (or settling tank), and the rich limits are extended upon proper fuel-air tuning.

The leading step of the cavity is profiled to yield a particular injection angle (accounting for centripetal forces from flow turning). The aft ramp may also be profiled to minimize the re-compression shock commonly observed at the aft edge of rectangular cavities. A moving ramp may also give the possibility to adapt the diverging section on the heat release in the cross-flow.

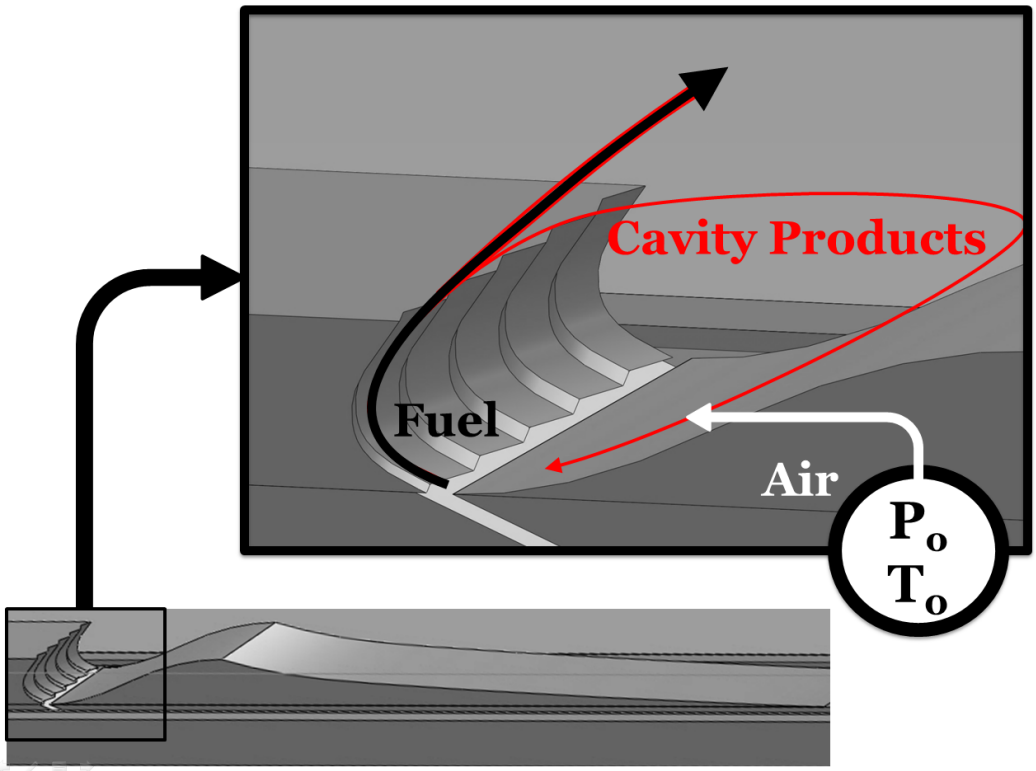

Figure 76: Cavity enhanced transverse injection. The cavity products are entrained by the fuel jet and penetrate the cross-flow. Early fuel breaking accelerates the reaction, and ignition occurs within a shorter distance than for a regular direct injection. To reach such high fuel flow rates, the cavity is also fueled with air bypassed from the diffuser. The triangular steps on the leading edge are designed to produce streamwise vorticity for mixing enhancement [30]. The aft ramp is profiled to reduce the stagnation pressure loss which may occur at the shear layer re-attachment point.

APPENDIX A

MACH 2.5 NOZZLE CONTOUR

Table 17: Coordinates for M=2.5 nozzle profile design, with boundary layer correction.

X	Y	X	Y	X	Y	X	Y	X	Y
-55.5427	26.854	-33.1012	12.704	-10.6597	6.598	0.2896	5.919	0.6276	5.920
-54.9817	26.365	-32.5402	12.466	-10.0987	6.529	0.2998	5.919	0.6351	5.920
-54.4206	25.885	-31.9791	12.234	-9.5376	6.463	0.3097	5.919	0.6426	5.920
-53.8596	25.414	-31.4181	12.005	-8.9766	6.401	0.3194	5.919	0.6502	5.920
-53.2985	24.951	-30.8570	11.782	-8.4156	6.342	0.3288	5.919	0.6578	5.920
-52.7375	24.495	-30.2960	11.563	-7.8545	6.288	0.3381	5.919	0.6655	5.920
-52.1765	24.048	-29.7350	11.349	-7.2935	6.237	0.3473	5.920	0.6729	5.920
-51.6154	23.609	-29.1739	11.139	-6.7324	6.190	0.3565	5.920	0.6804	5.920
-51.0544	23.177	-28.6129	10.934	-6.1714	6.147	0.3657	5.920	0.6879	5.920
-50.4934	22.752	-28.0519	10.734	-5.6104	6.108	0.3748	5.919	0.6955	5.920
-49.9323	22.335	-27.4908	10.537	-5.0493	6.072	0.3838	5.919	0.7031	5.920
-49.3713	21.925	-26.9298	10.346	-4.4883	6.040	0.3926	5.919	0.7104	5.920
-48.8102	21.522	-26.3688	10.158	-3.9273	6.012	0.4014	5.919	0.7179	5.920
-48.2492	21.126	-25.8077	9.976	-3.3662	5.988	0.4102	5.919	0.7253	5.920
-47.6882	20.737	-25.2467	9.797	-2.8052	5.967	0.4188	5.919	0.7328	5.920
-47.1271	20.354	-24.6856	9.623	-2.2441	5.950	0.4275	5.919	0.7404	5.920
-46.5661	19.978	-24.1246	9.453	-1.6831	5.937	0.4359	5.919	0.7477	5.920
-46.0051	19.609	-23.5636	9.287	-1.1221	5.928	0.4443	5.919	0.7551	5.920
-45.4440	19.246	-23.0025	9.125	-0.5610	5.922	0.4526	5.919	0.7625	5.920
-44.8830	18.889	-22.4415	8.968	0	5.921	0.4610	5.919	0.7700	5.920
-44.3219	18.538	-21.8805	8.815	0	5.921	0.4694	5.919	0.7775	5.920
-43.7609	18.194	-21.3194	8.666	0.0077	5.920	0.4776	5.920	0.7847	5.920
-43.1999	17.855	-20.7584	8.521	0.0167	5.919	0.4859	5.920	0.7920	5.920
-42.6388	17.522	-20.1973	8.380	0.0278	5.919	0.4941	5.920	0.7994	5.921
-42.0778	17.196	-19.6363	8.244	0.0418	5.919	0.5023	5.920	0.8068	5.921
-41.5168	16.875	-19.0753	8.111	0.0589	5.919	0.5105	5.919	0.8143	5.921
-40.9557	16.559	-18.5142	7.982	0.0802	5.919	0.5185	5.919	0.8216	5.921
-40.3947	16.249	-17.9532	7.858	0.1034	5.919	0.5264	5.919	0.8289	5.921
-39.8336	15.945	-17.3922	7.737	0.1274	5.919	0.5343	5.919	0.8363	5.921
-39.2726	15.646	-16.8311	7.621	0.1508	5.919	0.5422	5.919	0.8439	5.921
-38.7116	15.353	-16.2701	7.508	0.1722	5.919	0.5502	5.919	0.8514	5.922
-38.1505	15.065	-15.7090	7.400	0.1893	5.919	0.5579	5.919	0.8587	5.922
-37.5895	14.782	-15.1480	7.295	0.2035	5.919	0.5657	5.919	0.8660	5.922
-37.0285	14.505	-14.5870	7.194	0.2154	5.919	0.5735	5.919	0.8733	5.922
-36.4674	14.233	-14.0259	7.098	0.2256	5.919	0.5814	5.919	0.8808	5.922
-35.9064	13.965	-13.4649	7.005	0.2349	5.919	0.5893	5.919	0.8882	5.922
-35.3453	13.703	-12.9039	6.916	0.2454	5.919	0.5969	5.919	0.8954	5.922
-34.7843	13.446	-12.3428	6.831	0.2562	5.919	0.6045	5.919	0.9027	5.922
-34.2233	13.194	-11.7818	6.749	0.2672	5.919	0.6122	5.919	0.9101	5.922
-33.6622	12.946	-11.2207	6.672	0.2784	5.919	0.6199	5.919	0.9177	5.923

Table 18: Coordinates for M=2.5 nozzle profile design (continued).

X	Y	X	Y	X	Y	X	Y	X	Y
0.9253	5.9227	1.1882	5.9303	1.5095	5.9466	1.8689	5.9763	2.2835	6.0256
0.9326	5.9229	1.1957	5.9307	1.5178	5.9472	1.8782	5.9773	2.2943	6.0274
0.9400	5.9231	1.2033	5.931	1.5262	5.9477	1.8877	5.9782	2.3054	6.0292
0.9474	5.9232	1.2110	5.9313	1.5347	5.9483	1.8974	5.9792	2.3168	6.0307
0.9549	5.9234	1.2188	5.9316	1.5434	5.9489	1.9073	5.9802	2.3285	6.0323
0.9622	5.9235	1.2268	5.9319	1.5522	5.9494	1.9174	5.9812	2.3404	6.0339
0.9691	5.9236	1.2344	5.9322	1.5605	5.9499	1.9269	5.9822	2.3515	6.0355
0.9754	5.9238	1.2421	5.9325	1.5689	5.9504	1.9365	5.9831	2.3628	6.0373
0.9809	5.9239	1.2499	5.9328	1.5774	5.9509	1.9464	5.9842	2.3743	6.0391
0.9855	5.9239	1.2579	5.9331	1.5862	5.9514	1.9565	5.9852	2.3862	6.041
0.9891	5.924	1.2659	5.9334	1.5951	5.952	1.9667	5.9863	2.3983	6.0428
0.9908	5.924	1.2736	5.9336	1.6036	5.9526	1.9763	5.9873	2.4096	6.0446
0.9921	5.9241	1.2813	5.9339	1.6121	5.9532	1.9861	5.9884	2.4212	6.0464
0.9935	5.9241	1.2892	5.9342	1.6210	5.9539	1.9961	5.9895	2.4331	6.0482
0.9958	5.9242	1.2972	5.9344	1.6299	5.9546	2.0063	5.9907	2.4452	6.05
0.9992	5.9243	1.3053	5.9347	1.6391	5.9552	2.0168	5.9918	2.4575	6.0518
1.0045	5.9245	1.3131	5.9351	1.6476	5.9559	2.0266	5.993	2.4689	6.0537
1.0111	5.9248	1.3209	5.9354	1.6563	5.9566	2.0366	5.9941	2.4805	6.0556
1.0190	5.925	1.3289	5.9359	1.6652	5.9573	2.0468	5.9953	2.4926	6.0575
1.0276	5.9253	1.3370	5.9363	1.6743	5.9581	2.0574	5.9965	2.5052	6.0596
1.0366	5.9255	1.3452	5.9367	1.6835	5.9589	2.0681	5.9977	2.5182	6.0617
1.0445	5.9257	1.3529	5.9372	1.6922	5.9597	2.0781	5.9989	2.5304	6.0638
1.0521	5.9259	1.3607	5.9376	1.7010	5.9606	2.0883	6.0001	2.5428	6.066
1.0596	5.926	1.3687	5.9381	1.7101	5.9614	2.0988	6.0014	2.5555	6.0681
1.0669	5.9262	1.3770	5.9385	1.7193	5.9623	2.1095	6.0027	2.5681	6.0702
1.0742	5.9263	1.3856	5.939	1.7287	5.9631	2.1204	6.0041	2.5804	6.0722
1.0814	5.9264	1.3939	5.9394	1.7376	5.9638	2.1306	6.0056	2.5914	6.074
1.0887	5.9266	1.4024	5.9399	1.7466	5.9645	2.1410	6.007	2.6014	6.0757
1.0962	5.9267	1.4110	5.9403	1.7557	5.9652	2.1517	6.0083	2.6102	6.0771
1.1039	5.9269	1.4196	5.9408	1.7651	5.966	2.1626	6.0096	2.6176	6.0783
1.1118	5.9271	1.4282	5.9413	1.7747	5.9668	2.1737	6.0106	2.6236	6.0792
1.1191	5.9273	1.4360	5.9418	1.7837	5.9676	2.1841	6.0116	2.6265	6.0799
1.1266	5.9276	1.4438	5.9424	1.7928	5.9685	2.1948	6.0125	2.6291	6.0806
1.1343	5.9279	1.4516	5.943	1.8022	5.9695	2.2056	6.0134	2.6323	6.0813
1.1420	5.9283	1.4595	5.9435	1.8117	5.9705	2.2168	6.0145	2.6369	6.0822
1.1499	5.9286	1.4676	5.9441	1.8214	5.9715	2.2281	6.0159	2.6436	6.0835
1.1573	5.9289	1.4755	5.9446	1.8306	5.9725	2.2387	6.0175	2.6529	6.0851
1.1649	5.9293	1.4836	5.9451	1.8398	5.9735	2.2495	6.0194	2.6645	6.087
1.1725	5.9297	1.4920	5.9456	1.8493	5.9744	2.2605	6.0215	2.6781	6.0893
1.1803	5.93	1.5007	5.9461	1.8591	5.9754	2.2719	6.0236	2.6931	6.0918

Table 19: Coordinates for M=2.5 nozzle profile design (continued).

X	Y	X	Y	X	Y	X	Y	X	Y
2.7087	6.0944	3.2908	6.218	3.9131	6.3838	4.6078	6.6067	7.5380	7.6432
2.7222	6.097	3.3085	6.2222	3.9349	6.3901	4.6042	6.6076	7.6081	7.6682
2.7356	6.0996	3.3262	6.2263	3.9566	6.3963	4.6047	6.6098	7.6784	7.693
2.7488	6.1021	3.3432	6.2302	3.9774	6.4022	4.6143	6.6147	7.7491	7.7178
2.7620	6.1046	3.3589	6.2337	3.9964	6.4075	4.6375	6.6243	7.8202	7.7424
2.7752	6.1072	3.3726	6.2367	4.0127	6.412	4.6777	6.6396	7.8915	7.7669
2.7881	6.1097	3.3818	6.2393	4.0232	6.4156	4.7393	6.6608	7.9600	7.7913
2.8013	6.1123	3.3891	6.2413	4.0313	6.4185	4.8176	6.6876	8.0287	7.8156
2.8150	6.1149	3.3951	6.243	4.0378	6.4207	4.9093	6.719	8.0981	7.8398
2.8291	6.1176	3.4006	6.2445	4.0440	6.4229	5.0099	6.753	8.1680	7.864
2.8435	6.1204	3.4064	6.246	4.0508	6.4252	5.1145	6.7881	8.2382	7.888
2.8569	6.1231	3.4125	6.2477	4.0585	6.4279	5.2119	6.8231	8.3055	7.912
2.8705	6.1259	3.4202	6.2497	4.0686	6.4312	5.3071	6.8571	8.3733	7.9359
2.8844	6.1288	3.4300	6.2522	4.0815	6.4352	5.3994	6.8896	8.4417	7.9598
2.8988	6.1317	3.4422	6.2551	4.0971	6.4398	5.4891	6.9211	8.5108	7.9835
2.9134	6.1346	3.4564	6.2585	4.1153	6.4451	5.5768	6.9516	8.5804	8.0071
2.9271	6.1375	3.4711	6.2623	4.1336	6.451	5.6636	6.9814	8.6470	8.0307
2.9410	6.1404	3.4873	6.2665	4.1536	6.4573	5.7498	7.0109	8.7141	8.0542
2.9553	6.1433	3.5050	6.2711	4.1751	6.4639	5.8359	7.0402	8.7819	8.0776
2.9700	6.1463	3.5235	6.2757	4.1977	6.4709	5.9219	7.0696	8.8506	8.1009
2.9850	6.1493	3.5425	6.2805	4.2207	6.478	6.0076	7.099	8.9197	8.1243
2.9990	6.1523	3.5600	6.2853	4.2424	6.4852	6.0897	7.1286	8.9858	8.1475
3.0133	6.1554	3.5776	6.29	4.2641	6.4924	6.1715	7.1583	9.0523	8.1707
3.0280	6.1585	3.5953	6.2947	4.2859	6.4995	6.2532	7.188	9.1197	8.1939
3.0430	6.1616	3.6133	6.2993	4.3078	6.5063	6.3347	7.2174	9.1880	8.217
3.0584	6.1648	3.6314	6.304	4.3299	6.5129	6.4158	7.2464	9.2568	8.24
3.0728	6.168	3.6487	6.3087	4.3502	6.5194	6.4936	7.2748	9.3224	8.263
3.0875	6.1712	3.6664	6.3136	4.3713	6.5259	6.5710	7.3027	9.3887	8.2859
3.1026	6.1744	3.6846	6.3185	4.3936	6.5328	6.6482	7.33	9.4558	8.3088
3.1181	6.1777	3.7034	6.3235	4.4173	6.54	6.7254	7.357	9.5240	8.3316
3.1339	6.1811	3.7226	6.3287	4.4422	6.5479	6.8024	7.3837	9.5928	8.3543
3.1488	6.1845	3.7408	6.334	4.4660	6.5562	6.8766	7.4103	9.6585	8.3771
3.1641	6.188	3.7593	6.3394	4.4901	6.5648	6.9509	7.4368	9.7248	8.3998
3.1796	6.1916	3.7781	6.3448	4.5141	6.5734	7.0254	7.4632	9.7921	8.4226
3.1953	6.1952	3.7972	6.3502	4.5371	6.5816	7.1001	7.4895	9.8604	8.4454
3.2113	6.1988	3.8166	6.3556	4.5580	6.5891	7.1750	7.5156	9.9294	8.4682
3.2257	6.2024	3.8341	6.361	4.5757	6.5954	7.2471	7.5415	9.9949	8.491
3.2407	6.2061	3.8522	6.3664	4.5896	6.6004	7.3194	7.5672	10.0611	8.5139
3.2565	6.2099	3.8713	6.3719	4.5992	6.6039	7.3920	7.5927	10.1283	8.5367
3.2732	6.2139	3.8917	6.3777	4.6049	6.6058	7.4649	7.618	10.1966	8.5594

Table 20: Coordinates for M=2.5 nozzle profile design (continued).

X	Y	X	Y	X	Y	X	Y	X	Y
10.266	8.582	13.067	9.491	16.276	10.448	20.179	11.482	25.126	12.596
10.331	8.605	13.139	9.514	16.361	10.473	20.285	11.509	25.262	12.624
10.398	8.627	13.212	9.537	16.447	10.498	20.392	11.536	25.402	12.653
10.466	8.650	13.287	9.561	16.536	10.523	20.503	11.563	25.545	12.681
10.534	8.672	13.363	9.584	16.627	10.548	20.616	11.590	25.691	12.709
10.604	8.695	13.441	9.607	16.719	10.573	20.732	11.617	25.840	12.738
10.670	8.717	13.514	9.631	16.806	10.598	20.840	11.644	25.982	12.767
10.736	8.740	13.588	9.654	16.895	10.623	20.951	11.672	26.126	12.796
10.804	8.762	13.664	9.678	16.986	10.648	21.065	11.699	26.273	12.825
10.873	8.785	13.741	9.701	17.080	10.673	21.182	11.726	26.425	12.854
10.943	8.807	13.820	9.724	17.175	10.699	21.301	11.753	26.579	12.884
11.010	8.830	13.894	9.748	17.264	10.724	21.413	11.781	26.725	12.913
11.077	8.853	13.970	9.772	17.355	10.750	21.528	11.808	26.874	12.942
11.146	8.875	14.048	9.795	17.448	10.775	21.646	11.836	27.027	12.971
11.216	8.898	14.127	9.819	17.544	10.801	21.766	11.863	27.184	13.000
11.287	8.920	14.208	9.842	17.641	10.826	21.889	11.891	27.344	13.029
11.354	8.943	14.284	9.866	17.733	10.852	22.005	11.919	27.495	13.058
11.422	8.966	14.361	9.889	17.826	10.877	22.123	11.946	27.649	13.087
11.492	8.988	14.440	9.913	17.922	10.903	22.245	11.974	27.808	13.116
11.562	9.011	14.521	9.937	18.021	10.929	22.369	12.002	27.970	13.145
11.634	9.034	14.604	9.961	18.121	10.955	22.495	12.030	28.136	13.174
11.701	9.057	14.681	9.985	18.215	10.981	22.615	12.058	28.293	13.204
11.770	9.079	14.760	10.009	18.311	11.007	22.737	12.086	28.453	13.233
11.840	9.102	14.841	10.033	18.410	11.033	22.862	12.114	28.617	13.262
11.912	9.125	14.923	10.057	18.511	11.059	22.990	12.142	28.785	13.291
11.984	9.147	15.007	10.081	18.613	11.085	23.121	12.170	28.957	13.320
12.053	9.170	15.086	10.106	18.710	11.111	23.245	12.198	29.119	13.349
12.123	9.193	15.167	10.130	18.809	11.137	23.371	12.226	29.285	13.378
12.194	9.216	15.250	10.154	18.911	11.163	23.500	12.255	29.455	13.407
12.266	9.239	15.334	10.178	19.015	11.189	23.633	12.283	29.629	13.436
12.340	9.262	15.420	10.203	19.120	11.216	23.768	12.311	29.807	13.465
12.410	9.284	15.501	10.227	19.220	11.242	23.895	12.339	29.976	13.495
12.480	9.307	15.584	10.251	19.322	11.269	24.026	12.368	30.148	13.524
12.552	9.330	15.668	10.276	19.426	11.295	24.159	12.396	30.324	13.553
12.626	9.353	15.755	10.300	19.533	11.322	24.296	12.425	30.505	13.582
12.701	9.376	15.843	10.325	19.642	11.348	24.436	12.453	30.690	13.611
12.771	9.399	15.926	10.350	19.745	11.375	24.568	12.482	30.865	13.640
12.843	9.422	16.010	10.374	19.849	11.402	24.702	12.511	31.043	13.669
12.916	9.445	16.097	10.399	19.957	11.428	24.840	12.539	31.226	13.698
12.991	9.468	16.186	10.424	20.067	11.455	24.982	12.568	31.414	13.727

Table 21: Coordinates for M=2.5 nozzle profile design (continued).

X	Y	X	Y	X	Y
31.6047	13.7564	40.3423	14.8639	52.4667	15.6933
31.7863	13.7852	40.5916	14.8893	52.8186	15.7070
31.9716	13.8140	40.8457	14.9146	53.1775	15.7203
32.1616	13.8427	41.1061	14.9398	53.5450	15.7332
32.3564	13.8714	41.3726	14.9648	53.9213	15.7456
32.5549	13.9000	41.6441	14.9896	54.3044	15.7575
32.7437	13.9288	41.9029	15.0142	54.6719	15.7689
32.9362	13.9575	42.1667	15.0386	55.0462	15.7798
33.1336	13.9862	42.4372	15.0629	55.4294	15.7902
33.3359	14.0150	42.7145	15.0869	55.8216	15.8001
33.5420	14.0437	42.9974	15.1106	56.2214	15.8094
33.7380	14.0723	43.2683	15.1341	56.6056	15.8182
33.9378	14.1009	43.5448	15.1574	56.9979	15.8263
34.1427	14.1294	43.8283	15.1804	57.4002	15.8338
34.3526	14.1578	44.1186	15.2031	57.8127	15.8406
34.5666	14.1861	44.4142	15.2257	58.2336	15.8466
34.7703	14.2144	44.6962	15.2481	58.6387	15.8520
34.9781	14.2425	44.9836	15.2701	59.0514	15.8568
35.1912	14.2706	45.2779	15.2920	59.4729	15.8611
35.4096	14.2987	45.5793	15.3137	59.9023	15.8651
35.6321	14.3266	45.8866	15.3351	60.3369	15.8689
35.8441	14.3544	46.1810	15.3562	60.7512	15.8727
36.0603	14.3822	46.4814	15.3771	61.1685	15.8767
36.2819	14.4099	46.7894	15.3977	61.5899	15.8797
36.5089	14.4375	47.1050	15.4180	62.0148	15.8853
36.7403	14.4649	47.4266	15.4379		
36.9608	14.4923	47.7343	15.4575		
37.1856	14.5196	48.0481	15.4768		
37.4160	14.5468	48.3694	15.4958		
37.6521	14.5739	48.6985	15.5144		
37.8927	14.6008	49.0339	15.5326		
38.1222	14.6277	49.3553	15.5504		
38.3563	14.6545	49.6830	15.5679		
38.5962	14.6811	50.0186	15.5849		
38.8421	14.7077	50.3624	15.6016		
39.0926	14.7341	50.7126	15.6179		
39.3316	14.7604	51.0481	15.6338		
39.5754	14.7865	51.3903	15.6493		
39.8252	14.8124	51.7410	15.6644		
40.0813	14.8382	52.1003	15.6790		

APPENDIX B

CAPABILITY SUMMARY

Table 22: Current capability of the GT Scramjet facility.

Wind Tunnel	
Run time	27 - 45 min
Pre-heated air flow	300 - 750 ^oK
Stagnation Pressure	0.1 - 2.2 MPa
Air mass flow rate	0.7 - 2.26 kg/s (heated) and 3.2 kg/s (non-heated)
Embedded nozzle	Mach 2.5, boundary layer compensated.
Combustor	
Fuel	C_2H_6,C_2H_4,CH_4,H_2 and liquid fuel.
Injection Location	Leading edge, floor and aft ramp.
Instrumentation	Pressure, temperature, flow rate and Schlieren.
Cavity	Variable L/D from 0 to 5
Blow Down System	
Air Storage	16.7 m^3 at 19 MPa
Heater	810 ^oK
Delivery	Ambient or preheated at 2.2 MPa
Flow Control	
Air	Separate control panel for the 2.2 MPa line.
Fuel	Separate control panel for gross back pressure adjustments. Volumetric flow controllers for refined target.
DAQ	
Analog Channels	24 inputs and 4 outputs
Digital Channels	48 input/output
AD Conversion	250 kS/s multiplexed, 16 bits
DA Conversion	863 kHz, multiplexed
Main CPU	2.4 GHz quad core, 1024 FSB
RAM	3Gb, 800 MHz
Short Term Storage	320 Gb hard drive
Digital Control Panel	
Switches	24 Configurable touch sensors.
Control	Recorded user actions. Safety procedures.
Relay Box	Relays driven by TTL signals.
Feeding Voltages	5VDC, 12 VDC, 24 VDC and 110 VAC

APPENDIX C

IGNITION DELAY MAPS

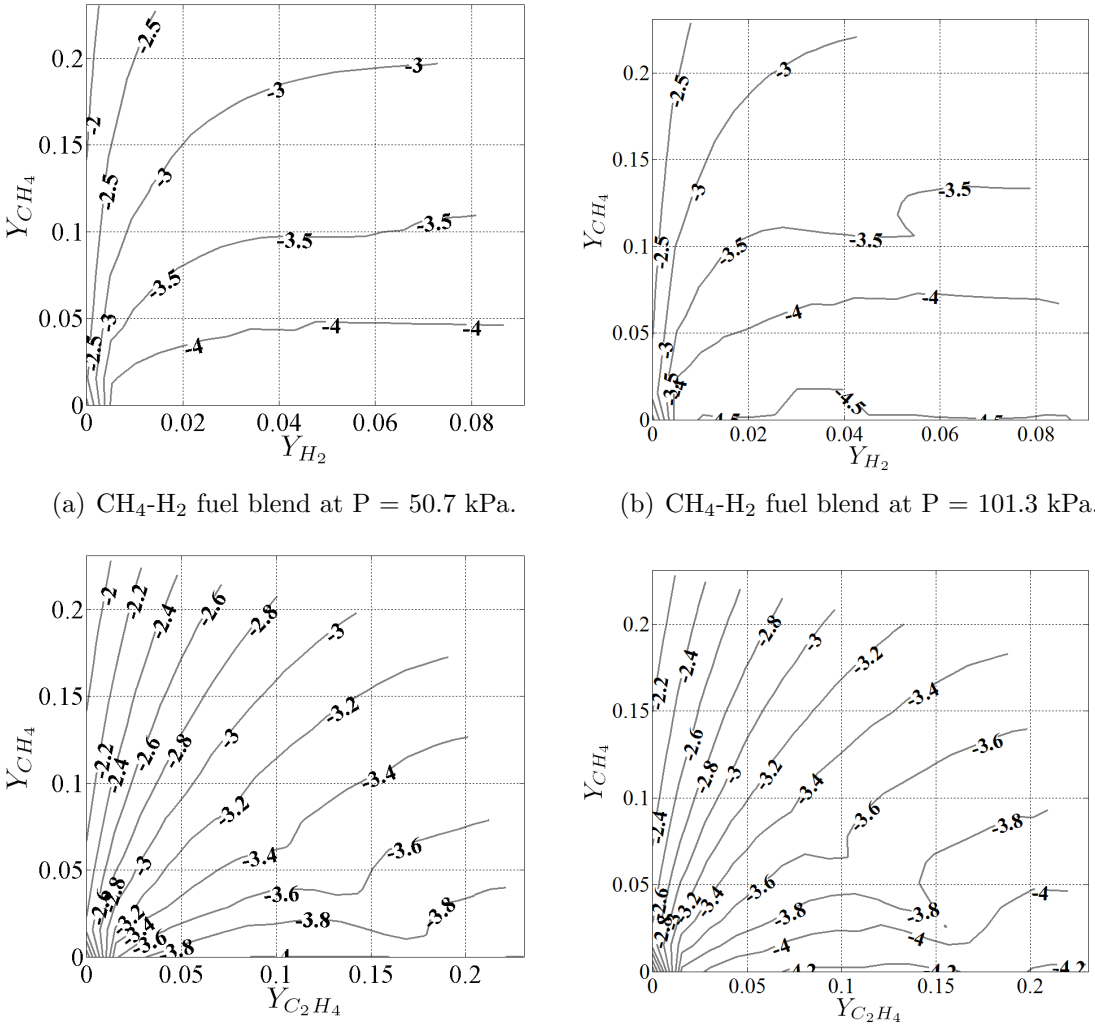

(a) CH_4-H_2 fuel blend at P = 50.7 kPa.

(b) CH_4-H_2 fuel blend at P = 101.3 kPa.

(c) CH_4-C_2H_4 fuel blend at P = 50.7 kPa.

(d) CH_4-C_2H_4 fuel blend at P = 101.3 kPa.

Figure 77: Ignition delays maps ($\log(\tau_{ign})$) in s, with an intial mixture temperature of 1400 ^{o}K.

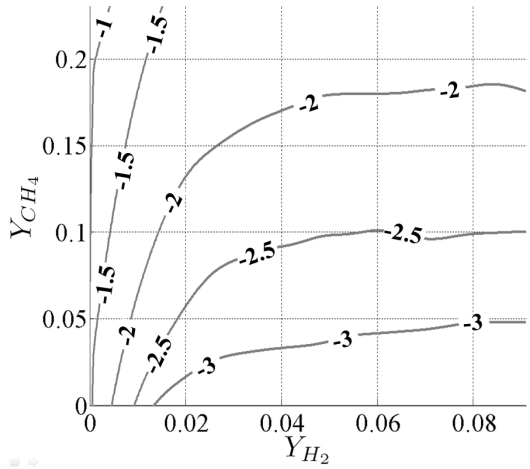

(a) CH_4-H_2 fuel blend with an intial mixture temperature of 1000 ^{o}K.

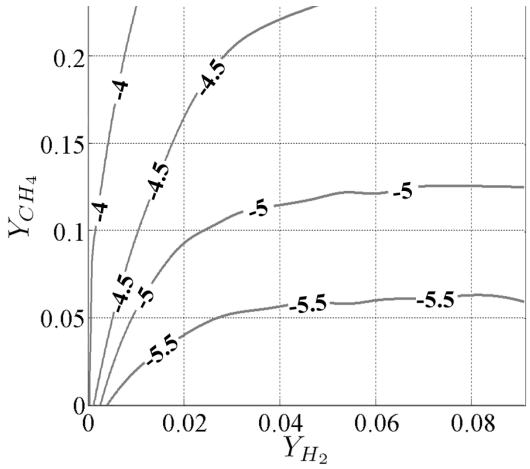

(b) CH_4-H_2 fuel blend with an intial mixture temperature of 2000 ^{o}K.

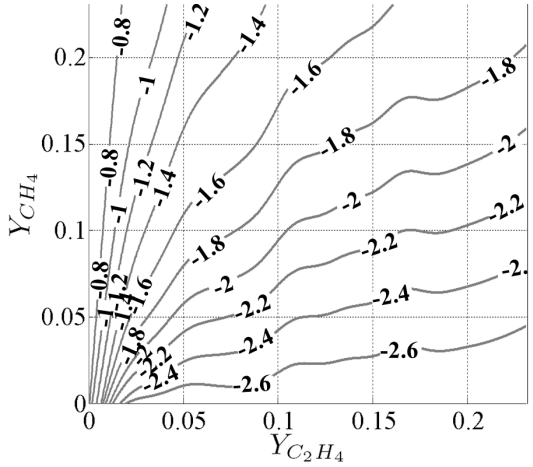

(c) CH_4-C_2H_4 fuel blend with an intial mixture temperature of 1000 ^{o}K.

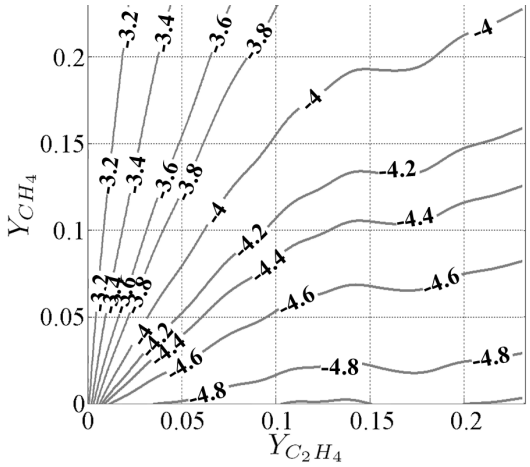

(d) CH_4-C_2H_4 fuel blend with an intial mixture temperature of 2000 ^{o}K.

Figure 78: Ignition delays maps ($\log(\tau_{ign})$) in s at P = 50.7 kPa.

APPENDIX D

INTERPOLATION-EXTRAPOLATION METHOD BASED ON THE HEAT EQUATION

Let $T(\mathbf{r},t)$ be the temperature distribution where $\mathbf{r} = [x_1, x_2, x_3] \in \mathbf{D} = [0, L_1] \times [0, L_2] \times [0, L_3]$ and $t \in [0, \infty[$. The heat equation relates the time rate of change of the temperature inside a volume element to the heat diffused at its boundary ($\mathrm{k}\Delta T = \nabla.(k\nabla T) = \nabla.\mathbf{q}$).

$$\frac{\partial T}{\partial t} = \alpha \Delta T \tag{79}$$

Equation (79) is written in the Cartesian frame :

$$\frac{\partial T}{\partial t} = \alpha \left(\frac{\partial^2 T}{\partial x_1^2} + \frac{\partial^2 T}{\partial x_2^2} + \frac{\partial^2 T}{\partial x_3^2} \right) \tag{80}$$

where $\alpha = \frac{k}{\rho C_p}$ is a property of the material. The method of separation of variable used to solve this type of equation suggests that the temperature distribution is the product of three function τ, X, Y and Z which depends only on t, x_1, x_2 and x_3, respectively.

$$T(\mathbf{r},t) = \tau(t) X(x_1) Y(x_2) Z(x_3) \tag{81}$$

Equation (81) is substituted in Eq. (80)

$$\frac{1}{\alpha} \tau' XYZ = \tau X'' YZ + \tau XY'' Z + \tau XYZ'' \tag{82}$$

dividing by $TXYZ$ yields

$$\frac{1}{\alpha}\frac{\tau'}{\tau} = \frac{X''}{X} + \frac{Y''}{Y} + \frac{Z''}{Z} \tag{83}$$

Equation (83) holds for at any time and location only if each fraction matches a constant. For time causality reason, this constant is negative: $-k^2$.

$$\frac{1}{\alpha}\frac{\tau'}{\tau} = -k^2 \tag{84}$$

$$\frac{X''}{X} = -k_1^2 \tag{85}$$

$$\frac{Y''}{Y} = -k_2^2 \tag{86}$$

$$\frac{Z''}{Z} = -k_3^2 \tag{87}$$

with the following dispersion relation $k^2 = k_1^2 + k_2^2 + k_3^2$. A general solution for T is therefore

$$\tau(t) = \tau_0 e^{-k^2 \alpha t} \tag{88}$$

$$X(x_1) = A\cos(k_1 x_1) + B\sin(k_1 x_1) \tag{89}$$

$$Y(x_2) = C\cos(k_2 x_2) + D\sin(k_2 x_2) \tag{90}$$

$$Z(x_3) = E\cos(k_3 x_3) + F\sin(k_3 x_3) \tag{91}$$

D.1 Boundary Conditions

The temperature distribution at the leading edge $(0, x_2, x_3)$ is imposed by the flame and the recirculating products in the cavity. Therefore the system has non-homogeneous boundary conditions, as heat is transferred from the cavity to the ramp structure. The system with non-homogenous boundary conditions **E** is

$$T(0, x_2, x_3) = f_1^-(x_2, x_3) \tag{92}$$

$$T(L_1, x_2, x_3) = f_1^+(x_2, x_3) \tag{93}$$

$$T(x_1, 0, x_3) = f_2^-(x_2, x_3) \tag{94}$$

$$T(x_1, L_2, x_3) = f_2^+(x_2, x_3) \tag{95}$$

$$T(x_1, x_2, 0) = f_3^-(x_1, x_2) \tag{96}$$

$$T(x_1, x_2, L_3) = f_3^+(x_1, x_2) \tag{97}$$

Therefore an orthogonal basis on which the non-homogeneous terms are decomposed, is determined by solving the homogeneous problem $\mathbf{E}_0$ with mixed boundary conditions. Using the superimposition property of the system, solution becomes a linear combination of the solution with Dirichlet and Neumann boundary conditions: $T = aT_D + bT_N$ with $a, b \in \mathbb{R}$. The Dirichlet boundary conditions is impose that

$$T_D(0, x_2, x_3) = 0 \tag{98}$$

$$T_D(L_1, x_2, x_3) = 0 \tag{99}$$

$$T_D(x_1, 0, x_3) = 0 \tag{100}$$

$$T_D(x_1, L_2, x_3) = 0 \tag{101}$$

$$T_D(x_1, x_2, 0) = 0 \tag{102}$$

$$T_D(x_1, x_2, L_3) = 0 \tag{103}$$

Similarly, the Neumann conditions are the homogeneous boundary conditions for the normal derivative of the temperature distribution.

$$\frac{\partial T_N}{\partial x_1}|_{0,x_2,x_3} = 0 \tag{104}$$

$$\frac{\partial T_N}{\partial x_1}|_{L_1,x_2,x_3} = 0 \tag{105}$$

$$\frac{\partial T_N}{\partial x_2}|_{x_1,0,x_3} = 0 \tag{106}$$

$$\frac{\partial T_N}{\partial x_2}|_{x_1,L_2,x_3} = 0 \tag{107}$$

$$\frac{\partial T_N}{\partial x_3}|_{x_1,x_2,0} = 0 \tag{108}$$

$$\frac{\partial T_N}{\partial x_3}|_{x_1,x_2,L_3} = 0 \tag{109}$$

D.1.1 Dirichlet Solution

Recalling the product form of the general solution in Eq. (81), Eqs. (98)-(103) simplify to

$$X(0) = 0 \tag{110}$$

$$X(L_1) = 0 \tag{111}$$

$$Y(0) = 0 \tag{112}$$

$$Y(L_2) = 0 \tag{113}$$

$$Z(0) = 0 \tag{114}$$

$$Z(L_3) = 0 \tag{115}$$

Equations (110)-(115) can be written under the following matricial form

$$\begin{bmatrix} 1 & 0 & 0 & 0 & 0 & 0 \\ \cos(k_1 L_1) & B\sin(k_1 L_1) & 0 & 0 & 0 & 0 \\ 0 & 0 & 1 & 0 & 0 & 0 \\ 0 & 0 & \cos(k_2 L_2) & \sin(k_2 L_2) & 0 & 0 \\ 0 & 0 & 0 & 0 & 1 & 0 \\ 0 & 0 & 0 & 0 & \cos(k_3 L_3) & \sin(k_3 L_3) \end{bmatrix} \begin{bmatrix} A \\ B \\ C \\ D \\ E \\ F \end{bmatrix} = \begin{bmatrix} 0 \\ 0 \\ 0 \\ 0 \\ 0 \\ 0 \end{bmatrix} \tag{116}$$

which is true for any A, B, C, D, E and $F \in \mathbb{R}$ if the determinant of the matrix is null.

$$\sin(k_1 L_1) = 0 \tag{117}$$

$$\sin(k_2 L_2) = 0 \tag{118}$$

$$\sin(k_3 L_3) = 0 \tag{119}$$

Therefore,

$$k_{1,i} = \frac{i\pi}{L_1} \tag{120}$$

$$k_{2,j} = \frac{j\pi}{L_2} \tag{121}$$

$$k_{3,k} = \frac{k\pi}{L_3} \tag{122}$$

where i, j and $k \in \mathbb{N}$. The steady state solution with Dirichlet boundary conditions is

$$T_D(\mathbf{r}) = \left\{ \sum_{i=1}^{\infty} B_i \sin\left(i\pi \frac{x_1}{L_1} \right) \right\} \left\{ \sum_{j=1}^{\infty} D_j \sin\left(j\pi \frac{x_2}{L_2} \right) \right\} \left\{ \sum_{k=1}^{\infty} E_k \sin\left(k\pi \frac{x_3}{L_3} \right) \right\} \tag{123}$$

D.1.2 Neumann Solution

Similarly to Eqs. (110)-(115), the Neumann condition translates into

$$X'(0) = 0 \tag{124}$$

$$X'(L_1) = 0 \tag{125}$$

$$Y'(0) = 0 \tag{126}$$

$$Y'(L_2) = 0 \tag{127}$$

$$Z'(0) = 0 \tag{128}$$

$$Z'(L_3) = 0 \tag{129}$$

The steady state solution with Neumann boundary conditions is therefore

$$T_N(\mathbf{r}) = \left\{ \sum_{i=1}^{\infty} A_i \cos\left(\frac{2i-1}{2} \pi \frac{x_1}{L_1} \right) \right\} \left\{ \sum_{j=1}^{\infty} C_j \cos\left(\frac{2j-1}{2} \pi \frac{x_2}{L_2} \right) \right\} \left\{ \sum_{k=1}^{\infty} D_k \cos\left(\frac{2k-1}{2} \pi \frac{x_3}{L_3} \right) \right\} \tag{130}$$

The sine and cosine terms are also called the Eigen functions, and are orthogonal with respect to the inner product $(,)$ on $[0, L_x] \times [0, L_y] \times [0, L_z]$, defined as

$$(u, v) = 2^3 \int_0^{L_1} \int_0^{L_2} \int_0^{L_3} u(x_1, x_2, x_3) v(x_1, x_2, x_3) dx_1 dx_2 dx_3 \tag{131}$$

The Eigen function basis for the problem with Dirichlet boundary conditions is

$$B_D : \left\{ \sin\left(i\pi\frac{x_1}{L_1}\right), \sin\left(j\pi\frac{x_2}{L_2}\right), \sin\left(k\pi\frac{x_3}{L_3}\right) \right\}, \ [i\ j\ k] \in \mathbb{N}^3 \tag{132}$$

Similarly, with Neumann boundary conditions

$$B_N : \left\{ \cos\left(\frac{2i-1}{2}\pi\frac{x_1}{L_1}\right), \cos\left(\frac{2j-1}{2}\pi\frac{x_2}{L_2}\right), \cos\left(\frac{2k-1}{2}\pi\frac{x_3}{L_3}\right) \right\} , \ [i\ j\ k] \in \mathbb{N}^3 \tag{133}$$

As mentioned previously, the Eigen functions form an orthogonal basis, and one can verify that

$$\left(\sin\left(i\pi\frac{x}{L}\right), \sin\left(j\pi\frac{x}{L}\right)\right) = 2^3 \int_0^L \sin\left(i\pi\frac{x}{L}\right) \sin\left(j\pi\frac{x}{L}\right) dx = 2^2\delta_{ij} \tag{134}$$

and

$$\begin{aligned} &\left(\cos\left(\frac{2i-1}{2}\pi\frac{x}{L}\right), \cos\left(\frac{2i-1}{2}\pi\frac{x}{L}\right)\right) \\ &= 2^3 \int_0^L \cos\left(\frac{2i-1}{2}\pi\frac{x}{L}\right) \cos\left(\frac{2i-1}{2}\pi\frac{x}{L}\right) dx \\ &= 2^2\delta_{ij} \end{aligned} \tag{135}$$

Furthermore both odd and even terms are orthogonal

$$\left(\sin\left(i\pi\frac{x}{L}\right), \cos\left(\frac{2i-1}{2}\pi\frac{x}{L}\right)\right) = 0 \tag{136}$$

which implies that both function spaces obtained from Dirichlet and Neumann problems are normal (or disjoint)

$$C_N \cap C_D = \oslash \tag{137}$$

The latter property is important when projecting the solution onto the Eigen space as no overlap term (or cross-term in Eq. (136)) need to be subtracted.

The temperature distribution is expressed as a linear combination of the Neumann and Dirichlet solutions

$$T(\mathbf{r}) = \left\{ \sum_{i=0}^{\infty} A_i \cos\left(\frac{2i-1}{2}\pi\frac{x_1}{L_1}\right) + B_i \sin\left(i\pi\frac{x_1}{L_1}\right) \right\} \left\{ \sum_{j=0}^{\infty} C_j \cos\left(\frac{2j-1}{2}\pi\frac{x_2}{L_2}\right) + D_j \sin\left(j\pi\frac{x_2}{L_2}\right) \right\} \left\{ \sum_{k=0}^{\infty} E_k \cos\left(\frac{2k-1}{2}\pi\frac{x_3}{L_3}\right) + F_k \sin\left(k\pi\frac{x_3}{L_3}\right) \right\} \tag{138}$$

D.1.3 Steady, Non-Homogeneous Solution

The orthogonally property of the Eigen functions allows coefficients A, B, C, D, E and F to be retrieved by projecting of the general solution in Eq. (138) onto the Eigen space. The temperature distribution on the boundary (Eqs. (92)-(97)) is captured by polynomials in the product form such as: $f(x_i, x_j) = P_1(x_i)P_2(x_j)$ where P_1 and P_2 are polynomials of order o_1 and o_2, respectively. Furthermore, the polynomial form is chosen based on the following assumptions:

1. The temperature distribution is smooth ($C^{3,\infty}$) and has a relatively low wavenumber (or spatial frequency), such that it may be reduced to a polynomial with a relatively low order.

2. There exists a polynomial of order sufficiently high to match the steady state solution which can be found via a Taylor expansion about a point in the domain.

3. The temperature distribution at the boundary has a product form, as in Eq. (81).

The next part of this section focuses on finding the temperature distribution inside the ramp, when imposing a polynomial form to the boundary temperature profile.

Given the product form of the solution, the projection can be carried out independently on each polynomial. For instance, Eq. (92) is written as follow:

$$f_1^-(x_2, x_3) = f_0^{1-} \left(\prod_{l=1}^{o_2} x_2 - \lambda_{2,l}^{1-} \right) \left(\prod_{n=1}^{o_3} x_3 - \lambda_{3,n}^{1-} \right) \tag{139}$$

where $\lambda_{3,n}^{1-}$ denotes the n-th root of the polynomial, along the 3-direction, evaluated at the side normal to the 1-direction. The $\pm$ upper script indicates whether the boundary is taken at $x = 0$ or $x = L$.

The polynomial form in Eq. (139) is expressed in term of the general solution found in Eq. (138), at the boundary ($x_1 = 0$)

$$\begin{aligned} T(0, x_2, x_3) = & \left\{ \sum_{i=0}^{\infty} A_i \right\} \\ & \left\{ \sum_{j=0}^{\infty} C_j \cos\left(\frac{2j-1}{2} \pi \frac{x_2}{L_2} \right) + D_j \sin\left(j\pi \frac{x_2}{L_2} \right) \right\} \\ & \left\{ \sum_{k=0}^{\infty} E_k \cos\left(\frac{2k-1}{2} \pi \frac{x_3}{L_3} \right) + F_k \sin\left(k\pi \frac{x_3}{L_3} \right) \right\} \\ = & f^{1-}(x_2, x_3) = f_0^{1-} \left(\prod_{l=1}^{o_1} x_2 - \lambda_{2,l}^{1-} \right) \left(\prod_{n=1}^{o_3} x_3 - \lambda_{3,n}^{1-} \right) \end{aligned} \tag{140}$$

The terms of same direction are then matched independently,

$$f_0^{1-} = \sum_{i=0}^{\infty} A_i \tag{141}$$

$$\prod_{l=1}^{5} x_2 - \lambda_{2,l}^{1-} = \sum_{j=0}^{\infty} C_j \cos\left(\frac{2j-1}{2} \pi \frac{x_2}{L_2} \right) + D_j \sin\left(j\pi \frac{x_2}{L_2} \right) \tag{142}$$

$$\prod_{n=1}^{5} x_3 - \lambda_{3,n}^{1-} = \sum_{k=0}^{\infty} E_k \cos\left(\frac{2k-1}{2} \pi \frac{x_3}{L_3} \right) + F_k \sin\left(k\pi \frac{x_3}{L_3} \right) \tag{143}$$

The coefficients C, D, E and F in Eqs. (142) and (143) are the Fourier coefficients

$$f_0^{1+} = \sum_{i=0}^{\infty} A_i \tag{144}$$

$$C_j = 2\int_0^{L_2} \left(\prod_{m=1}^{o_2} x_2 - \lambda_{2,m}^{1-} \right) \cos\left(\frac{2j-1}{2} \pi \frac{x_2}{L_2} \right) dx_2 \tag{145}$$

$$D_j = 2\int_0^{L_2} \left(\prod_{m=1}^{o_2} x_2 - \lambda_{2,m}^{1-} \right) \sin\left(j\pi \frac{x_2}{L_2} \right) dx_2 \tag{146}$$

$$E_k = 2\int_0^{L_3} \left(\prod_{n=1}^{o_3} x_3 - \lambda_{3,n}^{1-} \right) \cos\left(\frac{2k-1}{2} \pi \frac{x_3}{L_3} \right) dx_3 \tag{147}$$

$$F_k = 2\int_0^{L_3} \left(\prod_{n=1}^{o_3} x_3 - \lambda_{3,n}^{1-} \right) \sin\left(k\pi \frac{x_3}{L_3} \right) dx_3 \tag{148}$$

The same reasoning is carried out with the x_2-axis. At $x_2 = 0$,

$$\begin{aligned} T(x_1, 0, x_3) = & \left\{ \sum_{i=0}^{\infty} A_i \cos\left(\frac{2i-1}{2} \pi \frac{x_1}{L_1} \right) + B_i \sin\left(i\pi \frac{x_1}{L_1} \right) \right\} \\ & \left\{ \sum_{j=0}^{\infty} C_j \right\} \\ & \left\{ \sum_{k=0}^{\infty} E_k \cos\left(\frac{2k-1}{2} \pi \frac{x_3}{L_3} \right) + F_k \sin\left(k\pi \frac{x_3}{L_3} \right) \right\} \\ & = f_2^-(x_1, x_3) = f_0^{2-} \left(\prod_{l=1}^{o_1} x_1 - \lambda_{1,l}^{2-} \right) \left(\prod_{n=1}^{o_3} x_3 - \lambda_{3,n}^{2-} \right) \end{aligned} \tag{149}$$

which can be written in a form similar to Eqs. (144) - (148).

$$f_0^{2-} = \sum_{j=0}^{\infty} C_j \tag{150}$$

$$A_i = 2\int_0^{L_1} \left(\prod_{l=1}^{o_1} x_1 - \lambda_{1,l}^{2-} \right) \cos\left(\frac{2i-1}{2} \pi \frac{x_1}{L_1} \right) dx_1 \tag{151}$$

$$B_i = 2\int_0^{L_1} \left(\prod_{l=1}^{o_1} x_1 - \lambda_{1,l}^{2-} \right) \sin\left(i\pi \frac{x_1}{L_1} \right) dx_1 \tag{152}$$

$$E_k = 2\int_0^{L_3} \left(\prod_{n=1}^{o_3} x_3 - \lambda_{3,n}^{2-} \right) \cos\left(\frac{2k-1}{2} \pi \frac{x_3}{L_3} \right) dx_3 \tag{153}$$

$$F_k = 2\int_0^{L_3} \left(\prod_{n=1}^{o_3} x_3 - \lambda_{3,n}^{2-} \right) \sin\left(k\pi \frac{x_3}{L_3} \right) dx_3 \tag{154}$$

The boundary condition at $x_2 = L_2$ provides additional constraints on the coefficients A, B, E and F.

$$f_0^{2+} = \sum_{j=0}^{\infty} (-1)^j C_j \tag{155}$$

$$A_i = 2\int_0^{L_1} \left(\prod_{l=1}^{o_1} x_1 - \lambda_{1,l}^{2+} \right) \cos\left(\frac{2i-1}{2} \pi \frac{x_1}{L_1} \right) dx_1 \tag{156}$$

$$B_i = 2\int_0^{L_1} \left(\prod_{l=1}^{o_1} x_1 - \lambda_{1,l}^{2+} \right) \sin\left(i\pi \frac{x_1}{L_1} \right) dx_1 \tag{157}$$

$$E_k = 2\int_0^{L_3} \left(\prod_{n=1}^{o_3} x_3 - \lambda_{3,n}^{2+} \right) \cos\left(\frac{2k-1}{2} \pi \frac{x_3}{L_3} \right) dx_3 \tag{158}$$

$$F_k = 2\int_0^{L_3} \left(\prod_{n=1}^{o_3} x_3 - \lambda_{3,n}^{2+} \right) \sin\left(k\pi \frac{x_3}{L_3} \right) dx_3 \tag{159}$$

It implies that the solution at $x_2 = L_2$ is rescaled from the solution at $x_2 = 0$. This is in fact the similarity property induced by the separation of variable. Consequently,

$$\lambda_{1,l}^{2-} = \lambda_{1,l}^{2+} \tag{160}$$

$$\lambda_{3,n}^{2-} = \lambda_{3,n}^{2+} \tag{161}$$

$$\lambda_{3,n}^{2+} = \lambda_{3,n}^{1-} \tag{162}$$

Equation (162) is obtained by comparing Eqs. (147) and (148) with Eqs. (158) and (159). The same reasoning is carried out with the x_3-axis, at $x_3 = 0$

$$f_0^{3-} = \sum_{k=0}^{\infty} E_k \tag{163}$$

$$A_i = 2\int_0^{L_1} \left(\prod_{l=1}^{o_1} x_1 - \lambda_{1,l}^{3-} \right) \cos\left(\frac{2i-1}{2} \pi \frac{x_1}{L_1} \right) dx_1 \tag{164}$$

$$B_i = 2\int_0^{L_1} \left(\prod_{l=1}^{o_1} x_1 - \lambda_{1,l}^{3-} \right) \sin\left(i\pi \frac{x_1}{L_1} \right) dx_1 \tag{165}$$

$$C_j = 2\int_0^{L_2} \left(\prod_{m=1}^{o_2} x_2 - \lambda_{2,m}^{3-} \right) \cos\left(\frac{2j-1}{2} \pi \frac{x_2}{L_2} \right) dx_2 \tag{166}$$

$$D_j = 2\int_0^{L_2} \left(\prod_{m=1}^{o_2} x_2 - \lambda_{2,m}^{3-} \right) \sin\left(j\pi \frac{x_2}{L_2} \right) dx_2 \tag{167}$$

and at $x_3 = L_3$

$$f_0^{3+} = \sum_{k=0}^{\infty} (-1)^k E_k \tag{168}$$

$$A_i = 2\int_0^{L_1} \left(\prod_{l=1}^{o_1} x_1 - \lambda_{1,l}^{3+} \right) \cos\left(\frac{2i-1}{2} \pi \frac{x_1}{L_1} \right) dx_1 \tag{169}$$

$$B_i = 2\int_0^{L_1} \left(\prod_{l=1}^{o_1} x_1 - \lambda_{1,l}^{3+} \right) \sin\left(i\pi \frac{x_1}{L_1} \right) dx_1 \tag{170}$$

$$C_j = 2\int_0^{L_2} \left(\prod_{m=1}^{o_2} x_2 - \lambda_{2,m}^{3+} \right) \cos\left(\frac{2j-1}{2} \pi \frac{x_2}{L_2} \right) dx_2 \tag{171}$$

$$D_j = 2\int_0^{L_2} \left(\prod_{m=1}^{o_2} x_2 - \lambda_{2,m}^{3+} \right) \sin\left(j\pi \frac{x_2}{L_2} \right) dx_2 \tag{172}$$

which leads to

$$\lambda_{1,l}^{3-} = \lambda_{1,l}^{3+} \tag{173}$$

$$\lambda_{2,m}^{3-} = \lambda_{2,m}^{3+} \tag{174}$$

$$\lambda_{1,l}^{3-} = \lambda_{1,l}^{2-} \tag{175}$$

$$\lambda_{2,m}^{3-} = \lambda_{2,m}^{1-} \tag{176}$$

Equations on λ (Eqs. (160)-(162) and (173)-(176)) suggest that there is a common root for each direction (the upper scripts of $\lambda_{i,l}^{j}$ are not relevant to the problem).

$$f_1^-(x_2, x_3) = f_0^{1-} \left(\prod_{m=1}^{o_2} x_2 - \lambda_{2,m} \right) \left(\prod_{n=1}^{o_3} x_3 - \lambda_{3,n} \right) \tag{177}$$

$$f_2^-(x_1, x_3) = f_0^{2-} \left(\prod_{l=1}^{o_1} x_1 - \lambda_{1,l} \right) \left(\prod_{n=1}^{o_3} x_3 - \lambda_{3,n} \right) \tag{178}$$

$$f_2^+(x_1, x_3) = f_0^{2+} \left(\prod_{l=1}^{o_1} x_1 - \lambda_{1,l} \right) \left(\prod_{n=1}^{o_3} x_3 - \lambda_{3,n} \right) \tag{179}$$

$$f_3^-(x_1, x_2) = f_0^{3-} \left(\prod_{l=1}^{o_1} x_1 - \lambda_{1,l} \right) \left(\prod_{m=1}^{o_2} x_2 - \lambda_{2,m} \right) \tag{180}$$

$$f_3^+(x_1, x_2) = f_0^{3+} \left(\prod_{l=1}^{o_1} x_1 - \lambda_{1,l} \right) \left(\prod_{m=1}^{o_2} x_2 - \lambda_{2,m} \right) \tag{181}$$

and

$$f_0^{1-} = \sum_{i=0}^{\infty} A_i \tag{182}$$

$$f_0^{2-} = \sum_{j=0}^{\infty} C_j \tag{183}$$

$$f_0^{2+} = \sum_{j=0}^{\infty} (-1)^j C_j \tag{184}$$

$$f_0^{3-} = \sum_{k=0}^{\infty} E_k \tag{185}$$

$$f_0^{3+} = \sum_{k=0}^{\infty} (-1)^k E_k \tag{186}$$

where

$$A_i = 2\int_0^{L_1}\left(\prod_{l=1}^{o_1} x_1 - \lambda_{1,l}\right)\cos\left(\frac{2i-1}{2}\pi\frac{x_1}{L_1}\right)dx_1 \tag{187}$$

$$B_i = 2\int_0^{L_1}\left(\prod_{l=1}^{o_1} x_1 - \lambda_{1,l}\right)\sin\left(i\pi\frac{x_1}{L_1}\right)dx_1 \tag{188}$$

$$C_j = 2\int_0^{L_2}\left(\prod_{m=1}^{o_2} x_2 - \lambda_{2,m}\right)\cos\left(\frac{2j-1}{2}\pi\frac{x_2}{L_2}\right)dx_2 \tag{189}$$

$$D_j = 2\int_0^{L_2}\left(\prod_{m=1}^{o_2} x_2 - \lambda_{2,m}\right)\sin\left(j\pi\frac{x_2}{L_2}\right)dx_2 \tag{190}$$

$$E_k = 2\int_0^{L_3}\left(\prod_{n=1}^{o_3} x_3 - \lambda_{3,n}\right)\cos\left(\frac{2k-1}{2}\pi\frac{x_3}{L_3}\right)dx_3 \tag{191}$$

$$F_k = 2\int_0^{L_3}\left(\prod_{n=1}^{o_3} x_3 - \lambda_{3,n}\right)\sin\left(k\pi\frac{x_3}{L_3}\right)dx_3 \tag{192}$$

D.2 Resolution

Consequently, imposing a polynomial profile at the boundaries of the system implies that the internal temperature distribution is also a polynomial, as revealed by Eqs. (177)-(181) and (187)-(192). This is a result of the separation of variable method, which induces a similarity property of the temperature profile in each direction. Henceforth, the steady state solution is a product of three polynomials $P_1(x_1)$, $P_2(x_2)$ and $P_3(x_3)$.

$$T(\mathbf{r}) = \lambda_0\left(\prod_{i=1}^{5}(x_1-\lambda_i)\right)\left(\prod_{i=6}^{10}(x_2-\lambda_i)\right)\left(\prod_{i=11}^{15}(x_3-\lambda_i)\right) \tag{193}$$

and Eqs. (177)-(192) give the relations between the harmonic (commonly used to solve the heat equation) and the polynomial form. To ensure that the system can be resolved, the number of unknowns (λ_i) has to match the number of equations. There are 8 thermocouple probes located by $\mathbf{r}_{1,8}$, which gives the following system to minimize:

$$\frac{\tilde{T}(\mathbf{r}_j)}{\lambda_0} - \left(\prod_{i=1}^{5}(x_{1,j}-\lambda_i)\right)\left(\prod_{i=6}^{10}(x_{2,j}-\lambda_i)\right)\left(\prod_{i=11}^{15}(x_{3,j}-\lambda_i)\right) \to 0, \quad j \in [1:8] \tag{194}$$

where $\tilde{T}$ is the actual temperature measured by the thermocouples. In addition, the heat equation at steady state is evaluated at the thermocouple locations (Eq. (82) with null right hand side), and give 8 other equations:

$$\begin{aligned} &P_1(x_1,j)''P_2(x_2,j)P_3(x_3,j) + P_1(x_1,j)P_2(x_2,j)''P_3(x_3,j) \\ &\qquad + P_1(x_1,j)P_2(x_2,j)P_3(x_3,j)'' \to 0,\ j \in [1:8] \end{aligned} \tag{195}$$

In order to have a system properly constrained, the problem must have 16 unknowns. Therefore, P_1, P_2 and P_3 can be fifth order polynomials ($o_1 = o_2 = o_3 = 5$) since fifth order polynomials admit an analytic root solution (Galois group of polynomials), which ease the process of root placement in the minimization algorithm. The minimization problem involves a compromise between fitting the polynomial form on the experimental data (magnitude) and satisfying the steady state constraint (curvature). The minimization algorithm is based on Newton-Raphson and dichotomy methods with higher tolerances on Eq. (195). The initialization process is described in Section 3.6.

REFERENCES

[1] "Aerospaceweb, atmospheric properties calculator." http://www.aerospaceweb.org/design/scripts/atmosphere.

[2] "Gri-mech thermodynamic data, nasa polynomial format for chemkin-ii." http://www.me.berkeley.edu/gri-mech/data/species/thermo.dat.

[3] "Historique de l'institut aerotechnique de saint-cyr-l'ecole." http://www.iat.cnam.fr/institut/histoire/historique.htm.

[4] "Nasa, earth atmosphere model." http://www.grc.nasa.gov/WWW/k-12/airplane/atmosmet.html.

[5] "Pratt and whitney hypersonics, x-51a." www.pwrhypersonics.com.

[6] "Equations, tables, and charts for compressible flow," Tech. Rep. 1135, National Advisory Committee for Aeronautics, Washington, DC, 1953.

[7] "Wall heat flux measurements for uni-element rocket firings," Tech. Rep. NAG8-1792, The Pennsylvania State University, University Park, PA, 2004.

[8] Ali, M. C. M. and Kurian, J., "Performance of aft-ramp cavities for flame stabilization in supersonic flows," *Journal of Propulsion and Power*, vol. 24, pp. 635–637, 2008.

[9] Baurle, R. A. and Eklund, D. R., "Analysis of dual-mode hydrocarbon scramjet operation at mach 46.5," *Journal of Propulsion and Power*, vol. 18, pp. 990–1002, 2002.

[10] Baurle, R. A., Fuller, R. P., White, J. A., Chen, T. H., Gruber, M. R., and Nejad, A. S., "An investigation of advanced fuel injection schemes for scramjet combustion," (Reno, NV), 1998.

[11] Baurle, R. A. and Gruber, M. R., "A study of recessed cavity flowfields for supersonic combustion applications," (Reno, NV), 1998.

[12] Baurle, R. A., Mathur, T., Gruber, M. R., and Jackson, K. R., "Numerical and experimental investigation of a scramjet combustor for hypersonic missile applications," (Cleveland, OH), 1998.

[13] Baurle, R. A., Tarn, C.-J., and Dasgupta, S., "Analysis of unsteady cavity flows for scramjet applications," (Huntsville, AL), 2000.

[14] Ben-Yakar, A. and Hanson, R. K., "Cavity flameholders for ignition and flame stabilization in scramjets: Review and experimental study," (Cleveland, OH), 1998.

[15] Ben-Yakar, A. and Hanson, R. K., "Supersonic combustion of cross-flow jets and the influence of cavity flame-holders," (Reno, NV), 1999.

[16] Ben-Yakar, A., Kamel, M., Morris, C., and Hanson, R. K., "Experimental investigation of h2 transverse jet combustion in hypervelocity flows," (Seattle, WA), 1997.

[17] Ben-Yakar, A., Kamel, M., Morris, C., and Hanson, R. K., "Hypersonic combustion and mixing studies using simultaneous oh-plif and schlieren imaging," (Reno, NV), 1998.

[18] Blackwell, B. F., Gill, W., Dowding, K. J., and Voth, T. E., "Determination of thermal conductivity of 304 stainless steel using parameter estimation techniques," (Pittsburgh,, PA), 2000.

[19] Cabell, K., Hass, N., Storch, A., and Gruber, M. R., "Hifire direct-connect rig (hdcr) phase i scramjet test results from the nasa langley arc-heated scramjet test facility," (San Fransisco, CA), 2011.

[20] Cheng, R. K. and Oppenheim, A. K., "Autoignition in methane-hydrogen mixtures," *Combustion and Flames*, vol. 58, pp. 125–139, 1984.

[21] Choi, J. J., Ghodke, C., and Menon, S., "Large-eddy simulation of cavity flame-holding in a mach 2.5 cross flow," (Orlando, FL), 2010.

[22] Davis, D. L. and Bowersox, R. D. W., "Computational fluid dynamics analysis of cavity flame holders for scramjets," (Seattle, WA), 1997.

[23] deRidder, M. A., Helderman, D. A., Nugent, N. J., , and Anderson, W. E., "Measurement and analysis of heat transfer in a multi- element hydrogen/oxygen rocket combustor," (Hartford, CT), 2008.

[24] Dillman, B. A., Dillman, B. L., and Prill, F. W., "Methods of extinguishing fires." US Patent 2010/0218960 A1, 2010.

[25] Dimotakis, P. E., "Entrainment in a fully developed, two-dimensional shear layer," (Reno, NV), 1984.

[26] Dimotakis, P. E., "Two-dimensional shear-layer entrainment," *AIAA*, vol. 24, pp. 1791–1796, 1993.

[27] Driscoll, J. F. and Rasmussen, C. C., "Correlation and analysis of blowout limits of flames in high-speed airflows," *Journal of Propulsion and Power*, vol. 21, pp. 454–457, 2005.

[28] Dugger, G. L., "Comparison of hypersonic ramjet engines with subsonic and supersonic combustion," *High Mach Number Airbreathing Engines*, pp. 84–110, 1961.

[29] Edwards, T. and Anderson, S. D., "Results of high temperature jp-7 cracking assessment," *AIAA*, no. 0806, 1993.

[30] Fernando, E. M. and Menon, S., "Mixing enhancement in compressible mixing layers: An experimental study," *AIAA*, vol. 31, pp. 278–285, 1993.

[31] Gerlinger, P., Stoll, P., Schneider, M. K. F., and Aigner, M., "Numerical investigation of mixing and combustion enhancement in supersonic combustors by strut induced streamwise vorticity," *Aerospace Science and Technology*, vol. 12, pp. 159–168, 2008.

[32] Goyne, C. P., McDaniel, J. C., Krauss, R. H., and Whitehurst, W. B., "Test gas vitiation effects in a dual-mode scramjet combustor," *Journal of Propulsion and Power*, vol. 23, pp. 559–565, 2007.

[33] Gruber, M. R., Baurle, R. A., Mathur, T., and Hsu, K. Y., "Fundamental studies of cavity-based flameholder concepts for supersonic combustors," *Journal of Propulsion and Power*, vol. 17, pp. 146–153, 2001.

[34] Gruber, M. R., Carter, D. C., Montes, D. R., Haubelt, L. C., King, P. I., and Hsu, K. Y., "Experimental studies of pylon-aided fuel injection into a supersonic crossflow," *Journal of Propulsion and Power*, vol. 24, pp. 460–470, 2008.

[35] Gruber, M. R., Donbar, J., Jackson, K., Mathur, T., Baurle, R., Eklund, D., and Smith, C., "Newly developed direct-connect high-enthalpy supersonic combustion research facility," *Journal of Propulsion and Power*, vol. 17, pp. 1296–1306, 2001.

[36] Gruber, M. R., Donbar, J., Jackson, T., Mathur, T., Eklund, D., and Billig, F., "Performance of an aerodynamic ramp feel injector in a scramjet combustor," (Huntsville, AL), 2000.

[37] Gruber, M. R., Donbar, J. M., Carter, C. D., and Hsu, K. Y., "Mixing and combustion studies using cavity-based flameholders in a supersonic flow," *Journal of Propulsion and Power*, vol. 20, pp. 769–778, 2004.

[38] Gruber, M. R. and Nejad, A. S., "New supersonic combustion research facility," *Journal of Propulusion and Power*, vol. 11, pp. 1080–1082, 1995.

[39] Guy, R. W., Rogers, R. C., Puster, R. L., Rock, K. E., and Diskin, G. S., "The nasa langley scramjet test complex," (Lake Buena Vista, FL), 1996.

[40] Hammock, G. L., "Arc heater capability upgrade at aedc," *ITEA Journal*, vol. 31, pp. 321–323, 2010.

[41] Heller, H. and Delfs, J., "Cavity pressure oscillations : The generating mechanism visualized," *Journal of Sound and Vibration*, vol. 196, pp. 248–252, 1996.

[42] Heller, H. H. and Bliss, D. B., "Aerodynamically induced pressure oscillations in cavities - physical mechanisms and suppression concepts," *Performer: Bolt Beranek and Newman, Inc., Cambridge, MA. Feb 1975. 224p. Report: BBN-2884; AFFDLTR-74-133*, 1975.

[43] Holman, J. P., *Heat Transfer*. McGrawHill Companies, 1997.

[44] Hsu, K. Y., Carter, C., Crafton, J., Gruber, M. R., Donbar, J., Mathur, T., and Terry, D. S. W., "Fuel distribution about a cavity flameholder in supersonic flow," (Huntsville, AL), 2000.

[45] Hsu, K. Y., Carter, C. D., Gruber, M. R., and Barhorst, T., "Experimental study of cavity-strut combustion in supersonic flow," *Journal of Propulsion and Power*, vol. 26, pp. 1237–1246, 2007.

[46] Jacobsen, L. S., Carter, C. D., Jackson, T. A., Williams, S., Barnett, J., Tam., C. J., Baurle, R. A., Bivolaru, D., and Kuo, S., "Plasma-assisted ignition in scramjets," *Journal of Propulsion and Power*, vol. 24, pp. 641–654, 2008.

[47] Jeong, E., O'Byrne, S., Jeung, I. S., and Houwing, A. F. P., "Investigation of supersonic combustion with angled injection in a cavity-based combustor," *Journal of Propulsion and Power*, vol. 24, pp. 1258–1268, 2008.

[48] Jeong, E., O'Byrne, S., Jeung, I. S., and Houwing, A. F. P., "Supersonic combustion on hydrogen fuel injection locations in a cavity-based combustor," (Hartford, CT), 2008.

[49] Jones, G., Protz, C., Bullard, B., and Hulka, J., "Local heat flux measurements with single element coaxial injectors," (Sacramento, CA), 2006.

[50] Krauss, R. H. and McDaniel, J. C., "A clean air continuous flow propulsion facility," (Nashville, TN), 1992.

[51] Kundu, K., Banerjee, D., and Bhaduri, D., "Theoretical analysis on flame stabilization by a bluff-body," *Combustion Science and Technology*, vol. 17, pp. 153–162, 1977.

[52] Lahr, M. D., Pitz, R. W., Douglas, Z. W., and Carter, C. D., "Hydroxyl-tagging-velocimetry measurements of a supersonic flow over a cavity," vol. 26, pp. 790–797, 2010.

[53] Le, D. B., Goyne, C. P., Krauss, R. H., and McDaniel, J. C., "Experimental study of a dual-mode scramjet isolator," *Journal of Propulsion and Power*, vol. 24, pp. 1050–1057, 2008.

[54] Lin, K. C., Jackson, K., Behdadnia, R., Jackson, T. A., Ma, F., Li, J., and Yang, V., "Acoustic characterization of an ethylene-fueled scramjet combustor with a recessed cavity flameholder," (Cincinnati, OH), 2007.

[55] Lin, K. C., Tam, C. J., Boxx, I., Carter, C., Jackson, K., and Lindsey, M., "Flame characteristics and fuel entrainment inside a cavity flame holder in a scramjet combustor," (Cincinnati, OH), 2007.

[56] Mach, H., "Evaluating co, co2 and h2o concentration by partial integration of absorption band spectra," *Centre de Documentation de l'Armement, Report: ISL-R-110/88*, 1988.

[57] Marshall, W. M., Pal, S., Woodward, R. D., and Santoro, R. J., "Benchmark wall heat flux data for a go_2/gh_2 single element combustor," (Tuscon, AZ), 2005.

[58] Mathur, T., Cox-Stouffer, S., Hsu, K. Y., Crafton, J., Donbar, J., and Gruber, M. R., "Experimental assessment of a feel injector for scramjet applications," (Huntsville, AL), 2000.

[59] Mathur, T., Gruber, M. R., Jackson, K., Donbar, J., Donaldson, W., Jackson, T., and Billig, F., "Supersonic combustion experiments with a cavity-based fuel injector," *Journal of Propulsion and Power*, vol. 17, pp. 1305–1312, 2001.

[60] Mathur, T., Lin, K. C., Kennedy, P., Gruber, M. R., Donbar, J., Jackson, T., and Billig, F., "Liquid jp-7 combustion in a scramjet combustor," (Huntsville, AL), 2000.

[61] Mawid, M. A. and Park, T. W., "Development of a detailed chemical kinetic mechanism for combustion of jp-7 fuel," (Huntsville, AL), 2003.

[62] McGilvray, M., Kirchhartz, R., and Jazra, T., "Comparison of mach 10 scramjet measurements from different impulse facilities," *AIAA*, vol. 48, pp. 1647–1651, 2010.

[63] McGilvray, M. and Morgan, R. G., "Effects of upstream injection on scramjet performance using an entropy-based method," *Journal of Propulsion and Power*, vol. 25, pp. 295–302, 2009.

[64] McMillin, B. K., Seitzman, J. M., and Hanson, R. K., "Comparison of no and oh planar fluorescence temperature measurements in scramjet model flowfields," *AIAA*, vol. 32, pp. 1945–1952, 1994.

[65] Menon, S., "Shock-wave induced mixing enhancement in scramjet combustors," (Reno, NV), pp. 295–301, 1989.

[66] Mestre, L. and Viaud, A., "Application of supersonic combustion to ramjets," *Aircraft Engineering*, vol. 38, no. 2, pp. 15–17, 1966.

[67] Micka, D. J. and Driscoll, J. F., "Dual-mode combustion of a jet in crossflow with cavity flameholder," (Reno, NV), 2008.

[68] Mitani, T. and Izumikawa, M., "Criteria for flame holding in h_2-fueled scramjet engines," *Proceedings of the Combustion Institute*, vol. 28, pp. 689–695, 2000.

[69] Mohamed, A., Verant, J. L., Ootegem, B. V., Viguier, P., Soutadee, J., and Tran, P., "Mid-infrared diode laser absorption spectroscopy measurements in co/co2 hypersonic flows of f4 and simoun," *European Space Agency*, vol. 659, 2009.

[70] Montgomery, C. J., Tang, Q., Bozzelli, J. W., and White, J. A., "Improved chemical kinetic models for scramjet combustion simulation," (Reno, NV), 2007.

[71] Mungal, M., Dimotakis, P., and Hermanson, J., "Reynolds number effects on mixing and combustion in a reacting shear layer," (Reno, NV), 1984.

[72] Neely, A. J., Riley, C., Boyce, R. R., Mudford, N. R., Houwing, A. F. P., and Gruber, M. R., "Hydrocarbon and hydrogen-fueled scramjet cavity flamholder performance at high flight mach numbers," (Norfolk, VA), 2003.

[73] Neely, A. J., Stotz, I., O'Byrne, S., Boyce, R. R., and Mudford, N. R., "Flow studies on a hydrogen-fueled cavity flame-holder scramjet," (Capua, Italy), 2005.

[74] Ozawa, R. I., "Survey of basic data on flame stabilization and propagation for high speed combustion systems," *U.S. Air Force,AFAPLTechnical Rept. TR-70-81, Wright-Patterson AFB, OH*, 1966.

[75] Peet, M. J., Hasan, H. S., and Bhadeshia, H. K. D. H., "Prediction of thermal conductivity of steel," *International Journal of Heat and Mass Transfer*, vol. 54, pp. 2602–2608, 2011.

[76] Perry, R. B., "Miniature supersonic wind tunnel design and testing on a practical basis," (Washington, DC).

[77] Pitz, R. W., Grady, N. R., Shopoff, S. W., Hu, S., and Carter, C. D., "Uv raman scattering measurements of a mach 2 reacting flow over a piloted cavity," (Reno, NV), 2008.

[78] Pitz, R. and Daily, J., "Combustion in a turbulent mixing layer formed at a rearward-facing step," *AIAA*, vol. 21, pp. 1565–1570, 1983.

[79] Puri, P., Ma, F., Choi, J. Y., and Yang, V., "Ignition characteristics of cracked jp-7 fuel," *Combustion and Flame*, vol. 142, pp. 454–457, 2005.

[80] Rasmussen, C. C., Dhanuka, S. K., and Driscoll, J. F., "Visualization of flameholding mechanisms in a supersonic combustor using plif," *Proceedings of the Combustion Institute*, vol. 30, pp. 2505–2512, 2007.

[81] Rasmussen, C. C. and Driscoll, J. F., "Blowout limits of flames in high-speed airflows: Critical damkohler number," (Hartford, CT), 2008.

[82] Rasmussen, C. C., Driscoll, J. F., Carter, C. D., Gruber, M. R., Donbar, J. M., and Hsu, K. Y., "Blowout limits of supersonic cavity-stabilized flames," *AIAA 2004-3660, 40th AIAA/ASME/SAE/ASEE Joint Propulsion Conference and Exhibit*, 2004.

[83] Rasmussen, C. C., Driscoll, J. F., Carter, C. D., Gruber, M. R., Donbar, J. M., and Hsu, K. Y., "Stability limits of cavity-stabilized flames in supersonic flow," *Proceedings of the Combustion Institute*, vol. 30, pp. 2825–2833, 2005.

[84] Rasmussen, C. C., Driscoll, J. F., Carter, C. D., and Hsu, K. Y., "Characteristics of cavity-stabilized flames in a supersonic flow," *Journal of Propulsion and Power*, vol. 21, pp. 765–768, 2005.

[85] Rasmussen, C. C., Driscoll, J. F., Carter, C. D., and Hsu, K. Y., "Characteristics of cavity-stabilized flames in a supersonic flow," *Journal of Propulsion and Power*, vol. 21, pp. 765–768, 2005.

[86] Retaureau, G. J., Kovitch, S. B., Verma, S., and Menon, S., "Experimental studies of cavity flame-holding in a mach 2.5 cross flow," (Orlando, FL), 2009.

[87] Rossiter, J. E., "Wind-tunnel experiments on the flow over rectangular cavities at subsonic and transonic speeds," *United Kingdom*, 1966.

[88] Saad, M. A., *Compressible Fluid Flow*. Prentice Hall, 1992.

[89] Sato, N., Imamura, A., Shiba, S., Takahashi, S., Tsue, M., and Kono, M., "Advanced mixing control in supersonic airstream with a wall-mounted cavity," *Journal of Propulsion and Power*, vol. 15, pp. 358–360, 1999.

[90] Schetz, J. A., *Boundary Layer Analysis, Revised*. AIAA Education Series, 2010.

[91] Segal, C., Owens, M. G., and Tehranian, S., "Flameholding configurations for kerosene combustion in a mach 1.8 airflow," (Seattle, WA), 1997.

[92] Slessor, M. D., Zhuang, M., and Dimotakis, P. E., "Turbulent shear-layer mixing: Growth-rate compressibility scaling," *Journal of Fluid Mechanics*, vol. 414, pp. 35–45, 2000.

[93] Sun, M. B., Wang, Z. G., Liang, J. H., and Geng, H., "Flame characteristics in supersonic combustor with hydrogen injection upstream of cavity flameholder," *Journal of Propulsion and Power*, vol. 24, pp. 688–696, 2008.

[94] Swithenbank, J., "Experimental investigation of hypersonic ramjets," *Proceedings of the International Council of the Aeronautical Sciences, Third Congress*, pp. 951–977, 1964.

[95] Tomioka, S., Hiraiwa, T., Kobayashi, K., Izumikawa, M., Kishida, T., and Yamasaki, H., "Vitiation effects on scramjet engine performance in mach 6 flight conditions," *Journal of Propulsion and Power*, vol. 23, pp. 789–796, 2007.

[96] Vasil'ev, A. A., "Ignition delay in multifuel mixtures," *Combustion, Explosion, and Shock Waves*, vol. 43, pp. 282–285, 2007.

[97] Vinogradov, V. A., Kobigsky, S. A., and Petrov, M. D., "Experimental investigation of kerosene fuel combustion in supersonic flow," *Journal of Propulsion and Power*, vol. 11, pp. 130–134, 1995.

[98] Wang, H., Sun, M., Qin, N., Wu, H., and Wang, Z., "Characteristics of oscillations in supersonic open cavity flows," *Flow, Turbulence and Combustion*, vol. 31, pp. 321–323, 2010.

[99] Winterfeld, G., "On the process of turbulent exchange behindflame holders," *Proceedings of the Combustion Institute*, vol. 10, pp. 1265–1275, 1965.

[100] Winterfeld, G., "Investigations on the stabilization of hydrogen diffusion flames in supersonic flow," *Deutschen Forshungs-undVersuchsanstalt fur Luft und Raumfahrt, Rept. FB-76-35, Porz-Wahn, Germany*, 1976.

[101] Witte, D. W., Irby, R. G., Auslender, A. H., and Rock, K. E., "1998 calibration of the mach 4.7 and mach 6 arc-heated scramjet test facility nozzles," Tech. Rep. NASA/TM-2004-213250, National Aeronautics and Space Administration, Langley Research Center, Hampton, Virginia, 2004.

[102] Youngbin, Y., "Blowout stability limits of a hydrogen jet flame in a supersonic, heated, coflowing air stream," *Combustion Science and Technology*, vol. 97, pp. 137–156, 1994.

[103] Yu, G., Li, J. G., Chang, X. Y., and Chen, L. H., "Investigation of fuel injection and flame stabilization in liquid hydrocarbon-fueled supersonic combustors," (Salt Lake City, UT), 2001.

[104] Yu, G., Li, J. G., Chang, X. Y., Chen, L. H., and Sung, C. J., "Investigation of fuel injection and flame stabilization in liquid hydrocarbon-fueled supersonic combustors," (Salt Lake City, UT).

[105] Yu, K., Wilson, K. J., Smith, R. A., and Schadow, K. C., "Experimental investigation on dual-purpose cavity in supersonic reacting flows," (Reno, NV), 1998.

[106] Yu, K. H. and Schadow, K. C., "Cavity-actuated supersonic mixing and combustion control," *Combustion and Flame*, vol. 99, pp. 295–301, 1994.

[107] Yu, K. H., Wilson, K. J., and Schadow, K. C., "Effect of flame-holding cavities on supersonic combustion performance," *Journal of Propulsion and Power*, vol. 17, pp. 1287–1295, 2001.

[108] Zhong, Z. and Song, W., "Investigation of design method of the resistance heated facility for supersonic combustion," (Orlando, FL), 2009.

[109] Zhuang, N., Alvi, F. S., Alkislar, M. B., and Shih, C., "Supersonic cavity flows and their control," *AIAA Journal*, vol. 44, pp. 2118–2128, 2006.

[110] Zukoski, E. E. and Marble, F. E., "Experiments concerning the mechanism of flame blowoff from bluff-bodies," *Proceedings of the Gas Dynamics Symposium on Thermochemistry*, pp. 205–255, 1956.

VITA

Ghislain Jean-Robert Retaureau was born on April 17, 1981 in Versailles, France to Catherine and Francois Retaureau. He grew up in the small village of Boinville-Le-Gaillard in France. His earliest childhood memories involve experimentation with energy, fire and acoustics. At the age of ten, he attempted unsuccessfully to build a nuclear reactor with a pressure cooker in his family treehouse and received 2nd degree burns. His fascination with pyrotechnics expanded to include acoustics, where he studied acoustical mechanics after earning his Baccalaurat in 2000. His undergraduate research focused heavily on resonating bodies and modeling acoustical instruments. At Universite du Maine he earned two Bachelors of Science degrees: Acoustics and Signal Processing (2002) and Quantum Physics (2003). He went on to pursue 3 Masters of Science degrees: Acoustics and Sensors in 2006 at ENSIM (France), Mechanical Engineering in 2006 at Georgia Institute of Technology (2006), and Aerospace Engineering in 2010 again at the Georgia Institute of Technology.

In addition to his ongoing academic appetite for engineering, Ghislain has pursued fashion design, narrative cinematography, and playing guitar in various bands in France and the United States. He currently resides in Atlanta, Georgia.